

Yerevan State University

Hayk Hakobyan

Observation of Quark Propagation Pattern in Nuclear Medium

Thesis for acquiring the degree of candidate of physical-mathematical science in
division 01.04.16 “nuclear, elementary particles and cosmic ray physics”

Scientific supervisors: Prof. W. Brooks and Prof A. Danagulyan

Yerevan 2008

TABLE OF CONTENTS

Introduction-----	5
1 Physics Motivation-----	9
1.1 Deep Inelastic Scattering and the Simple Quark-Parton Model-----	9
1.1.1 Strong coupling constant α_s -----	13
1.2 Semi-Inclusive Deep Inelastic Scattering-----	13
1.2.1 Semi-Inclusive DIS Cross Section-----	14
1.2.2 Hadronization in the Nuclear Medium-----	15
1.3 Theoretical Models-----	23
1.3.1 Lattice-----	24
1.3.2 BDMPS and Quark Energy Loss-----	25
1.3.3 Gluon Bremsstrahlung Model-----	25
1.4 Previous experimental measurements-----	29
1.5 Experimental requirements-----	31
2 Experimental Setup-----	33
2.1 Continuous Electron Beam Accelerator Facility-----	33
2.2 CLAS Detector-----	35
2.2.1 Multiwire Drift Chambers-----	37
2.2.2 Cherenkov Counters-----	40
2.2.3 Time-of-Flight System-----	42
2.2.4 Forward Electromagnetic Colorimeter-----	44
2.3 EG2 Experiment Target-----	47
2.4 Trigger System and Data Acquisition-----	56

3 Data Taking, Calibration and Processing During EG2 Experiment-----	59
3.1 Data Processing-----	59
3.2 TOF Calibration-----	61
3.3 Cherenkov Counters Calibration-----	66
3.4 Drift Chamber Calibration-----	67
3.5 Electromagnetic Calorimeter Time Calibration-----	69
4 Data Analysis-----	71
4.1 Particle Identification Scheme-----	71
4.1.1 Particle Identification Scheme for Electron-----	71
4.1.2 Particle Identification Scheme for π^+ -----	74
4.2 DIS Kinematics-----	77
4.3 Simulations and Acceptance-----	78
4.3.1 PYTHIA 6.319 Adaptation to the EG2 Experiment-----	82
4.3.2 EG2 Target in the GSIM-----	91
4.3.3 Acceptance Calculation and Simulation Results-----	94
4.3.4 Fiducial Cuts and Their Effect on the Final Results-----	103
5 Analysis Results and Conclusions-----	107
5.1 Transverse Momentum Broadening Measurements-----	109
5.2 Hadronic Multiplicity Ratio Measurements-----	112
5.2.1 Dependence on z_{π^+} -----	113
5.2.2 Dependence on ν -----	115
5.2.3 Dependence on Q^2 -----	117
5.3 The “Cronin effect”-----	119

5.4 Systematic Error Estimate-----	122
5.5 Conclusions-----	124
Bibliography-----	126
Acknowledgments-----	132
Appendix-----	133

Introduction

Modern experiments in elementary particle physics investigate the composition of the structure of matter by searching for the most fundamental constituents of matter, and characterizing their interactions with each other.

The idea that all matter is composed of elementary particles dates to at least the 6th century BC, when the philosophical doctrine of atomism was developed. Starting in the 1950s and 1960s, a bewildering variety of particles was found in scattering experiments. This was referred to as the “particle zoo”. This term was deprecated after the formulation of the Standard model during the 1970s, in which the large number of particles was explained as combinations of small numbers of fundamental particles.

The current state of classification of elementary particles is referred to as the “Standard Model”. It describes the fundamental weak, strong and electromagnetic forces using force-mediating gauge bosons. The species of gauge bosons include the gluons, W^- , W^+ and Z bosons, and the photons. The model also contains 24 fundamental particles (including antiparticles), which are the constituents of matter. Finally, it predicts the existence of a type of boson known as the Higgs boson, which has not yet been discovered.

The elementary constituents of hadrons were first referred to as “quarks” by M. Gell-Mann and G. Zweig in the constituent quark model, and later as partons by R. Feynman who introduced the “parton model” [47]. In both models the constituents of hadrons are point-like spin-1/2 particles carrying a fraction of the electric charge e , and are distinguished by different flavors. But while in the constituent quark model only 3 quarks share the total mass of a nucleon (proton or neutron), the parton model predicts a nucleon to be made of a very large number of quark-antiquark pairs of very small mass. These two models were subsequently merged into the “Quark-Parton model” [47].

Deep inelastic scattering is the name given to a process used to probe the interior of hadrons (particularly baryons such as protons and neutrons), using leptons [47]. It provided the

first convincing evidence of the reality of quarks, which up until that point had been considered by many to be a purely mathematical description. It is a relatively new process, first attempted in the 1960s and 1970s, and it is conceptually similar to Rutherford scattering, but with important differences.

Further investigations with high resolution (i.e., high energy particle probes) lead to the idea of “asymptotic freedom”, which is the property of some gauge theories in which the interactions between particles, such as quarks, becomes arbitrary weak at ever shorter distances, i.e. length scales that asymptotically converge to zero, or equivalently, energy scales that become arbitrary large. Asymptotic freedom implies that in high-energy scattering the quark moves within nucleons, such as the neutron or proton, mostly as free, non-interacting particles. It allows reliable calculation of the cross-sections of various events in particle physics using the partonic concepts.

Another important feature of particle physics is “color confinement,” which says that color-charged particles cannot be isolated under steady-state conditions [47]. Color charge is the QCD analogy to electric charge, including three color charges and their corresponding anti-charges; quarks possess color, and gluons are bi-colored, i.e., have both one color and another conjugate color. In the equilibrium state, the quarks are confined to be near other quarks by the strong interaction to form quark-antiquark pairs or 3-quark triplets such that the net color charge is neutral.

To understand these two very peculiar properties, the Quantum Chromodynamics (QCD) theory was introduced, which describes the strong interaction between the quarks. Though there is no analytic proof that in QCD quarks should be confined, it intuitively assumes confinement due to the force-carrying gluons having bicolor charge. The strength of the interaction is given by the strong coupling constant α_s , which, in distinction to the electromagnetic coupling constant α , becomes weaker with decreasing distances. QCD is an important part of the Standard Model of particle physics.

When choosing a lower resolution, corresponding to a larger distance scale, the onset of confinement is expected to become visible. Under these conditions α_s increases up to values close

to unity, and perturbative treatment of QCD is no longer possible. While much is known about the perturbative (short distance) properties of QCD, the understanding of the non-perturbative (long distance) aspects of QCD and hadron structure is still very limited, and is therefore mostly based on phenomenological models. It is the purpose of this thesis to collect and assess new data on hadronic structure in semi-inclusive deep inelastic scattering for further understanding of the quark propagation and hadron formation processes in nuclear physics.

The subject of this thesis is the propagation of quarks through the nuclear medium. The primary processes affecting quarks propagating through nuclei are energy loss through gluon radiation [77] and elastic scatterings inside nucleon, as well as the hadronization process [53, 36].

“Hadronization” is the process in which hadrons are formed out of quarks and gluons. This occurs in deep inelastic scattering of leptons off nucleons or after high energy collisions in a particle collider in which temporarily ‘free’ quarks or gluons are created. Due to color confinement, these cannot exist individually in the steady state, therefore, they combine with quarks and antiquarks spontaneously created from the vacuum to form hadrons. The details of that process are not yet understood, although some aspects are known. The tight cones of particles created by the hadronization of the single quark are called “jets” at high energy. “Jets” are observed in particle detectors, rather than quarks, whose existence must be inferred.

According to the “string model” description of the meson formation process, a new quark-antiquark pair is created when the increase in potential energy is large enough; the string breaks, eventually leading to the formation of a “jet” of hadrons. This is the simplest way to describe the process of hadron formation, or in other words, “string fragmentation“.

The analysis results shown in this thesis are based on the data from the EG2 run period carried out at the CLAS (CEBAF Large Acceptance Spectrometer) at TJNAF (Thomas Jefferson National Accelerator Facility, or Jefferson Lab, or JLab, see chapter 2). During this run period, 5.015 GeV electrons were scattered simultaneously on solid and liquid cryotargets located in close proximity. The specific composition of the solid target was varied during the experiment, and consisted of carbon, aluminum, iron, tin, and lead, in particular periods of time (see chapter 2.3).

The choice of different species of solid target covers a wide range of nuclei, with atomic numbers starting from 12 for carbon up to 207 for lead, giving the opportunity for a detailed investigation of the nuclear medium influence on the hadronization process.

The detection of hadrons (in the case of this thesis, π^+) in the final state of a deep inelastic scattering event (i.e. semi-inclusive deep inelastic scattering) enabled the experimental study of the fragmentation process, which gave access to new information on hadron formation times and parton energy loss mechanisms by measuring the attenuation of hadrons (i.e. the reduction of the hadron multiplicity) and transverse momentum broadening (relative to the direction of virtual photon) on various targets (see chapter 4 and 5).

Chapter 1 of this work is devoted to a theoretical introduction on inclusive and semi-inclusive deep inelastic scattering as well to the discussion of the experimental requirements and to a brief description of experiments exploring similar topics at HERMES (DESY). In Chapter 2, a detailed explanation of the EG2 experimental setup is given, including the CEBAF accelerator, the CLAS detector, and the EG2 target system. In Chapter 3 one can find a brief explanation of the CLAS data reconstruction procedure with a few demonstrations of its results for the EG2 experiment. The data analysis itself is described in greater detail in Chapter 4. The results of this work are presented and discussed as well as the sequence of the main physics conclusions and future perspectives are summarized in Chapter 5.

1. Physics Motivation

1.1 Deep Inelastic Scattering and the Simple Quark-Parton Model.

Deep inelastic scattering (DIS) in the most trivial picture might be considered as electromagnetic scattering of an electron off a quark inside a nucleon. In Figure 1-1 a schematic drawing of the DIS process is shown, where the four-momentum of the proton is P , p is the initial four-momentum of the quark, and the initial and final four-momenta of the electron are denoted as k and k' respectively. If the final four-momentum is measured then the momentum transferred to the hadron system by the virtual photon is equal to: $q = k - k'$, where q is a spacelike vector which is conventionally denoted as $q^2 = -Q^2$.

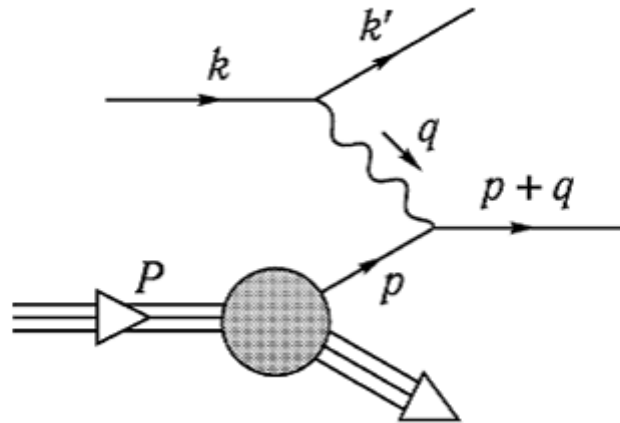


Figure 1-1. Deep Inelastic Scattering in QCD. The diagram shows the stream of momentum during the scattering of a high energy electron off a quark, whose wave function is incorporated inside the proton's wave function.

If Q^2 is high enough then the quark is knocked out from the proton so that the following soft processes cannot balance the reaction. However, the soft processes such as gluon emission and quark-antiquark pair production are ultimately neutralizing the color, transforming the knocked-out quark to the “jet” of hadrons propagating in the direction of the electron's transferred momentum.

In order to get in first approximation the cross section of electron-proton scattering, let us consider the process in the center of mass reference frame, where the electron and proton are propagating towards each other in the case where the total energy is high enough that the mass of the proton can be ignored. Hence the proton has almost light-like momentum along the collision axis. Because of that the proton's constituent quarks also have light-like momenta, which are almost collinear to the momentum of the proton (the quark can acquire large transverse momentum only through the exchange of hard gluons, which is suppressed by the smallness of the α_s parameter at large energy scales). Therefore, in first order approximation of QCD perturbative theory:

$$p = \xi P \tag{1.1}$$

where $0 < \xi < 1$ is the longitudinal fraction of the constituent quark's momentum. In leading order approximation one can also ignore the gluon emission and exchange during the collision. As a result, the cross section of electron-proton scattering is equal to the cross section of electron-quark scattering for given ξ , multiplied by the probability that the proton contains a quark with ξ longitudinal momentum fraction, integrated over ξ .

However the probability that the proton contains a quark with a particular momentum cannot be calculated by perturbative QCD, since that depends on the soft processes that define the structure of the proton as a bound state of quarks and gluons. Therefore one can consider that probability as an unknown function, which should be measured in experiment. Those kinds of probability functions (called parton distribution functions) are used for all species of quarks, anti-quarks and gluons, which are incorporated inside the proton's wave function. For each parton f the parton distribution function is defined as:

$$P_f(\xi) = f_f(\xi) d\xi \tag{1.2}$$

Therefore the cross section of inelastic scattering of the electron off the proton in leading order approximation is equal to:

$$\begin{aligned}
\sigma(e^-(k)p(P) \rightarrow e^-(k') + X) &= \\
&= \int_0^1 d\xi \sum_f f_f(\xi) \sigma(e^-(k)q_f(\xi P) \rightarrow e^-(k') + q_f(p')) \quad (1.3)
\end{aligned}$$

where X indicates the final hadronic state. One should remember that equation (1.3) is not an exact QCD prediction, but can be viewed as the first term in an expansion in α_s ; that approximation is called the *parton model* [47].

In parton model the cross section has the following form:

$$\frac{d^2\sigma}{dxdy}(e^-p \rightarrow e^-X) = \left(\sum_f x f_f(x, Q^2) Q_f^2 \right) \frac{2\pi\alpha \cdot s}{Q^4} [1 + (1-y)^2] \quad (1.4),$$

where s is the square of total energy of electron and proton, Q_f is the charge of parton f ,

$x \equiv \frac{Q^2}{2P \cdot q}$ is the Bjorken variable and $y \equiv \frac{2P \cdot q}{2P \cdot k} = \frac{2P \cdot q}{s}$. In the proton's rest frame $y = \frac{q^0}{k^0}$,

therefore it is the fraction of energy transferred to the hadron's system from the incoming electron.

Because of gluon radiation, in equation (1.4) there is a weak dependence of the parton distribution functions on Q^2 , which leads to Bjorken scaling violation [47]. When the structure functions are known for certain values of Q^2 , they can be evolved to other Q^2 values using the Dokshitzer-Gribov-Lipatov-Altarelli-Parisi (DGLAP) equations [36].

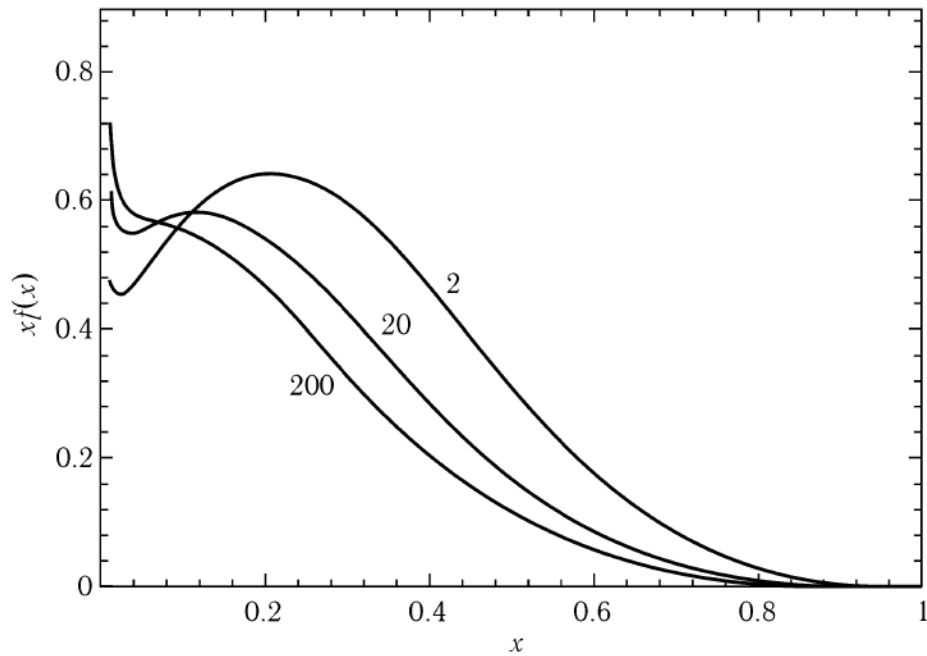


Figure 1-2. $x f_f(x)$ parton distribution functions for u quark, when $Q=2, 20, 200 \text{ GeV}$, showing the parton evolution effect according to the Altarelli-Parisi equations.

In Figure 1-2 are shown the predictions of the Altarelli-Parisi equations for evolution of the parton distribution functions dependence on Q^2 . Partons with large x are tending to radiate and transfer to the states with lower x . At the same time, as a result of those radiations new partons are produced with low x values. With an increase in Q^2 the parton distributions are decreasing for large x values, while they increase much faster for low x values. At low Q^2 the wavelength of the virtual photon becomes so large that the partons inside the proton are not fully resolved any longer. As a result the proton is probed as a whole. The validity range for the QCD-extended parton model is not precisely known, but it is assumed to be valid for $Q^2 > 1 \text{ GeV}^2$, which corresponds to a spatial resolution of about 0.2 fm.

1.1.1 Strong coupling constant α_s .

For perturbative QCD calculations it is important to have the experimental values of the strong coupling constant α_s . To compare α_s values measured in different experiments, one should determine the overall scale of renormalization, which is usually selected to be the mass of neutral Bose particle Z^0 ($m_Z = 91.19\text{GeV}$), and also one should fix the scheme of renormalization, which defines the coupling constant in a given scale. The experimental results for α_s one can see in Figure 1-3, where the dependence of coupling constant on momentum scale can be observed.

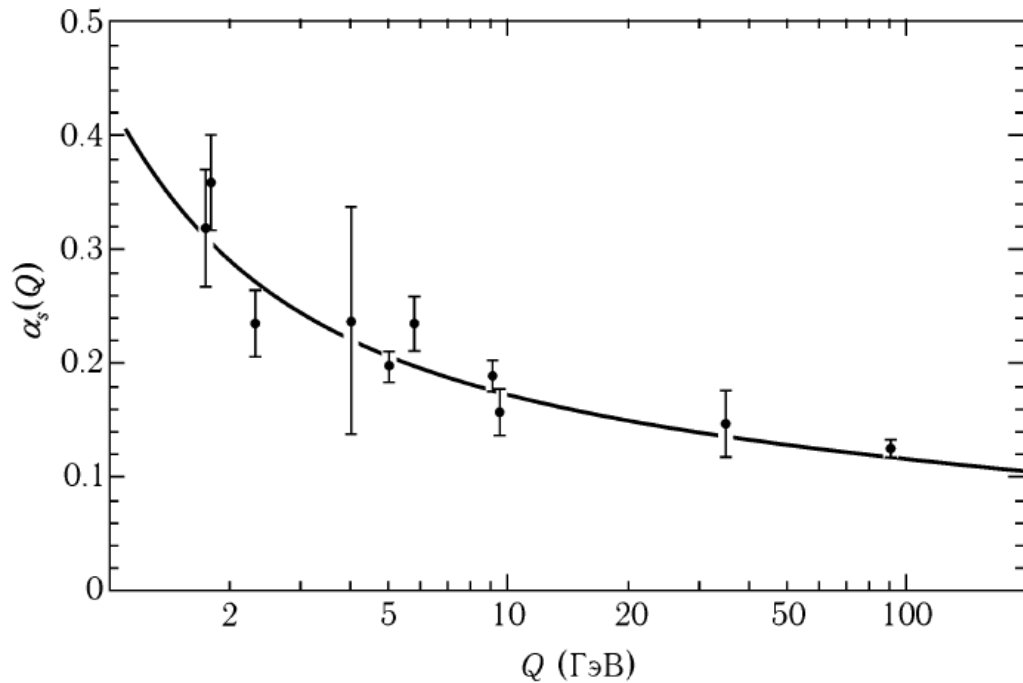


Figure 1-3. Experimentally measured α_s dependence on Q . These values are compared with theoretical predictions of renormalized evolution with initial $\alpha_s(m_Z) = 0.117$.

1.2 Semi-Inclusive Deep Inelastic Scattering.

In the previous chapter, inclusive reactions have been considered where the only particle detected is the scattered electron. If in addition to the scattered electron one of the produced

hadrons is identified the event is called *semi-inclusive*. A schematic representation of a semi-inclusive event in first order approximation is given in Figure 1-4. The hadron carries information on the flavor of the struck quark. The flavor dependence of *Semi-Inclusive Deep Inelastic Scattering* (SIDIS) can be only exploited for hadrons originating from struck quarks. These so-called *current fragments* must be separated from the ones originating from the target remnants (*target fragments*).

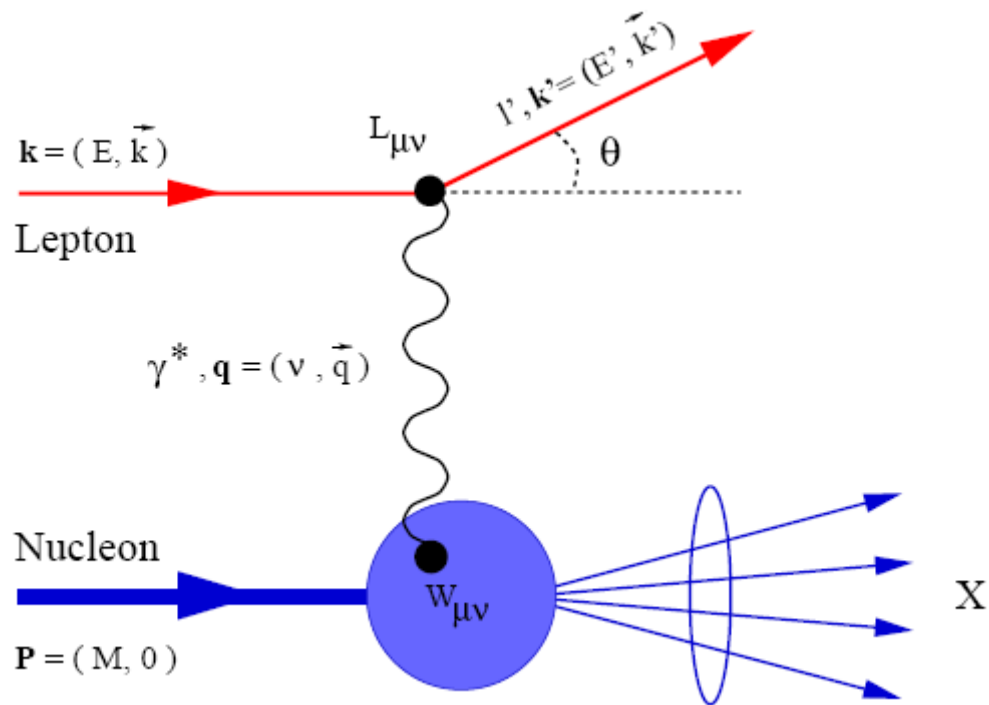


Figure 1-4. Semi-inclusive deep inelastic scattering of a lepton off a nucleon, the first order approximation.

1.2.1 Semi-Inclusive DIS Cross Section.

In SIDIS it is assumed that the timescale for the absorption of a virtual photon is very short as compared to the timescale needed for the quark to fragment into a hadron. The fragmentation process is not calculable in pQCD since it involves long distance processes, and thus corresponds to very low Q^2 values where pQCD techniques cannot be used. Therefore, the fragmentation

process in semi-inclusive scattering is parameterized by fragmentation functions $D_f^h(Q^2, z)$, which represent the probability that a quark of flavor f fragments into a hadron of type h with a fraction z of the virtual photon energy ($E_h = z\nu$).

In the quark-parton model the cross section for the process $eN \rightarrow ehX$ is assumed to be the product of the differential cross section from equation (1.4), and the fragmentation probability to find a hadron h originating from a quark of flavor f .

$$\frac{d^3\sigma(eN \rightarrow ehX)}{dx dQ^2 dz} = \frac{d^2\sigma(eN \rightarrow eX)}{dx dQ^2} \frac{\sum_f e_f^2 q_f(x, Q^2) D_f^h(Q^2, z)}{\sum_f e_f^2 q_f(x, Q^2)} \quad (1.5)$$

Here it is assumed that the quasi-free scattering process (related to the quark momentum distribution $q_f(x)$) and the fragmentation process (described by the fragmentation function $D_f^h(z)$) enter as two independent factors in the cross section (as flavor level). This is known as *factorization*.

From equation (1.5) the hadron multiplicity per DIS event is obtained:

$$M_h(Q^2, z) \equiv \frac{1}{\sigma} \frac{d^3\sigma(eN \rightarrow ehX)}{dQ^2 dz} = \frac{\int dx \sum_f e_f^2 q_f(x, Q^2) D_f^h(Q^2, z)}{\int dx \sum_f e_f^2 q_f(x, Q^2)} \quad (1.6)$$

where σ is the differential inclusive DIS cross section $\frac{d^2\sigma(eN \rightarrow eX)}{dx dQ^2}$.

1.2.2 Hadronization in the Nuclear Medium.

When embedded in a nuclear medium, the hadronization process is influenced by quark energy loss through gluon radiation and multiple quark-nucleon scattering as the quark propagates through the medium. Furthermore, hadron-nucleon interactions also affect the process if the hadron is formed while inside the nucleus. The primary experimental observable to access the hadronization process is the multiplicity of hadrons produced on a dense nucleus as compared to

the one produced on deuterium. In the absence of any kind of attenuation produced by interactions in the medium these two quantities would be identical (i.e. the ratio of the two multiplicities would be unity). The ratio of hadron multiplicities or the *attenuation ratio* is defined as:

$$R_{att}^h(z, \nu) = \frac{\left(\frac{1}{\sigma} \frac{d^2\sigma(eN \rightarrow ehX)}{dzd\nu} \right)_A}{\left(\frac{1}{\sigma} \frac{d^2\sigma(eN \rightarrow ehX)}{dzd\nu} \right)_{^2H}} \quad (1.7)$$

where the derivative with respect to Q^2 is substituted by the one with respect to ν because of the further application of this equation. The ν and z dependence of the attenuation ratio can be used to investigate the nature of the hadron formation mechanism.

One class of observable that can be isolated is the *characteristic times* for distinct stages of the hadron formation process. The initial stage is the absorption of a virtual photon by a quark on a time scale that is presumably brief, $\ll 1$ fm/c, and which is governed by the virtual photon wavelength. There must follow a stage during which the colored quark propagates over a distance as essentially a quasi-free particle, and in this stage the quark radiates gluons with a differential spectrum given by pQCD as:

$$d\omega^{q \rightarrow qg} = \frac{\alpha_s(k_\perp^2)}{4\pi} 2 \frac{4}{3} \left[1 + \left(1 - \frac{k}{E} \right)^2 \right] \frac{dk}{k} \frac{dk_\perp^2}{k_\perp^2} \quad (1.8)$$

where E is the quark energy, k_μ is the 4-momentum of the gluon and k_\perp is the gluon transverse momentum. The characteristic time associated with this stage has been called the *production time* by various authors [53]:

production time: the time interval during which a quark is deconfined

The production time is a characteristic of a propagating quark, and in principle it should be independent of which final state hadron is formed.

In a third stage of the process, the gluon radiation ceases, which can only happen if the struck quark has found partner quarks to neutralize its color. During this stage, a 'pre-hadron'

evolves to become an 'ordinary' hadron. This characteristic time is the *formation time* for the hadron:

formation time: the time required to form the color field of a hadron

Unlike the production time, the magnitude of the hadron formation time is expected to depend in detail on the hadron species being formed.

The existence of the production time and the formation time is dictated by two of the most fundamental properties of QCD, namely, that a colored quark can only propagate for a limited distance (confinement), and the equilibrium color field of a hadron cannot be formed instantaneously (causality).

Production Time

It is possible to obtain simple estimates for the production time from basic considerations. To a very good approximation, in deep inelastic kinematics and at $x_B > 0.1$, the struck quark absorbs all the energy of the virtual photon. Thus, the initial energy of the struck quark is known to be ν , neglecting the quark's mass. Conservation of energy dictates that the final energy of the hadron containing the struck quark must be no greater than ν . If, however, the quark radiates gluons as it propagates, this constitutes a loss in energy which drives the hadron's energy below ν . The energy loss due to gluon emission can be estimated from the string model: the main parameter of the string model [17] is the string tension κ , where $\kappa \approx 1$ GeV/fm. In the string model there is no explicit gluon emission, however, the growth of the string creates an effective energy loss for the struck quark that is governed by the value of κ . Thus, in this picture, the best estimate for the rate of (vacuum) energy loss is:

$$\frac{dE}{dx} \Big|_{\text{vacuum}} \approx 1 \text{ GeV} / \text{fm} \quad (1.9)$$

If $z_h = E_h/\nu$ is the fraction of the struck quark's initial energy retained by the hadron, then $\nu(1 - z_h)$ is the energy lost through gluon emission by the struck quark. Thus an estimate of the distance over which gluons are emitted is:

$$l_p = \frac{v(1-z_h)}{\kappa} \quad (1.10)$$

the production length (*production time* is $\tau_p = l_p / c$) [53].

For example, for a 5 GeV pion with $z_h = 0.6$, $l_p = 3.3$ fm. Thus, the production time is of the order of a few fm at JLab energies.

Hadron Formation Time

The second example of a characteristic time is the *hadron formation time*. Unlike the production time, the formation time is not directly related to the confinement property of QCD; rather, it is a measure of the time required to form the non-perturbative color field of the hadron starting from a small color-singlet object. This field-regeneration time has a well-known analog in QED.

It is possible to construct simple estimates for the formation time. To form a hadron of radius R starting from a pointlike, bare color singlet object, the speed at which the field can arise in its rest frame is bounded by the speed of light:

$$\tau_{formation}^{rest} > \frac{R}{c} \quad (1.11)$$

In the lab frame, the Lorentz boost adds an additional factor for time dilation:

$$\tau_{formation}^{lab} > \frac{E}{m^*} \frac{R}{c} \quad (1.12)$$

where m^* is the mass of the propagating color-singlet object. In principle, m^* ranges from the mass of two bare quarks at a minimum to the fully formed hadron mass m_h at a maximum. A lower limit for the formation time is given by setting $m^* = m_h$.

While the above estimate has been posed as a classical calculation, a quantum mechanical analysis that takes into account the gluon wavelengths involved arrives at the same formula [36]. The Fourier component of the gluonic field associated with the longest wavelengths $\lambda \approx R$ takes the longest time to come to full strength, and this sets the scale of the hadron formation time. In

this quantum-mechanical picture, the assumption of a pointlike initial configuration made in the paragraph above is no longer necessary, since the lowest-momentum wavefunction components control the completion of the hadron formation process.

To give a concrete example using the formula above, for a 5 GeV pion with a radius of 0.7 fm, the formation time estimate is:

$$\tau_{formation}^{lab,\pi} > 25 \text{ fm} \quad (1.13)$$

This simplistic estimate sets the scale for formation times: pion formation times are expected to be of order 10 fm at JLab energies.

More simplistic presentation of process of hadronization, based on Bialas picture[20], can be described in terms of the just hadron formation time τ_f (different from formation time introduced above), the time between the moment that the quark is struck by the virtual photon and the moment that the final hadron is formed. Figure 1-5 shows the quark propagating over a distance $l_f = c\tau_f$ before the hadron is formed. Hard partonic interactions are also drawn as gluon exchange lines. Not shown are possible interactions of the produced hadrons with the medium, subsequent to its formation.

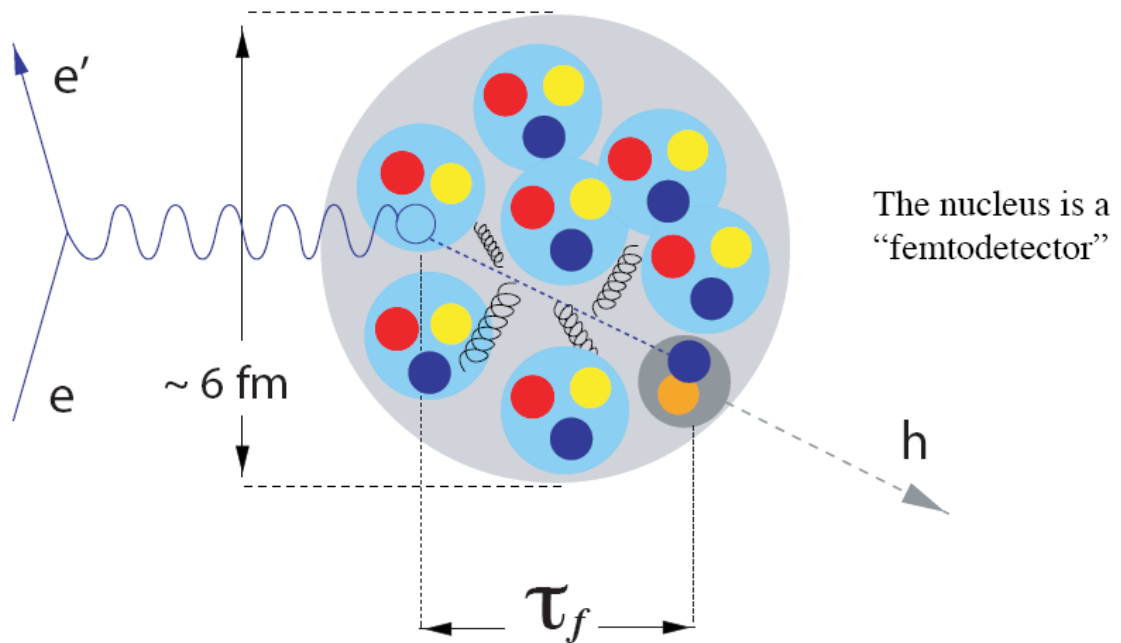


Figure 1-5. Hadron formation process in the nuclear medium.

Depending on the nuclear size and the formation length the hadron may still be formed inside the nucleus and therefore interact with the nucleons. These interactions are described by hadron-nucleus cross sections. This process is referred to as nuclear rescattering or absorption. While different theoretical models are used to describe the hadron formation process corresponding to different descriptions of the hadron formation time, the nuclear absorption of the formed hadron in the medium is always described by the same formalism.

After its formation in a nucleus A the hadron undergoes nuclear absorption if the formation time is short enough. The absorption can be factorized out of the attenuation ratio R_{att}^h as expressed in equation (1.13). Let us consider deep inelastic scattering of a lepton off nucleus with atomic number A at the (b, z) coordinate, where the z coordinate is located on the axis coincident with the direction of the virtual photon. Because of that interaction a quark with energy $E_q = \nu$ is produced, where ν is the energy of the virtual photon. The quark, propagating through the nucleus, will fragment into the leading hadron with energy E_h with some probability. The probability that at coordinate (b, z') , with $(z' \geq z)$, the intermediate state is a quark, is equal to $P_q(z' - z) = \exp[-(z - z')/\tau_f]$, while the probability that it is a fragment of hadron, is: $P_h(z' - z) = 1 - P_q(z' - z)$ [20]. Therefore, the probability that the leading fragment is not absorbed by the single nucleon in nucleus, is equal to:

$$S_A(b, z) = 1 - \sigma_q \int_z^\infty dz' \rho_A(b, z') P_q(z' - z) - \sigma_h \int_z^\infty dz' \rho_A(b, z') P_h(z' - z) \quad (1.14)$$

where σ_q and σ_h are cross sections of the quark and hadron absorption, respectively. One can use the Woods-Saxon formula for normalization of the nuclear density at the (b, z) coordinate [29]:

$$\rho_A(r) = \rho_0 / \{1 + \exp[(r - r_A)/a]\} \quad (1.15)$$

where $r_A = (0.978 + 0.0206A^{1/3})A^{1/3}$ and $a = 0.54$.

As mentioned above, actually the definition of hadron attenuation R_A , which is the ratio of hadrons produced from nucleus A and a single nucleon (in case of equal number of lepton events), is based on the prediction that there is no absorption on the remaining $(A-1)$ nucleons. If one ignores the correlations between nucleons inside the target, then:

$$R_A = \frac{dN_A}{dN_1} = \int db^2 \int_{-\infty}^{\infty} dz \rho_A(b, z) [S_A(b, z)]^{A-1} \quad (1.16)$$

One of the most elementary theories describing the fragmentation process is the *string* or *color flux tube model* [17]. In this picture, a quark removed from a hadron forms a *string* or *chromo-electric flux tube* which extends over a space-time region. The string has a ‘*tension*’ κ with a magnitude of approximately $1 \text{ GeV}/\text{fm}$ in free space. Given adequate energy, $q\bar{q}$ pairs can ‘tunnel up’ from the vacuum and ‘*break*’ the string into two strings. If one denotes the energy fraction of the produced hadron relative to the virtual photon energy as $z_h = E_h/\nu$, then the energy lost by the struck quark, before the hadron is produced, is equal to $E_h(1-z_h)$. Therefore, according to the string model picture the formation length estimate [17] is:

$$l_f = \frac{E_h(1-z_h)}{\kappa} \quad (1.17)$$

which can also be expressed as the formation time τ_f . Hence, from equation (1.17) one can take the estimate for formation time as $\tau_f = \text{const} \cdot (1-z_h) \cdot \nu \cdot z_h$.

The equation (1.16) for R_A nuclear attenuation has actually two parameters; the constant inside the τ_f and the σ_q . The dependence on other parameters (like z_h , ν , Q^2) exists through those two parameters. Since one can assume that the nucleon is ‘*transparent*’ for the struck quark [53, 7], then $\sigma_q = 0$. Good agreement with the HERMES nitrogen data was obtained using $\sigma_h = 20\text{mb}$ and $\text{const}=1.4$ [20, 7].

In figures 1-6, 1-7 and 1-8 are presented the dependences of the nuclear attenuation R_A on ν and z_h (pictures with index a), and separately R_A versus ν , when $z_h=0.5$ (pictures with index

b) and R_A versus z_h , when $\nu=3$ GeV (pictures with index c) respectively for carbon ($A=12$), iron ($A=56$), and lead ($A=207$). One can notice that for the heavier nuclei the nuclear attenuation is larger, and as ν and z_h increase, the nuclear attenuation is getting smaller and larger, respectively. These calculation results are qualitatively in good agreement with the experimental results from CLAS presented in Chapter 5, as well as the experimental results measured at HERMES [7].

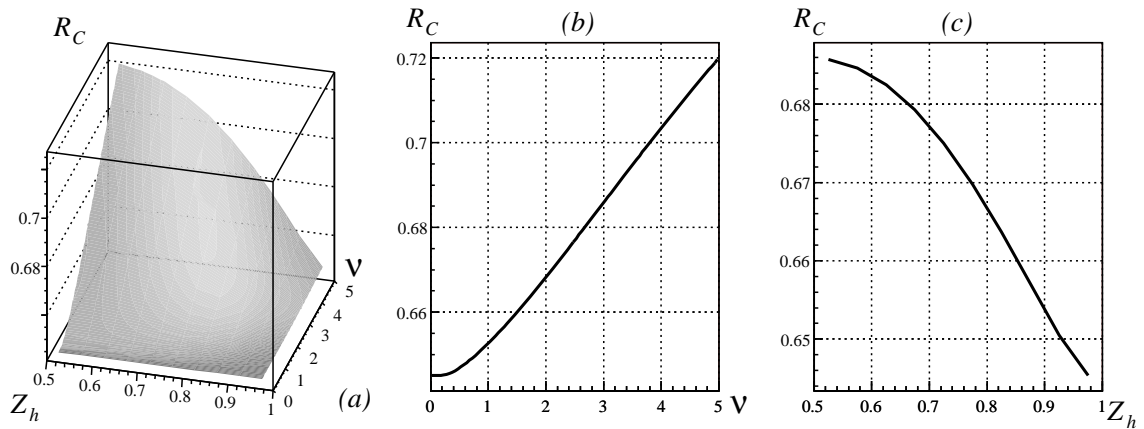


Figure 1-6. a) Two dimensional dependence of nuclear attenuation R_A on ν and z_h for carbon. b) Nuclear attenuation R_A dependence on ν , when $z_h=0.5$, for carbon. c) Nuclear attenuation R_A dependence on z_h , when $\nu=3$ GeV, for carbon.

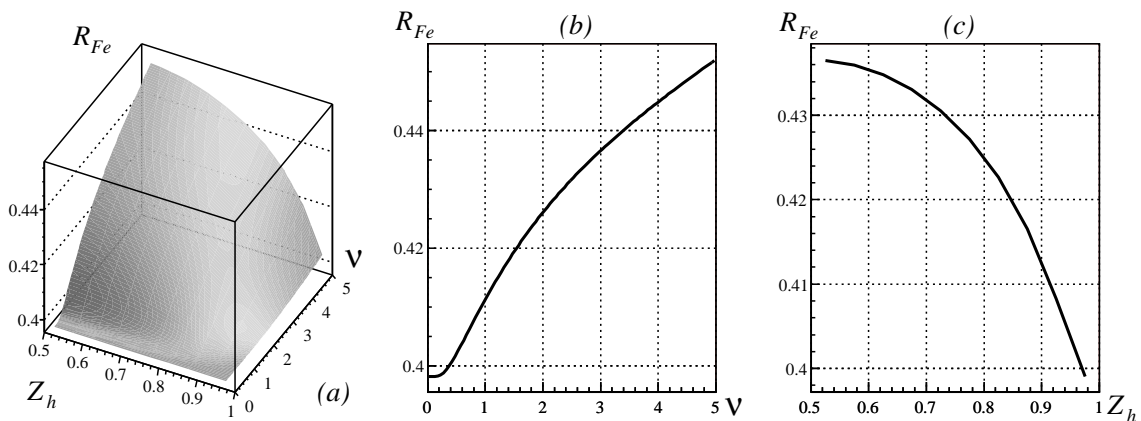


Figure 1-7. a) Two dimensional dependence of nuclear attenuation R_A on ν and z_h for iron. b) Nuclear attenuation R_A dependence on ν , when $z_h=0.5$, for iron. c) Nuclear attenuation R_A dependence on z_h , when $\nu=3$ GeV, for iron.

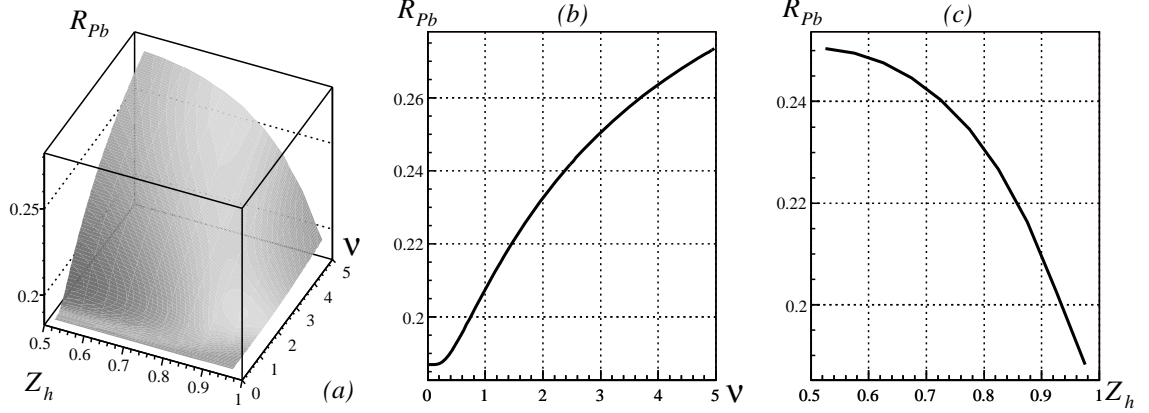


Figure 1-8. a) Two dimensional dependence of nuclear attenuation R_A on ν and z_h for lead. b) Nuclear attenuation R_A dependence on ν , when $z_h=0.5$, for lead. c) Nuclear attenuation R_A dependence on z_h , when $\nu=3$ GeV, for lead.

Part of the problem of this presentation is the Biallas picture [20], which does not distinguish between the two distinct phases. One can only use κ here for the production time, since as the color-neutral pre-hadron forms there is no gluon emission anymore, thus no energy loss at all (vs. 1 GeV/fm during the production time phase). So this is not an estimate for the formation time, but rather the production time. The formation time depends on how large the object being formed is, i.e., there should be either a mass or radius in the expression.

1.3 Theoretical Models.

Much theoretical work was stimulated by the European Muon Collaboration data in the early 1980's [18] comparing F_2 in heavy nuclei to light nuclei, and ultimately uncovering the famous 'EMC' effect. An example of such a theoretical work is the effort by Jaffe, Close, Roberts,

and Ross [49] which proposed that the nuclear medium slightly modified the confinement scale for bound nucleons and suggested a non-zero probability for multi-quark configurations in nuclei beyond the ordinary baryons. A collection of models accumulated as a consequence of these data, many not able to be tested against data until the advent of the HERMES nitrogen measurements [7] for hadron attenuation beginning in the late 1990's. The HERMES data immediately ruled out several of these model predictions for how hadron attenuation would behave at high z . Since that time HERMES has published more data for krypton targets, including fully identified hadrons in the final state. These data have stimulated a new wave of modeling from various points of view. All of the new models are able to describe the HERMES data in some measure, although they are based on somewhat different physical pictures. A very brief account will be given here; the reader is referred to one recent paper for each approach if more background information is desired. Before describing the hadron attenuation models, a brief mention of Lattice QCD and the pQCD calculations of quark energy loss by BDMPS will be given.

1.3.1 Lattice.

Ideally one would confront hadron attenuation data with Lattice QCD. Initially this would seem nearly impossible for technical reasons: a Minkowski space calculation is needed, and a non-zero baryon density medium is needed. However, there may be some alternative approaches. These measurements are intended to determine what happens in vacuum hadronization by examining the small modifications brought about by the nuclear medium, and interpreting the data in terms of what is known about nuclei. Thus, the simpler questions really being asked are: how long does it take for two bare quarks to expand to a full-sized pion, and how does it happen? How far can a quark of a given energy propagate before its color is neutralized? While still far from mainstream lattice topics, there are a few calculations that begin in a primitive way to address these simpler questions. Still, it will be many years before there could be hoped to be any firm conclusions from the lattice on these topics.

1.3.2 BDMPS and Quark Energy Loss.

There has been a long series of calculations in perturbative QCD by Baier, Dokshitzer, Mueller, Peigne and Schiff addressing the topic of quark energy loss in both cold and hot nuclear matter [19]. Using perturbative QCD, they connect the dependence of the medium simulated transverse momentum broadening to the quark energy loss as:

$$\frac{dE}{dx_{medium}} = \frac{3}{4} \alpha_s \Delta p_T^2 \quad (1.18).$$

The mechanism of energy loss is primary medium-stimulated gluon radiation, although collisional losses are also treated. Although they do consider ‘cold’ nuclear matter (i.e. nuclei), they do not specifically address the HERMES data.

1.3.3 Gluon Bremsstrahlung Model

The gluon bremsstrahlung model [53] pre-dates the HERMES data by several years, and thus it constitutes an actual prediction that fits the data well. In its initial form it addressed leading pions ($z > 0.5$) but has now been expanded to include positive kaons. It emphasizes the role of hadronization in explaining the HERMES data; medium-stimulated energy loss has only a small effect in this approach. The proponents extend the consequences of their conclusions to relativistic heavy ion collisions.

The production of fast leading mesons in nuclei is described in terms of a modification of the fragmentation function in the medium due to energy loss caused by gluon radiation, in combination with hadron rescattering. The approximation is made that the medium modification of the distribution function $q_A(x, Q^2)$ is negligible. If it is also assumed that one flavor is dominant in the fragmentation process, the summation in eq. (1.5) reduces to one term, and the attenuation ratio can be written as:

$$R_{att}^h = \frac{D_f^{h/A}(z)}{D_f^h(z)} N_A \quad (1.19)$$

where the factor N_A accounts for nuclear absorption and $D_f^{h/A}$ is the nuclear modified fragmentation function. The modification is evaluated by calculating the energy loss due to gluon radiation, which is proportional to the energy of the virtual photon, to the fraction of energy carried by the hadron, and inversely proportional to the time during which the struck quark propagates freely before the hadron is formed:

$$-\frac{dE}{dt} = \frac{\varepsilon\nu(1-z)}{t} \quad (1.20)$$

where $\varepsilon = 4\alpha_s(k_T^2)/3\pi$ is calculated perturbatively, with the running QCD coupling constant $\alpha_s(k_T^2)$ fixed to $\alpha_s(k_0^2)$ for values of the quark transverse momentum $k_T \leq k_0$. The value of the gluon-gluon correlation radius $k_0 \approx 0.7$ GeV is chosen such that the amount of energy radiated per fm in this model is in agreement with the string tension used to describe the soft part of hadronization in the framework of color strings, $dE/dt \approx 1$ GeV/fm. From equation (1.20) one can derive a distribution of formation times from which the following average formation time is derived:

$$\tau_f = c_h\nu(1-z) \quad (1.21)$$

with c_h the formation time constant. The dependence of the formation time on Q^2 is supposed to be small. The z dependence of equation (1.21) can be understood in terms of the following argument. The maximum energy which a hadron of observed total energy $E_h = z\nu$ may have lost by gluon radiation is $(1-z)\nu$. A high z hadron carries most of the virtual photon energy, and therefore has to be formed fast, otherwise gluon radiation would have reduced its energy. The hadrons formed early inside the nucleus have more time (length) to reinteract with the nuclear constituents, and therefore they get more strongly suppressed. This dependence suggests that a stronger attenuation at high z should be observed in the data.

The z and ν dependence of the attenuation ratio as predicted by this model are compared to existing HERMES data [53] in Figure 1-9. The decrease of the attenuation ratio R_M^π at large values of z is shown to be larger for smaller average energy.

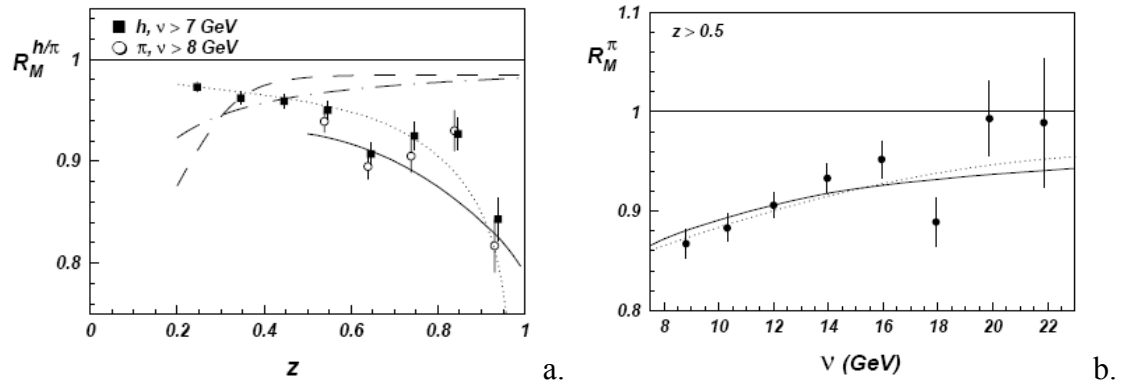


Figure 1-9. a) The multiplicity ratio as a function of z for all charged pions (open circles) and all charged hadrons including pions (closed squares) for the nitrogen target in the HERMES experiment. The full curve represents a gluon-bremsstrahlung model calculation for pions. The dotted, dashed and dot-dashed curves represent phenomenological formation-time calculations. The plot is taken from [9, Fig. 3]. b) The multiplicity ratio as a function of ν for charged pions with $z > 0.5$ for the nitrogen target in the HERMES experiment. The solid curve represent a gluon-bremsstrahlung model calculation. The dotted curve is the result of a one time-scale model calculation assuming a $(1-z)\nu$ -dependence of the formation time. The plot is taken from [9, Fig.

4].

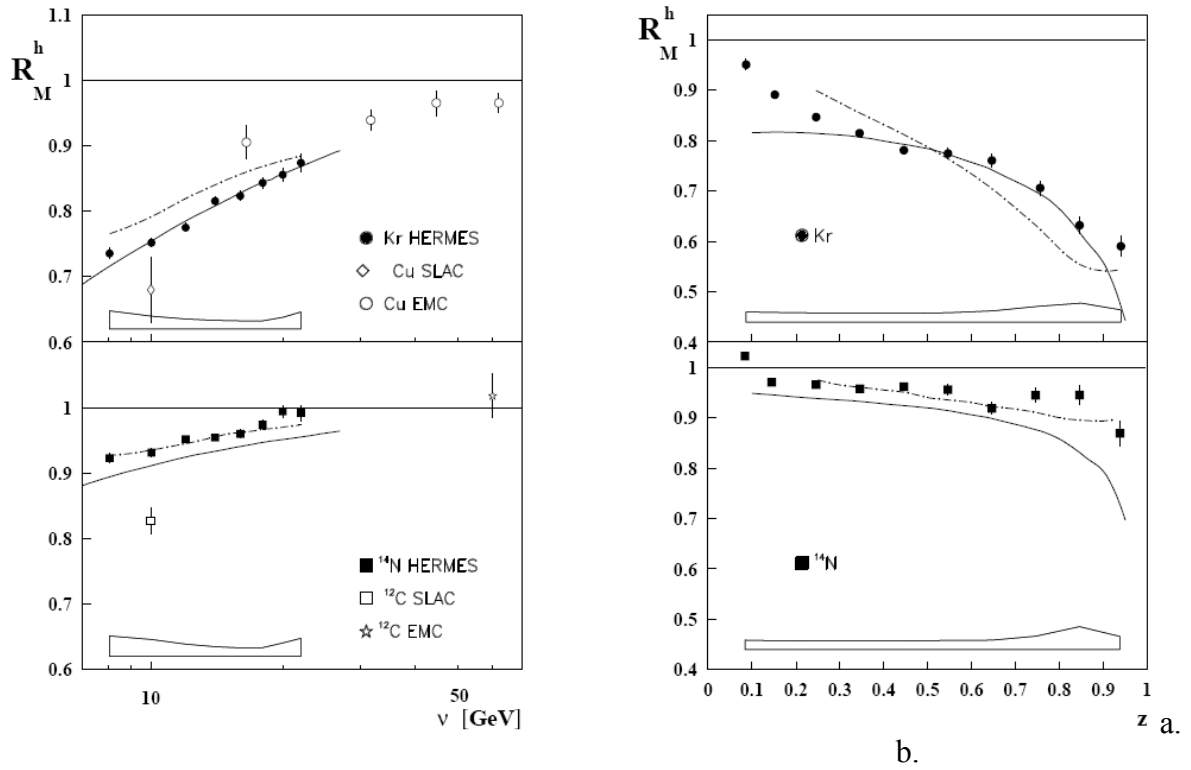


Figure 1-10. a) Charged hadron multiplicity ratio R_M^{π} as a function of ν for $z > 0.2$. In the upper panel the HERMES data on Kr are compared to SLAC [63] and CERN [18] data on Cu. In the lower panel the HERMES data on ^{14}N [9] are compared with CERN and SLAC data on ^{12}C . The error bars represent the statistical uncertainties, and the systematic uncertainty is shown as the band at the bottom of the plot. The solid curves are calculations from [2] and dot-dashed curves are calculations from [75, 76]. The plot is taken from [8]. b) Charged hadron multiplicities R_M^h as a function of z for $\nu > 7$ GeV. The data are compared to the same calculations as in Figure a. The error bars represent the statistical uncertainties and the systematic uncertainty is shown as the band. The plot is taken from [8].

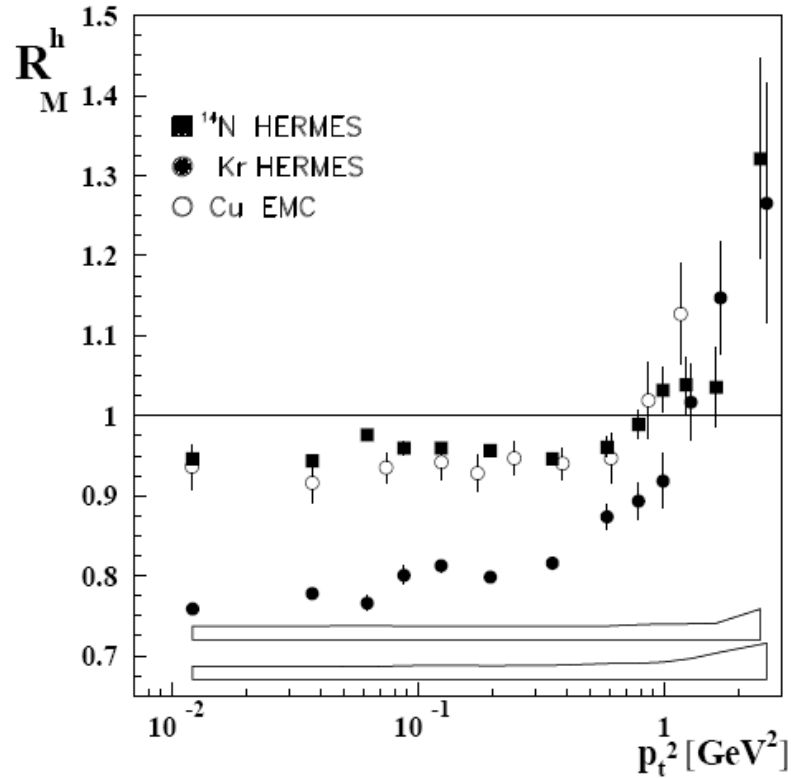


Figure 1-11. Multiplicity ratio for charged hadrons versus p_T^2 for $\nu > 7$ GeV and $z > 0.2$. The HERMES data on Kr and ^{14}N are compared to the EMC [18] data for Cu in the range $10 < \nu < 80$ GeV. The error bars represent the statistical uncertainties. The systematic uncertainty for Kr (^{14}N) is shown as the lower (upper) band. The plot is taken from [8].

1.4 Previous experimental measurements.

One of the pioneering measurements of the hadronization length was done in the 1970's at SLAC [63]. By comparing the attenuation of the number of hadrons produced from nuclei compared with deuterium, normalized to the number of DIS events in each case, they concluded that the hadronization occurred within the distance scale of the nucleus (averaged over the Q^2 and ν kinematics of their DIS events). Although their statistical uncertainties were large, the technique of the multiplicity ratio continues to be valuable today.

Additional data on the multiplicity ratio were measured by the E665 experiment at Fermilab [4] and the EMC experiment [18] using ultra-high-energy muons on various nuclear targets from C to Pb. These data confirmed the fact that hadrons at high z_h are attenuated in nuclei compared with deuterium. Since particles with $z_h > 0.5$ are typically considered to be the leading hadron (containing the struck quark), the attenuation in nuclei suggested that hadronization was taking place inside the nucleus. In addition, the response of nuclei to DIS events was measured by detecting low energy neutrons at backward angles [5] which come from thermalization of the residual nucleons. These data showed clearly that the majority of DIS events in Ca left a “cold” residual nucleus, whereas in a Pb target the residual nucleus was “hot” as expected for hadronization inside the nuclear radius. Although limited in statistics, the E665 results provided motivation for the next generation of experiments at HERMES and CLAS.

The HERMES collaboration published an impressive set of data on the multiplicity ratio for a variety of hadrons ($\pi^\pm, \pi^0, K^\pm, p, \bar{p}$) from ^{14}N and Kr targets [8]. These data showed, for the first time, a clear trend of more attenuation as z_h increases (averaged over Q^2 and $\nu > 7$). They also observed less attenuation as ν increases (averaged over Q^2 and $z_h > 0.2$). Both of these trends were predicted by theoretical models based on increasing formation time as a function of ν and effective string tensions in the medium. In addition, HERMES found that the multiplicity ratio depends on p_T and that R_M^h is maximal and rising above unity for high p_T .

These data have been the subject of a number of theoretical models in recent years [53, 76, 39, 16, 1], and show definitely that the hadrons are not fully dressed as they propagate through the nucleus, else models that properly describe final state interactions (FSI) for a wide range of hadron-scattering reactions cannot predict the HERMES multiplicity ratios. As a result of having precise data for multiplicity ratios and p_T -broadening, theorists now have the information they need to construct effective models of the process by which a struck quark goes from deconfinement to confinement inside a hadron. Several models now show that a period of “pre-hadron” propagation is likely, where the object under consideration (usually a $q\bar{q}$ pair or qqq

triplet) is not fully dressed, and hence is more transparent to the nuclear medium. This interpretation would not be possible without the experimental data as a basis.

1.5 Experimental requirements

The requirements for the target, based on the above explained experiments, were as follows:

- 1) Large acceptance for semi-inclusive and exclusive kinematics, plus a good match to the CLAS spectrometer acceptance
- 2) Minimal mass for low-energy particles at large angles (70-140 degrees relative to the beam direction) as well as forward-going particles
- 3) Approximately equal scattering rates for two targets in the beam simultaneously
- 4) One of the targets needed to be a stable deuterium cryotarget
- 5) Less than 2-3% of a radiation length of any target material to suppress secondary electromagnetic processes
- 6) Minimal entrance/exit window thicknesses for cryotarget to maximize target/window ratio
- 7) Rapid target changes for the heavy nuclear targets
- 8) Minimal mass in support structure

In addition to these requirements, an effort was also made to precisely determine the solid target thicknesses and to monitor the cryotarget thickness, as an aid in further reducing systematic uncertainties. The requirement to have approximately equal scattering rates for the two targets precluded two cryotargets in series since the heavier nuclear targets such as xenon would require a very different cryotarget length; a pressurized gas cell would have been another possibility, but the practical target-to-window ratio in that case would have been significantly worse and entailed higher-Z entrance and exit foils for two cells. Thus, solid targets were used for the heavy nuclei. Because the typical operation of CLAS involves only few-nA beams, melting of the solid targets or boiling of the cryotargets was not of concern, thus a convection-cooled deuterium cryotarget in combination with small solid targets was chosen as the basic design configuration. The cryotarget

was located upstream of the solid targets, limiting the effects of secondary electromagnetic processes contributing to the flux incident on either target.

2. Experimental Setup

2.1 Continuous Electron Beam Accelerator Facility.

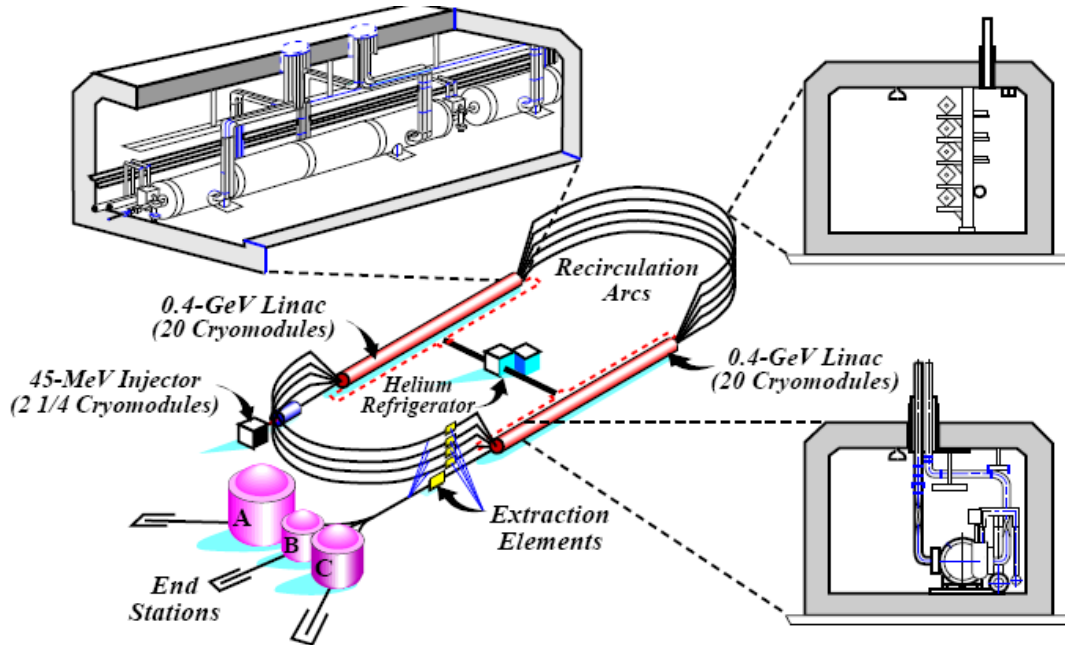


Figure 2-1. The schematic diagram of the Continuous Electron Beam Accelerator Facility (CEBAF). In the main picture one can see two linear accelerators and the bending arcs. The electron beam starts at the injector and terminates at the experimental halls (Hall A, B, C). In the upper left corner, the blowup shows a linac cryomodule. In the right upper corner, the cross section of five recirculating arcs in the tunnel is shown. In the right lower corner the cross section of a cryomodule is shown.

The CEBAF (Continuous Electron Beam Accelerator Facility) superconducting radio frequency (RF) electron accelerator at TJNAF (Thomas Jefferson National Accelerator Facility, or Jefferson Lab) is designed for experimental investigations of the electromagnetic structure of mesons, nucleons and nuclei through high energy electron and photon beams with energies up to 6 GeV, with a momentum resolution of $<0.01\%$, and 100% duty cycle. A schematic drawing of the accelerator is shown in the Figure 2-1. The accelerator is designed using the technology of superconducting niobium resonators. The linac injector emits 45 MeV polarized or non-polarized

electrons. The electrons are emitted with a frequency of 1.4971 GHz, synchronized with the accelerating electromagnetic wave of the same frequency in the superconducting cryomodule of the first linac, where they are accelerated through 20 cryomodules up to approximately 0.6 GeV energy. Each cryomodule contains eight niobium cavities, which are kept superconducting at a temperature of approximately 2 K using liquid helium, produced at the Central Helium Liquefier (CHL) located between the two linacs. The beam then passes through a recirculating arc, entering the second linac, which is of the same design as the first linac. The second linac accelerates the electron bunch by another 0.6 GeV. After passing through the second linac, the beam may be sent either to the experimental halls with 1.2 GeV energy, or, using the recirculating arcs, may be forwarded to the next acceleration cycle. An RF chopper system (operating at 499 MHz) is used to develop a 3-beam 1.4971 GHz bunch train at 100 keV. The beam is longitudinally compressed into 2 ps bunches separated by 2/3 ns intervals. While the beam is in the accelerator, it is focused and steered with quadrupole and dipole magnets. The CEBAF accelerator delivers beam currents sufficient to achieve luminosities of several times $10^{38} \text{ cm}^{-2} \text{ s}^{-1}$ to halls A and C. The luminosity achievable in hall B is limited by the maximum rates in the detector to about $2 \times 10^{34} \text{ cm}^{-2} \text{ s}^{-1}$.

2.2 CLAS Detector.

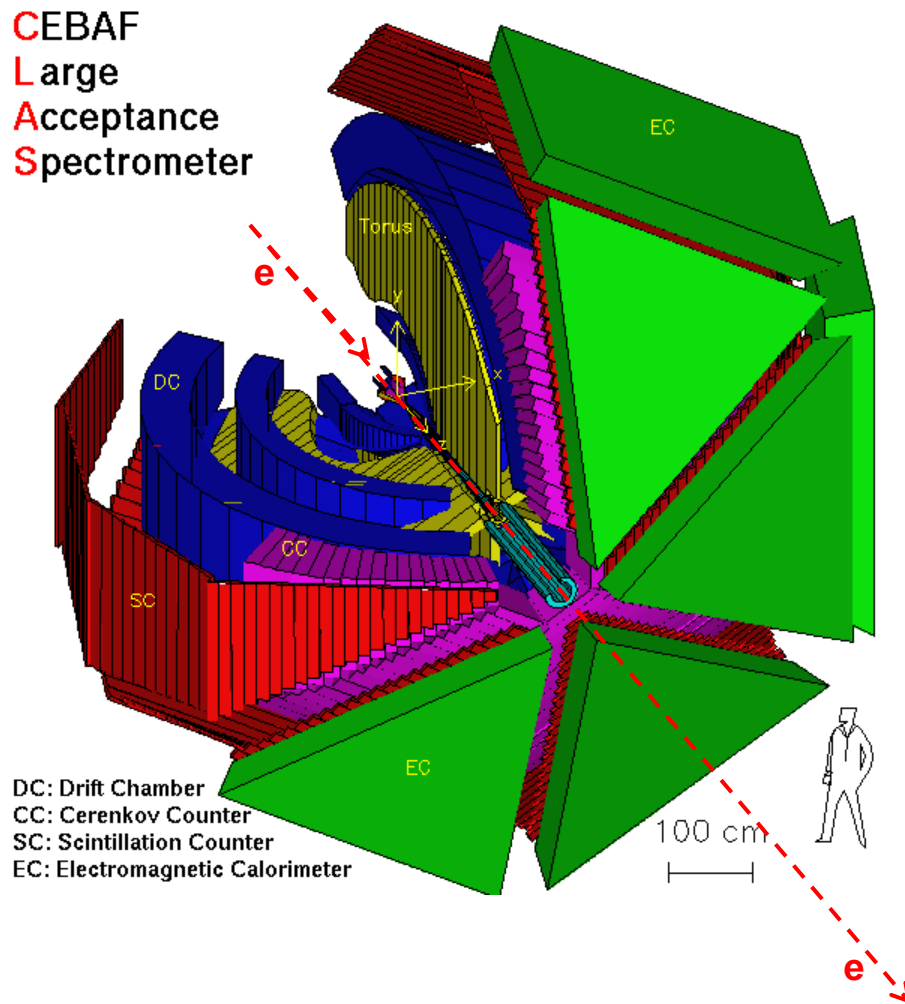


Figure 2-2. The schematic diagram of the CEBAF Large Acceptance Spectrometer, CLAS. The dashed red-colored line indicates the beam direction coming from the accelerator. Drift chambers are colored in blue and marked as ‘DC’. The six coils of the superconducting toroidal magnet are colored in yellow and marked as ‘Torus’. Gas Cherenkov counters are colored in pink and marked as CC. Scintillation counters for time-of-flight measurements are colored in red and marked as SC.

Electromagnetic calorimeters are colored in green and marked as EC. The figure presents the scheme of CLAS scaled 100 times compared to the real detector, which is about 8 m in diameter.

Currently there are three experimental halls at JLab (Hall A, B, C) (Fig 2-1) and a fourth hall (Hall D) has started construction as part of the 12 GeV upgrade.

The CLAS detector [32] is installed in Hall B (Fig. 2-2). It has almost 4π acceptance in solid angle and covers angles between 8° and 142° relative to the direction of the incoming beam from the accelerator. The target is located inside the detector on the beam axis. The total charge of the beam passing through the target is measured by a Faraday Cap (FC) located at the end of the beam line.

CLAS is divided into six identical sectors (each of them functioning as a separate spectrometer) with 5 meter long superconducting coils of toroidal magnets placed in-between the sectors (Fig 2-3), which are producing a toroidal field in the azimuthal direction.

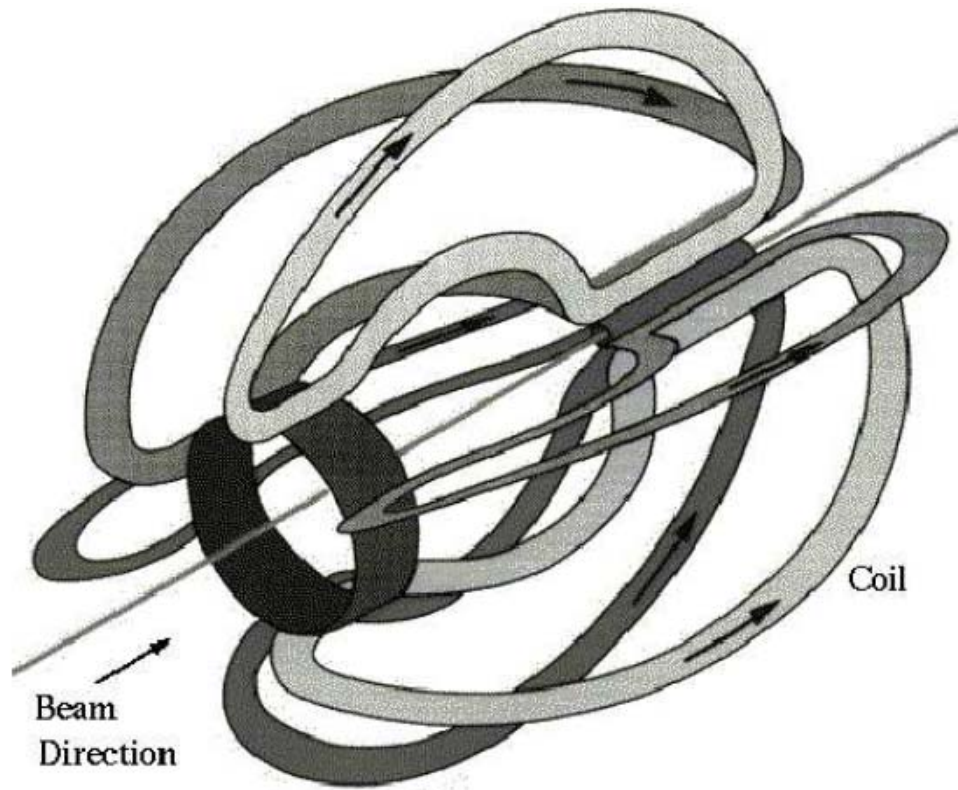


Figure 2-3. The schematic diagram of six coils of superconducting toroidal magnet.

The toroidal magnetic field ($\int Bdl$) inside the detector changes from 2 Tm in the forward direction to 0.5 Tm for backward angles. Such a choice gives an opportunity to measure the momentum of the charged particles with good resolution in a large range in lab angles, leaving the

area around the target unaffected by magnetic field which allows implementation of dynamically polarized targets. The advantage of the toroidal magnetic field is that it is nearly constant in the azimuthal direction, hence bending charged particles only in the polar direction. Depending on the field direction, negatively charged particles are either in-bending or out-bending compared to the direction of beam. For CLAS experiments the most standard is the former (which is the case also for EG2), while experiments with out-bending configurations allow covering a wider range of kinematics for scattered electrons and other charged particles. For shielding the detectors from charged electromagnetic background coming from target, CLAS is equipped with a second magnet (mini-torus) which surrounds the target placed in the center. The magnetic field strength of the mini-torus is only 1-5% of the main torus and it has little effect on the high energy charged particles.

The gaps between the cryostats are filled with six individually instrumented detector packages, which form six independent magnetic spectrometers (as mentioned above). This makes a good basis for carrying out experiments that require two or more particles in coincidence in the final state, with 1/1000 or better signal to background ratio at luminosities up to $2 \times 10^{34} \text{ cm}^{-2} \text{ sec}^{-1}$.

The particle detection system itself consists of drift chambers [60, 30, and 66] used for detecting trajectories of charged particles, gas Cerenkov counters [3] for identifying light charged particles, time-of-flight counters [71], and electromagnetic calorimeters [10, 14] for identifying showering particles (electrons and photons) as well as neutrons. While the six CLAS segments are equipped as totally independent magnetic spectrometers, they share the target, trigger, and data acquisition system.

2.2.1 Multiwire Drift Chambers.

To measure the trajectories of the charged particles and determine their momentum, the CLAS detector is equipped with the Drift Chambers (DC), which are in total 18 wire chambers (three in each of the six sectors). The bending of the track of the charged particle gives the

information about its momentum. The structure of the chambers allows tracking of the particles with energies down to 200 MeV/c or less, if detected particles in the backward angles, and covers a range from 8° to 142° in polar angle and an average of 80% of the azimuthal range. For timing resolution purposes the drift chambers should reconstruct tracks with 0.5% precision for momentum of the particle and with 2 milliradian precision for angle. That is achieved by using the measurement of the track in the three regions along its route.

The region of the chambers surrounding the target, where the magnetic field is comparatively weak, is called ‘Region 1’; the ‘Region 2’ chamber is larger and it is placed between the magnetic coils where the field is the strongest, and finally ‘Region 3’ has the largest chambers, placed outside the region of the magnetic field influence. ‘Region 1’ and ‘Region 3’ are used to determine the charged particle’s initial and final directions while passing through the DC, meanwhile, the ‘Region 2’ is used to determine the particle track’s maximum curvature. The chambers were constructed wedge-shaped to accommodate them in the space between the magnetic coils.

To minimize multiple scattering, the design stipulated that the amount of material in the region of particle tracking would be less than 1% of a radiation length. The current implementation has approximately 1 g/cm^2 of material, consisting primarily of air, drift chamber gas, and plastic windows.

Drift chambers of the CLAS contain approximately 130,000 wires. Wires are made from 30 μm thick gold-coated tungsten. Each region of the Drift Chambers consists of two super-layers of wires; one of them (axial) strung parallel to the magnetic field lines, the other one (stereo) strung at 6° with respect to the axial wires. This design provides accurate measurement of the polar angle θ and the azimuthal angle ϕ . Each super-layer consists of six layers of hexagonal wire cells (Fig. 2-4) (the exception is for the ‘Region 1’ stereo, where there are only four layers). Each drift cell has a sense wire in the center surrounded by six shared field wires, which form a hexagonal-shaped pattern. The hexagonal shape of the cells provides a good approximation to the circular cell in which the time/drift relation is independent of the particle’s entrance angle.

The fundamental principle of operation of drift chambers is based on the ability of high-energy particles to ionize matter. The volume of each region of drift chamber is filled with a 90% argon, 10% CO_2 non-flammable gas mixture, which provides a drift velocity of up to $0.04 \text{ m}/\mu\text{sec}$ and an operating voltage plateau of several hundred volts. The average efficiency to detect particle tracks for each layer is greater than 98% [60].

The charged particle passing through the drift chamber cell ionizes the atoms of gas. The electrons produced by the ionization drift toward the sense wire, and when close to the wire, create an avalanche of electrons. The signal thus induced on the sense wire is then amplified and discriminated by the chamber electronics, and recorded in the data acquisition system. Most of the inefficiency comes from tracks passing very close to the sense wire which give rise to signals with low pulse height and long durations.

The tracking, i.e., the reconstruction of the momentum and angle of the tracks, is performed in two stages. First, the hits in a super-layer are combined to form a “track segment.” Then the found “track segments” from different super-layers are linked to form a track. At this point the reconstructed momentum is within 3% to 5% of the true value of the momentum of the particle. In the second stage the start time information from the scintillator counters is used to obtain the drift time and then to convert it into the distance from the center of the cell. In overall average the tracking efficiency remains >95% for chamber hit occupancies up to 4% with a momentum resolution better than 0.4% [60].

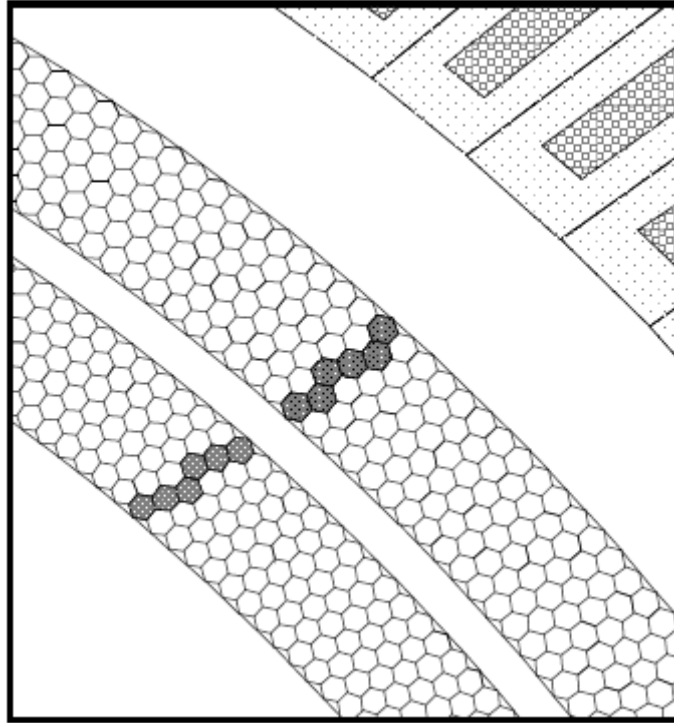


Figure 2-4. Layout of superlayers in Region 3. The sense wires are located in the center of each cell, while the field wires are located in the vertices of the hexagons. The shadowed hexagons represent the cells containing the sense wires which produced a signal for a representative track.

2.2.2 Cherenkov Counters.

The Cherenkov Counter (CC) serves the dual function of triggering on electrons and separating electrons from pions [33]. CLAS is equipped with threshold Cherenkov counters in the forward region in every sector covering polar angles up to $\theta = 45^\circ$. The main principle of CC is based on the physical phenomenon found by Cherenkov [56], which says that the particle passing through some matter emits electromagnetic radiation if its own velocity exceeds the speed of light in that matter. The speed of light in the matter is equal to: $v=c/n$, where c is the speed of light in a vacuum and n is the index of refraction in the given medium. The limit for Cherenkov radiation is:

$$\beta = v/c = 1/n. \quad (2.1)$$

The radiator gas used in the Cherenkov counters in CLAS is perfluorobutane (C_4F_{10}) with index of refraction of 1.00153 [32].

Because of the toroidal configuration of the magnetic field in the detector, the trajectories of particles incident on the CC surface approximately maintain their ϕ azimuthal angle, therefore optics for CC was constructed to accumulate light in ϕ direction [3]. The CC counter in each sector consists of two identical sub-sectors, each consisting of 18 optical modules (Fig. 2-5). Each of the modules is equipped with elliptical, hyperbolic and cylindrical mirrors, to direct the light into the light collection cone (Winston cone) with the PMT attached to its end (Fig. 2-6). The components of the Cherenkov counters are mounted on a triangular shaped aluminum frame and protected with a 0.08 mm Tedlar PVF film sandwiched around a sheet of Mylar. The PMTs are mounted in the region obscured by the torus so that they do not increase the material in the path of particles passing through CLAS. In general the Cherenkov radiation is strongly peaked in the ultraviolet. The gain of the PMTs of the Cherenkov counters is equalized by single-photoelectron response of the photomultiplier. An electron traveling through the active volume of the detector typically produces 4-5 photoelectrons [3].

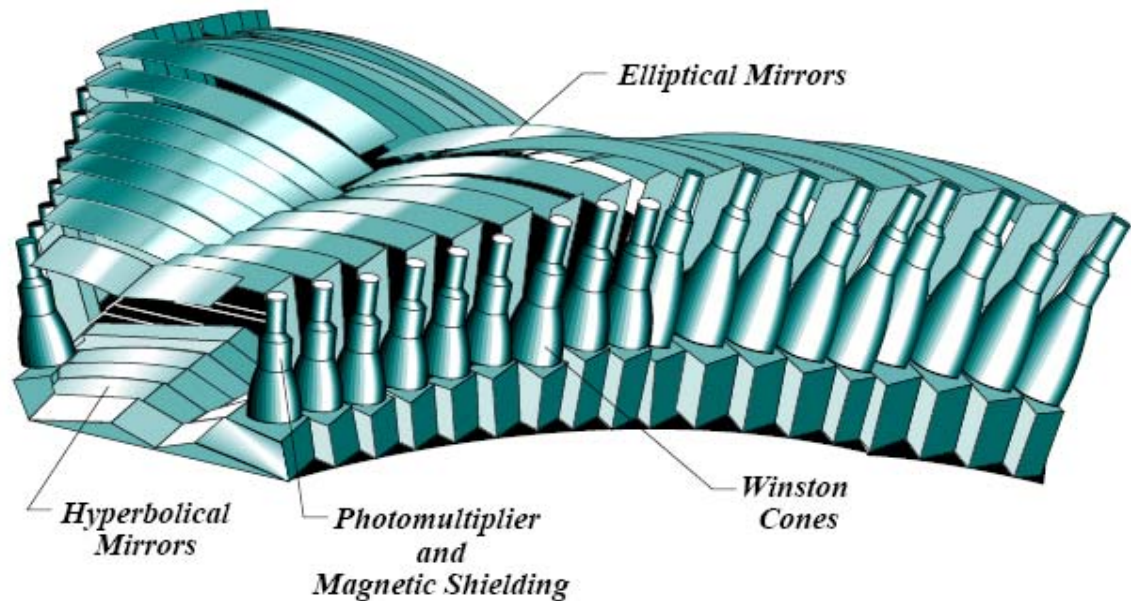


Figure 2-5. Arrangement of the CC modules of one sector.

The efficiency of the Cherenkov counters as determined from the measured photoelectron yield is better than 98% in the fiducial active detection region [3]. Outside the fiducial regions the efficiency has a very strong variation, and therefore events with the electrons in these regions are usually excluded from the analyzed data sample by a fiducial cut (see paragraph 4.3.4).

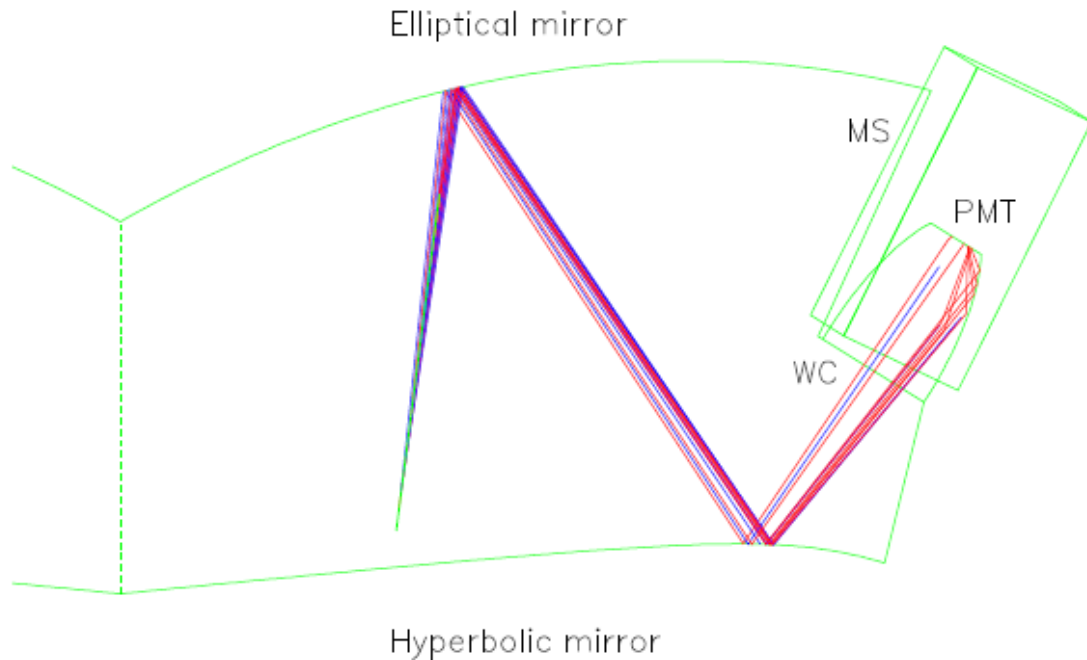


Figure 2-6. One optical module of the CLAS Cherenkov counter, showing the detector components and hypothetical light paths from electrons. Cherenkov light from electrons is reflected twice from the mirrors into the Winston Cone, surrounded by the magnetic shield. The Winston cones are used to collect the light onto the surface of the photo-multiplier tubes (PMT).

2.2.3 Time-of-Flight System.

The time-of-Flight (TOF) system of CLAS [70] covers the polar angles from 8° to 142° . Scintillators are placed radially outside the tracking system and Cherenkov counters, just in front of the calorimeters (Fig. 2-2). Each sector of the TOF consists of 57 scintillators (Bicron BC-408) aligned perpendicular to the beam direction, each covering an approximate scattering angle of 1.5° . The first 23 and last 4 counters have widths of 15 cm and 22 cm, respectively. The width was

chosen to optimize the timing resolution of a single counter and still have sufficient granularity for the triggering process. The scintillator thickness of 5.08 cm is uniform throughout, chosen to give a large signal for traveling minimum-ionizing particles. The length is from 32 cm to 450 cm. Each of the TOF counters (“paddles”) has one PMT at each end (Fig. 2-7). The last 18 counters in each sector, covering the back angles, are paired into 9 logical counters connected to single time-digital converters (TDC) or amplitude-digital converters (ADC), so that there are 48 logical counters per sector.

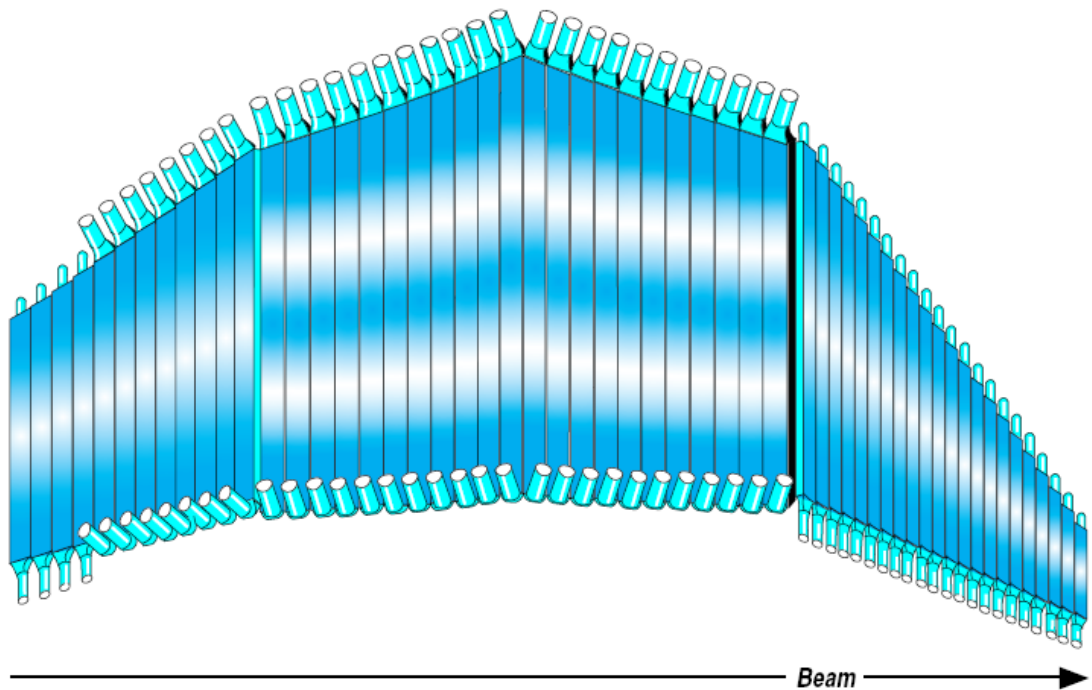


Figure 2-7. TOF system for one sector. The length, the width and the readout configurations are different for different paddles.

The TOF system serves as the main tool for particle identification. It measures the time interval during which the particle is passing from the point of interaction in the target to the external boundary of the CLAS detector, where the TOF system is located. Also using the information about the length of trajectory measured with the DC, the velocity of the particle can be calculated as $\beta = S_{sc} / (t * c)$, where S_{sc} is the length of the trajectory, t is the time of flight and $c=29.97$ cm/nsec is the speed of light. The drift chambers of CLAS are measuring the particle

momentum also, using the particle trajectory curvature. Therefore the particle mass can be reconstructed as $m = (p\sqrt{1 - \beta^2}) / \beta$.

The timing resolution for a single counter varies with the length and the width of the strip, with a better resolution of 130 psec for the forward counters, and 300 psec for angles above 90° [70]. These timing characteristics allow for a reliable pion-kaon separation up to a momentum of 2 GeV.

2.2.4 Forward Electromagnetic Calorimeter.

At the forward part of each sector in the CLAS detector are located lead-scintillation electromagnetic calorimeters (EC) [10]. The main purpose of EC is detection and triggering of electrons with energies larger than a given threshold (e.g., 0.5 GeV), detection of photons with energies larger than 0.2 GeV (e.g., for the purpose of reconstructing π^0 and η by means of measurements of their decay to 2γ , or for direct detection of single photons from DVCS or other radiative processes) and detection of neutrons (for separation of neutrons from photons, EC timing measurements are used). The EC covers the θ polar angle up to 45° . In two of the sectors the coverage is extended up to 70° by the Large Angle Calorimeter (LAC). The detector is constructed from sandwiching layers of scintillator strips between lead sheets with a total thickness equal to 16 radiation lengths [10]. The ratio between thicknesses of lead and scintillator is 0.24, resulting in 8.4 cm lead and 39 cm of scintillator per module. In such a configuration about 1/3 of the energy of showering particles is deposited in the scintillators. EC modules have the shape of approximately equilateral triangles and they match to the hexagonal geometry of the CLAS detector. Each of the modules is a sandwich of 39 layers with 10 mm thick BC412 scintillators and 2.3 mm thick lead sheets (Fig. 2-8). The area of layers increases to optimize position resolution for neutral particles coming from the target.

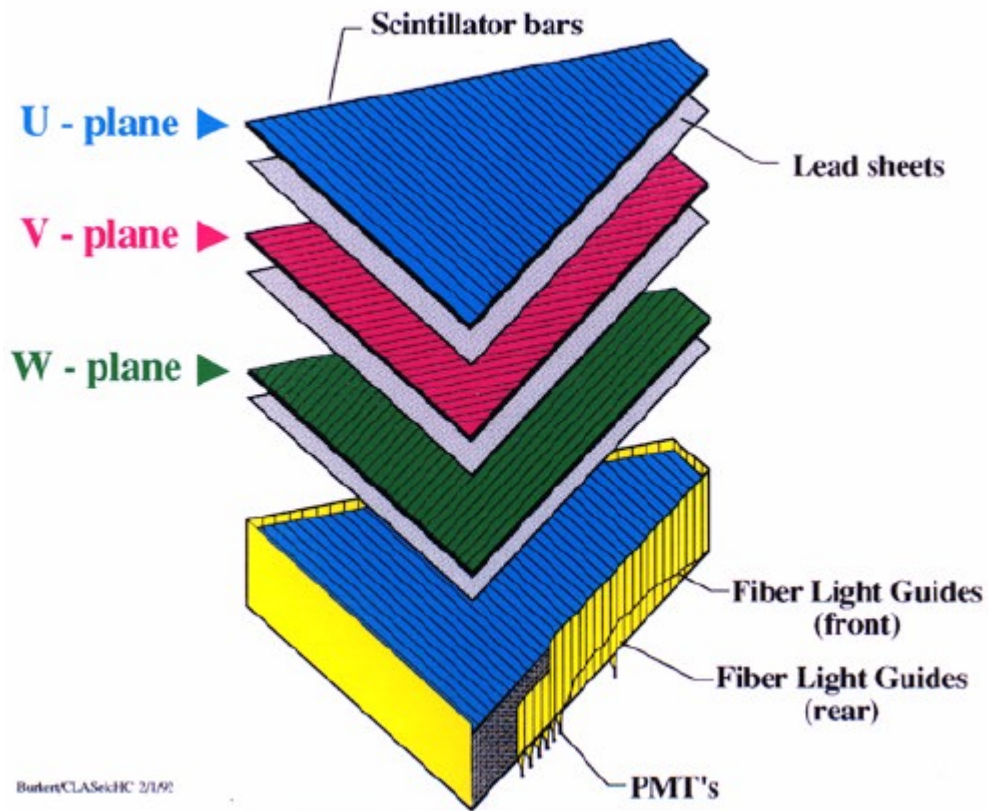


Figure 2-8. Exploded view of one of the six CLAS electromagnetic calorimeter modules.

Each layer is composed of 36 scintillator strips parallel to one side of the triangle (Fig. 2-8), the orientation changing by approximately 120° between two adjacent layers. The three orientations, called views, are labeled U, V and W, each containing 13 layers. The design provides stereo information on the hit position. The entire detector is subdivided into inner and outer stacks, containing 5 and 8 layers for each view, respectively. This provides longitudinal sampling of the shower for improved hadron identification. In Figure 2-9 one can see the readout scheme. Each module requires $36(\text{strips}) \times 3(\text{views}) \times 2(\text{layers}) = 216$ photomultipliers. Altogether there are 8424 scintillator strips and 1296 photomultipliers. The two Large Angle Calorimeters are implemented only in sectors 1 and 2 (Fig. 2-2). They consist of 33 layers, each composed of a 0.2 cm thick lead sheet and of 10 cm wide and 1.5 cm thick NE110A scintillator strips. The layers form a 40×24 matrix with cell size $10 \times 10 \text{ cm}^2$, and each consecutive layer is rotated by 90° . Each

module of the LAC is divided into inner and outer parts providing better electron/pion discrimination. To avoid optical cross-talk, each pair of contiguous scintillators are separated by Teflon strips of 0.2 mm thickness, and another layer of Teflon (0.2 mm thick) is inserted between the lead sheets and the scintillators. The module thickness corresponds to 12.9 radiation lengths.

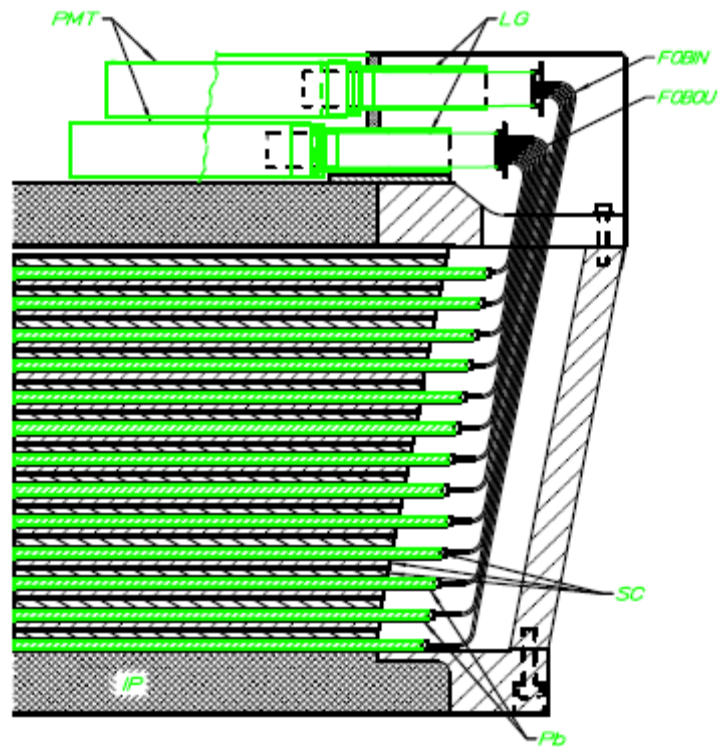


Figure 2-9. Electromagnetic Calorimeter readout scheme. PMT – photomultiplier, LG – Light Guide, FOBIN – Fiber Optic Bundle Inner, FOBOU – Fiber Optic Bundle Outer, SC – Scintillators, Pb – 2.3 mm Lead Sheets, IP – Inner Plane (Composed of two 1.905 mm Stainless Steel Face Sheets and 72.2 mm Foam Core Plate.)

The calibrations and analysis of the production runs showed that the calorimeter has an e/γ energy resolution $\frac{\sigma}{E} \leq \frac{0.1}{\sqrt{E(\text{GeV})}}$, a position resolution $\delta r \approx 2 \text{ cm}$ at 1 GeV, e/π rejection $>$

99% at energies greater than 1 GeV, a mass resolution for 2-photon decays $\frac{\delta m}{m} \leq 0.15$, neutron detection efficiency $> 50\%$ for $E_n > 0.5$ GeV, and a timing resolution ≈ 400 psec [10].

2.3 EG2 Experiment Target.

The complete target system consisted of a liquid target and a solid target, which were in the beam simultaneously [45]. The main experimental requirements for the target were as follows:

1. Large acceptance for semi-inclusive and exclusive kinematics, plus a good match to the CLAS spectrometer acceptance
2. Minimal mass for low-energy particles at large angles (70-140 degrees relative to the beam direction) as well as forward-going particles
3. Approximately equal scattering rates for two targets in the beam simultaneously
4. One of the targets needed to be a stable deuterium cryotarget
5. Less than 2-3% of a radiation length of any target material to suppress secondary electromagnetic processes
6. Minimal entrance/exit window thicknesses for cryotarget to maximize target/window ratio
7. Rapid target changes for the heavy nuclear targets
8. Minimal mass in support structure

The support structure for these targets was designed to minimize the impact on the experimental acceptance and the quality of the data. Nevertheless, the potential for some impact was unavoidable, and the main goal of the run requires a high-precision comparison of the targets. Because of that it was very important to implement a highly detailed simulation of the system into GSIM (see chapter 4.3.1). GSIM is the GEANT simulation package for the CLAS detector [79].

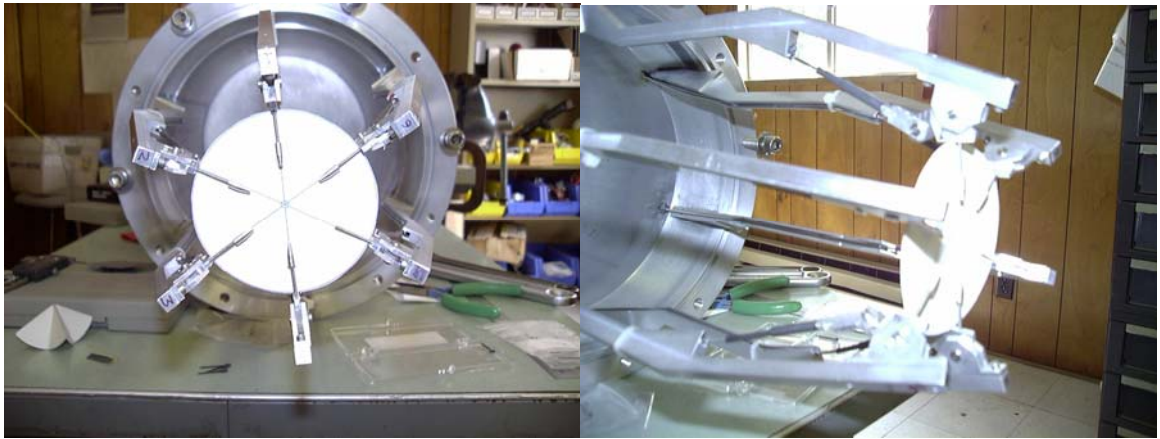


Figure 2-10. Photos of the EG2 target with all solid target holders at the in-beam position.

The whole EG2 target is a complex composition of the target materials of interest and support structure (Fig. 2-10, Fig. 2-11). During the experiment, two target materials were exposed simultaneously to the incoming electron beam. The beam passed first through the liquid substance (e.g. deuterium) which we refer to here as the liquid target, and then through the solid material (the solid target).



Figure 2-11. The full double-target assembly, showing one solid target inserted, five solid targets retracted, and the thermally insulated cryotarget cell.

For most of the experiment the cell for the liquid target was filled with deuterium, but for a short period it was filled with hydrogen and for some time it was just “empty” (filled with cold gas at 30 Kelvin). The liquid target cell itself was constructed from Kapton. In Fig 2-12a one can see the picture of the cell made from Kapton from CLAS/GSIM (see chapter 4.3.1 for more details) colored in yellow, where the blue color shows the deuterium liquid which is actually inside the Kapton shell. The length of the liquid target is approximately 2 cm. The plane projection of the target one can see in Figure 2-12b. On the entrance and exit locations of the liquid target there are placed thin aluminum foils and also at the exit there is a vacuum tube sealed by aluminum foils.

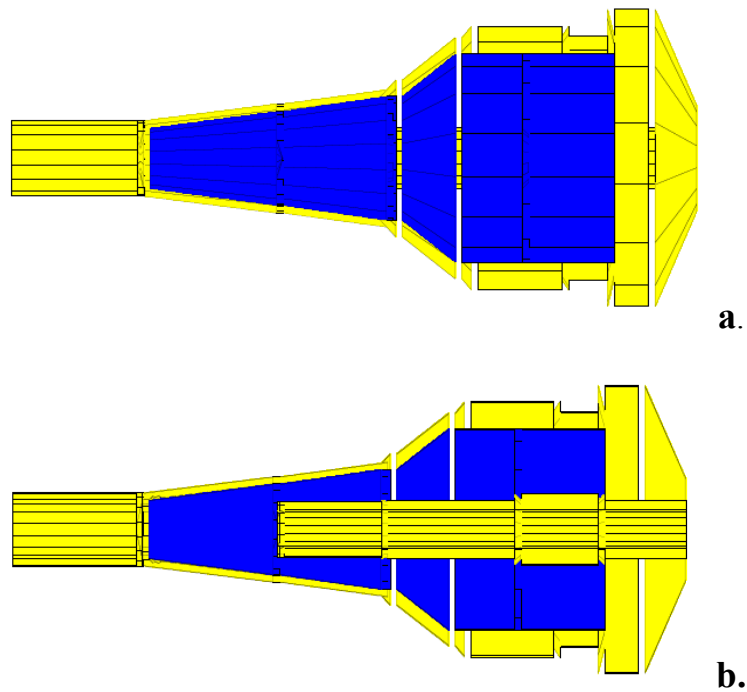


Figure 2-12. a) The Kapton liquid target cell colored in yellow inside the CLAS/GSIM. The blue color shows the deuterium part which is actually inside the kapton shell. b) The liquid target cell plane projection. The blue color shows the deuterium part.

For the solid target six different target materials were used. All of them had the form of a small circular disk (Fig. 2-13). The disk itself was suspended from the whole target system by a

tiny carbon fiber rod, with a loop that surrounded the disk as shown in Figure 2-13a and in Figure 2-13b.

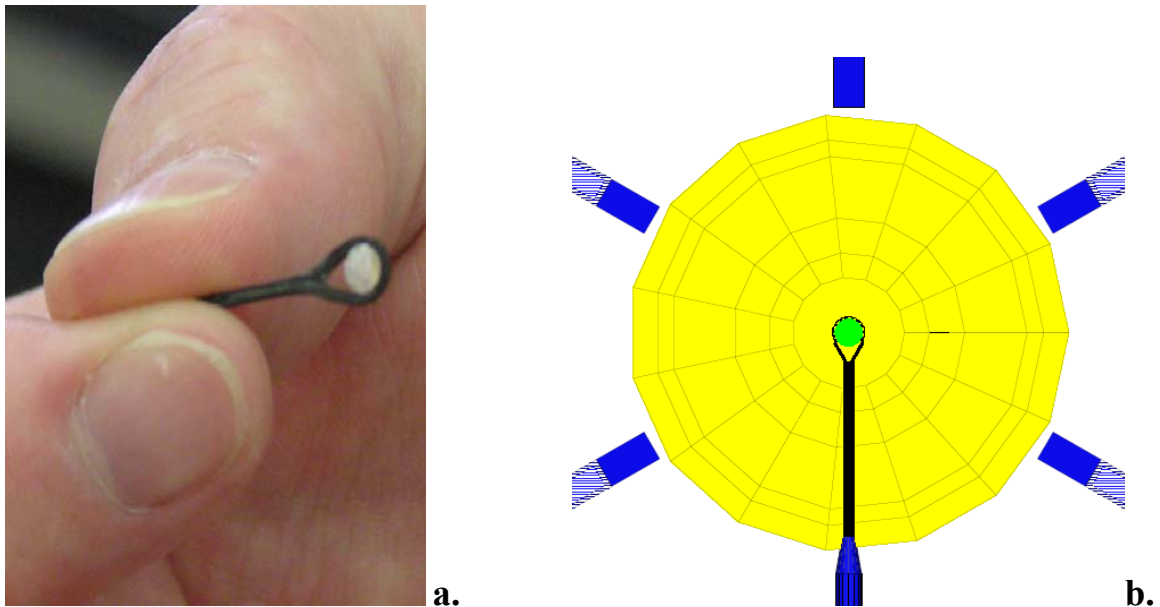


Figure 2-13. a) A photograph of one of six solid targets surrounded by a carbon fiber loop at the end of a carbon fiber rod. Notice the small size of the target. b) The solid target in the in-beam position inside CLAS/GSIM.

Here is the list of solid targets with their geometrical parameters for the long production run beginning February 2004:

1. Carbon target with radius equal to 0.15 cm and thickness equal to 0.1723 cm
2. Iron target with radius equal to 0.15 cm and thickness equal to 0.04 cm
3. Lead target with radius equal to 0.15 cm and thickness equal to 0.014 cm
4. Thin aluminum target with radius equal to 0.15 cm and thickness equal to 0.0015 cm
5. Thick aluminum target with radius equal to 0.15 cm and thickness equal to 0.058 cm
6. Tin target with radius equal to 0.15 cm and thickness equal to 0.0312 cm

Initially the deuterium, carbon, iron, lead and tin target thicknesses were selected in order to get an equal number of nuclei along the target length for all cases. Later it was found that there was excessive background in the case of lead, and because of that the thickness of the lead target

was reduced by a factor of two. The largest data sets for the EG2 experiment were for the carbon, iron and lead targets.

While one of the solid targets was exposed to the incoming beam, the other solid targets were held away from beam-line by using special fixtures as shown in Figure 2-11. The targets were interchanged remotely via an EPICS interface that controlled the six pneumatic actuators used to move the target, ensuring only one target was inserted at a time.

The separation distance between the solid and liquid targets was approximately equal to 4 cm. During the experiment the solid target was placed at $z = -25$ cm inside CLAS, while the 2 cm liquid target was at $z = -30$ cm correspondingly (we assume that $z = 0$ corresponds to the center of the CLAS).

All solid targets were supported in the target system by so-called aluminum 'fingers'; while these fingers were positioned in the shadow of the CLAS coils to minimize their impact, in principle they could cause distortions in the measurements of some observables. For instance, pions striking the fingers could be scattered into the detector acceptance, be reconstructed, and they would then contribute to the measured p_T of the detected particles' transverse momentum spectrum. Because these fingers are close to the target region, the solid angles subtending them from the deuterium and solid targets are different, which could also distort the measurement of p_T as well as other variables. These concerns necessitated a detailed simulation of the EG2 target.

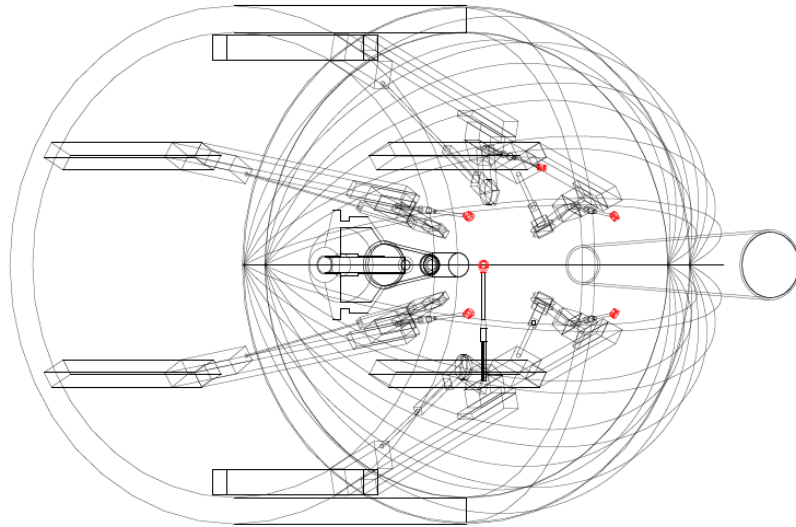


Figure 2-14. An X-ray view of EG2 target inside CLAS/GSIM. One can see the contours of the foam chamber covering the whole target.

To avoid multiple scattering, the target was kept in vacuum inside a foam scattering chamber. One can see it in Figure 2-14 from the simulation. A photograph of the actual chamber is shown in Figure 2-15. The vacuum surrounding the cryotarget was maintained by a foam scattering chamber fabricated from Rohacell 110XT or 110WF, which has an approximate density of 110 mg/cc. To keep the two targets in close proximity to each other, the solid target was also located within this vacuum volume. The scattering chamber consisted of a spherical end cap shell glued to a cylindrical tube that was in turn fastened to an aluminum ring for mounting to the rest of the vacuum system. The thickness of the spherical shell was 9.5 mm while the thickness of the cylinder was 12.2 mm. Because large-sized blocks of Rohacell were not commercially available for fabricating these pieces, the required material thickness was achieved by fastening 40 mm thick layers together using epoxy. The epoxy used was a mixture of WEST 105/205 resin/hardener and WEST 410 low-density filler material mixed to a nearly dry paste to keep the local density of the glued joints to a minimum while maintaining a leak tight bond. The vacuum properties of the chamber were found to be more than adequate for the level of vacuum needed (6×10^{-6} mBar) without any coating of the inner or outer chamber surface, following a one-day outgassing phase. The

chamber was enclosed in a sheer nylon net as a safety precaution in case of rupture, due to the proximity to fragile drift chamber windows. The exit foil for the chamber was located on an extended conical tube in order to preserve minimal mass at the smallest angles within the acceptance. This conical tube was made of a carbon fiber lay-up 0.84 mm thick, which resulted in a very rigid structure that was still quite low in mass. Because it was glued to an extension of the spherical part of the chamber, it added beneficially to the mechanical strength of the spherical section. In order not to present a potential “thick target” for particles scattered from the main targets, the conical cone was made of two cone sections; the smaller cone “pointed” to a location downstream of the primary targets, and the larger cone “pointed” to a location upstream of the primary targets. This design limits the thickness of the conical tube through which particles emerging from the primary targets could pass.



Figure 2-15. A photograph of the foam vacuum chamber that surrounded the whole target system.

The commissioning of the target required a few specific procedures before production data taking could begin. In addition to visual verification of the solid target identity as a check on the control software, a period of alignment of the electron beam was required. The procedure involved vertical and horizontal stepping of the beam in increments of approximately 0.1 mm. First, the profile of the beam was determined using a wire scanner and was verified to be Gaussian in shape

with an RMS of approximately 50-100 microns. The cryogenic target was emptied, and the thin aluminum window was inserted as the solid target. Online reconstruction of the electron tracks along the beam line access was performed, and the vertex location along the beam line axis was determined. Figure 2-16 shows a plot of the vertex location of electron tracks under these conditions; the four peaks correspond to the cryotarget entrance and exit foils, a cryogenic isolation foil, and the thin aluminum target. Plots such as the one in Figure 2-16 were analyzed to determine the yield from the cryotarget entrance window, exit window, and the solid target as a function of the relative transverse beam coordinates (x,y). When the beam position began to near the edge of the solid target or cryotarget windows, the yield increased dramatically, providing an efficient measure of edges. 'Flat' regions were observed, and the beam was positioned in the middle of these regions. During production data taking, the position of the beam was measured continuously and non-invasively using a pair of resonant cavity position monitors, and the stability of the position was significantly better than 0.1 mm. Empty cryotarget runs were taken periodically, in combination with the thicker aluminum target, for the aluminum entrance/exit window corrections to the data.

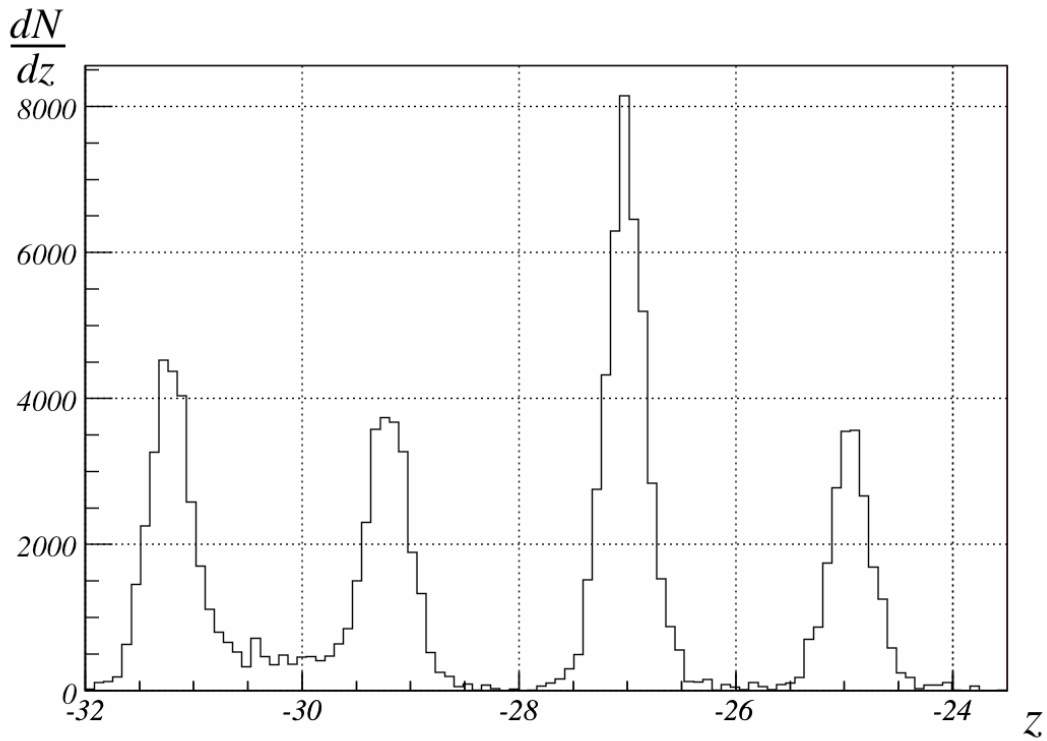


Figure 2-16. A plot of the vertex location of electron tracks for an “empty” cryotarget (filled with cold deuterium gas) and the thin aluminum target; the four peaks, from left to right, correspond to the cryotarget entrance and exit foils, a cryogenic isolation foil, and the thin aluminum target. The areas under the peaks are consistent with the relative thicknesses of the four foils.

Figure 2-17 shows the target profile with a full cryotarget and with the carbon target inserted. As can be seen, the two targets can easily be distinguished from each other and from the thin cryogenic isolation foil using only the electron track.

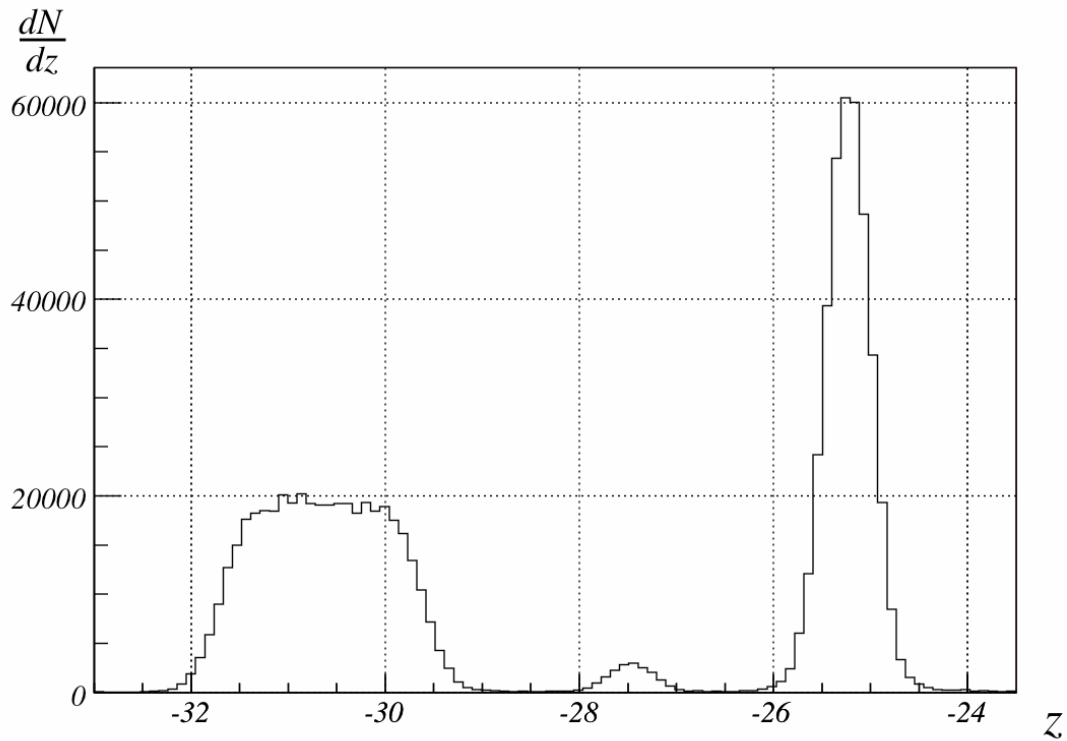


Figure 7. The target profile with a full deuterium cryotarget and with the carbon target inserted. The two targets are seen to be well isolated from each other and from the cryogenic insulation foil. The plot represents about 1.4% of all deuterium + carbon target events.

2.4 Trigger System and Data Acquisition.

The main purpose of the triggering system is the “interesting events” selection. There is a double-level trigger system for experiments in CLAS. The first level trigger (Level-1) is a fast response system for possible event candidate’s preliminary identification. Most electroproduction experiments in CLAS require the scattered electron to be detected. The Level-1 trigger serves the purpose to select events with a possible electron in the detector and triggers the data acquisition system to record the event, which will be further analyzed. The Level-1 trigger uses information from the pretrigger boards of the EC, CC and TOF to form a coincidence signal which is sent to Read-Out-Controllers (ROCs). This level only ensures that there was sufficient energy deposited in the calorimeter and there was a signal in the Cherenkov counter (EC and CC are in coincidence for

each sector separately). To improve the event/background ratio even more the Level-2 trigger was implemented in CLAS, which identifies possible track candidates in the drift chambers. The Level-2 trigger reads information from the Drift Chamber wires and searches for track segments. The CLAS data acquisition (DAQ) system consists of 17 ROCs communicating with a Trigger Supervisor board which makes the decision whether the event should be read out. If there is a trigger, the data signals are read out, and sent to the Event Builder (EB) process, which forms a complete event by putting together data from different parts of the detector and stores it in the Event Transfer (ET) system. The ET system used shared memory and a variety of protocols to allow more than one process to access the event for writing it out and analyzing at the same time. The Event Recorder (ER) process writes data from the ET system to the RAIDs (Redundant Array of Inexpensive Disks). The data from the RAIDs are later transferred to a tape silo for permanent storage. The schematic of the DAQ is shown in figure 2-16 [43]. Some subsets of events from the ET system are constantly being processed to monitor data quality and identify problems. The status of detector components is constantly monitored during the experiment and stored in the database for offline analysis.

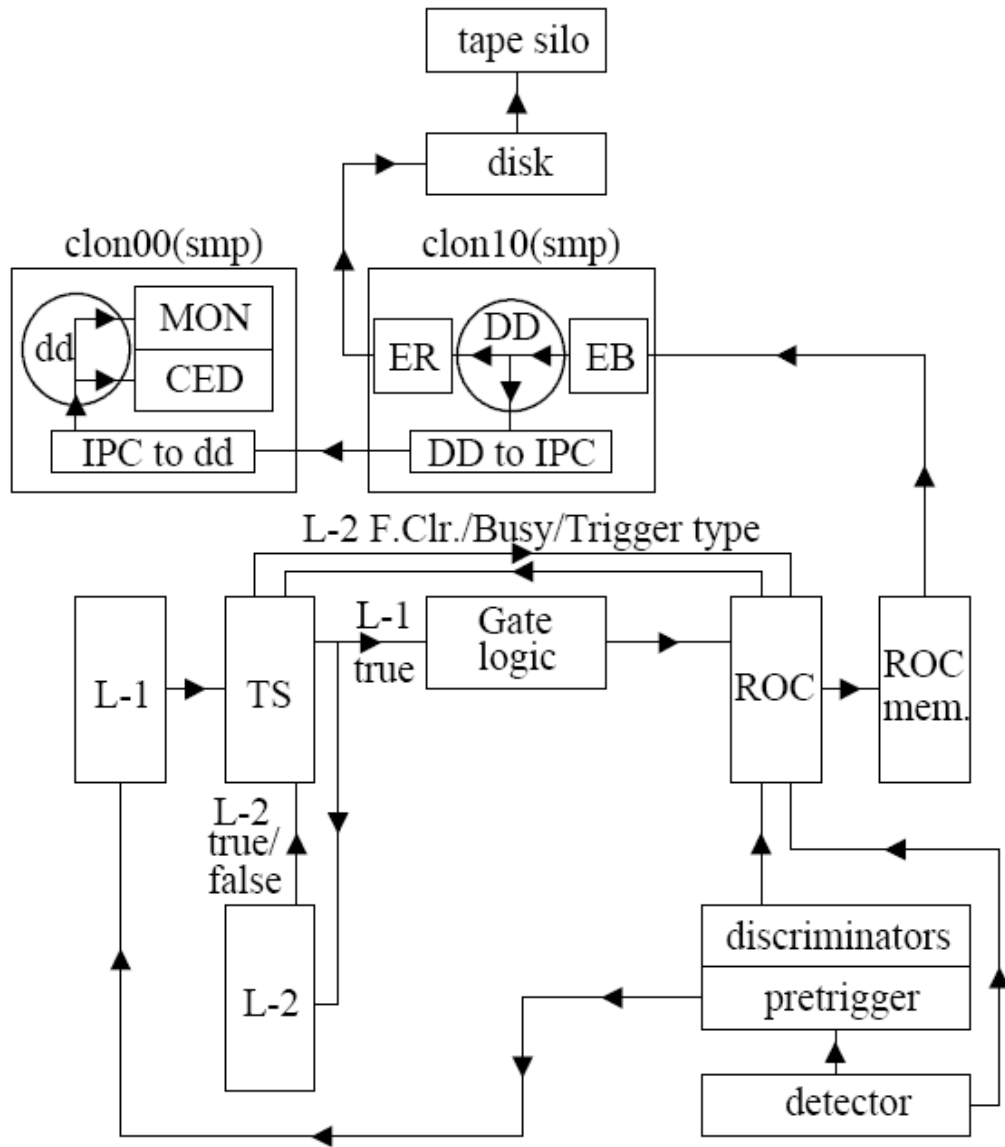


Figure 2-18. CLAS Data Acquisition System schematic view. Abbreviations used on figure are corresponding to the following components: L-1 is the Level-1 trigger, L-2 is the Level-2 trigger, TS is the trigger supervisor, ROC is the Read-Out-Controllers, EB is the event builder, ER is the event recorder, DD and dd are the Event Transfer system, IPC is the Inter-Process control, MON is the monitor and user software and CED corresponds to the single-event display.

3. Data Taking, Calibration and Processing During EG2 Experiment

Here is presented the analysis results of the CLAS/EG2 experiment [28], which was carried out during the period February-March in 2004. It measured electroproduction on liquid and solid targets simultaneously placed in the beam. The data from the experiment are saved in separate files for each run, containing $\cong 10\text{M}$ events; this limitation comes from the event size and the fact that files are limited to a size of 2 GBytes. The RAW data are saved in BOS [22] format. For analysis these files are processed by the offline reconstruction program (RECSIS [41]) in order to identify particles in the events (the process of reconstruction is referred to as “cooking”). Part of the data is processed to calibrate the various detector components in order to achieve the optimum resolution from each detector element. The “cooking” and calibration procedures were performed by Lamiaa Elfassi and Lorenzo Zana.

3.1 Data Processing.

The RAW data reconstruction procedure is called “cooking.” The “cooking” procedure is carried out. The whole process of reconstruction can be divided into three stages.

During the first stage, from the raw information of channel ID, ADC, and TDC the hits are reconstructed in each detector by its own stand-alone reconstruction package. The output results are recorded in the intermediate BOS banks in BOS data format. In the second stage the output from all detectors is processed through event builder program (SEB) [72] to initiate time-based tracking and combine the different detector hits for identification of individual particles in the events. The resulting event information is recorded in BOS banks and written to disk files for further analysis. The SEB package performs the procedure of geometrical match of tracks and hits, identifies the trigger particle, calculates the trigger time, defines particle identification (PID), and builds an event which RECSIS then writes to output. The concept of geometrical matching is to define distances between the detector hit position (r_i) and the position on the detector plane (r_{pl})

defined by a track. For each hit the squared sum of the differences between the coordinates of the track and the detector hit is divided by the error of the coordinates:

$$C_i^2 = \sum_{i=x}^z \frac{(r_{pl} - r_i)^2}{\sigma_{r_i}^2} \quad (3.1)$$

where i runs over the x, y and z coordinates for a given detector, and σ_{r_i} is the error estimate for these coordinates. The hit with the minimum C_i is taken as a match. First the matching is done for all charged tracks reconstructed in an event, then the remaining hits in the electromagnetic calorimeters that were not associated with any track are considered as candidates for neutral particles. Afterwards, the trigger particle is identified, for which (for electron scattering experiments) it is required to have a negative track and a showering hit in the EC. From all the possible candidates the one is chosen that is best matched to an electron candidate.

The time of the interaction in the target (vertex time) is defined as:

$$t_{\text{int}} = t_{\text{det}} - \frac{S_{\text{det}}}{\beta c} \quad (3.2)$$

where t_{det} is the time for trigger particle measured by the detector, S_{det} is the path length of the particle, and β is the particle velocity in units of the speed of light (determined using the particle momentum). This interaction time is used to select the correct electron beam bunch time, which is then used as the vertex time. An example of SEB hit matching is shown in Figure 3-1. When the trigger particle is defined, β is calculated for each of the remaining particle candidates based on the detector measured time and path length from the target to the detector:

$$\beta = \frac{S_{\text{trk}}}{(t_{\text{det}} - t_{\text{vertex}}) \cdot c} \quad (3.3)$$

Afterwards, the charged particles are identified using the β vs. momentum dependence. To calculate β for neutral particles, the time measured in EC is used. If β of the neutral particle is within 5% of 1.0, the particle is distinguished as a photon, and otherwise it is marked as a neutron.

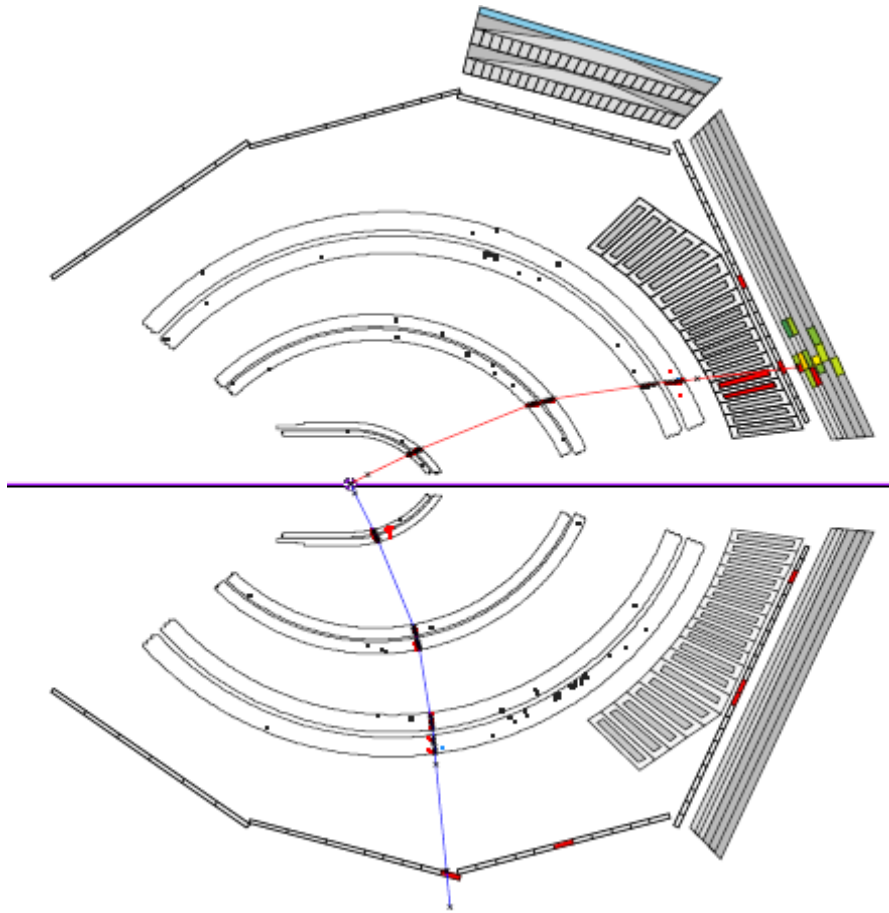


Figure 3-1. An event reconstructed by RECSIS. The in-bending track colored in red corresponds to the electron that triggered the event and the out-bending track colored in blue corresponds to a positively charged particle.

3.2 TOF Calibration.

The TOF calibration consists of four steps: calibration of individual TDC and ADC channels, the left and right PMT alignment, the attenuation length calibration and the counter-to-counter calibration.

The pedestal of the ADC is the channel where an effective zero measurement would fall [71]. It depends on the level of noise in all the components hooked up to the ADC. These pedestals were measured by taking runs with random triggers. An offset of 40 ADC channels was added to the pedestals to avoid reading low voltage noise in the ADC [71]. These data are analyzed and saved in the calibration database. The TDCs were calibrated using runs taken with a special DAQ

pulser configuration [71]. Every counter in the TOF was pulsed and the response of each TDC was analyzed for various delays between “start” and “stop” signals. The actual time was parameterized in terms of the measured TDC time as:

$$t = c_0 + c_1T + c_2T^2 \quad (3.4)$$

The constants c_1 and c_2 are saved in the calibration database. The parameter c_0 is not relevant, since the left-right calibration is subsequently performed to equalize the left-right difference for each counter.

The time-walk corrections were obtained using a laser system which delivered a light pulse to the center of each scintillator counter [71]. The intensity of the light was varied using a neutral density filter, and the pulse height and the times were measured at the both ends of the counter. The time, corrected for amplitude dependent delays, is determined using the formula:

$$t_\omega = t - f_\omega\left(\frac{A-P}{Th}\right) + f_\omega\left(\frac{600}{Th}\right).$$

$$f_\omega = \frac{\omega_2}{x^{\omega_3}}, \quad \text{if } x < \omega_0.$$

$$f_\omega = \frac{\omega_2}{\omega_0^{\omega_3}}(1 + \omega_3) - \frac{\omega_2\omega_3}{\omega_0^{\omega_3+1}}x, \quad \text{if } x > \omega_0. \quad (3.5)$$

where t is the measured uncorrected time, A is the pedestal non-removed ADC channel number. P is the position of the pedestal. Th is the channel corresponding to the lead-edge discriminator threshold of 20 mV, and $f_w(x)$ is the time walk correction function, obtain from fitting laser calibration data. The three variables in Eq.(3.5) ω_0 , ω_2 , ω_3 are the calibrations parameters obtained from the fit.

The position of the hit in the TOF counter is determined by the time delay in the left and right PMT. Therefore the offset between the left and right counter must be determined to provide an accurate measurement of the position. For each counter the quantity:

$$l = L_{TDC}^{LEFT} - L_{TDC}^{RIGHT} \quad (3.6)$$

should be centered around zero. If this is not the case, the offset $\Delta t = \frac{l}{v_{eff}}$ is added to this value, where v_{eff} is the effective velocity of the light in the TOF calculated using hit position information provided by tracking [71].

In the case of very low momentum particles the separation between pions and protons may be performed using the information of deposited energy in the scintillators without using timing information, since the dependence of the deposited energy ($\delta E / \delta x$) on the particle momentum is different for protons and pions.

In figure the deposited energy ($\delta E / \delta x$) of hadrons versus hadron momentum is plotted after energy calibration. At low energies, protons and pions can be well separated. At higher momentum, starting from 0.8 GeV/c, as protons become minimum ionizing, the two bands start to merge. This method of pion identification is not used in standard data analysis; its main purpose is to provide a reasonably clean sample of pions for further calibration.

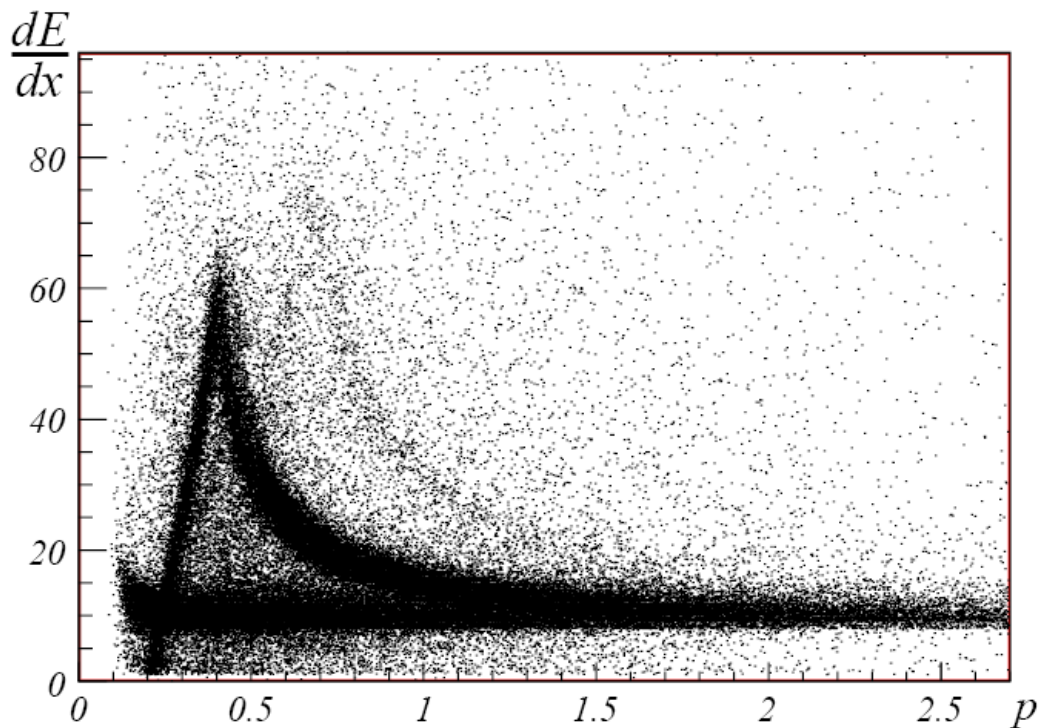


Figure 3-2. Energy deposited in the TOF scintillators by hadrons versus hadron momentum.

Once all individual scintillator paddles have been calibrated, it is important to obtain constants for offline correction of the delays of paddles to the same reference frame. The time of the hit in the counter is calculated as:

$$T_{SC} = \frac{T_{left} + T_{Right}}{2} - \frac{V_{right} - V_{left}}{2V_{right}V_{left}} y \quad (3.7)$$

where T_{Left} (T_{Right}) is the time measured by the Left (Right) PMT, y is the hit position, and V_{left} (V_{right}) is the speed of the light propagation toward the left (right) PMT. First, timing of each scintillating counter is aligned to the timing of the accelerator's RF-signal. The difference of the event start time and RF time is calculated as:

$$\Delta\tau = T_{SC} - T_{flight} - T_{RF} \quad (3.8)$$

where T_{flight} is the time of the flight of the particle, calculated from the information provided by tracking (using the path length the particle has traveled and assumption that $\beta = 1$ for electron candidates), T_{RF} is the time of the RF-signal.

The RF-signal is provided by the injector to the accelerator. The signal is generated with each electron bunch (length of the bunches are $\cong 2ps$, and distance between the bunches $\cong 2ns$) with frequency $\nu = 1.4971$ GHz in the injector. The RF-signal is sent to all three experimental halls with a prescale factor of 40. Bunches delivered to each hall are separated by time intervals of:

$$\Delta T = \frac{3}{\nu} = \frac{3}{1.4971 \text{ GHz}} = 2.0039 \text{ ns} \quad (3.9)$$

where ν is the accelerator frequency, and the factor 3 appears because the beam from the injector is shared among three experimental halls.

For each scintillator counter the time-offset is calculated as [38]:

$$R = \text{mod} \left| T_{SC} - T_{flight} - T_{RF} + 100 \cdot \Delta T, \Delta T \right| - \frac{\Delta T}{2} \quad (3.10)$$

which defines the time delay for the particular scintillation counter with respect to the RF-signal. This value must be subtracted from the measured time by the scintillation counter when calculating

the mass of the particle. The detailed procedure of RF-signal calibration one can find at [71]. Once the RF-signal has been calibrated the \mathbf{R} (given by equation 3.10) for each counter is fitted to find the mean value (the shift from zero). These constants, called “fine tuning constants,” are saved in the database, and the time measured by a particular scintillation counter will be corrected with the corresponding time delay constant in software. Since electrons are mainly produced in the forward direction, to calibrate backward counters pions are used. In case of pions the time of flight is calculated using the tracking information.

The procedure described above was applied to EG2 experimental data to perform the Time-Of-Flight calibration. In Figure 3-3 is plotted positively charged particle velocity β in units of speed of light versus the particle momentum. The colored lines correspond to kinematical curves of those quantities for e^+ , π^+ , K^+ and protons. In Figure 3-4 one can see the positively charged particle square mass distributions in different momentum ranges.

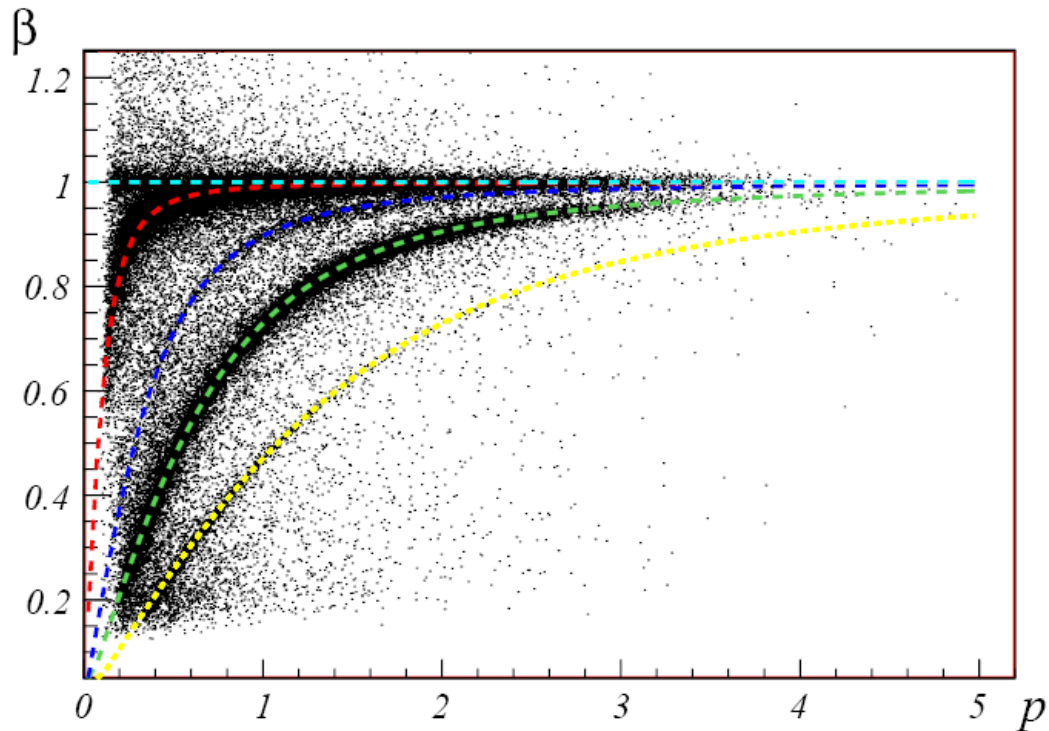


Figure 3-3. Positively charged particle velocity β in units of speed of light versus the particle momentum. The colored lines correspond to kinematical curves of those quantities for e^+ , π^+ , K^+ and protons.

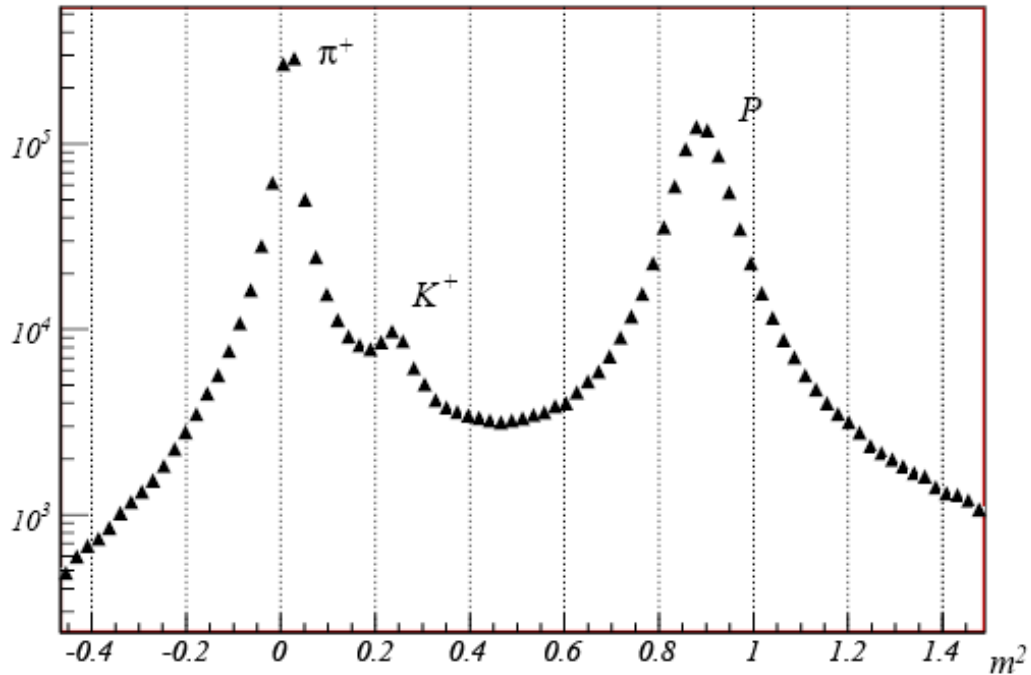


Figure 3-4. Positively charged particle square mass distributions in different momentum ranges.

As one can notice from Figure 3-3 the time-of-flight particle identification is adequate for particles with momenta up to 2 GeV, while at higher momenta the TOF technique cannot uniquely separate between pions and kaons.

3.3 Cherenkov Counters Calibration.

For calibration of the parameters for the Cherenkov counters (CC), a variety of techniques are used, employing beam interactions, cosmic rays, intrinsic photo-multiplier single photoelectron emission [74], and electronic pulsers. The part of the calibration which is done without the beam interactions help to determine the T1 (TDC channel to time constant), pedestals and Single-Photoelectron ADC position. The T1 constant is calibrated using a pulser signal sent to each TDC channel with different time delays. The response of each TDC is fitted with a linear function with

T1 as the slope parameter, and the obtained T1 parameter is saved in the calibration database for each TDC channel. For accurate ADC measurements the pedestals need to be calibrated. Usual values of pedestals vary from 300 to 800 channels, and sigma is about 2-3 channels. The pedestal calibration of the CC is a part of the pedestal calibrations for all detector groups.

For the Single Photo-Electron (SPE) calibration, the self-trigger of the Cherenkov detector is used to measure the noise function and to define the position of the SPE peak. To measure the SPE location, one needs to accumulate the ADC distribution for every PMT, which is then fitted with a Gaussian function to determine the SPE position. In the case of large amounts of noise in addition to the signal, the background is parameterized with $f(x) = a \cdot e^{-bx}$.

In order to obtain improved timing information from the Cherenkov detector one needs to obtain the time offset for each PMT. The constant, called T0, is obtained using timing information from the TOF scintillator counters. The offset can be calculated using time information from the CC and the TOF, and knowing the track length from the target to the CC plane and the SC plane. The difference between the CC and TOF reported times is fitted for each PMT and stored in the calibration database for off-line time correction.

3.4 Drift Chamber Calibration.

The track reconstruction in the Drift Chambers is done in two stages. In the first stage, individual tracks are fit to wire positions (“hit-based tracking”). In this stage, the hits inside the super-layer are combined into track segments, which are then linked together to form tracks across all three regions. At this stage, due to the comparatively small size of the drift cells and large number of wire layers, the track momentum can be reconstructed with 3-5% resolution [60]. In the second stage, the time-of-flight information, obtained from scintillator counters, is used to calculate the drift times. Then these drift times are converted to drift distances using pre-determined time-to-distance constants. The corrected hit positions are then used to determine the final track parameters. This last stage is called time-based-tracking (TBT). The drift time is given by:

$$t_{drift} = t_{start} + t_0 - t_{TDC} - t_{flight} - t_{prop} - t_{walk} \quad (3.11)$$

where t_{start} is the event start time (measured by TOF), t_{TDC} is the time measured by the Drift Chamber's TDC, t_{flight} is the particle flight time from the reaction vertex to the wire, t_{prop} is the signal propagation time in the wire, and t_{walk} is a small time-walk correction due to different ionization for slow and fast particles.

In Figure 3-5 one can see the schematic view of the Drift Chambers (for a detailed description of the DC system see Chapter 2.2.1). When a charged particle goes through the drift chambers, each of the 34 layers is hit (see chapter 2.2.1). Each hit detected in the chamber is used to determine the particle's track via a least squares fit performed in the CLAS reconstruction program. One of the measured quantities is the DOCA (Distance of Closest Approach), which is the distance from track to the sense wire determined by time-based tracking. This quantity is obtained from fits to the global track that includes all layers. The other variable is the DIST, which is the predicted distance from the sense wire to the track, which is calculated from the drift time and other parameters. The drift time is determined from the TDC values for the wire corrected with fixed cable delays and track dependent delays such as flight time. The difference between these quantities is called the "time residual", which is taken as a measure of the resolution of the Drift Chambers.

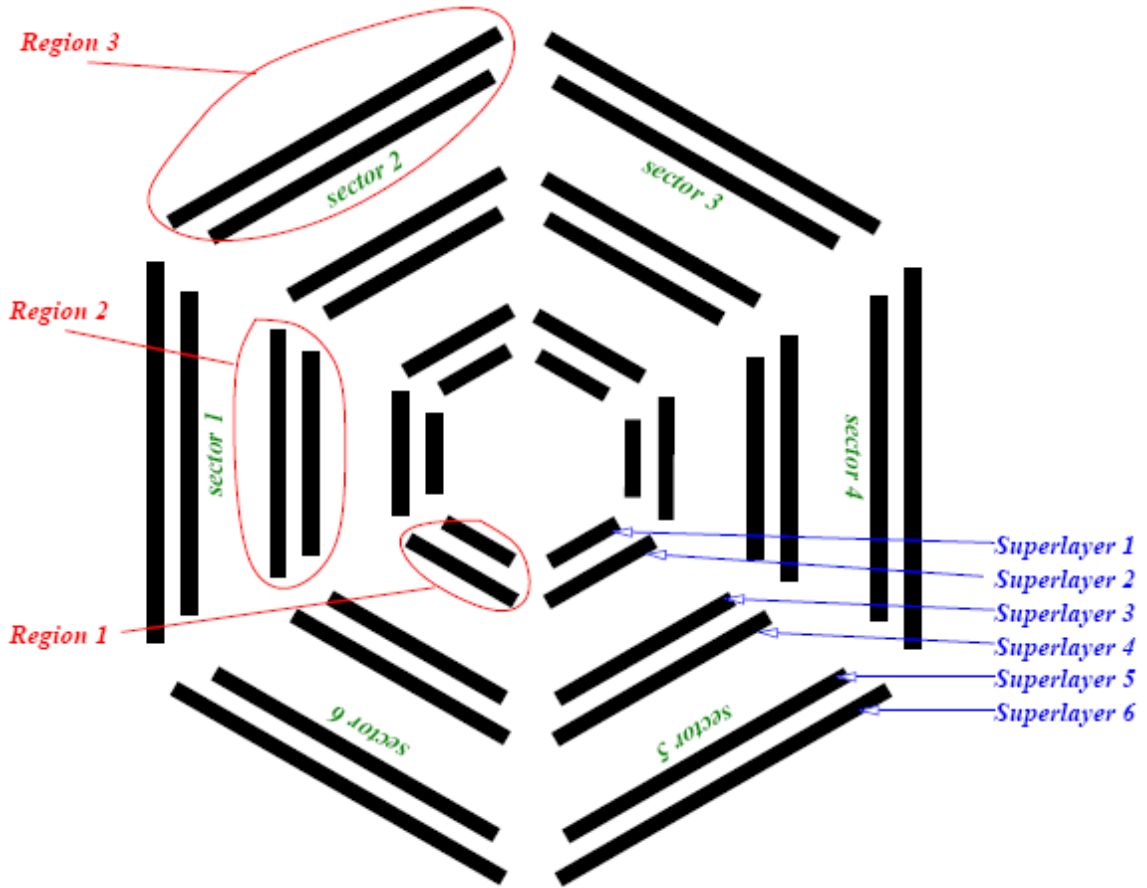


Figure 3-5. Schematic view of CLAS Drift Chambers. The view presents a slice in the XY plane through the drift chamber at the target position. One can see the six superlayers in each sector.

3.5 Electromagnetic Calorimeter Time Calibration.

The Electromagnetic Calorimeter calibration is performed using the electron time measured by the Time-of-Flight counters. Since there is no magnetic field between the scintillator counters and the electromagnetic calorimeter, the track of the particle is straight. After calibrating the Time-of-Flight system, one can predict the time measured by the EC as:

$$T_{EC} = T_{SC} + \frac{d_{track} \cdot \cos(\alpha)}{c} \quad (3.12)$$

where T_{SC} is the time measured by TOF, d_{track} is the distance between TOF and EC strips, and α is the particle impact angle on the EC plane. The time measured by EC T_{EC} is assigned to the strip

with largest ADC signal in each of three views. Then the time dependence is fitted with the function:

$$T_{EC} = P_0 + P_1 \cdot A_{TDC} + \frac{P_2}{\sqrt{A_{ADC}}} + P_3 \cdot L^2 + P_4 \cdot L^3 - \frac{L}{v_{eff}} \quad (3.13)$$

where L is the distance from the hit point to the EC readout edge, v_{eff} is the speed of light in the scintillator material, and A_{ADC} and A_{TDC} are the ADC and TDC values, respectively. The first two terms are the linear responses of the TDCs, the third term is the time-walk correction, the fourth and fifth terms are small corrections for the fact that the signals arrive to the readout edge at slightly different times for scintillator bars connected to the same PMT, and the last term compensates the time for scintillator light to travel from the hit position to the readout edge. The fit parameters are saved in the calibration database.

4. Data Analysis.

4.1 Particle Identification Scheme.

As it is mentioned in Chapter 1, the main goal of this data analysis is the identification of π^+ s produced as a result of Deep Inelastic Scattering of an electron off the nucleon (within the nucleus). For that purpose one should first identify from the whole data set the deep inelastically scattered electrons by selecting all DIS events, and at the next step in DIS events set identify π^+ s. During the cooking process the event builder SEB selects possible electron candidates based on the measured sign of the charge of the particle, deposited energy in EC and a hit in the CC. SEB marks these candidates with particle id 11 or 0 depending on whether they pass a certain set of cuts or not. In CLAS charged hadrons are identified by charge (in-bending or out-bending track in DC), momentum and the time-of-flight calculated from the SC measured time. The CLAS TOF system allows the separation of pions and protons up to 2.5 GeV, and pions and kaons up to 2 GeV. The preliminary identification of particles is done using the distribution of particle momenta versus β , $\beta = L/t_{TOF}$, where L is the path length and t_{TOF} is the time-of-flight from the interaction vertex to the SC counter. For π^+ s the program assigns the id number 211. After the cooking process one needs to do a more careful particle id for electrons and other particles used in the analysis.

4.1.1 Particle Identification Scheme for Electron.

One of the most important challenges in the EG2 experiment analysis is the DIS electron identification. For that issue there were taken up only first hits in the EVNT bank.

CLAS electron identification at the trigger level is done by requiring a minimum amount of energy in the electromagnetic calorimeter (EC) in coincidence with a signal in the Cherenkov counter (CC). During offline analysis there were applied additional requirements for good electron selection. It was required that CC hits are geometrically matched with a track reconstructed in the drift chambers (DC) ($TRK \otimes CC$ smaller than 5°). To get rid of accidental background and to help reject negative pions, a sampling fraction cut in the EC was used. The energy deposited in the

calorimeter can be analyzed in two ways that emphasize different aspects of the information obtained. One can consider the EC as one monolithic unit or as two separated units, inner and outer, and add two energies reconstructed in these two units when the hits geometrically match. The two approaches discussed below give very close numbers for most events and the differences occur due to close multiple hits in the calorimeter. Distributions of E_{total} versus electron momentum (first method) and dependence of the ratio of E_{inner} and E_{outer} to the electron momentum (second method) are shown as the a and b plots correspondingly on Figure 4-1.

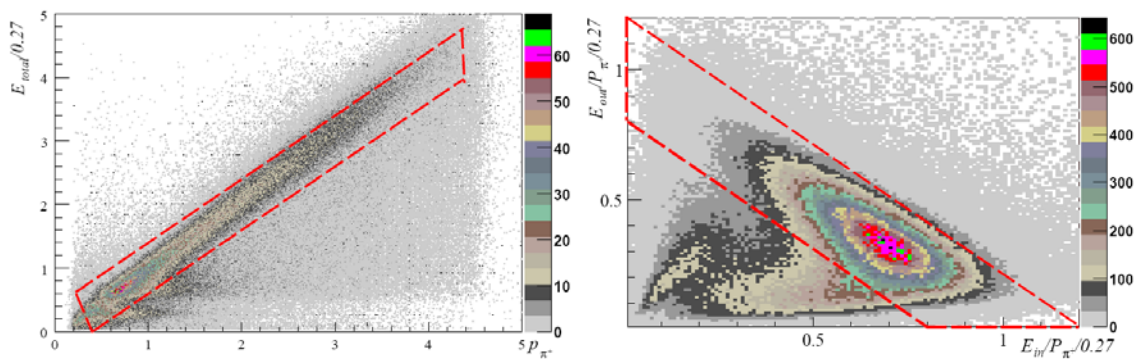


Figure 4-1. a) The dependence of E_{total} versus electron momentum. The region separated by the dashed frame indicates the applied cut. b) The dependence of fraction of E_{inner} and electron P momentum versus the same for E_{outer} . The region separated by the dashed frame indicates the applied cut.

According to the first method there was an electron separation from π^- using the dependence of the particles' total energy deposition in EC E_{total} on the particle momentum (see Figure 4-1a). Since the pions at these energies have a high probability to interact as minimum ionizing particles, the energy deposited in the calorimeter should be the same, independent of their momentum. As can be seen in the plot, the lower band corresponds to pions. Alternatively, one can consider the EC as two separate units, inner and outer, and use the energy values deposited into those units. The electromagnetic shower produced by the electron is expected, on average, to leave

more energy in the inner part of the calorimeter, while for minimum ionizing particles (such as pions with high energy) the energy deposited in the inner and outer parts should depend only on the length of the path through the scintillating material. Let us denote those energy values correspondingly as E_{inner} and E_{outer} . In Figure 4-2b the distribution of deposited energy in the inner part of the EC is plotted versus the energy deposited in the outer part, both normalized to the particle momentum. Pions can be visually distinguished in the left bottom corner of the plots. The actual applied cuts are denoted by dashed lines.

The next cut used to identify electrons is a cut on the number of photoelectrons produced by the electron candidate in the Cherenkov detector. The cut $N_{ph} > 2.5$ was used to reject pions (where N_{ph} is the number of photoelectrons in CC).

Last, a cut was applied on the two target edges (solid and liquid) along the incoming electron beam direction separately in each sector of the CLAS detector. The shaded region shown in Figure 4-2 indicates the data selected by these cuts.

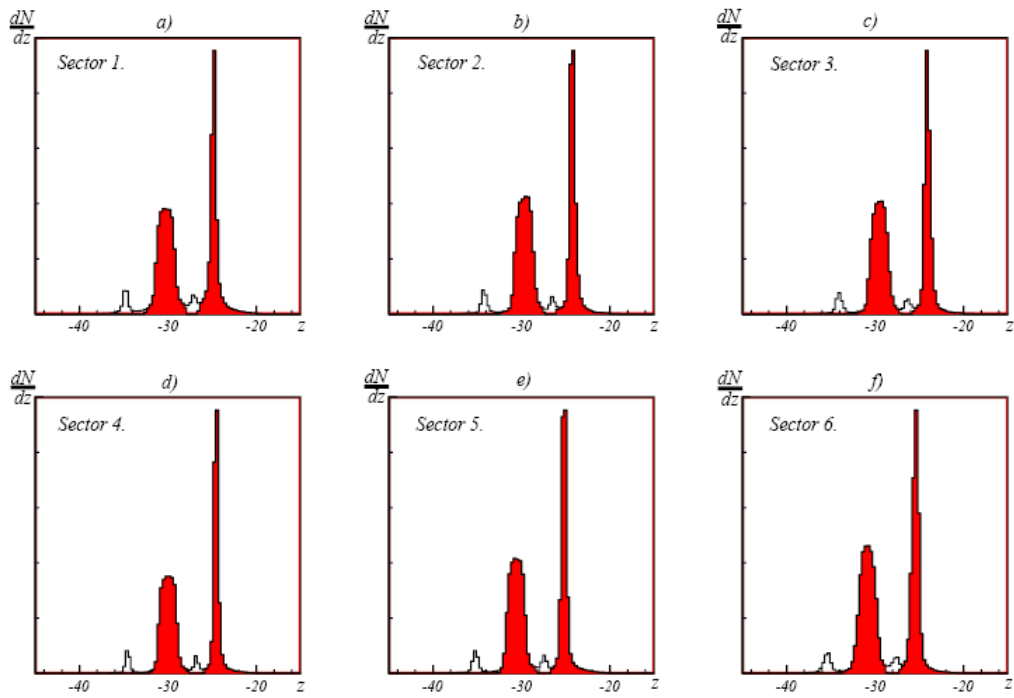


Figure 4-2. z coordinate (which is along the incoming electron beam direction) distributions for detected electrons in each sector of the CLAS detector. The shaded regions indicate the data selected by the targets edges cut.

4.1.2 Particle Identification Scheme for π^+ .

To identify π^+ 's all positive hits are separated in two groups: hits with momentum more than 2.7 GeV and hits with smaller momentum. For hits from the first group, the so-called Cherenkov counter identification technique is used, and for the second one the time-of-flight technique is used.

The main problem that arises when we try to determine the masses of different particles using the time-of-flight technique is that we can't precisely determine β due to experimental time and momentum resolution.

In terms of particle mass and momentum, $\beta = \frac{P}{E} = \frac{c}{\sqrt{1 + \frac{m^2 c^2}{P^2}}}$, so that

for particles with $P \gg mc$, $\beta \approx 1$ independent of particle mass. Therefore, all particles with $P \gg mc$ are indistinguishable using β . The Cherenkov counter serves the dual function of triggering on

electrons and separating electrons from pions. Cherenkov radiation arises when a charged particle in a material medium moves faster than the speed of light in the same medium. This speed is given by

$$\beta c = v = \frac{c}{n} \quad (4.1)$$

where n is the index of refraction and c is the speed of light in a vacuum. A particle emitting Cherenkov radiation must therefore have the velocity

$$v_{part} > \frac{c}{n} \quad (4.2)$$

In such case, an electromagnetic ‘shock wave’ is created. The coherent wave front formed is conical in shape and is emitted at an angle

$$\cos \theta = \frac{1}{\beta n} \quad (4.3)$$

with respect to the trajectory of the particle. In general, a continuous spectrum of frequencies is radiated with the photons being linearly polarized. The dependence of the emission angle of Cherenkov radiation on particle velocity has been particularly exploited by particle physicists in the form of Cherenkov counters.

Using the information provided above one can determine that the pion momentum threshold in the Cherenkov counter is 2.7 GeV, and the threshold for the heavier particles (kaons and protons) is greater than the beam momentum for the EG2 run. So requiring more than 2.5 photoelectrons emitted in Cherenkov counters for the hit we can do a good selection of with some positron contamination. To get rid of positrons, the electron identification cuts for positively charged particles were applied (see section 4.1).

In case of hits with momentum less than 2.7 GeV, the time-of-flight technique is used. For this analysis, additional selections were made using the information from tracking and the time-of-flight system to determine the timing difference between a positive hit in an event and the outgoing electron.

$$\Delta t = \frac{L_{flight}^{e^-}}{c} - t_{flight}^{e^-} + t_{flight} - T_{RF1} - \frac{L_{flight}}{\sqrt{\left(\frac{M_{\pi^+}}{p}\right)^2 + 1}} \quad (4.4)$$

where $t_{flight}^{e^-}$ and t_{flight} are correspondingly outgoing electron's and positively charged particle's time of flight from the interaction vertex to the scintillator plane; likewise $L_{flight}^{e^-}$ and L_{flight} are pathlengths along the track from the vertex to the TOF counters, M_{π^+} is the π^+ mass, p is the positively charged particle's momentum, and the T_{RF1} is an additional timing correction using the 'radio frequency' signal sent from the accelerator injector.

In figure 4-3 is presented the dependence of the positively charged particle's velocity β on their momentum where the red colored points correspond to events surviving the Δt cut.

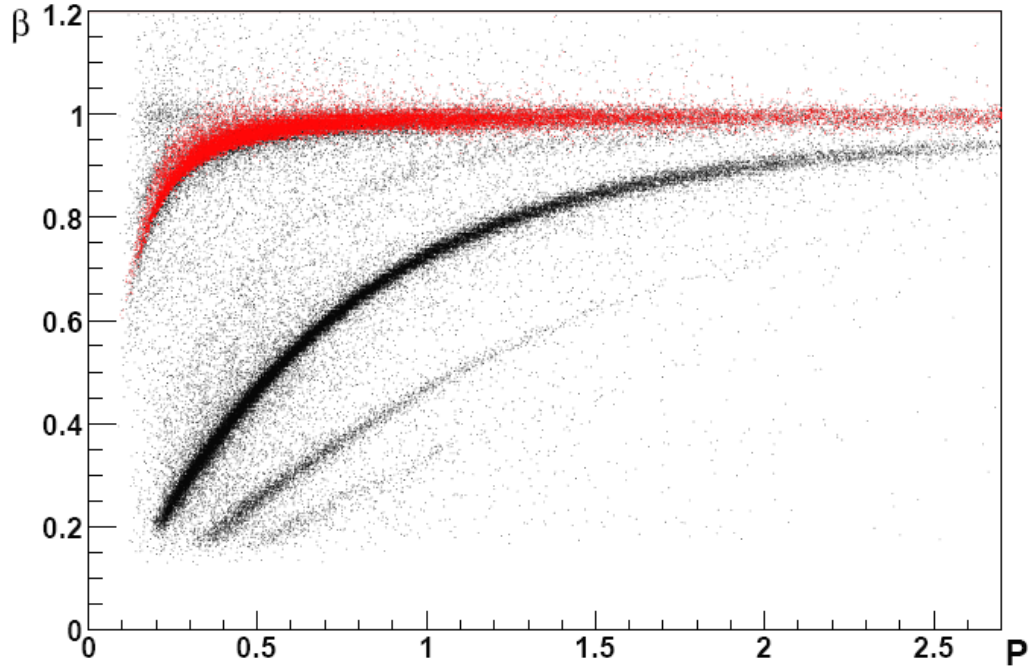


Figure 4-3. Beta (p) dependence of positively charged particles on momentum (P). Red colored dots correspond to events surviving the Δt cut ($-1.46 < \Delta t < 0.15$ ns if P is less than 1 GeV and $-1.38 < \Delta t < 0.53$ ns if $P > 1$ GeV).

On the figure 4-4 is presented the energy deposit in the time-of-flight counters for low-momentum particles. Red points are for identified pions, while black points are for identified protons. Although this information was not used in the analysis, it gives confidence that the time-of-flight technique is working well in the low-momentum region.

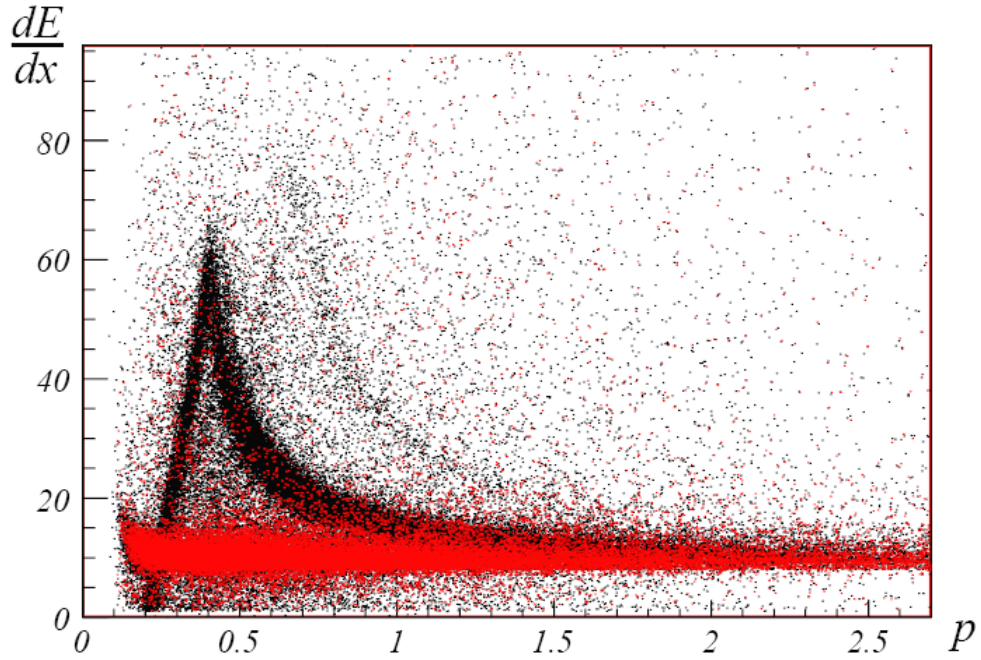


Figure 4-4. Energy deposit in the time-of-flight counters for low-momentum particles. Red points are for identified pions, while black points are for identified protons. Although this information was not used in the analysis, it gives confidence that the time-of-flight technique is working well in the low-momentum region.

4.2 DIS Kinematics.

Scattered electrons were selected by imposing the constraints $Q^2 > 1 \text{ GeV}^2$, $W = \sqrt{2M\nu + M^2 - Q^2} > 2 \text{ GeV}$ for the invariant mass of the photon-nucleon system where M is the nucleon mass, and $y = \nu/E < 0.85$ for the energy fraction of the virtual photon. The requirements on W and y are applied to exclude nucleon resonances and to limit the magnitude of

the radiative corrections, respectively. In Figure 4-5a one can see the Q^2 versus ν after DIS kinematical cuts applied and in Figure 4-5b is shown the Bjorken x_B logarithmic distribution after DIS cuts. As one can see, $0.1 < x_B < 0.55$ for these data.

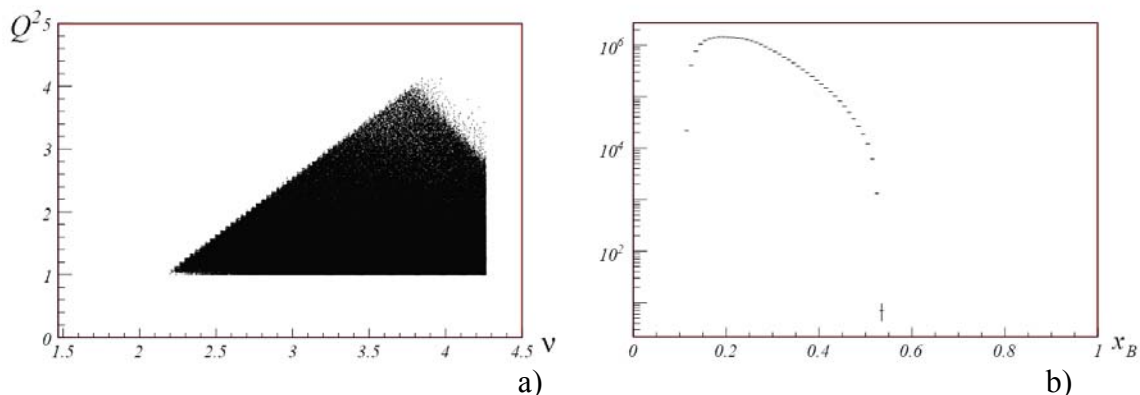


Figure 4-5. a) Q^2 versus ν after deep inelastic scattering kinematical cuts were applied. b)

Bjorken x_B logarithmic distribution after DIS kinematical cuts applied. As one can see,

$$0.1 < x_B < 0.55 .$$

4.3 Simulations and Acceptance.

To get reliable physics analysis results, it is necessary to calculate the acceptance of the experimental setup (including the CLAS detector and the EG2 target system) and apply the corresponding correction factor to the data. The acceptance correction factor is simply the ratio of reconstructed events to the number of generated events in the each kinematics bin. By ‘reconstructed events’ is meant the generated events after passing through the *Monte – Carlo* \rightarrow *GSIM* \rightarrow *GPP* \rightarrow *RECSIS* sequence.

Since the two main observables we are measuring are the multiplicity ratio $R_M^{\pi^+}$ of cross sections to produce π^+ in the $A(e, e' \pi^+)$ reaction on two different nuclei, and the transverse momentum broadening squared Δp_T^2 , one could suppose that the effect of acceptance is negligible. However, the polar and azimuthal angular coverage of the CLAS detector is actually less than 4π , therefore there are real events which are missed in the detector system. Besides, the CLAS detector

material or the different size, shape and position of solid and liquid targets (see chapter 2.3) or target system support structures also can create secondary scatterings with some contribution to the final experimental data. Therefore it is imperative to apply an acceptance correction procedure to the analyzed data set.

Since the detector has a finite resolution it is possible that an event produced in one bin is reconstructed in a different bin, and therefore one would need a matrix to fully account for such bin migration effects. If the number of events created in the i -th bin is N_i and the number of reconstructed events created in the j -th bin is P_j , then:

$$P_i = \sum_j M_{ij} N_j \quad (4.5)$$

$$N_i = \sum_j M_{ij}^{-1} R_j \quad (4.6)$$

where M_{ij} is a large $N_{bin} \times N_{bin}$ square matrix. The plain usage of this method requires a very large number of simulated events, which is not affordable due to the slow speed of the detector simulation program (GSIM) [79]. In addition, the determination of the inverse of such a large square matrix is known to be a very unstable procedure. Because of that a realistic event generator is used for deep inelastic scattering (DIS) reactions.

Pythia 6.319 was the event generator used, which is discussed in detail in section 4.3.1. To the output of the event generator sample, additional particle transverse momentum was added (relative to the direction of the virtual photon, see section 1.2), primarily to simulate the effect of Fermi momentum. The convolution was performed with a Gaussian distribution with σ equal to 1/6 of initial transverse momentum. This procedure results in better agreement between the simulated and real experimental data (see section 4.3.3). This procedure is especially important for the p_T^2 transverse momentum distribution tails. To run Pythia 6.319, the ROOT C++ version 5.08 package was used, which has text format output.

In order to feed the events into GSIM [79], the output file of the Monte-Carlo simulation was converted into BOS database format [22] containing the “PART” banks containing the

information from the event generator. The GSIM program creates an idealized software model of the CLAS spectrometer. The GSIM program is built on the base of the GEANT simulation package [65] (a package of CERN software) and allows to model the response of the spectrometer to the passage of particles through it including such processes as energy loss and radiation of secondary particles during transport through different parts of CLAS. GSIM can re-create different configurations of CLAS depending on certain experimental conditions by making changes in a configuration file. The only part of the experimental setup one must change is the target system which is discussed in detail in section 4.3.2. As mentioned above, the input data to GSIM is the set of four-momentum of particles created by the event generator.

In order to eliminate signals from known dead channels, the GSIM Post Processor (GPP) program was used to remove signals from dead wires in the drift chambers and bad tubes in the scintillator counters. In Figure 4-6 one can see the comparison of the efficiencies for experimental and simulation.

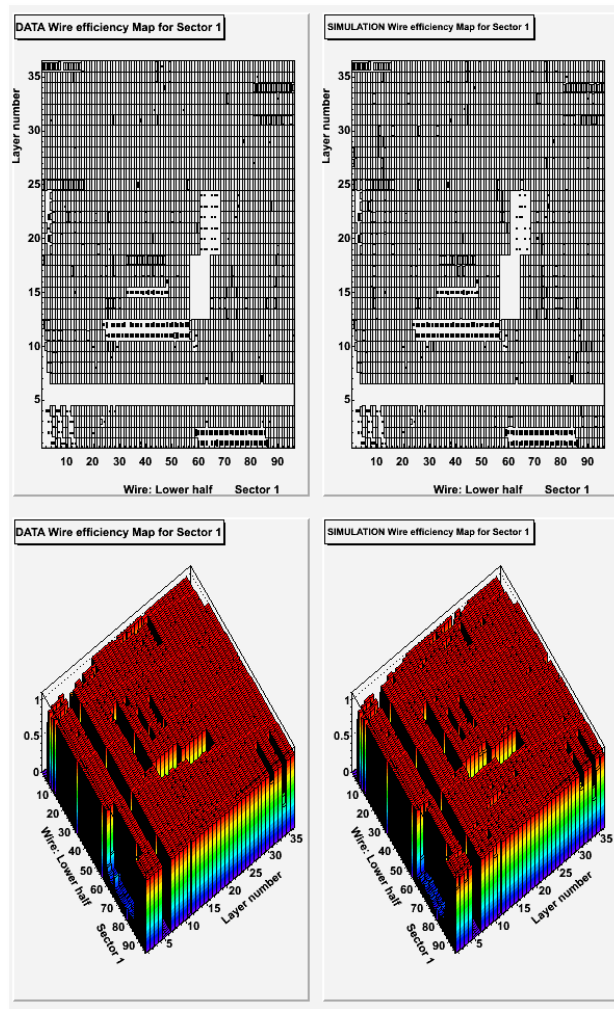


Figure 4-6. The comparison of the efficiencies for data (right) and simulation (left) showed in a behavior (top) and in a lego one (bottom) for appreciate more the fact that a fractional number was associated to represent efficiencies and correlations.

Then the GSIM files were processed with the RECSIS program (see Chapter 3 for more details) to reconstruct the simulated events. The executable of the reconstruction program was built with the same libraries which were used for processing the actual data from the EG2 running period. In the final stage the same cuts used on the experimental data were also applied to the simulated output data to determine the acceptance (see section 4.3.3 for more details).

4.3.1 PYTHIA 6.319 Adaptation to the EG2 Experiment.

Event generators are software libraries that generate simulated high-energy particle physics events. Despite the simple structure of the tree-level perturbative quantum field theory description of the collision and decay process in an event, the observed high energy process usually contains a significant number of modifications, like photon and gluon bremsstrahlung or loop diagram corrections, that usually are too complex to be simply evaluated in real calculations directly on the diagrammatic level. Furthermore, the non-perturbative nature of QCD bound states makes it necessary to include information that is outside the perturbative quantum field theory. The collective behavior of the system involves a phenomenological description that also can't be easily obtained from the fundamental field theory by a simple calculation.

Any realistic test of an underlying physical process in a particle accelerator experiment therefore requires an adequate inclusion of these complex behaviors surrounding the actual process. Based on the fact that for most of the processes, a factorization of a full process into individual problems is possible (which means a negligible effect from interference), these individual processes are calculated separately, and the probabilistic branching is performed between them using Monte Carlo methods.

Over the years, many event generators have appeared. A few famous particle generators were developed on the base of the Lund [11, 12] model from the University of Lund in Sweden. One of them is the LEPTO generator [48], which simulates only the leading order and next to the leading order processes in DIS. The version of the LEPTO generator modified to satisfy polarized leptonproduction is called PEPSI [58]. The other Monte-Carlo generator is Pythia 6.319 [69], which in contrast to LEPTO contains a model of soft (non-perturbative) as well as perturbative DIS processes and spans the whole region from real to quasireal photoproduction to high Q^2 DIS. For this reason Pythia was chosen to be the generator used to drive the final results of the data analysis. In order to achieve some reliability of the Monte Carlo information it has to be shown that the model describes the data in the relevant observables.

Actually, the recent versions of Pythia are the result of the merge of two closely connected programs JETSET [12] and Pythia. JETSET has its roots in the efforts of the Lund group to understand the hadronization process. The so-called string fragmentation model was developed as an explicit and detailed framework, within which the long-range confinement forces are allowed to distribute the energies and flavors of a parton configuration among a collection of primary hadrons, which subsequently may decay further. This model, known as the Lund string model contained a number of specific predictions, which were later confirmed by experimental data. The Lund string model is still one of the most elaborate and widely used fragmentation models. It remains the core of the Pythia program. Meanwhile the old Pythia versions evolved out of early studies of fixed-target proton-proton processes, addressed mainly at issues related to string drawing.

Here is a list of some of the main areas where the Pythia programs contain original research:

- The string fragmentation model.
- The string effect.
- Baryon production (diquark/popcorn)
- Small-mass string fragmentation.
- Fragmentation of multiparton systems.
- Color rearrangement and Bose-Einstein effects.
- Fragmentation effects on α_s determinations.
- Initial-state parton showers.
- Final-state parton showers.
- Photon radiation from quarks.
- Deeply inelastic scattering.
- Photoproduction, $\gamma\gamma$ and $\gamma^* p / \gamma^* \gamma / \gamma^* \gamma^*$ physics.
- Parton distributions of photon.

- Color flow in hard scatterings.
- Elastic and diffractive cross sections.
- Minijets (multiple parton-parton interactions).
- Rapidity gaps.
- Jet clustering in k_{\perp} .

The Lund model [11, 12] is based on the effective string picture of QCD at strong coupling. The conventional Lund model (by the ‘conventional’ Lund model one should understand the original 1+1 dimensional formulation not containing the extension to gluonic strings [13]) gives a description of the break-up of a color string into produced hadronic states. It is directly applicable in the context of processes where the initial $q\bar{q}$ pair is produced at a single point, the partons then fly away from each other, and a color string is stretched between them, which eventually breaks up, producing hadrons. Such a description actually invokes the idea of the quantum mechanical tunneling process. A fundamental property of confining strings is the so-called area law [78], from which the probability formula in the Lund model may be derived.

The model is basically 1+1 dimensional; the transverse momentum of generated mesons is taken into account by substituting the masses m^2 by $m_{\perp}^2 = m^2 + p_{\perp}^2$, so that the tunneling probability is given by:

$$\exp\left(-\frac{\pi m_{\perp}^2}{\kappa}\right) = \exp\left(-\frac{\pi m^2}{\kappa}\right) \cdot \exp\left(-\frac{\pi p_{\perp}^2}{\kappa}\right) \quad (4.7)$$

In particular the transverse momentum is considered to be in principle randomly distributed, decorrelated along the chain of mesonic emissions and also uncorrelated with rapidity. The factorization of the transverse momentum and the mass terms leads to a flavor independent Gaussian spectrum for the p_x and p_y components of $q\bar{q}$ pairs. The assumption of a Gaussian shape may be a good first approximation, but there remains the possibility of non-Gaussian tails that can be important in some situations.

In a perturbative QCD framework, a hard scattering is associated with gluon radiation, and further contributions to what is naively called fragmentation p_{\perp} comes from unresolved radiation. This is used as an explanation of why the experimental $\langle p_{\perp} \rangle$ is somewhat higher than obtained by formula (4.7). That problem in EG2 experimental data was solved by using the empirical procedure of smearing the initial transverse momentum distribution with Gaussian distribution with σ equal to 1/6 of its value as mentioned above.

During determination of the energy and the longitudinal momentum of the hadron, one should take into account the fact that only one variable can be selected independently, since the momentum of the hadron is constrained by the already determined hadron transverse mass m_{\perp} ,

$$(E + p_z)(E - p_z) = E^2 - p_z^2 = m_{\perp}^2 = m^2 + p_x^2 + p_y^2 \quad (4.8).$$

In an iteration from the quark end, one is led (by the desire for longitudinal boost invariance) to select the z variable as the fraction of $E + p_z$ taken by the hadron, out of available $E + p_z$. As hadrons are split off, the $E + p_z$ (and $E - p_z$) left for subsequent steps is reduced accordingly:

$$\begin{aligned} (E + p_z)_{new} &= (1 - z) \cdot (E + p_z)_{old} \\ (E - p_z)_{new} &= (E - p_z)_{old} - \frac{m_{\perp}^2}{z(E + p_z)_{old}} \end{aligned} \quad (4.9)$$

The fragmentation function $f(z)$, which expresses the probability that given z is picked, could in principle be arbitrary. While, if one requires that the fragmentation process as a whole should look the same, irrespectively of whether the iterative procedure is performed from the q end of the \bar{q} one ('left-right symmetry'), the choice is essentially unique [12], which is the 'Lund symmetric fragmentation function',

$$f(z) \propto \frac{1}{z} z^{\alpha_a} \left(\frac{1-z}{z} \right)^{\alpha_b} \exp\left(-\frac{bm_{\perp}^2}{z} \right) \quad (4.10).$$

There is one separate parameter a for each flavor, with the index α corresponding to the ‘old’ flavor in the iteration process, and β to the ‘new’ flavor. It is customary to put all $a_{\alpha,\beta}$ the same, and thus arrive at the simplified expression.

$$f(z) \propto z^{-1}(1-z)^a \exp\left(-\frac{bm_{\perp}^2}{z}\right) \quad (4.11)$$

In the program only two separate a values can be given, that for quark pair production and that for diquark one. In addition, there is the b parameter, which is universal.

The important part of the Pythia model for this analysis is the description of the ep(n) cross section through the properties of the emitted virtual photon and the nucleon. This model can be used by choosing the option γ^*/e with fixed target to define the beam particles. To run Pythia for particular tasks one should set up the corresponding parameters in the Pythia parameter input file.

The Pythia default parameter set is intended for energies much greater than available for CLAS. To tune up Pythia to the EG2 experiment it was resorted to the experience previously made in HERMES [57], in which the Pythia is fitted to the HERMES kinematics. Changing a few more parameters, Pythia was tuned up to the generator which is covering the semi-inclusive region of CLAS.

To access to the subroutines of the Pythia 6.319 (Pythia 6.319’s programming code is in FORTRAN77), a C++ wrapper provided in ROOT version 5.08 was used using the TPythia6 class.

In the following is the list of parameters (with their value and short explanation) which are different from the default value in Pythia 6.319:

MSTP(1)=2: defines the maximum number of generations equal to two;

MSTP(2)=1: strong coupling constant $\alpha_s = 0.20$ is fixed (including also for parton showers);

MSTP(13)=2: to set the range of Q^2 over which electrons are assumed to radiate photons by the user-determined Q_{\max}^2 , given in PARP(13) (see below in the list);

MSTP(20)=0: do not suppress resolved (VMD or GVMD) cross sections, introduced to compensate for an overlap with DIS processes in the region of intermediate Q^2 and rather small W^2 ;

MSTP(38)=4: to use the massless approximation throughout for $gg \rightarrow \gamma\gamma$ and $gg \rightarrow g\gamma$, assuming the presence of four effectively massless quark species (at the most, eight) to satisfy the CLAS kinematics;

MSTP(41)=1: to put master switch for all resonance decays on;

MSTP(58)=4: to put maximum number of quark flavors used in parton distributions equal to four, and thus also for initial-state space-like showers;

MSTP(61)=0: to put master switch for initial-state QCD and QED radiation off;

MSTP(81)=0: to put master switch for multiple interactions off;

MSTP(82)=1: to assume the same probability for multiple interaction in all events, with an abrupt $p_{\perp\min}$ cut-off at 1.9 GeV;

MSTP(92)=4: to set energy partitioning hadron or resolved photon remnant proportional to $(1-\chi)^k / \sqrt{\chi^2 + c_{\min}^2}$, where χ is the energy fraction taken by one of the two objects, $k=1$ when a meson or resolved photon remnant is split into two fragments and $k=3$ when nucleon remnant is split into a diquark and a quark fragment, with χ giving the energy fraction taken by the quark jet and $c_{\min} = 0.6 \text{ GeV} / E_{cm} \approx 2 < m_q > / E_{cm}$ for both cases;

MSTP(101)=1: to set the structure of diffractive system as forward moving diquark plus interacting quark.

PARP(2)=3: to set the lowest center of mass energy for the event as a whole equal to 3 GeV;

PARP(18)=0.17: to scale k_ρ by 0.17 to set the cross section of a GVMD state of scale k_\perp is suppressed by a factor k_ρ^2 / k_\perp^2 relative to those of a VMD state;

PARP(62)=0.5: to set effective cut-off Q or k_{\perp} value equal to 0.5 GeV/c, below which space-like parton showers are not evolved. Primarily intended for QCD showers in incoming hadrons, but also applied to $q \rightarrow q\gamma$ branching;

PARP(65)=0.5: to set effective minimum energy (in c.m. frame) of time-like or on-shell parton emitted in space-like shower equal to 0.5 GeV;

PARP(91)=0.44: to set the width of Gaussian primordial k_{\perp} distribution inside hadron equal to 0.44 GeV/c, i.e. $\exp(-k_{\perp}^2 / \sigma^2)k_{\perp} dk_{\perp}$ with $\sigma = 0.44$ and $\langle k_{\perp}^2 \rangle = 0.44^2$;

PARP(93)=2: to set the upper cut-off for primordial k_{\perp} distribution inside hadron equal to 2 GeV/c;

PARP(99)=0.44: to set the width parameter of primordial k_{\perp} distribution inside photon equal to 0.44 GeV/c;

PARP(100)=2: to set the upper cut-off for primordial k_{\perp} distribution inside photon equal to 2 GeV/c;

PARP(102)=0.5: the mass spectrum of diffractive states (in single and double diffractive scattering) is assumed to start 0.5 GeV above the mass of the particle that is diffractively excited. In this connection, an incoming γ is taken to have the selected VMD meson mass, i.e. m_{ρ} , m_{ω} or m_{ϕ} ;

PARP(103)=0.5: to assume that if the mass of a diffractive state is less than 0.5 GeV above the mass of the particle that is diffractively excited, the state is forced to decay isotropically into the two-body channel. In this connection, an incoming γ is taken to have the selected VMD meson mass, i.e. m_{ρ} , m_{ω} or m_{ϕ} . If the mass is higher than the threshold, the standard string machinery is used;

PARP(104)=0.3: to set the minimum energy above threshold for which hadron-hadron total, elastic and diffractive cross sections are defined, equal to 0.3 GeV;

PART(111)=0: do not put lower limit to the invariant mass of the remnant hadronic system (i.e. when interacting partons have been taken away), together with original parton masses and extra parton masses.

PARP(161)=2.69: to set the coupling $f_V^2 / 4\pi$ of the photon to the ρ^0 equal to 2.69;

PARP(162)=24.6: to set the coupling $f_V^2 / 4\pi$ of the photon to the ω equal to 2.69;

PARP(163)=18.8: to set the coupling $f_V^2 / 4\pi$ of the photon to the ϕ equal to 2.69;

PARP(165)=0.33: to apply multiplicative factor equal to 0.33 to the cross section for the transverse resolved photons to take into account the effects of longitudinal resolved photons;

PARJ(1)=0.025: to set the suppression of diquark-antidiquark pair production in the color field $P(qq)/P(q)=0.025$, compared with quark-antiquark production;

PARJ(2)=0.120: to set the suppression of s quark pair production in the field compared with **u** or **d** pair production;

PARJ(3)=0.25: to set the extra suppression of strange diquark production compared with the normal suppression of strange quark $(P(us)/P(ud))(P(s)/P(d))=0.25$;

PARJ(11)=0.25: to set the probability that a light meson (containing **u** and **d** quarks only) has spin 1 equal to 0.25 (with correspondingly probability 0.75 for spin 0);

PARJ(12)=0.3: to set the probability that a strange meson has spin 1, equal to 0.3;

PARJ(21)=0.63: to set the width $\sigma = 0.63$ in the Gaussian p_x and p_y transverse momentum distributions of for primary hadrons;

PARJ(23)=0.3, PARJ(24)=5: to set a fraction 0.3 of the Gaussian transverse momentum distribution is taken to be a factor 5 larger than input in PARJ(21). This gives a simple parameterization of non-Gaussian tails to the Gaussian shape assumed above.

PARJ(33)=0.6: to define the remaining energy below which the fragmentation of a parton system is stopped and two final hadrons formed, equal to 0.6 GeV;

PARJ(41)=1.13, PARJ(42)=0.37: to set the $a=1.13$ and $b=0.37 \text{ GeV}^{-2}$ parameters of the symmetric Lund fragmentation function;

PARJ(45)=0.8: to set the effective \mathbf{a} parameter in the Lund flavor dependent symmetric fragmentation function to be by 0.8 larger than the normal \mathbf{a} when diquarks is produced. More specifically, referring to equation 4.10 $a_\alpha = PARJ(41)$ when considering the fragmentation of a quark and equal to PARJ(41)+PARJ(45) for the fragmentation of a diquark, with corresponding expression for a_β depending on whether the newly created object is a quark or diquark;

MSTJ(12)=1: to assume that in baryon production model diquark-antidiquark pair production allowed; diquark treated as a unit;

MSTJ(45)=4: to set the maximum flavor that can be produced in shower by $g \rightarrow q\bar{q}$ equal to 4;

MSTU(112)=4: to set the nominal number of flavors assumed in the α_s expression equal to 4, with respect to which Λ is defined;

MSTU(113)=4: to set the minimum number of flavors that may be assumed in the α_s expression equal to 4;

MSTU(114)=4: to set the maximum number of flavors that may be assumed in the α_s expression equal to 4;

CKIN(1)=1, CKIN(2)=-1: to set the range of allowed $\hat{m} = \sqrt{\hat{s}}$ greater than 2 GeV;

CKIN(3)=0, CKIN(4)=2: to set the range of allowed $0 < \hat{p}_\perp < 2GeV$ for hard $2 \rightarrow 2$ processes, with transverse momentum \hat{p}_\perp defined in the rest frame of the hard interaction. These limits can also be used in $2 \rightarrow 1 \rightarrow 2$ processes. Here, however, the product masses are not known and hence are assumed to be vanishing in the event selection. The actual p_\perp range for massive products thus shifted downwards with respect to the nominal one;

CKIN(65)=1, CKIN(66)=4: to set the range of for the spacelike virtuality of the photon $1 < Q^2 < 4GeV^2$;

CKIN(77)=2, CKIN(78)=-1: to set the range for invariant mass $W > 2 GeV$.

4.3.2 EG2 Target in the GSIM.

While the standard CLAS simulation program GSIM [79] already provided a detailed GEANT3 [65] description of the base CLAS equipment, the double target system needed to be added. This was crucial for a high-precision comparison of the cryotarget properties to the solid target properties for at least two reasons. First, since the targets were displaced from each other along the beam axis by approximately 4 cm, the acceptances for the two targets were slightly different. This was particularly important to measurements of processes where the scattered particles predominantly emerge near the edge of the geometric acceptance of CLAS, such as in low- t hadron production. Second, for some small percentage of events, it is possible for hadrons produced in the event to pass through parts of the target support structure, emerging within the CLAS acceptance with somewhat degraded energy and angle properties. This is more probable for particles coming from the deuterium target, since it is upstream of the solid target with its support structure. Such particles will not be efficiently removed by software cuts on the data for many kinds of studies on nuclear targets, such as semi-inclusive hadron production. Thus it was necessary to perform simulations with realistic and detailed geometries of the target structures [46].

The geometries included in the simulation for the cryotarget cell included the cone, standoff, and entrance and exit foils. The solid target support structure geometries included a complete replication of the target material, carbon fiber target frame, and the aluminum frame holder together with the steel threaded rod and pivoting arm. These items were most critical since they were close to the beam line axis. In addition, the geometrical layout for a particular target was replicated, i.e., the target geometry for the inserted solid target depended on which target was inserted, to replicate any sector-dependent behavior. The non-pivoting portion of the aluminum fingers was approximated by a rectangular cross section structure at the same location, and the most upstream portions of the cryotarget and solid target assemblies were represented by simplified structures. The foam scattering chamber, including the carbon fiber exit cone, was implemented with the exact geometries and densities as the actual chamber. In total, 47 unique

volumes, most of which were replicated with a six-fold symmetry, were required for the full description.

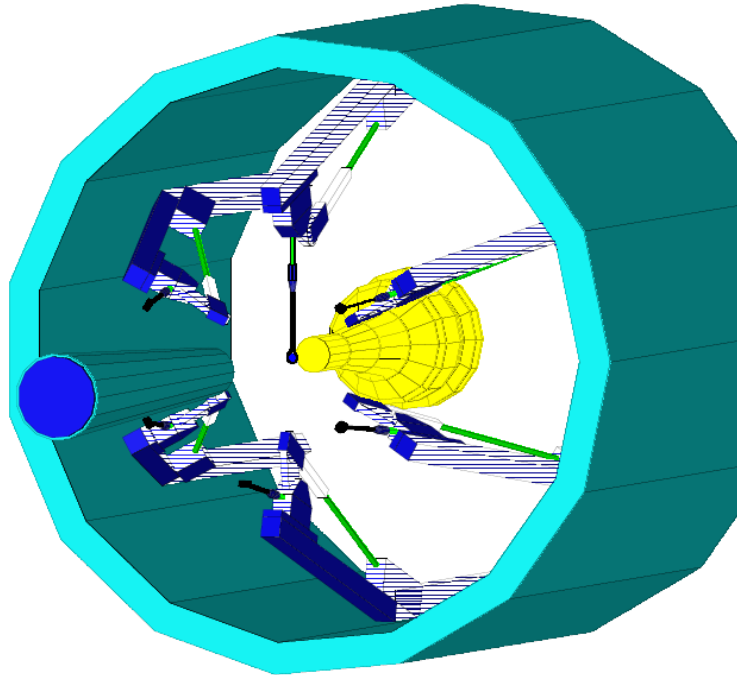


Figure 4-7. The EG2 target inside the CLAS/GSIM with the top (spherical shell) not shown.

The target exists in the production version of GSIM in the CLAS software repository. In Figure 4-7 one can see the target inside the GSIM (for a more detailed description of the target with photographs and many other pictures from GSIM see section 2.3). To run the simulation program with specific conditions for target and CLAS there are special include files called “ffread files”, where one can define special KEYS implemented in GSIM and created especially for the EG2 target. Here is an example of a typical fread file for the EG2 target used during the analysis:

```
CUTS 1.e-4 1.e-4 1.e-4 1.e-4 1.e-4  
CCCUTS 1.e-3 1.e-3 1.e-3 1.e-3 1.e-3  
DCCUTS 1.e-4 1.e-4 1.e-4 1.e-4 1.e-4  
ECCUTS 1.e-4 1.e-4 1.e-4 1.e-4 1.e-4  
SCCUTS 1.e-4 1.e-4 1.e-4 1.e-4 1.e-4
```

```
MLIST
MAGTYPE 3
MAGSCALE .5829 0.75
CHAMBER 6
TARGET 'eg2'
TGTP 207
KINE 1
VEG2 1
RUNG 10
RNDM 995558755 303061258
NOSEC 'TORU' 'MINI'
NOGEOM 'PTG ' 'ST'
TRIG 100000
STOP
```

A discussion of the target-related entries in the ffreed file is provided below.

To switch on the EG2 target inside CLAS/GSIM one should specify the target type key - TARGET as 'eg2'. In order to put the corresponding foam chamber one should define the CHAMBER key as number 6.

As mentioned in the previous section, in the target system there were six solid targets which were suspended on aluminum fingers and these were positioned in the beam in different production runs. The TGTP key specifies which target is in the beam. For the lead target one should put 207, for iron 56, for carbon 12, for tin 119, for thin aluminum 27 and finally for thick aluminum 28. Putting the specific number means that the corresponding target will be in the beam while all other targets will be located in their “out” position. For ease of use, these numbers are equal to the corresponding target's atomic number's closest integer, except for thick aluminum where that number is increased by unity to distinguish it from the thin aluminum case.

To define the vertex origin for the thrown particle there is introduced the vertex key VEG2 which specifies whether particles should start from the liquid target or from the solid target. When the VEG2 key is equal to 1, particles are thrown from the liquid target randomly distributed along the z axis inside the target and when VEG2 is equal to 2, particles are thrown from the solid target (randomly distributed along the z axis inside the target). Finally, when it is 3 the vertex origin is just $x=y=z=0$.

The target with the keys described above is working for two of the available GSIM generator settings, KINE=0 and KINE=1. For KINE=0 the kinematics are determined using the CLAS/GSIM internal Monte-Carlo generator. For KINE=1, the events are specified in an external input file.

Finally the TEG2POS key was introduced, using which one can place the target wherever one wants inside CLAS. Since during the entire experiment the whole EG2 target system remained stationary in its location, then it is sufficient to specify only one (x,y,z) coordinate to place all remaining components in the right position. Following that feature the TEG2POS key defines the central coordinates of the solid target. Here is an example of this key application:

```
TEG2POS 0. 0. -23.
```

where numbers are correspondingly the x, y and z coordinates of the center of the solid target. It is important to notice that if one needs to simulate data with target placed in the position it was during the EG2 experiment, then she/he should not use this key at all.

4.3.3 Acceptance Calculation and Simulation Results.

Because the Δp_T^2 measurement relies on a difference between the mean p_T^2 distributions of two targets that are in close proximity, it has always been anticipated that the acceptance differences would be small. This expectation has been validated by the simulation results that follow. A second expectation was that the mean value of the p_T^2 distribution would be very insensitive to acceptance corrections. This is expected because there is little correlation between

p_T^2 and the lab-frame angles of the virtual photon, θ_γ^* and ϕ_γ^* for semi-inclusive DIS pions being. Thus, edge effects that limit θ_γ^* and ϕ_γ^* coverage have little impact on the p_T^2 distribution. To the extent that the acceptance is flat in p_T^2 , the mean value of p_T^2 is unaffected and thus the difference Δp_T^2 is also unaffected.

For single pion electro-production at fixed beam energy one needs to specify six independent kinematical variables to uniquely determine all other kinematical quantities (three for the deep inelastically scattered electron and three for the identified positive pion from that reaction). But one of these quantities can be chosen to be the electron polar angle ϕ_e in the laboratory frame. In the absence of any transverse polarization of the target or the beam, the cross section of the pion electro-production is uniform in ϕ_e , therefore averaging over 2π does not introduce any uncertainty, and only increases the statistical accuracy in the bins. The list with binning of the remaining five variables is presented in the table below:

<i>Variable</i>	<i># of bins</i>	<i>Lower limit</i>	<i>Upper limit</i>	<i>Width</i>
Q^2	6	1 GeV ²	4.2 GeV ²	Variable(GeV ²)
ν	6	2.2 GeV	4.3 GeV	Variable (GeV)
z_{π^+}	10	0	1	0.1
p_T^2	120	0 GeV ²	3 GeV ²	Variable(GeV ²)
$\phi_{q\wedge\pi^+}$	12	-180°	180°	30°

The first column corresponds to the list of independent variables. In addition to Q^2 and ν , which are defined above, the variables used here are; $z_{\pi^+} = E_{\pi^+}/\nu$ is the fraction of the struck quark's initial energy that is carried by the produced positive pion (by definition $0 < z_{\pi^+} < 1$, neglecting Fermi momentum); p_T^2 is the produced positive pion's momentum transverse component to the direction of the virtual photon radiated by scattered electron; $\phi_{q\wedge\pi^+}$ is the produced positive pion's azimuthal angle around the direction of virtual photon. The second column presents the number of bins for each variable used during the acceptance calculation. The

third and fourth columns correspond to the lower and upper limits of the variables' distributions; the last column presents the bin size if the distribution of the corresponding variable was divided to equal sized bins, otherwise it is marked as 'variable' if the size of bins was changing depending on the shape of the corresponding quantity's distribution. The size of bins was determined by the resolution of detectors, the sensitivity of the physics analysis procedure to the shapes of the distributions, and available statistics.

The acceptance correction was applied on a bin-by-bin basis. The content of each bin was weighted by a factor determined from an acceptance curve distribution, which is defined as the ratio of the number of events reconstructed in a given six dimensional bin divided by the number of generated events.

$$A = \frac{N_{rec}}{N_{sim}} \quad (4.12)$$

The event reconstruction used the same procedure as during the data analysis of the raw data described above.

In order to calculate the acceptance, 400 million events were generated in deep inelastic kinematics, 100 million events each for carbon, iron, lead and deuterium targets. As mentioned above, a five variable acceptance correction was employed, therefore, to the extent that the bin widths were correctly chosen, the whole procedure was model independent. In Figures 4-8 a), b), c), d) and e) one can find the ratios of experimental data distributions to the reconstructed distributions for that variable set (each one is presented in integrated kinematical region for other variables).

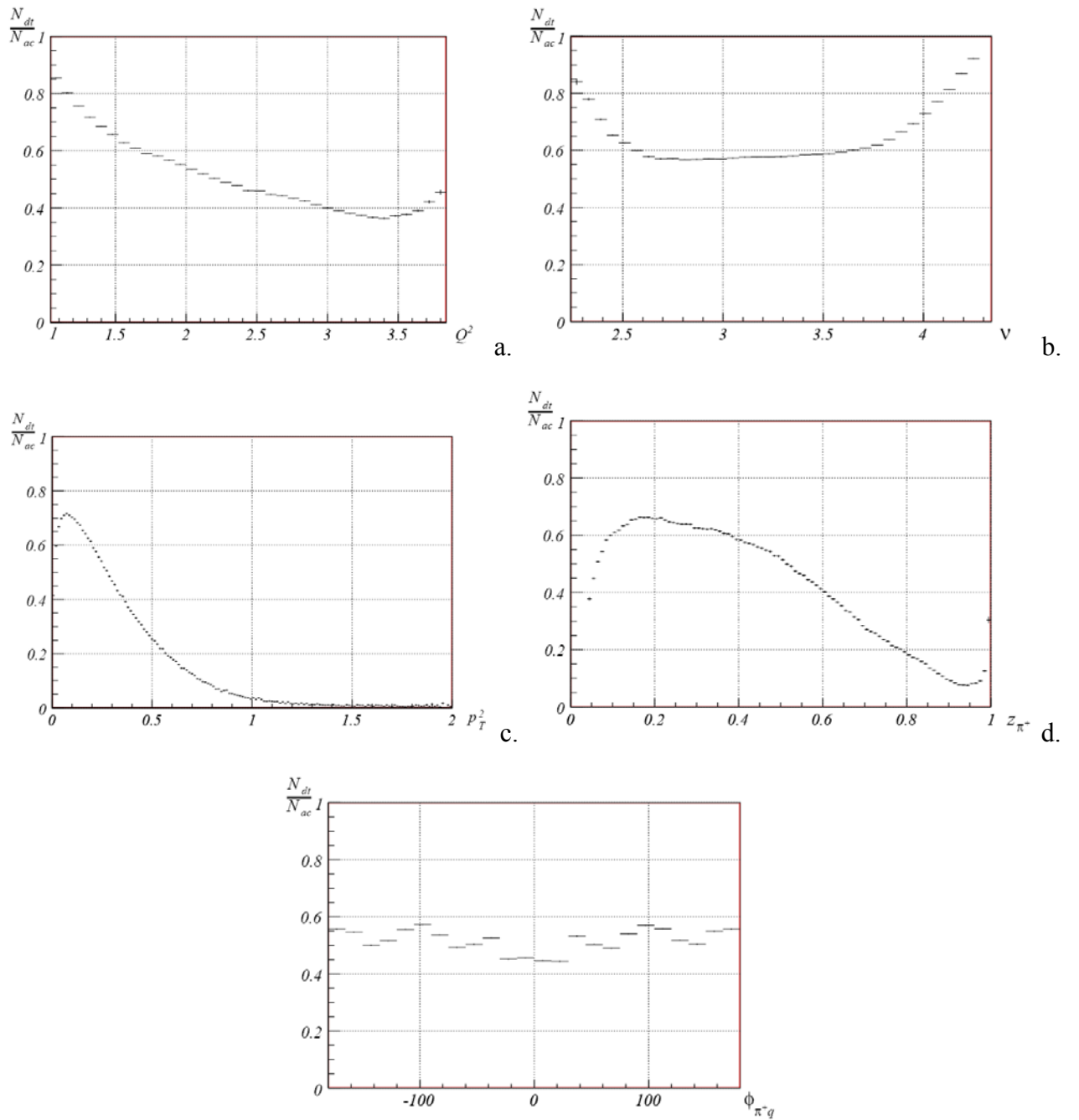


Figure 4-8. a) The ratio of the Q^2 distribution of the experimental data and the simulated event output after GSIM. b) The ratio of the ν distribution of the experimental data and the simulated event output after GSIM. c) The ratio of p_T^2 distribution of the experimental data and the simulated event output after GSIM. d) The ratio of z_{π^+} distribution of the experimental data and the simulated event output after GSIM for positive pions. e) The ratio of ϕ_{π^+q} distribution of the experimental data and the simulated event output after GSIM for positive pions.

As mentioned before (see section 2.3) the distance between the solid target and the deuterium target was equal to 4 cm. A plot in Figure 4-9 shows the ratio of acceptances calculated for the two targets as a function of transverse momentum. As can be seen, the target dependence is small but not negligible.

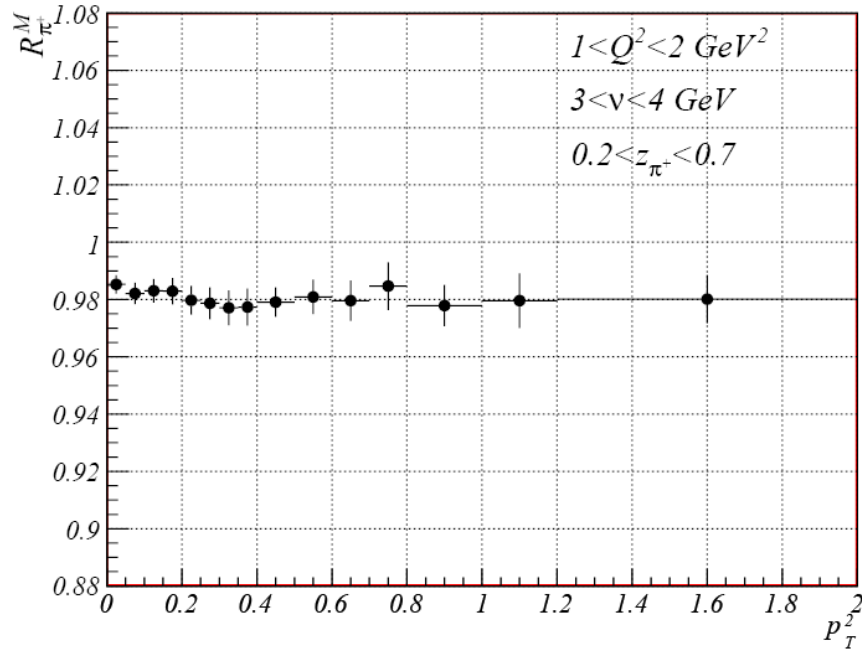


Figure 4-9. The ratio of acceptances for positive pions from the solid target to the liquid target as a function of transverse momentum squared as calculated from the simulation using a realistic event generator. As can be seen from the plot, the acceptances from the two targets are different by only a small amount, approximately 2%, and in this variable the ratio is nearly structureless.

A strong confirmation of the validity of the applied acceptance correction might be found in the shape of the reconstructed $\phi_{q^+\pi^+}$ (the distribution of the azimuthal angle of produced positive pions around the direction of the virtual photon). The cross section of single π^+ electro-production with unpolarized beam and target can be written as [40]:

$$\frac{\partial^5 \sigma}{\partial E_f \partial \Omega_f \partial \Omega_{\pi^+}} = \Gamma \cdot \frac{d\sigma}{d\Omega_{\pi^+}},$$

$$\frac{d\sigma}{d\Omega_{\pi^+}} = \sigma_T + \varepsilon \sigma_L + \sigma_{TT} \cos 2\phi + \sqrt{2\varepsilon(1+\varepsilon)} \sigma_{TL} \cos \phi \quad (4.13)$$

where ε is the virtual photon polarization parameter, Γ is the virtual photon flux, and $\frac{d\sigma}{d\Omega_{\pi^+}}$ is the photoabsorption cross section. Therefore, the reconstructed distribution for $\phi_{q^+\pi^+}$ of positive pions produced from the deuterium target should have the following form:

$$F(\phi_{q^+\pi^+}) = C_1 + C_2 \cos \phi_{q^+\pi^+} + C_3 \cos 2\phi_{q^+\pi^+} \quad (4.14)$$

where C_1 , C_2 and C_3 are some constants. The fits of $\phi_{q^+\pi^+}$ distributions were performed for different $(Q^2, \nu, \theta_{\pi^+})$ bins, where θ_{π^+} is the polar angle of positive pions in the laboratory frame. In Figure 4-10 one can see the results of fitting in particular (Q^2, ν) bins with increasing θ_{π^+} range. The χ^2 per degree of freedom generally is close to unity. Results for different bins can be found in Appendix I.

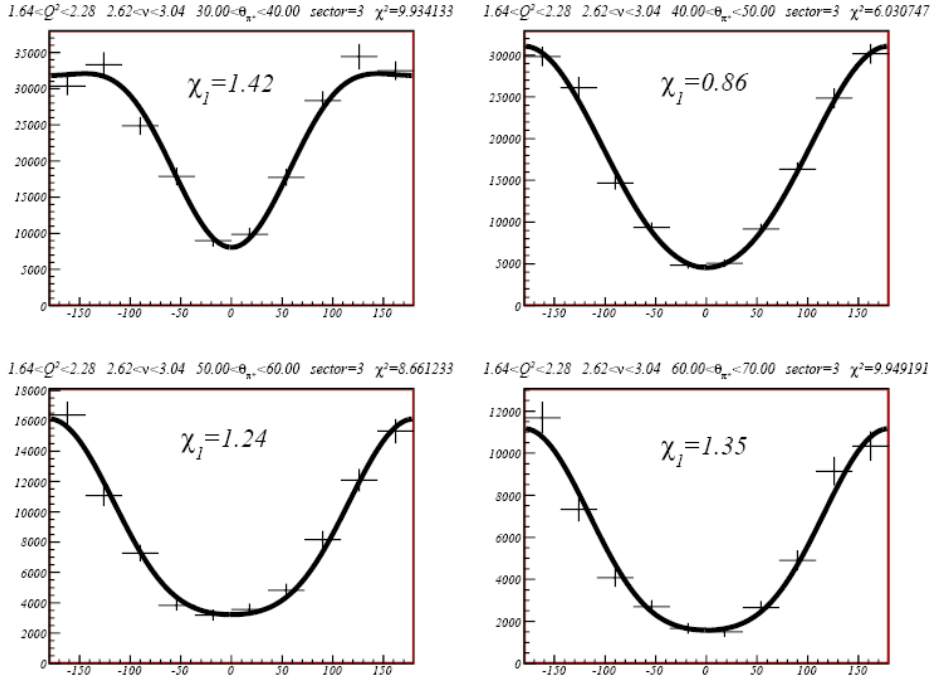


Figure 4-10. The $\phi_{q^{\pi^+}}$ distribution fit with the function $F(\phi_{q^{\pi^+}}) = C_1 + C_2 \cos \phi_{q^{\pi^+}} + C_3 \cos 2\phi_{q^{\pi^+}}$ in $1.64 < Q^2 < 2.28$, $2.62 < \nu < 3.04$ and increasing θ_{π^+} bins. The χ^2 per degree of freedom is close to unity.

As mentioned in the Introduction and Chapter 1, one of the main observables measured in the data analysis is the transverse momentum broadening:

$$\Delta p_T^2 = p_T^2(A) - p_T^2(D_2) \quad (4.15)$$

which is the difference of the average $p_T^2(A)$ and $p_T^2(D_2)$ for positively charged pions respectively produced from a nucleus with atomic number A , and deuterium. The other observable is the hadronic multiplicity ratio:

$$R_M^{\pi^+}(z_{\pi^+}, \nu, p_T^2, Q^2, \phi_{q^{\pi^+}}) = \frac{\left\{ \frac{N_{\pi^+}^{DIS}(z_{\pi^+}, \nu, p_T^2, Q^2, \phi_{q^{\pi^+}})}{N_e^{DIS}(\nu, Q^2)} \right\}_A}{\left\{ \frac{N_{\pi^+}^{DIS}(z_{\pi^+}, \nu, p_T^2, Q^2, \phi_{q^{\pi^+}})}{N_e^{DIS}(\nu, Q^2)} \right\}_{D_2}} \quad (4.16)$$

which is the ratio of ratios of number of positive pions to number of DIS electrons produced on a nucleus with atomic number A , and the same on deuterium.

In Figure 4-11 one can see an example of the transverse broadening dependence on $A^{1/3}$ in particular (Q^2, ν, z_{π^+}) bins before and after acceptance correction. In Appendix II are located plots for all (Q^2, ν, z_{π^+}) bins. Comparing the acceptance corrected results for different bins we can come to conclusion that the correction factor is less than 14%.

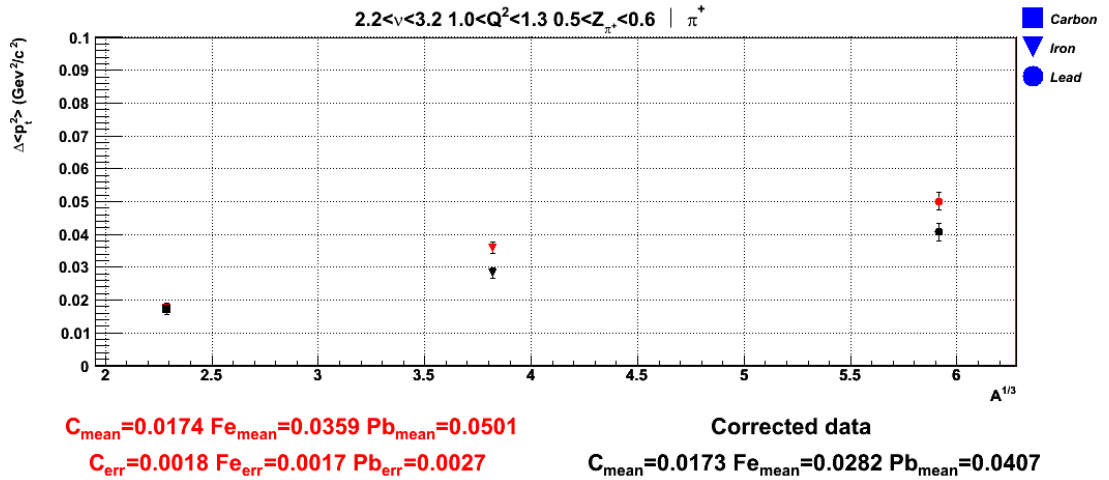


Figure 4-11. Transverse momentum broadening dependence on $A^{1/3}$ for $2.2 < \nu < 3.2 \text{ GeV}$, $1 < Q^2 < 1.3 \text{ GeV}^2$ and $0.5 < z_{\pi^+} < 0.6$ for carbon, iron and lead targets. The red colored (upper) points correspond to measurements without the acceptance correction applied, and the black colored points correspond to measurements with the acceptance correction applied. In the bottom of the plot one can find the values of transverse momentum broadening without (red) and with acceptance correction. The plotted errors are statistical errors for the data.

In Figures 4-12 a), b), c) and d) are presented sample plots of the hadronic multiplicity ratio dependence on z_{π^+} , Q^2 , ν and p_T^2 with (solid points) and without (hollow points) acceptance

correction in particular (Q^2, ν, z_{π^+}) bins. In Appendix II one can find the plots for other kinematical bins. The acceptance correction factor for the hadronic multiplicity ratio measurements is only a few percent.

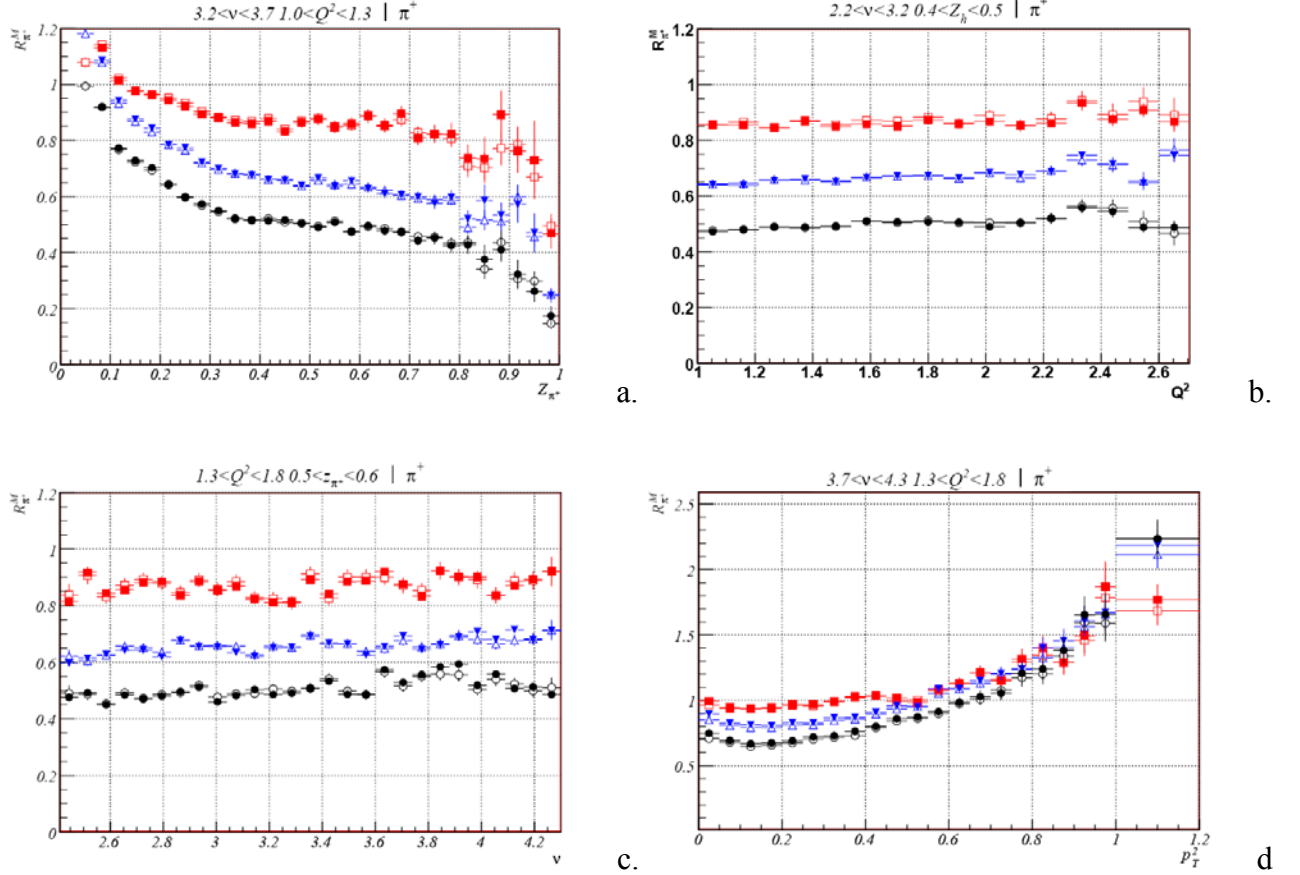


Figure 4-12. At the plots red corresponds to carbon, blue to iron and black to lead targets. The hollow points correspond to measurements without the acceptance correction applied; the solid points correspond to measurements with the acceptance correction applied. The plotted errors are statistical errors for the data. a) Hadronic multiplicity ratio dependence on z_{π^+} when $3.2 < \nu < 3.7$ GeV , $1 < Q^2 < 1.3$ GeV^2 . b) Hadronic multiplicity ratio dependence on Q^2 when $2.2 < \nu < 3.2$ GeV , $0.4 < z_{\pi^+} < 0.5$. c) The hadronic multiplicity ratio dependence on ν when $1.3 < Q^2 < 1.8$ GeV^2 , $0.5 < z_{\pi^+} < 0.6$. d) The hadronic multiplicity ratio dependence on p_T^2 when $3.7 < \nu < 4.3$ GeV , $1.3 < Q^2 < 1.8$ GeV^2 .

4.3.4 Fiducial Cuts and Their Effect on the Final Results.

Let us define the “fiducial cut” as a two dimensional and twice bent surface in the three dimensional (p, θ, ϕ) space bounding a region which satisfies certain selection criteria. In our case the criterion is a uniform (flat distributed) acceptance.

In order to select the regions of the detector which could be reliably reproduced by the GSIM simulation program, fiducial cuts were applied. For instance, the Cherenkov counter’s efficiency distribution versus θ_{e^-} and ϕ_{e^-} at the edges of a sector has a very complicated pattern. Because there is no reliable way to account for these losses, fiducial cuts were developed to isolate the regions with uniform efficiency distributions. Since the toroidal magnetic field bends electrons forward, the fiducial cuts in θ_{e^-} and ϕ_{e^-} will depend on the momentum of the electron. The CLAS detector efficiency for electrons is shown in Figure 4-14 as a function of the electron laboratory angles θ_{e^-} and ϕ_{e^-} . The different graphs represent different bins in the electron momentum. The black curves show the fiducial cuts for the central momentum of that bin. Only events with electrons lying within these black curves were used in the analysis. Electrons with momentum $p_{e^-} < 500$ MeV were rejected in order to avoid possible inefficiencies due to non-uniformity of the EC pre-trigger for deposited energies close to the E_{total} (from EC) threshold.

The whole procedure is a sequence of the following steps. First the whole momentum spectrum was divided into small bins each 0.1 GeV wide; for individual momentum bins in each CLAS sector separately the θ vs. ϕ dependence was plotted (see Figure 4-14). As one can notice from Figure 4-14 the inner regions of the distribution have a constant density while the boundary area is smeared by reduced efficiency. To get a flat acceptance region, all these distributions were fitted with a set of $\phi(\theta, p_n, s)$ functions, where p_n is the n-th momentum bin and s indicates the sector.

Likewise, to define the flat acceptance region boundaries, the polar θ angle was divided into 1° wide bins. For each (s_n, p_n, θ_n) bin the corresponding ϕ distribution was fitted by a trapezoid and the vertices of the smaller parallel side were accepted as flat region boundaries (an example for such a fit, in a randomly selected (s_n, p_n, θ_n) bin, one can see in Figure 4-13). Therefore the total number of such fits is equal to $6(\text{sectors}) \times 42(\text{momentum bins}) \times 73(\text{polar } \theta \text{ angle bins}) = 9996(\text{bins})$.

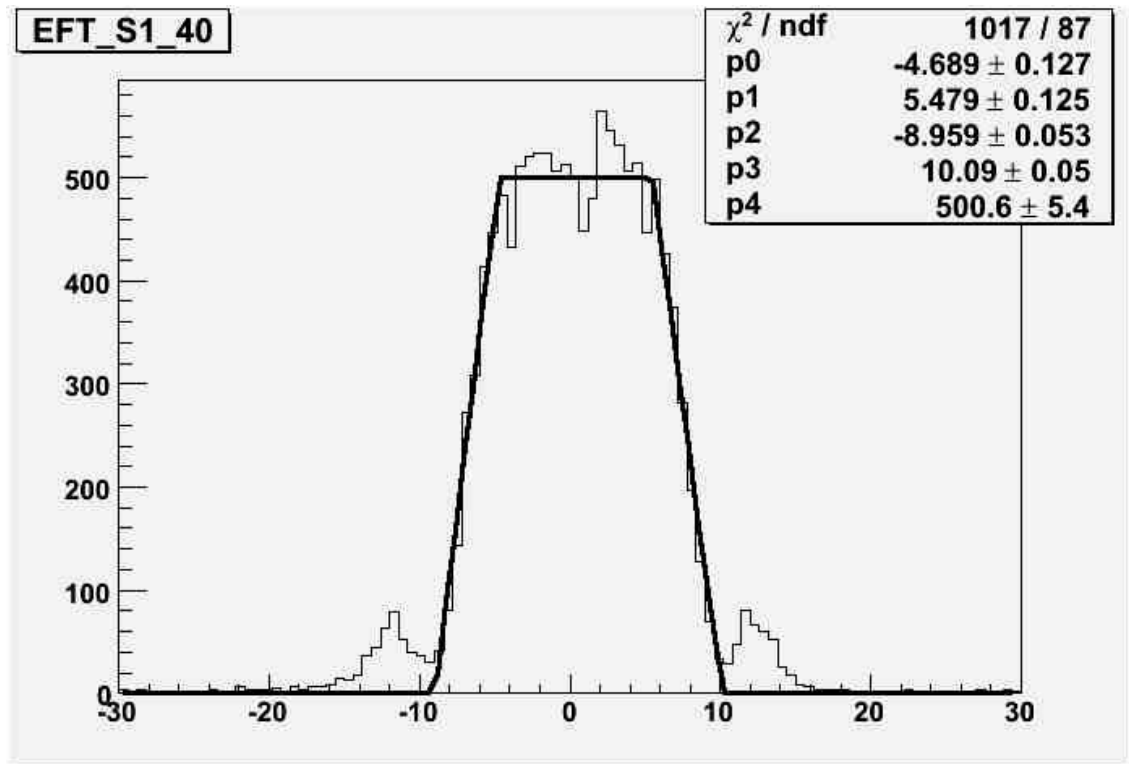


Figure 4-13. A randomly selected distribution of ϕ azimuthal angles for events for a particular CLAS sector, 0.1 GeV momentum bin and 1° wide polar (θ) angle bin. The distribution is fitted with a trapezoid fit, where the smaller side vertices are the fiducial flat region boundaries for this bin.

The procedure explained above was performed for solid and liquid targets separately, which was required because of the different geometrical shapes and different locations of the targets in the beam line.

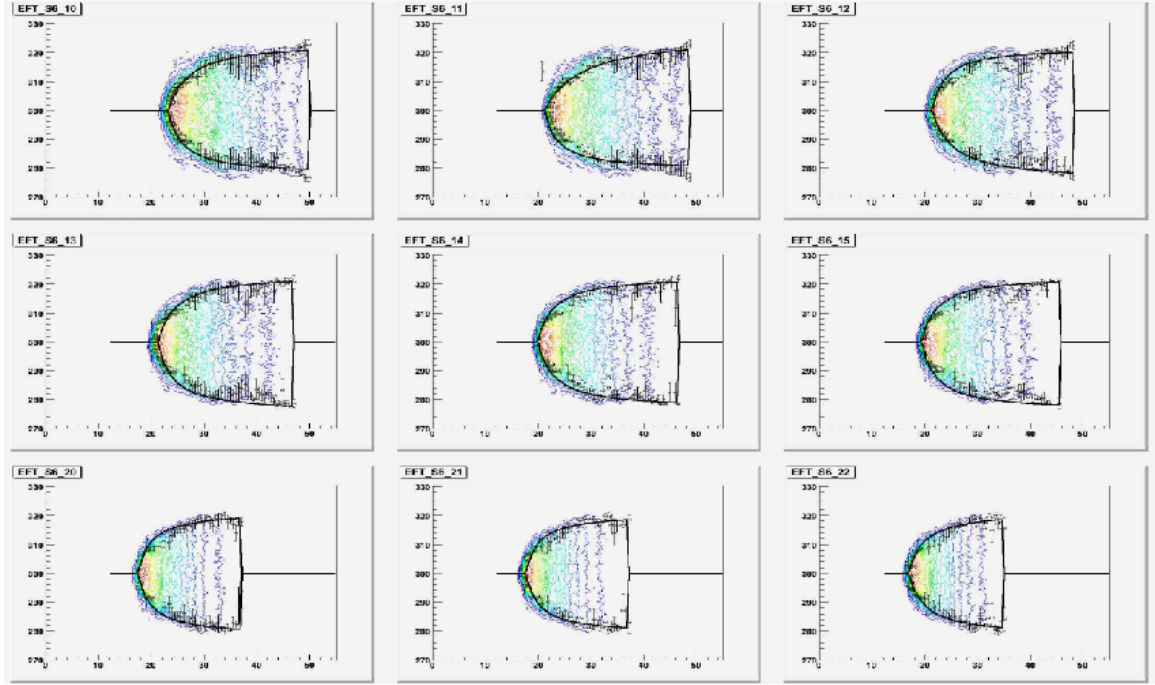


Figure 4-14. θ_{e^-} and ϕ_{e^-} for nine electron momentum bins in Sector 6. The black curves indicate the fiducial cuts for the central momentum. Only events with electrons in-between the black curves were used.

The same calculation procedure was done for the π^+ fiducial cut. An example of the π^+ fiducial cut on θ_{π^+} vs. ϕ_{π^+} one can see in Figure 4-15.

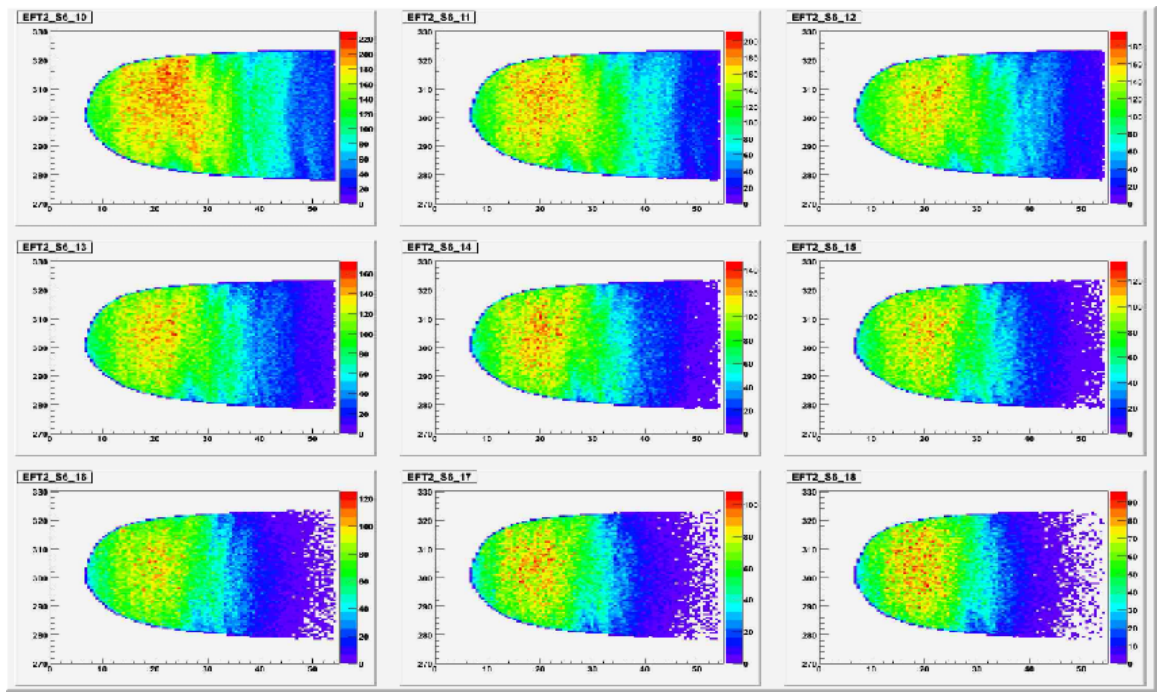


Figure 4-15. θ_{π^+} versus ϕ_{π^+} for nine pion momentum bins in Sector 6 for data which passes the fiducial cuts for the central momentum.

5. Analysis Results and Conclusions

As discussed in earlier chapters, during the analysis of the experiment, semi-inclusive production of hadrons in deep-inelastic scattering of leptons off nuclei was investigated. These data provide important information about the space-time development of in-medium hadronization. In the kinematic region under consideration, $x_{Bjorken}$ is sufficiently large ($x_{Bjorken} > 0.1$), therefore the lepton interacts incoherently with only one bound nucleon via single photon exchange; the resulting hadron shower produced consists of pions, kaons, protons and other hadrons. This region is dominated by valence quarks, so that we can treat the DIS as electron-quark scattering. At small $x_{Bjorken}$, which is dominated by the sea, the process of DIS looks different (in the nuclear rest frame); the virtual photon produces two jets, q and \bar{q} , which share the full energy ν . Here are presented the measurement results for positively charged pions.

According to the gluon bremsstrahlung model [52] predictions absorption of the produced colorless prehadron is the main source of nuclear suppression. The knocked out quark propagating through the medium radiates gluons which in turn might produce quark-antiquark pairs. This process continues until the colorless pre-hadronic stage is developed. Afterwards the hadron formation period starts, which ends with the formation of the final hadron. Thus one can describe the whole process in two distinct dynamical stages, each with a characteristic time scale [26]. The production time is the time during which the quark emitting gluons is deconfined. This period is signaled by medium-stimulated energy loss via gluon emission and production of the colorless pre-hadronic stage at the end. For investigation of that stage, observation of transverse momentum broadening is important (see formula in section 4.3.3). Here is a simple formula for estimation of production time:

$$\tau_p \approx \frac{\nu(1-z_h)}{c \frac{dE}{dx}} \quad (5.1)$$

which is simply the fraction of total energy lost by the quark to produce the pre-hadron at a given energy loss rate. The formation time is the time required to form the color field of the hadron, signaled by interactions with known hadronic cross sections. No gluon emission occurs during that stage. To study that process, observation of hadron attenuation is important (see hadronic multiplicity ratio formula in section 4.3.3).

According to pQCD studies of energy loss the dominant mechanism is gluon radiation and the effect of elastic scatterings is considered minor [19]. In that case coherence effects become important. Bremsstrahlung is usually treated in second order perturbation theory of QED, yielding the well-known Bethe-Heitler formula [55]. In dense media, medium effects have to be accounted for. Successive scattering of high energy electrons in amorphous media [61] significantly suppresses the photon spectrum at low photon energies compared to Bethe-Heitler theory. This effect, known as the Landau-Pomeranchuk-Migdal effect [15], has recently been confirmed in high energy experiments [51].

One can imagine a very energetic quark of energy E propagating through a QCD medium of finite length L . Multiple scattering of this projectile in the medium induces gluon radiation, which gives rise to the quark energy loss. The main assumption is that the scattering centers are static and uncorrelated, thus one can focus on purely radiative processes, since the collisional energy loss vanishes in the case of static centers. In equation (5.2) is defined the coherence length as the formation time of a gluon radiated by a group of scattering centers acting as a single source of radiation,

$$l_c \approx \frac{\omega}{\langle k_{\perp}^2 \rangle_{l_c}} \quad (5.2)$$

ω and k_{\perp} are the gluon's energy and transverse component of momentum, respectively.

If we consider λ as the parton mean free path in the medium, for small $l_c < \lambda$ incoherent radiation takes place on L/λ scattering centers and thus we can derive the differential energy spectrum per unit length in the so-called Bethe-Heitler regime for incoherent radiation. The interesting regime of coherent radiation, the LPM regime, is defined by $l_c < \lambda < L$ ($N_c > 1$),

where we can see the suppression of the radiation spectrum. N_c here is the number of scattering centers. In case of $l_c > L$, effectively only one scattering center is active (the ‘factorization regime’). After integration, two conditions emerge, separated by the critical length (see Figure 5-1). When $L < L_{crit}$, the energy loss is proportional to L , and in case of $L > L_{crit}$ it is proportional to the square root of E . So the total energy loss quadratic dependence on L turns to linear with increasing L . For a detailed explanation see [19].

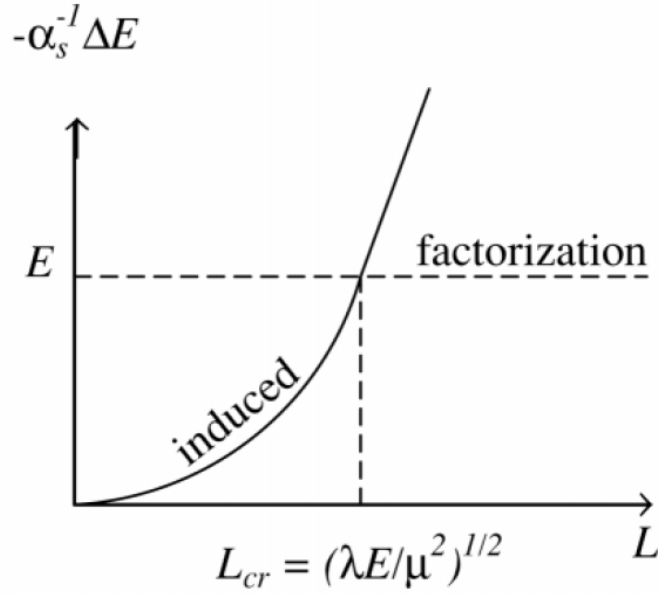


Figure 5-1. Generic energy loss of a parton as a function of the medium size L . Plot taken from [19].

5.1 Transverse Momentum Broadening Measurements.

As mentioned above, the transverse momentum broadening (Δp_T^2) measurements might be the most sensitive probe for the *production time* since it provides a direct measurement of the production time particularly in [52] model. This is because the hadronizing quark only contributes in the time intervals $t < t_p$ to the Δp_T^2 . As soon as the pre-hadron is formed, no further broadening occurs, because inelastic interactions are suppressed for the pre-hadron, thus only broadening via

elastic rescattering is still possible. However, the elastic cross section is so small that even for pions the mean free path in nuclear matter is about 20 fm.

The black colored data points in the plots in Appendix II present the transverse momentum broadening dependence on $A^{1/3}$ (A is the nuclear atomic number) for positive pions in different (ν, Q^2, z_{π^+}) kinematical bins for carbon, iron and lead. $A^{1/3}$ for each nucleus is proportional to its radius. At the top of each plot is presented the corresponding (ν, Q^2, z_{π^+}) kinematical bin. The values of transverse momentum broadening one can find below each plot.

In Table 5-1 below one can find the values of the data points with the corresponding statistical errors in different (Q^2, ν, z_{π^+}) kinematical bins.

ν range	Q^2 range	z_{π^+} range	C	C error	Fe	Fe error	Pb	Pb error
2.2-3.2	1.0-1.3	0.4-0.5	0.0189	0.0013	0.0355	0.0012	0.0434	0.0019
2.2-3.2	1.0-1.3	0.5-0.6	0.0173	0.0018	0.0282	0.0017	0.0407	0.0027
2.2-3.2	1.0-1.3	0.6-0.7	0.0129	0.0023	0.0290	0.0021	0.0320	0.0034
2.2-3.2	1.3-1.8	0.4-0.5	0.0167	0.0013	0.0360	0.0012	0.0403	0.0019
2.2-3.2	1.3-1.8	0.5-0.6	0.0160	0.0018	0.0309	0.0016	0.0335	0.0026
2.2-3.2	1.3-1.8	0.6-0.7	0.0155	0.0022	0.0249	0.0019	0.0311	0.0032
2.2-3.2	1.8-4.2	0.4-0.5	0.0176	0.0017	0.0368	0.0015	0.0466	0.0027
2.2-3.2	1.8-4.2	0.5-0.6	0.0124	0.0022	0.0285	0.0021	0.0394	0.0036
2.2-3.2	1.8-4.2	0.6-0.7	0.0127	0.0028	0.0242	0.0026	0.0263	0.0044
3.2-3.7	1.0-1.3	0.4-0.5	0.0138	0.0018	0.0375	0.0017	0.0460	0.0028
3.2-3.7	1.0-1.3	0.5-0.6	0.0127	0.0026	0.0335	0.0024	0.0373	0.0039
3.2-3.7	1.0-1.3	0.6-0.7	0.0273	0.0035	0.0318	0.0032	0.0470	0.0054
3.2-3.7	1.3-1.8	0.4-0.5	0.0267	0.0017	0.0338	0.0016	0.0509	0.0027
3.2-3.7	1.3-1.8	0.5-0.6	0.0156	0.0025	0.0368	0.0023	0.0424	0.0038
3.2-3.7	1.3-1.8	0.6-0.7	0.0123	0.0034	0.0253	0.0031	0.0380	0.0051
3.2-3.7	1.8-4.2	0.4-0.5	0.0220	0.0014	0.0355	0.0014	0.0410	0.0024
3.2-3.7	1.8-4.2	0.5-0.6	0.0191	0.0019	0.0355	0.0019	0.0465	0.0031
3.2-3.7	1.8-4.2	0.6-0.7	0.0125	0.0026	0.0301	0.0025	0.0427	0.0042
3.7-4.3	1.0-1.3	0.4-0.5	0.0216	0.0022	0.0425	0.0020	0.0447	0.0031
3.7-4.3	1.0-1.3	0.5-0.6	0.0223	0.0031	0.0427	0.0029	0.0404	0.0045
3.7-4.3	1.0-1.3	0.6-0.7	0.0192	0.0047	0.0206	0.0046	0.0476	0.0078
3.7-4.3	1.3-1.8	0.4-0.5	0.0165	0.0021	0.0341	0.0020	0.0451	0.0032
3.7-4.3	1.3-1.8	0.5-0.6	0.0233	0.0031	0.0277	0.0029	0.0460	0.0048
3.7-4.3	1.3-1.8	0.6-0.7	0.0133	0.0047	0.0444	0.0046	0.0507	0.0071
3.7-4.3	1.8-4.2	0.4-0.5	0.0061	0.0017	0.0383	0.0016	0.0477	0.0028
3.7-4.3	1.8-4.2	0.5-0.6	0.0130	0.0025	0.0424	0.0025	0.0453	0.0041
3.7-4.3	1.8-4.2	0.6-0.7	0.0165	0.0038	0.0310	0.0036	0.0412	0.0061

Table 5-1. Data points for transverse momentum broadening dependence on $A^{1/3}$ (A is the nuclear atomic number) for positive pions in different (ν, Q^2, z_{π^+}) kinematical bins. The first, second and third columns show the kinematical ranges for ν , Q^2 and z_{π^+} , respectively. The following

columns give the transverse momentum broadening values and statistical errors for carbon, iron and lead, respectively.

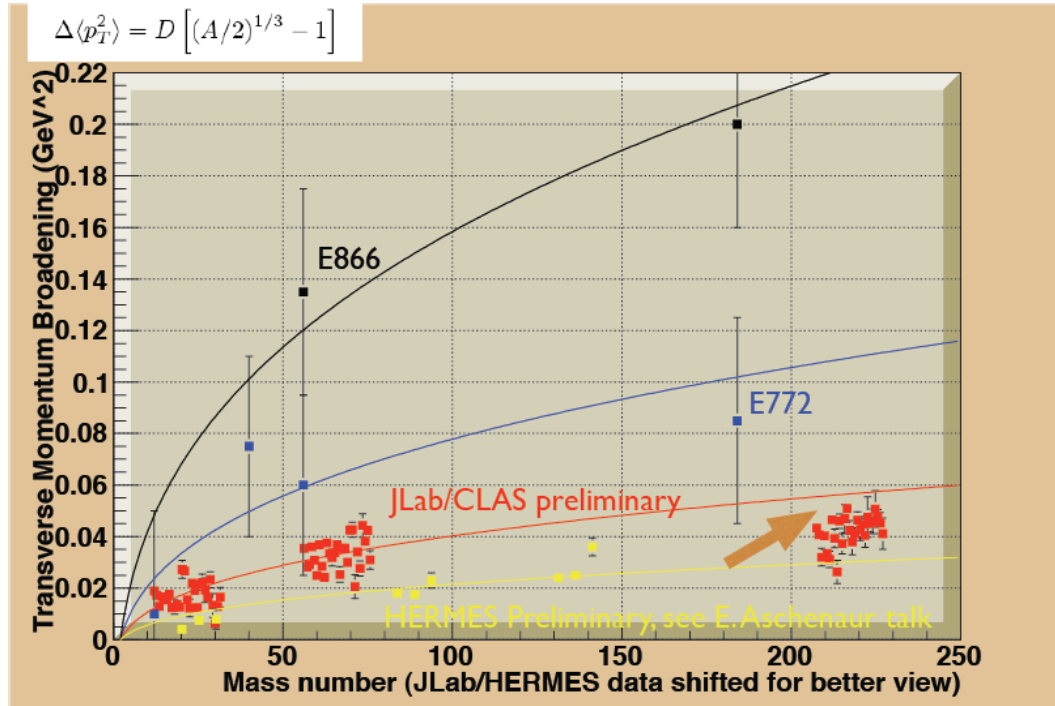


Figure 5-2. Data from Drell-Yan measurements (black and blue data points), preliminary data from the HERMES experiment (yellow data points), and the JLab/CLAS data (red data points), comparing transverse momentum broadening. The Drell-Yan broadening is extracted from muon pairs with an 800 GeV proton beam, the HERMES data are for charged pions and positive kaons produced with a 27 GeV positron beam, while the JLab data are for positive pions produced with a 5 GeV electron beam.

The superposition of transverse momentum broadening dependence on A atomic number from different experiments are presented on Figure 5-2 (including Drell Yan measurements, Hermes preliminary data and CLAS/Eg2 results presented in this thesis).

The following statements in this sub-chapter require more theoretical work for quantitative extraction. On Figure 5-3 is presented the transverse momentum broadening Δp_T^2 dependence on ν in $1 < Q^2 < 2 \text{ GeV}^2$ and $0.5 < z_{\pi^+} < 0.6$ kinematic region. As one can notice, with increasing

ν transverse momentum broadening increases too, eventually elevating to plateau. If assume that gluon emission dominates then from (1.18) pQCD formula one gets that energy loss is approximately equals to 100 MeV/fm at 6 fm, which is the size of lead nuclei, for a few GeV quark at zero temperature ($\alpha_s \approx 0.4$ in our kinematical region, see Figure 1-3). Besides that the set of plots from Appendix II show that to the first approximation if transverse momentum broadening is proportional to the energy loss then the total energy loss shows quadratic behavior.

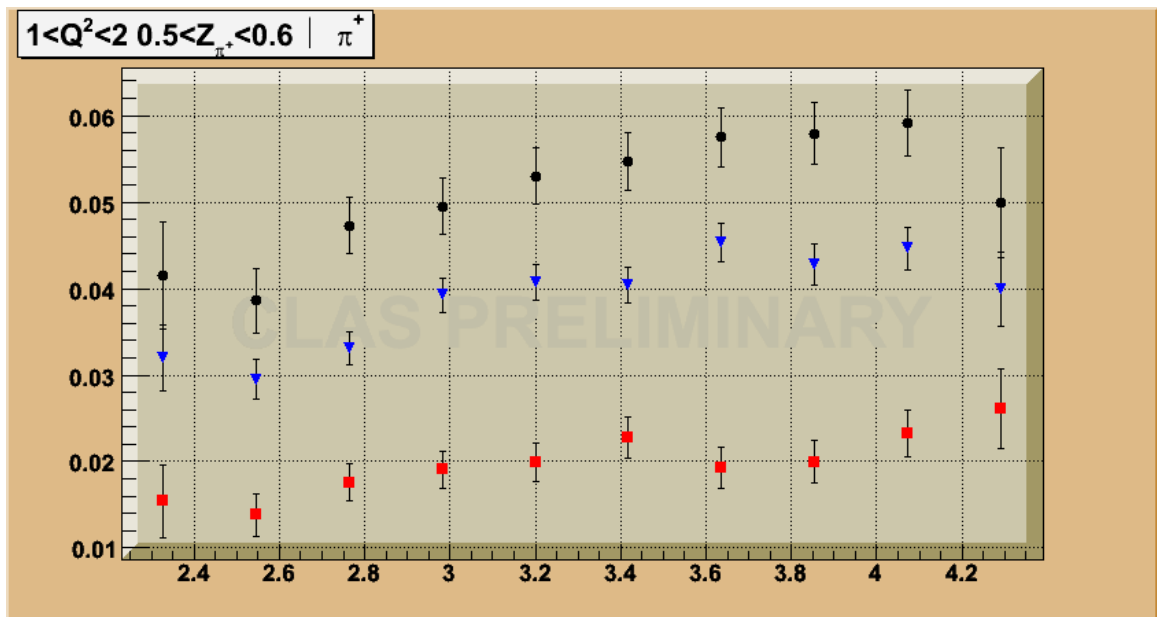


Figure 5-3. Transverse momentum broadening Δp_T^2 dependence on ν in $1 < Q^2 < 2 \text{ GeV}^2$ and $0.5 < z_{\pi^+} < 0.6$ kinematic region. Red data points correspond to carbon, blue points to iron and black points to lead.

5.2 Hadronic Multiplicity Ratio Measurements

The hadronic multiplicity ratio for positively charged pions has been measured as a three dimensional function of either z_{π^+} , ν or Q^2 in (Q^2, ν) , (Q^2, z_{π^+}) and (ν, z_{π^+}) kinematical bins respectively. The observed dependences are discussed in the following sections.

5.2.1 Dependence on z_{π^+} .

In Appendix III are presented the CLAS experiment plots for positive pions with hadronic multiplicity ratio dependence on z_{π^+} in different (Q^2, ν) kinematical bins. Red colored solid squares correspond to carbon data, blue colored solid triangles correspond to iron data, and black colored solid circles correspond to lead data. At the top of each plot is presented the corresponding (Q^2, ν) kinematical bin. On Table A2 Appendix III one can find the values of data points with corresponding statistical errors in different (Q^2, ν, z_{π^+}) kinematical bins. The data are presented in three kinematical bins of z_{π^+} with limits $0.4 < z_{\pi^+} < 0.7$ where it is expected that the target fragmentation contribution is suppressed and the factorization requirement is satisfied for CLAS [23].

As can be seen from the plots in Appendix III, the hadronic multiplicity ratio decreases with increasing z_{π^+} for all solid targets. The same behavior was observed in the HERMES experiment [8, 9]. In absorption-type models the overall decrease of hadronic multiplicity ratio with increasing z_{π^+} is assumed to be due to a decrease in the production length in combination with pre-hadron absorption.

In Figure 5-4a) is presented the superposition of the hadronic multiplicity ratio dependence on z_{π^+} for different (Q^2, ν) kinematical bins. In Figure 5-4b) one can see the same distributions as in the plot of Figure 5-4a) except that $0.4 < z_{\pi^+} < 0.5$. The plots in Figure 5-4b) were fitted with a linear function $f(z_{\pi^+}) = a + b \cdot z_{\pi^+}$; the results are shown on Table 5-2. As one can notice the χ_1^2 per degree of freedom is close to unity for all cases.

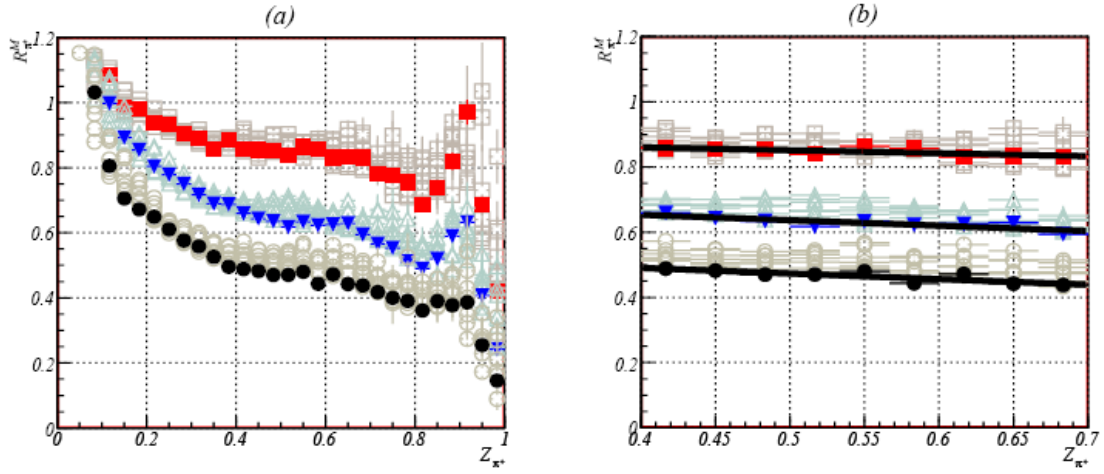


Figure 5-4. a) The hadronic multiplicity ratio dependence on z_{π^+} with different (Q^2, ν) kinematical bins superimposed. The squares correspond to the carbon data, triangles to iron, and circles to lead. The arbitrarily selected data with solid symbols correspond to the kinematical bin with $1 < Q^2 < 1.33 \text{ GeV}^2$ and $2.2 < \nu < 3.2 \text{ GeV}$. b) The same distributions as in plot a) except with $0.4 < z_{\pi^+} < 0.5$. The separated graphs are fitted with the linear function $f(z_{\pi^+}) = a + b \cdot z_{\pi^+}$.

ν range	Q^2 range	a (C)	b (C)	χ_1^2 (C)	a (Fe)	b (Fe)	χ_1^2 (Fe)	a (Pb)	b (Pb)	χ_1^2 (Pb)
2.2-3.2	1-1.33	0.897	-0.0912	0.374	0.720	-0.167	1.197	0.560	-0.172	1.132
2.2-3.2	1.33-1.76	0.959	-0.217	1.676	0.748	-0.198	0.590	0.581	-0.183	0.592
2.2-3.2	1.76-4.2	0.989	-0.262	1.460	0.826	-0.312	0.584	0.627	-0.248	1.439
3.2-3.73	1-1.33	0.816	0.0883	0.823	0.740	-0.183	0.879	0.580	-0.155	0.421
3.2-3.73	1.33-1.76	0.902	-0.0710	1.483	0.779	-0.217	0.556	0.577	-0.135	0.750
3.2-3.73	1.76-4.2	0.977	-0.183	1.906	0.778	-0.177	0.901	0.560	-0.0676	0.0546
3.73-4.3	1.33-1.76	0.920	-0.0586	0.399	0.752	-0.136	0.524	0.589	-0.0916	0.986
3.73-4.3	1.76-4.2	0.923	-0.0884	1.271	0.745	-0.106	2.140	0.627	-0.165	1.418

Table 5-2. The fit results of the hadronic multiplicity ratio dependence on z_{π^+} for different (Q^2, ν) kinematical bins and in the range $0.4 < z_{\pi^+} < 0.7$ with the linear function $f(z_{\pi^+}) = a + b \cdot z_{\pi^+}$. The first column shows the ν ranges, the second column shows the Q^2 ranges, and the following columns show the a parameter, b parameter and χ_1^2 per degree of freedom for carbon, iron and lead, respectively. As one can notice, the χ_1^2 is close to unity for all cases.

In Figure 5-5 is shown the mean value of the parameter a from the dependence on $A^{1/3}$ (A is the atomic number of the nucleus) for carbon, iron, and lead shown in Table 5-2. The errors shown on the plot are the statistical errors for fluctuation of the parameter a in different kinematical bins. The result is fitted with linear function with $\chi_1^2 = 0.60$ and resulting function $\langle a \rangle(A^{1/3}) = 1.12 - 0.09A^{1/3}$. Therefore the amount of attenuation for positive pions on different nuclear has a linear dependence on $A^{1/3}$ for $0.4 < z_{\pi^+} < 0.7$.

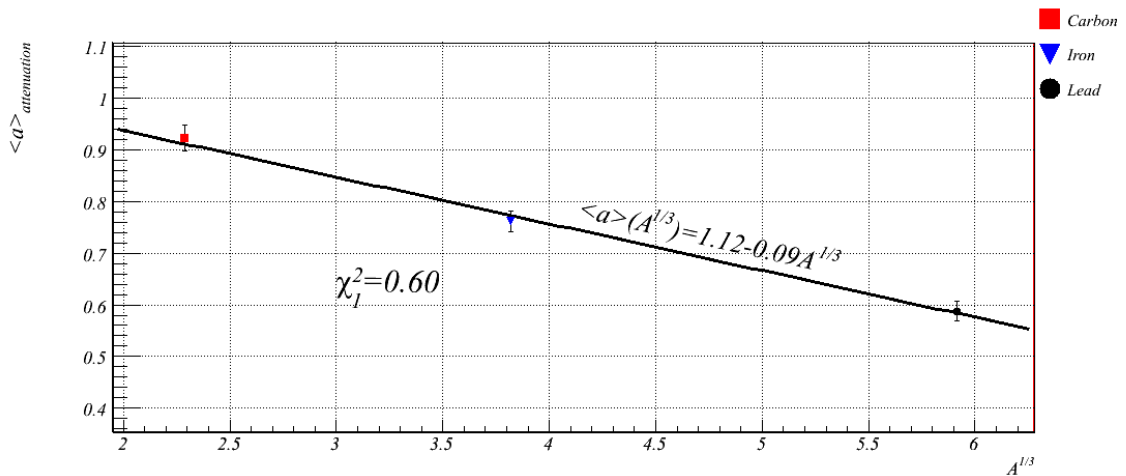


Figure 5-5. The mean value of parameter a from the dependence on $A^{1/3}$ (A is the atomic number of nuclear) for carbon, iron and lead from Table 3. The errors shown on the plot are the statistical errors for the fluctuation of the parameter a in different kinematical bins. The result is fitted with a linear function with $\chi_1^2 = 0.60$ and the resulting function is $\langle a \rangle(A^{1/3}) = 1.12 - 0.09A^{1/3}$.

5.2.2 Dependence on ν .

In Appendix IV are presented the CLAS experimental plots for positive pions of the hadronic multiplicity ratio dependence on ν in different (Q^2, z_{π^+}) kinematical bins. Red solid squares correspond to carbon data, blue solid triangles correspond to iron data, and black solid

circles correspond to lead data. At the top of each plot is presented the corresponding (Q^2, z_{π^+}) kinematical bin. On Table A3 in Appendix IV one can find the values of data points with corresponding statistical errors in different (Q^2, z_{π^+}, ν) kinematical bins. The data are presented in three kinematical bins of z_{π^+} with limits $0.4 < z_{\pi^+} < 0.7$ the target fragmentation contribution is suppressed and the factorization requirement is satisfied for CLAS [23].

As can be seen from plots in Appendix IV, the hadronic attenuation slightly decreases (the value of hadronic multiplicity ratio increases) with increasing values of ν . In absorption-type models this is explained as being due to an increase of the formation length in the rest frame of the nucleus at higher ν due to Lorentz dilation, resulting in a larger fraction of the hadronization taking place outside the nucleus.

In Figure 5-6 is shown the superposition of the hadronic multiplicity ratio dependence on ν for different (Q^2, z_{π^+}) kinematical bins. The solid markers correspond to the same dependence for the kinematical region integrated over Q^2 and z_{π^+} .

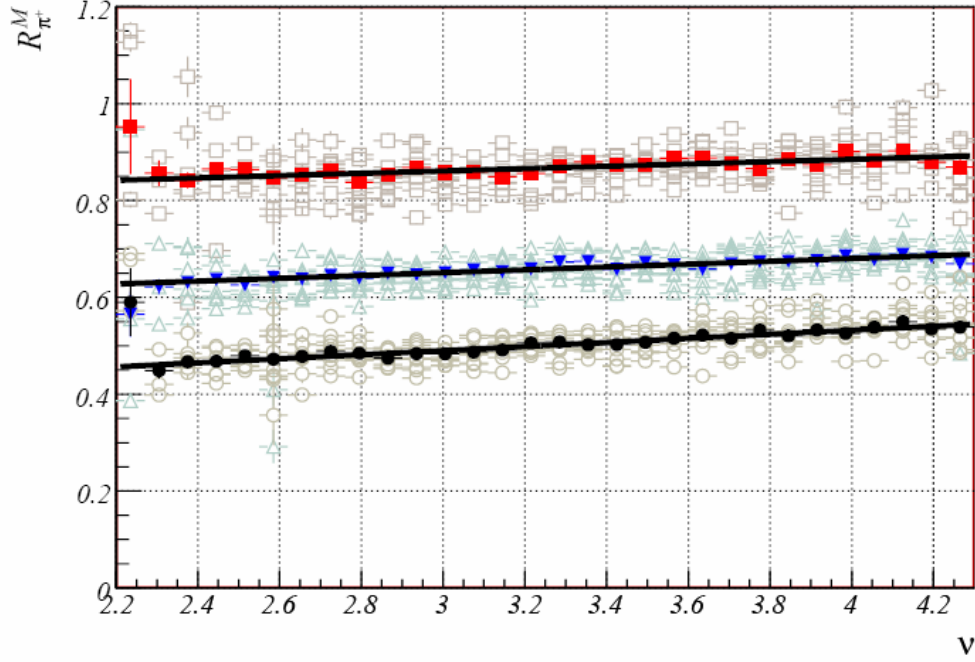


Figure 5-6. The superposition of the hadronic multiplicity ratio dependence on ν for different (Q^2, z_{π^+}) kinematical bins. The squares correspond to carbon data, the triangles correspond to iron, and the circles correspond to lead. The solid symbols correspond to the same dependence for this kinematical region integrated over the Q^2 and z_{π^+} . The solid points are fitted with a linear function, yielding $\chi_1^2(C) = 1.31$, $\chi_1^2(Fe) = 1.28$ and $\chi_1^2(Pb) = 1.29$ per degree of freedom correspondingly for carbon, iron and lead. The resulting functions have the following forms:
 $R_{\pi^+}^C(\nu) = 0.789 + 0.0241 \cdot \nu$, $R_{\pi^+}^{Fe}(\nu) = 0.563 + 0.0293 \cdot \nu$, and $R_{\pi^+}^C(\nu) = 0.364 + 0.0421 \cdot \nu$.

5.2.3 Dependence on Q^2 .

The hadronic multiplicity ratio dependence on Q^2 in different (ν, z_{π^+}) kinematical bins is presented in Appendix V for positive pions from the CLAS data. The red solid squares correspond to carbon data, blue solid triangles correspond to iron data and black solid circles correspond to lead data. At the top of each plot is shown the corresponding (ν, z_{π^+}) kinematical bin. On Table A4 in Appendix V one can find the values of the data points and corresponding statistical errors in

different (ν, z_{π^+}, Q^2) kinematical bins. The data are presented in three kinematical bins of z_{π^+} with limits $0.4 < z_{\pi^+} < 0.7$ where the target fragmentation contribution is suppressed and the factorization requirement is satisfied for CLAS [23].

As one can notice from the plots in Appendix V, there is a small Q^2 -dependence, which is slightly stronger for heavier nuclei.

In Figure 5-7 is shown a superposition of the hadronic multiplicity ratio dependence on Q^2 for different (ν, z_{π^+}) kinematical bins. The squares correspond to carbon data, triangles correspond to iron and circles correspond to lead. The solid symbols correspond to the same dependence for this kinematical region integrated over ν and z_{π^+} .

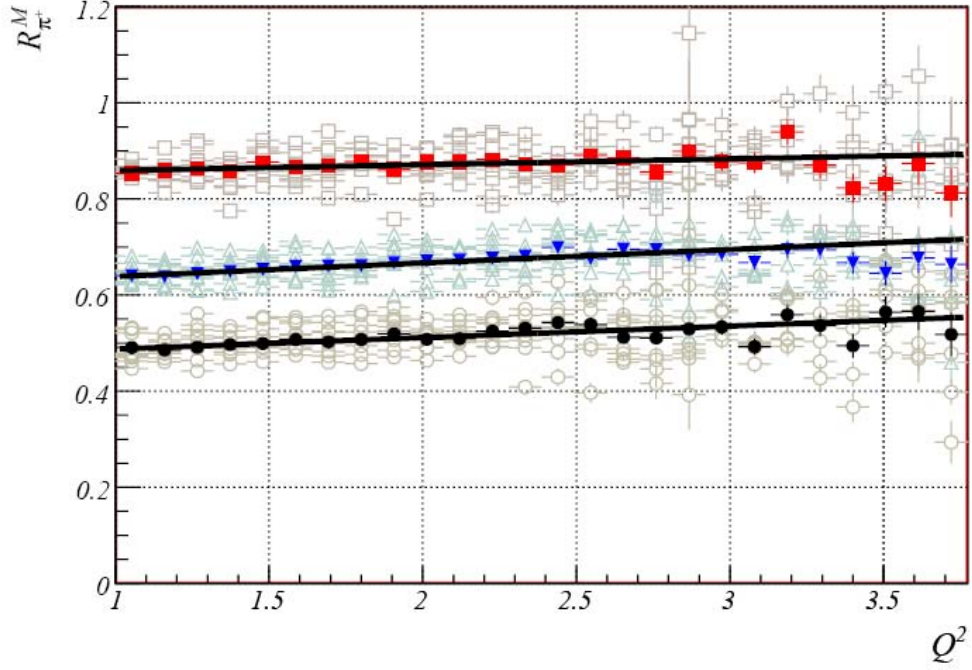


Figure 5-7. The superposition of the hadronic multiplicity ratio dependence on Q^2 for different (ν, z_{π^+}) kinematical bins. The squares correspond to carbon data, triangles correspond to iron, and circles correspond to lead. The solid symbols correspond to the same dependence for this kinematical region integrated over the ν and z_{π^+} . The solid points are fitted with a linear function with $\chi_1^2(C)=1.12$, $\chi_1^2(Fe)=1.22$ and $\chi_1^2(Pb)=1.49$ per degree of freedom correspondingly for carbon, iron and lead. The resulting functions are:

$$R_{\pi^+}^C(Q^2) = 0.846 + 0.0121 \cdot Q^2, R_{\pi^+}^{Fe}(Q^2) = 0.611 + 0.0280 \cdot Q^2, \text{ and}$$

$$R_{\pi^+}^{Pb}(Q^2) = 0.464 + 0.0237 \cdot Q^2.$$

5.3 The ‘‘Cronin effect’’.

The p_T distribution of the observed hadrons is expected to be broadened on a nuclear target compared to a deuterium target due to multiple scattering of the propagating quark and hadron. This effect is known as the Cronin effect [35] and first has been observed in heavy-ion and

hadron-nucleus reactions [18]. A nuclear enhancement at high p_T^2 is also observed in the HERMES for the available nitrogen and krypton data [7, 8, and 9].

The Cronin effect in the CLAS data is shown in Appendix VI in different (Q^2, ν) kinematical bins. The red solid squares correspond to carbon data, the blue solid triangles correspond to iron data, and the black solid circles correspond to lead data. At the top of each plot is shown the corresponding (Q^2, ν) kinematical bin. On Table A5 in Appendix VI one can find the values of the data points and the corresponding statistical errors in different (Q^2, ν, p_T^2) kinematical bins. It is important to notice that the data is presented in the $0.4 < z_{\pi^+} < 0.7$ region in which the target fragmentation contribution is suppressed and the factorization requirement is satisfied for CLAS [23].

In Figure 5-8 is shown the hadronic multiplicity ratio dependence on p_T^2 for positive pions in different x_B (Bjorken x) bins correspondingly for carbon (a), iron (b) and lead (c). One can notice that the attenuation dependence on x_B is significant only for large p_T^2 .

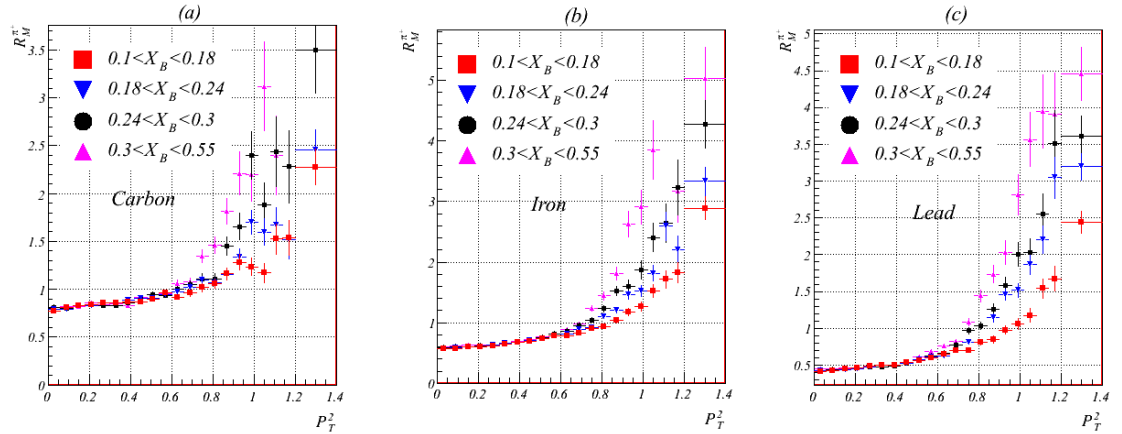


Figure 5-8. Hadronic multiplicity ratio dependence on p_T^2 for positive pions in different x_B (Bjorken x) bins correspondingly for carbon (a), iron (b), and lead (c). One can see that the attenuation dependence on x_B is significant only for large p_T^2 .

According to [52], nuclear broadening of the transverse momentum distribution might be the most sensitive probe for the production length, and provides direct measurements of l_p , since $\Delta p_T^2 \propto l_p$. Indeed, only the hadronizing quark at short time intervals $t < t_p$ contributes to the broadening. As soon as the pre-hadron is created, no further broadening occurs, since inelastic interactions are prohibited for the pre-hadron, and only broadening via elastic rescattering is possible. However, the elastic cross section is so small that even for pions the mean free path in nuclear matter is about 20 fm. It is even longer for small-size pre-hadron due to color transparency. Therefore, one should expect a disappearance of the broadening effect at large $z_h \rightarrow 1$ since $t_p \rightarrow 0$. In Figure 5-9 is the prediction for the nuclear ratio as a function of p_T^2 for different z_h bins.

B.Z. Kopeliovich et al. / Nuclear Physics A 740 (2004) 211–245

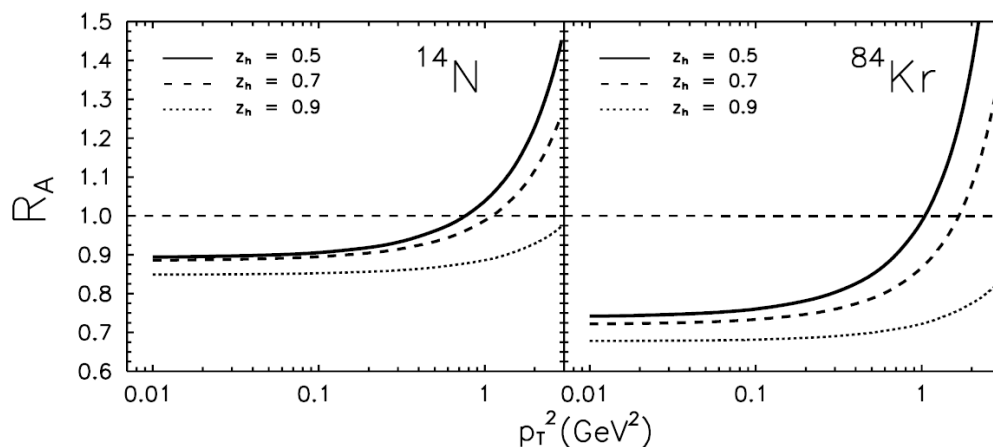


Figure 5-9. p_T^2 -dependence of nucleus-to-deuteron ratios binned in z_h for hadroproduction in DIS on nitrogen (left) and krypton (right).

The same measurements for positive pions from the EG2 data set in the bins for $z_h = 0.5$ and $z_h = 0.7$ for carbon, iron and lead are presented in Figure 5-10. As one can see there is a good

qualitative match between the shapes of the data and the prediction, while in the EG2 measurements the ‘‘Cronin effect’’ itself is larger.

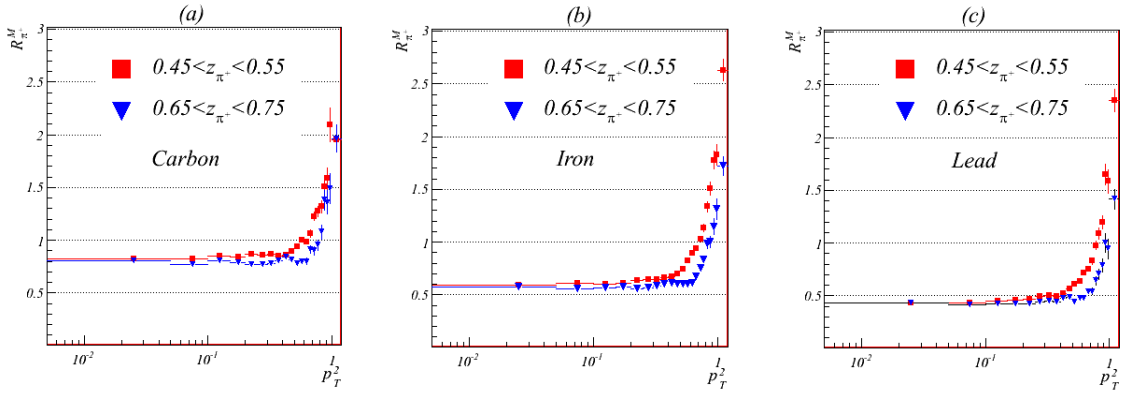


Figure 5-10. The hadronic multiplicity ratio dependence on p_T^2 for positive pions for carbon (a), iron (b), and lead (c). The red squares correspond to $0.45 < z_{\pi^+} < 0.55$ and the blue triangles correspond to $0.65 < z_{\pi^+} < 0.75$.

5.4 Systematic Error Estimate.

The design of the experiment had as a primary goal the minimization of systematic uncertainties. Time-varying effects, such as fluctuation of beam currents, phototube gains, or the occurrence of dead channels during data taking, were the same for both the solid and liquid targets, since they were both in the beam at the same time. Acceptance-related effects were minimized by positioning the two targets close together; their 4 cm separation distance is small relative to the much larger CLAS dimensions. The experimental observables chosen also reduced systematic uncertainties; for instance, the multiplicity ratio is a super-ratio in which luminosity cancels in first order, as does the acceptance correction. The transverse momentum broadening observable, which is derived by taking the difference of the mean values of two spectra, is also insensitive to luminosity and has only a small acceptance correction. Therefore most systematic errors cancel out or are minimized; the residual systematic uncertainties are discussed in the following sections.

Acceptance error

One of the main residual sources of systematic errors is the acceptance correction error. Because of the finite bin size, the result of averaging the acceptance over an acceptance bin depends on the distribution of events in that bin. The introduced error depends on the shape of the acceptance function and the shape of the corrected distribution as well as on the acceptance bin size. Reducing the acceptance bin size obviously will reduce the error associated with averaging over the bin. Besides that, since the CLAS detector has a finite resolution, some of the events produced in one acceptance bin will be reconstructed in a different bin. It is especially the case for distributions with large curvatures, when the resolution of the detector can cause significant distortions. Even for distributions with a small curvature there is a significant effect at the edges, where events can migrate only in one direction. Unlike the effects from averaging over an acceptance bin, this kind of systematic uncertainty cannot be reduced by decreasing the bin size. The GSIM detector simulation package reproduces the resolution of the CLAS detector, which gives a correct accounting of bin migration effects. Besides that, all measured physical variables $(Q^2, \nu, z_{\pi^+}, p_T^2, \phi_{\hat{q}\pi^+})$ have smooth shapes (with small gradients including the edges).

Target geometry and experimental conditions error

As mentioned in section 1.5, the solid target thicknesses and the cryotarget thickness were precisely determined. The scattering rates for the two targets were approximately equal. Because the typical operation of CLAS involves only few-nA beams, melting of the solid targets or boiling of the cryotargets was not of concern, thus a convection-cooled deuterium cryotarget in combination with small solid targets was chosen as the basic design configuration. The cryotarget was located upstream of the solid targets, limiting the effects of secondary electromagnetic processes contributing to the flux incident on either target. The cryotarget had aluminum windows approximately 15 microns in thickness, resulting in 2.5% of the cryotarget being aluminum of approximately 99% purity, thus other elements in the foil are negligible in thickness. Empty target

runs were taken in order to have an explicit measurement of the effects of these windows. In practice, the nuclear effects were so small for the light nuclei (e.g., carbon and aluminum) that the 2.5% contribution from the windows produced a systematic shift that was very much smaller than the statistical errors, and thus it was not corrected.

Positive pion identification errors

The information used to identify the positive pions was the same for both targets. Thus, while the cuts on the mass-related variables did decrease the pion efficiency due to events in the distribution tails being excluded, this small inefficiency was essentially identical for the two targets, and thus it cancelled out.

For pions with momenta less than 2.7 GeV, the time-of-flight technique described in detail in section 4.1.2 was used. Since the pion/kaon masses begin to overlap above about 2 GeV, a small kaon contamination (e.g., kaons misidentified as a π^+) for particles with momenta greater than 2 GeV and less than 2.7 GeV is present. This effect is almost negligible for these data for several reasons. First, the measured positive kaon rate is approximately 3% of the positive pion rate for these data, partly because the intrinsic production rate is smaller, and partly because kaon decays lead to smaller acceptances for pions than kaons. Second, the attenuation and broadening characteristics of these particles are comparable, based both on the HERMES data and on theoretical expectations; thus the distortion of the pion information is small. Finally, even though the discrimination power of the time-of-flight method is decreasing, it still does preferentially remove kaons even at these momenta. Thus the kaon contamination effect on the pion observables is small, e.g., of the order of 0.1% for the hadron attenuation observable.

5.5 Conclusions.

The thesis consisted of the analysis of electron deep inelastic scattering data on three heavy nuclear targets – carbon, iron, and lead – and to compare the positive pions produced from these targets to the same reaction on the light nucleus, deuterium. It was analyzed the data in terms of

five kinematic variables: the 4-momentum transfer, the energy transfer, the transverse momentum, the relative pion energy, and the angle of the reaction plane around the virtual photon direction. In terms of these kinematic variables, it was studied two primary observables: the transverse momentum broadening (equation 4.15), and the hadronic attenuation ratio (equation 4.16). This was a high-precision measurement, and is the world's first measurement of these quantities on these specific nuclei. Preliminary conclusions about the scale of magnitude of the production length for light quarks and the formation lengths of positive pions can be derived from these data.

The results presented in this thesis have been reported at annual conferences at Jlab (from 2005-2008), as well as more than dozen of international conferences. On the base of the results obtained in this thesis new proposal, regarding the same topic, was accepted at PAC30 at Jlab [28], experiment for which will be performed after CEBAF upgrade to 12 GeV.

Following is the list of the main results obtained by the author of this work:

1. First time there was performed high-precision measurement of *transverse momentum broadening* for positively charged pions produced in deep inelastic scattering of electron on nuclear targets of carbon, iron and lead [44][80].
2. There was performed high-precision measurement of *hadronic multiplicity ratio* for positively charged pions produced in deep inelastic scattering of electron on nuclear targets of carbon, iron and lead [44][80].
3. There was observed the “Cronin effect” in the kinematical region of $1 < Q^2 < 2 \text{ GeV}^2$ and $0.1 < x_B < 0.55$ [44].
4. Measured quantities of transverse momentum broadening and hadronic multiplicity ratio give the opportunity to estimate the *production time* and *formation time* of produced positive pions[44].

Bibliography

1. A. Accardi, D. Grunewald, V. Muccifora, and H.J. Pirner, Atomic mass dependence of hadron production in deep inelastic scattering on nuclei. Nucl. Phys., A761:67-91, 2005.
2. A. Accardi, V. Muccifora, H.J. Pirner, Hadron production in deep inelastic lepton nucleus scattering. Nucl. Phys. A720:131-156, 2003.
3. G. Adams, V. Burkett et al., The CLAS Cherenkov Detector. Nucl. Instr. and Meth., A465:414-427, 2001.
4. M.R. Adams et al, Scaled energy (z) distributions of charged hadrons observed in deep inelastic muon scattering at 490-GeV from xenon and deuterium targets. Phys. Rev., D50:1836-1873, 1994.
5. M.R. Adams et al, Perturbative QCD effects observed in 490-GeV deep inelastic muon scattering. Phys. Rev., D48:5057-5066, 1993.
6. S.S. Adler et al, High $p(T)$ charged hadron suppression in Au + Au collisions at $\sqrt{s(NN)} = 200$ -GeV. Phys. Rev., C69:034910, 2004.
7. A. Airapetian et al, The Q^2 dependence of nuclear transparency for exclusive ρ^0 production. Phys. Rev., Lett. 90:052501, 2003.
8. A. Airapetian et al, Quark fragmentation to π^+ , π^0 , K^+ , p and anti- p in the nuclear environment. Phys. Rev., Lett. B577:37, 2003.
9. A. Airapetian et al, Hadron formation in deep-inelastic positron scattering in a nuclear environment. Eur. Phys. J. C20:479-486, 2001.
10. M. Amarian et al, The CLAS Forward Electromagnetic Calorimeter. Nucl. Instr. and Meth., A460:239 – 265, 2001.
11. B. Anderson, G. Gustafson, G. Ingelman and T. Sjostrand, Baryon Production in Lepton - Nucleon Scattering and Diquark Fragmentation. Z. Phys. C13:361, 1982.
12. B. Anderson, G. Gustafson and B. Soderberg, A General Model for Jet Fragmentation. Z. Phys. C20:317, 1983.

13. B. Anderson, S. Mohanty and F. Soderberg, Recent developments in the Lund model. hep-ph/0212122.
14. M. Anghinolfi et al, Response to Cosmic Rays of the Large Angle Electromagnetic Shower Calorimeter of the CLAS Detector. Nucl. Instr. and Meth., A447:424–431, 2000.
15. P.L. Anthony, et al, Bremsstrahlung suppression due to the LPM and dielectric effects in a variety of materials. Phys. Rev. D56:1373-1390, 1997.
16. F. Arleo, Quenching of hadron spectra in dis on nuclear target. Eur. Phys. J., C30:213-221, 2003.
17. X. Artu and G. Mennesier, String model and multiproduction. Nucl. Phys., B70:93-115, 1974.
18. J. Ashman et al, Comparison of forward hadrons produced in muon interactions on nuclear target and deuterium. Z. Phys. C52:1-12, 1991.
19. R. Baier, D. Schiff, B.G. Zakharov, Energy loss in perturbative QCD. Annu. Rev. Nucl. Part. Sci. 50:37-69, 2000.
20. A. Bialas, T. Chmaj, Leptoproduction of hadrons from nuclear targets and fragmentation of quarks into hadrons. Phys. Lett., B133:241-243, 1983.
21. A. Bialas, Attenuation of High Energy Particles Leptoproduced In Nuclear Matter. Acta Phys. Pol. B11:475, 1980.
22. V. Bobel and CLAS software group, The BOS system for CLAS software. November 25 1995.
23. P.E. Bosted, Factorization and Transverse Momentum in SIDIS at JLab. Nucl. Phys. A782:142-149, 2007.
24. J. Botts, et al, CTEQ parton distributions and flavor dependence of sea quarks. Phys. Lett. B304:159-166, 1993.
25. S.J. Brodsky et al, Inelastic Scattering at the Amplitude Level. AIP Conf. Proc. 792:1084-1088, 2005.

26. S. J. Brodsky, Topics in nuclear chromodynamics: color transparency and hadronization in the nucleus. SLAC-PUB-4551:1-68, 1988.
27. W. Brooks, et al, A Large Acceptance Spectrometer for Intermediate-Energy Electromagnetic Nuclear Physics. Nucl. Phys., A663:1077 –1080, 2000.
28. W. Brooks etc, Quark Propagation and Hadron Formation. A CLAS12 Proposal to PAC30, 2007
29. W. Busza, Review of Experimental Data on Hadron-Nucleus Collisions at High-Energies. Acta Phys. Polon., B8:333, 1977.
30. D.S. Carman et al, The Region One Drift Chamber for the CLAS Spectrometer. Nucl. Instr. and Meth., A419:315 – 319, 1998.
31. A. Casher, H. Neuberger, and S. Nussimov, Chromoelectric Flux Tube Model of Particle Production. Phys. Rev D20:179-188, 1978.
32. CLAS Collaboration. The CEBAF Large Acceptance Spectrometer (CLAS). Nucl. Inst. and Meth. A503:513-553, 2003.
33. J.R. Comfort and B.C. Karp, Scattering and Reaction Dynamics for the C-12 + P System. Phys. Rev. C21:2162-2176, 1980.
34. G. Corcella, I.G. Knowles, G. Marchesini, S. Moretti, K. Odagiri, P. Richardson, M.H. Seymour, and B.R. Webber, HERWIG 6: An Event generator for hadron emission reactions with interfering gluons (including supersymmetric processes). JHEP, 0101:010, 2001.
35. J.W. Cronin et al, Production of hadrons with large transverse momentum at 200 GeV, 300 GeV, and 400 GeV. Phys. Rev., D11:3105, 1975.
36. Y.L. Dokshitzer, V.A. Khoze, A.H. Mueller, and S.I. Troyan, Basics of Perturbative QCD. Editions Frontieres, 1991.
37. V. Del Duca, S.J. Brodsky, and P. Hoyer, Space-time structure of deep inelastic lepton-hadron scattering. Phys. Rev. D:931-943, 1992.

38. H. Egiyan, Single π^+ electroproduction in the first and second resonance regions using CLAS. PhD thesis, College of William and Mary, 2001.
39. T. Falter, W. Cassing, K. Gallmeister, and U. Mosel, Hadron attenuation in deep inelastic lepton-nucleus scattering. Phys. Rev. C70:054609, 2004.
40. F. Foster, and G. Hughes, Electroproduction of nuclear resonances, Rept. Prog. Phys. 46:1445-1489, 1983.
41. A. Freyberger. CLAS reconstruction and analysis framework. <http://www.jlab.org/freyberg/recsis.html>
42. J.F. Gunion and G. Bertsch, Hadronization by Color Bremsstrahlung. Phys. Rev., D25:746, 1982.
43. V. Gurjyan. CLAS DAQ system. Private communications.
- 44. H. Hakobyan, W. Brooks, Quark propagation and hadron formation in the nucleus. APS April meeting, H16 2:88, 2007.**
- 45. H. Hakobyan, W. Brooks et al, A Double-Target System for Precision Measurements of Nuclear Medium Effects. NIMA-D-08-00169R1, Nucl. Inst. and Meth. in Phys. Res., A, 2008.**
- 46. H. Hakobyan, The CLAS/EG2 target implementation in GSIM. CLAS-Note 2008-02:1-15, 2008.**
47. F. Halzen and A.D. Martin, Quarks and Leptons. Jhon Willey and sons, 1984.
48. G. Ingelman et al, Lepto 6.5: A Monte Carlo generator for deep inelastic lepton-nucleon scattering. Comput. Phys. Commun. 101:108-134, 1997.
49. R. L. Jaffe, F.E. Close, R.G. Roberts, and G.G. Ross, On the Nuclear Dependence of Electroproduction. Phys. Lett., B134:449, 1984.
50. M.B. Johnson, B.Z. Kopeliovich, and A.V. Tarasov, Broadening of the transverse momentum of protons propagating through a medium. Phys., Rev., C63:63-73, 2001.
51. S. Klein, Suppression of Bremsstrahlung and pair production due to environmental factors. Rev. Mod. Phys. 71:1501-1538, 1999.

52. B.Z. Kopeliovich. Private communication.
53. B.Z. Kopeliovich et al, Nuclear hadronization: within or without?. Nucl. Phys. A740:211-245, 2004.
54. B.Z. Kopeliovich and F. Niedermayer, Color Dynamics in Large P(T) Hadron Production on Nuclei. Sov. J. Nucl. Phys., 42:504, 1985.
55. L.D. Landau, I.Y. Pomeranchuk, Electron cascade process at very high-energies. Dokl. Akad. Nauk SSSR 92:735-738, 1953.
56. W.R. Leo, Techniques for Nuclear and Particle Physics Experiments. Springer-Verlag, 1994.
57. P. Liebing, Can the gluon polarization in the nuclear be extracted from HERMES data on single high - p_T hadrons?. PhD thesis, Desy, Hamburg, June 2004.
58. Mankiewicz et al, PEPSI: A Monte Carlo generator for polarized lepton production. Comput. Phys. Commun. 71:305-318, 1992.
59. P.L. McGaughey, J.C. Peng, and J.M. Moss, High-energy hadron induced dilepton production from nucleons and nuclei. Ann. Rev. Nucl. Part. Sci., 49:217-253, 1999.
60. M.D. Mestayer et al, The CLAS drift chamber system. Nucl. Inst. And Meth. A449:81-111, 2000.
61. A.B. Migdal, Bremsstrahlung and pair production in condensed media at high-energies. Phys. Rev. 103:1811-1820, 1956.
62. F. Niedermayer. Phys. Rev. D 25:3494, 1986.
63. L.S. Osborne et al, Electroproduction of Hadrons from Nuclei. Phys. Rev. Lett., 40:1624, 1978.
64. J.S. Poucher, et. al, High-Energy Single-Arm Inelastic e-p and e-d Scattering at 6-Degrees and 10-Degrees. Phys. Rev. Lett. 32:118, 1974.
65. Program Library Long Writeup W5013 Copyright CERN. Geneva, GEANT, 1993.
66. L.M. Qin et al, Prototype Studies and Design Consideration for the CLAS Region 2 Drift Chambers. Nucl. Instr. and Meth., A411:265 – 274, 1998.

67. J. Schwinger, On gauge invariance and vacuum polarization. Phys. Rev., 82:664-679, 1951.
68. E.V. Shurya, Quark-Gluon Plasma and Hadronic Production of Leptons, Photons and Psions. Phys. Lett., B78:150, 1978.
69. T. Sjostrand et al. Pythia 6.3, Physics and Manual.hep-ph/0308153 LU TP 03-38, 2003.
70. E.S. Smith et al, The Time-of-Flight System for CLAS. Nucl. Instr. and Meth., A443:265–298, 1999.
71. E.S. Smith et al, Calibration of the CLAS TOF system. CLAS-NOTE 1999-011, JLAB, 1999.
72. S. Stepanyan, Simple event builder (SEB) in the framework of RECSIS. CLAS Internal Document, Private Communications, 1999.
73. G. Sterman, et al, Handbook of perturbative QCD: Version 1.0. Rev. Mod. Phys. 67:157-248, 1995.
74. Al. V. Vlassov et al, CLAS Cherenkov detector calibrations. CLAS-NOTE-005, 1999.
75. E. Wang and X.-N. Wang, Jet tomography of dense and nuclear matter. Phys. Rev. Lett. 89:162301, 2002.
76. X.-N. Wang, Discovery of jet quenching and beyond. Nucl. Phys., A750:98-120, 2005
77. A. Majumder and X.-N. Wang, High Pt hadron-hadron correlations. J. Phys. G31:S533-S540, 2005.
78. K.G. Wilson, Confinement of Quarks. Phys. Rev. D10:2445-2459, 1974.
79. E. Wolin, GSIM User's Guide Version CERN 1.0, 1995.
- 80. В. Брукс, А.Л. Акопян, Наблюдение распространения кварка и формирование адрона в ядре на установке CLAS (углеродные данные), Ученые записки ЕГУ, т.2, ст. 57-63, 2008.**

ACKNOWLEDGMENTS

I thank my advisor Will Brooks for his constant leadership, encouragement and support throughout my graduate school years, thanks to whom this thesis became reality. I thank my advisor Alita Danagulyan for her support in Yerevan State University. Thanks to my colleagues Kawtar Hafidi, Lamiaa El Fasi, Maurik Holtrop, Lorenzo Zana, Cathrine Silvester, Taysia Mineeva and everyone in Eg2 experiment group. Thanks to Jefferson laboratory and CLAS collaboration for the unique opportunity they gave me to work on my thesis.

Thanks to my family for their support and love.

Thanks to the entire Armenian community of Newport News working at Jefferson laboratory.

Thanks to Yerevan Physics Institute for giving me the opportunity to defend my PhD thesis.

Thanks to Roland Avagyan, Anahit Balabekyan and Lyudvig Vardanyan for their support.

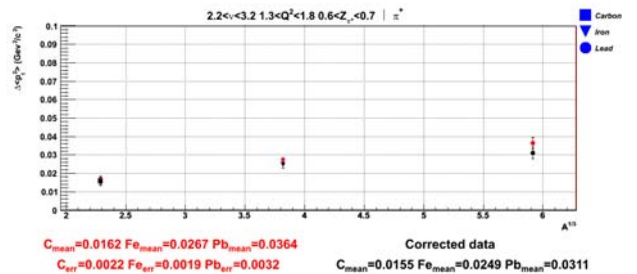
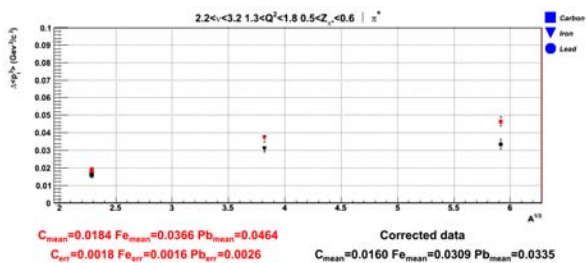
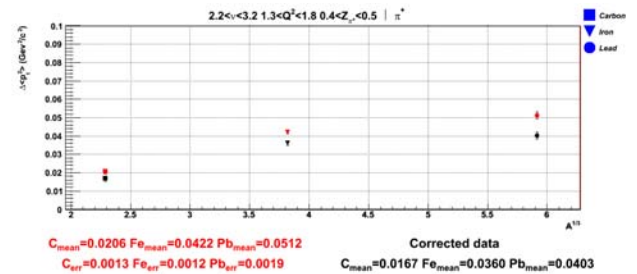
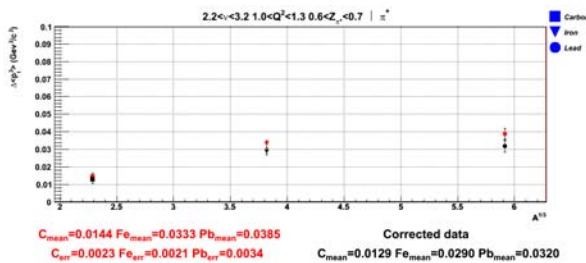
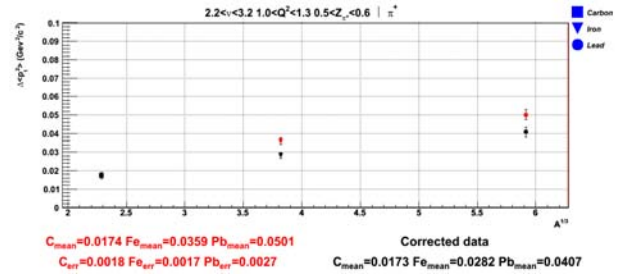
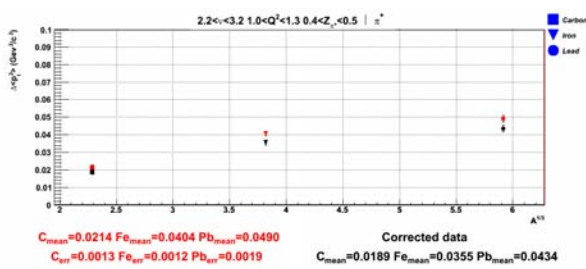
Appendix I

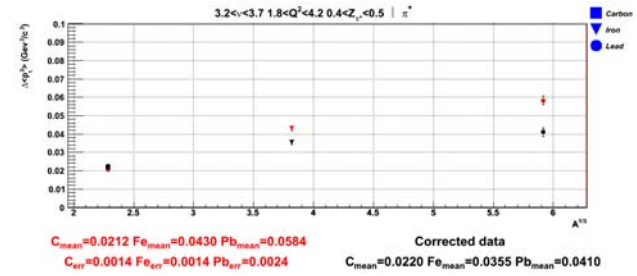
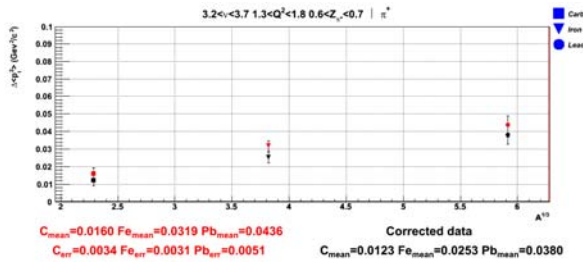
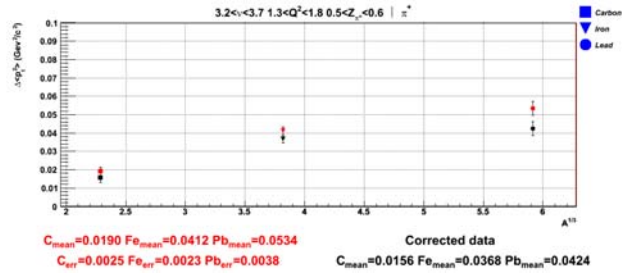
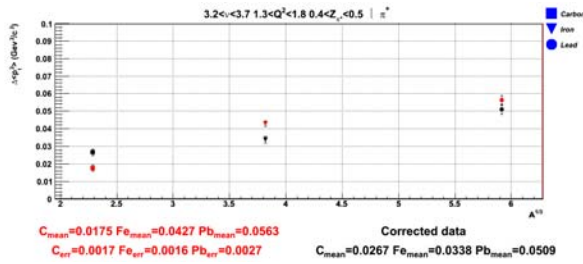
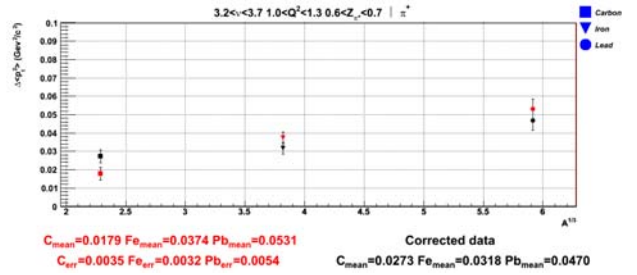
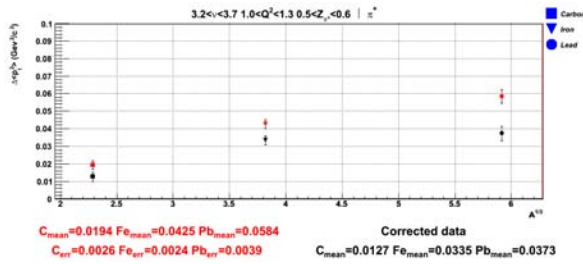
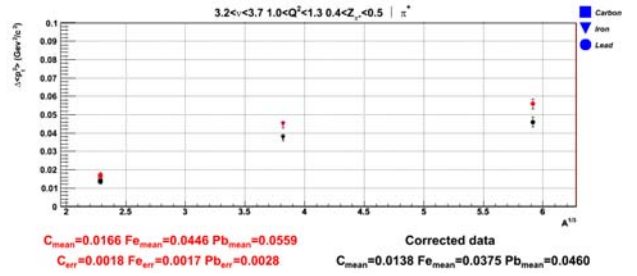
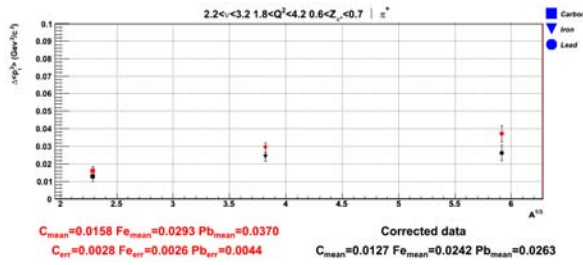
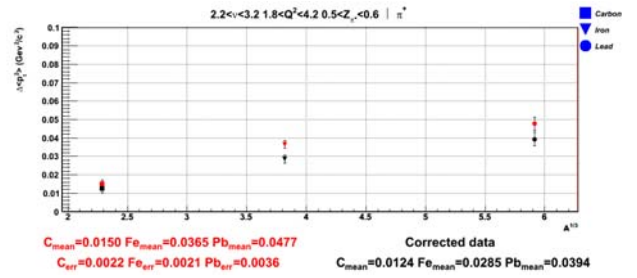
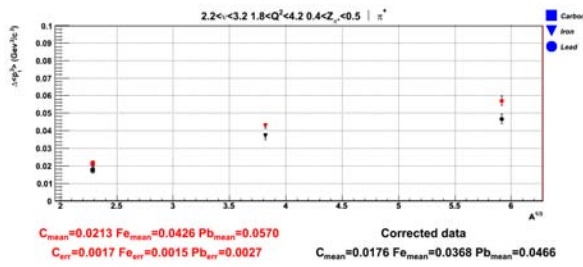
Table A1.

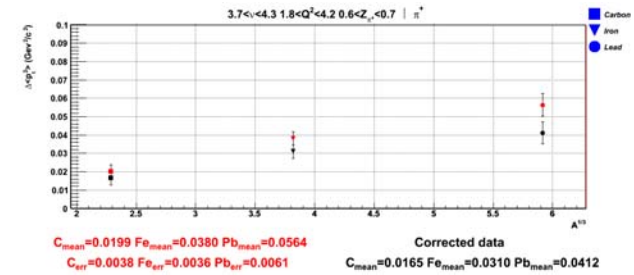
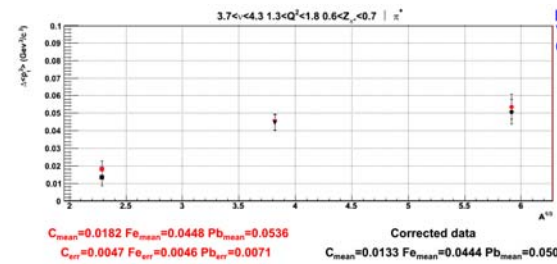
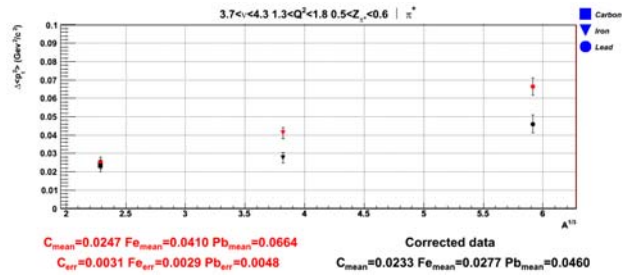
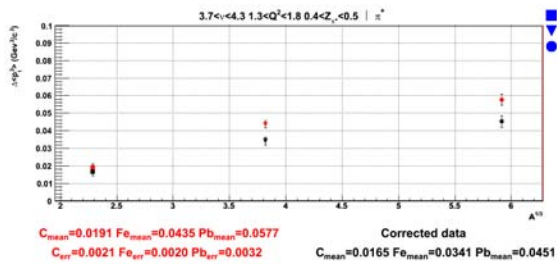
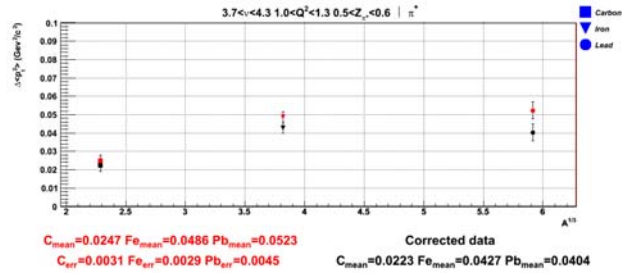
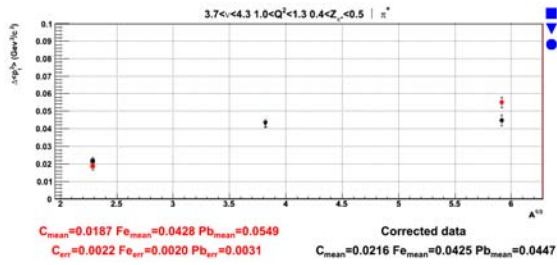
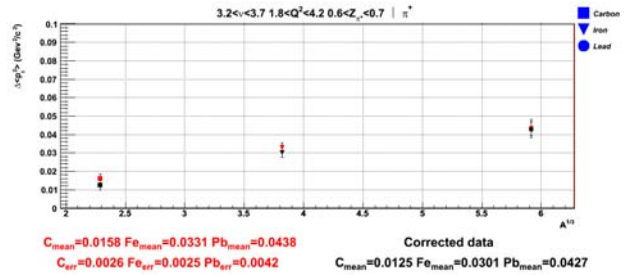
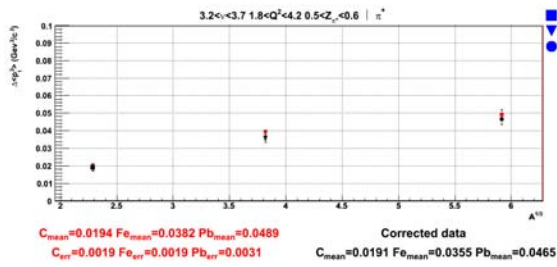
Q^2 range	V range	θ_{π^+} range	χ^2_7	Q^2 range	V range	θ_{π^+} range	χ^2_7
1.00-1.64	2.20-2.62	20-30	44.978	1.00-1.64	2.20-2.62	30-40	12.613
1.00-1.64	2.20-2.62	40-50	33.191	1.00-1.64	2.20-2.62	50-60	6.312
1.00-1.64	2.20-2.62	60-70	7.540	1.00-1.64	2.20-2.62	70-80	4.052
1.00-1.64	2.20-2.62	80-90	10.850	1.00-1.64	2.20-2.62	90-100	17.033
1.00-1.64	2.20-2.62	100-110	13.352	1.00-1.64	2.62-3.04	20-30	43.203
1.00-1.64	2.62-3.04	30-40	25.863	1.00-1.64	2.62-3.04	40-50	29.286
1.00-1.64	2.62-3.04	50-60	23.472	1.00-1.64	2.62-3.04	60-70	11.654
1.00-1.64	2.62-3.04	70-80	5.729	1.00-1.64	2.62-3.04	80-90	8.135
1.00-1.64	2.62-3.04	90-100	12.278	1.00-1.64	2.62-3.04	100-110	7.901
1.00-1.64	3.04-3.46	20-30	9.961	1.00-1.64	3.04-3.46	30-40	20.968
1.00-1.64	3.04-3.46	40-50	26.400	1.00-1.64	3.04-3.46	50-60	4.625
1.00-1.64	3.04-3.46	60-70	11.019	1.00-1.64	3.04-3.46	70-80	2.341
1.00-1.64	3.04-3.46	80-90	8.953	1.00-1.64	3.04-3.46	90-100	23.609
1.00-1.64	3.04-3.46	100-110	9.487	1.00-1.64	3.46-3.88	20-30	8.243
1.00-1.64	3.46-3.88	30-40	8.466	1.00-1.64	3.46-3.88	40-50	11.514
1.00-1.64	3.46-3.88	50-60	4.962	1.00-1.64	3.46-3.88	60-70	2.053
1.00-1.64	3.46-3.88	70-80	8.465	1.00-1.64	3.46-3.88	80-90	4.669
1.00-1.64	3.46-3.88	90-100	16.500	1.00-1.64	3.46-3.88	100-110	2.136
1.00-1.64	3.88-4.30	10-20	14.855	1.00-1.64	3.88-4.30	20-30	41.463
1.00-1.64	3.88-4.30	30-40	60.249	1.00-1.64	3.88-4.30	40-50	10.624
1.00-1.64	3.88-4.30	50-60	11.526	1.00-1.64	3.88-4.30	60-70	20.576
1.00-1.64	3.88-4.30	70-80	6.686	1.00-1.64	3.88-4.30	80-90	16.109
1.00-1.64	3.88-4.30	90-100	17.356	1.00-1.64	3.88-4.30	100-110	12.670
1.64-2.28	2.20-2.62	20-30	8.029	1.64-2.28	2.20-2.62	30-40	12.688
1.64-2.28	2.20-2.62	40-50	2.855	1.64-2.28	2.20-2.62	50-60	5.253
1.64-2.28	2.20-2.62	60-70	3.204	1.64-2.28	2.62-3.04	20-30	39.854
1.64-2.28	2.62-3.04	30-40	9.934	1.64-2.28	2.62-3.04	40-50	6.030
1.64-2.28	2.62-3.04	50-60	8.661	1.64-2.28	2.62-3.04	60-70	9.949
1.64-2.28	2.62-3.04	70-80	6.959	1.64-2.28	2.62-3.04	80-90	9.113
1.64-2.28	2.62-3.04	90-100	25.754	1.64-2.28	2.62-3.04	100-110	2.772
1.64-2.28	3.04-3.46	20-30	28.454	1.64-2.28	3.04-3.46	30-40	11.433
1.64-2.28	3.04-3.46	40-50	7.081	1.64-2.28	3.04-3.46	50-60	23.440
1.64-2.28	3.04-3.46	60-70	5.938	1.64-2.28	3.04-3.46	70-80	4.626
1.64-2.28	3.04-3.46	80-90	4.697	1.64-2.28	3.04-3.46	90-100	5.777
1.64-2.28	3.04-3.46	100-110	1.956	1.64-2.28	3.46-3.88	20-30	5.608
1.64-2.28	3.46-3.88	30-40	8.566	1.64-2.28	3.46-3.88	40-50	7.944
1.64-2.28	3.46-3.88	50-60	14.649	1.64-2.28	3.46-3.88	60-70	8.408
1.64-2.28	3.46-3.88	70-80	3.029	1.64-2.28	3.46-3.88	80-90	6.623
1.64-2.28	3.46-3.88	90-100	7.518	1.64-2.28	3.46-3.88	100-110	7.303
1.64-2.28	3.88-4.30	20-30	12.995	1.64-2.28	3.88-4.30	30-40	27.403
1.64-2.28	3.88-4.30	40-50	13.511	1.64-2.28	3.88-4.30	50-60	14.519
1.64-2.28	3.88-4.30	60-70	7.794	1.64-2.28	3.88-4.30	70-80	2.527
1.64-2.28	3.88-4.30	80-90	1.700	1.64-2.28	3.88-4.30	90-100	3.825
1.64-2.28	3.88-4.30	100-110	4.716	2.28-2.92	2.62-3.04	20-30	18.589
2.28-2.92	2.62-3.04	30-40	6.053	2.28-2.92	2.62-3.04	40-50	12.706
2.28-2.92	2.62-3.04	50-60	9.424	2.28-2.92	2.62-3.04	60-70	1.648
2.28-2.92	2.62-3.04	90-100	0.351	2.28-2.92	3.04-3.46	20-30	35.944
2.28-2.92	3.04-3.46	30-40	14.981	2.28-2.92	3.04-3.46	40-50	11.946
2.28-2.92	3.04-3.46	50-60	5.917	2.28-2.92	3.04-3.46	60-70	12.939
2.28-2.92	3.04-3.46	70-80	0.457	2.28-2.92	3.04-3.46	80-90	0.804
2.28-2.92	3.04-3.46	90-100	5.0363	2.28-2.92	3.04-3.46	100-110	1.328
2.28-2.92	3.46-3.88	20-30	3.077	2.28-2.92	3.46-3.88	30-40	3.995
2.28-2.92	3.46-3.88	40-50	7.303	2.28-2.92	3.46-3.88	50-60	8.042
2.28-2.92	3.46-3.88	60-70	3.869	2.28-2.92	3.46-3.88	70-80	2.988
2.28-2.92	3.46-3.88	80-90	1.262	2.28-2.92	3.46-3.88	90-100	3.140
2.28-2.92	3.46-3.88	100-110	0.071	2.28-2.92	3.88-4.30	20-30	16.191
2.28-2.92	3.88-4.30	30-40	6.404	2.28-2.92	3.88-4.30	40-50	15.980
2.28-2.92	3.88-4.30	50-60	5.326	2.28-2.92	3.88-4.30	60-70	4.473

2.28-2.92	3.88-4.30	70-80	2.406	2.28-2.92	3.88-4.30	80-90	1.532
2.28-2.92	3.88-4.30	90-10	2.553	2.28-2.92	3.88-4.30	100-110	0.116
2.92-3.56	3.04-3.46	20-30	5.356	2.92-3.56	3.04-3.46	30-40	9.202
2.92-3.56	3.04-3.46	40-50	1.595	2.92-3.56	3.04-3.46	50-60	9.404
2.92-3.56	3.04-3.46	60-70	1.599	2.92-3.56	3.04-3.46	70-80	0.117
2.92-3.56	3.46-3.88	20-30	8.274	2.92-3.56	3.46-3.88	30-40	6.704
2.92-3.56	3.46-3.88	40-50	6.946	2.92-3.56	3.46-3.88	50-60	9.782
2.92-3.56	3.46-3.88	60-70	6.360	2.92-3.56	3.46-3.88	70-80	1.178
2.92-3.56	3.46-3.88	90-100	0.402	2.92-3.56	3.88-4.30	10-20	10.383
2.92-3.56	3.88-4.30	20-30	22.364	2.92-3.56	3.88-4.30	30-40	6.850
2.92-3.56	3.88-4.30	40-50	5.186	2.92-3.56	3.88-4.30	50-60	7.402
2.92-3.56	3.88-4.30	60-70	7.051	2.92-3.56	3.88-4.30	80-90	0.644
2.92-3.56	3.88-4.30	90-100	0.246	3.56-4.20	3.46-3.88	10-20	59.346
3.56-4.20	3.46-3.88	20-30	2.695	3.56-4.20	3.46-3.88	30-40	3.645
3.56-4.20	3.46-3.88	40-50	7.608	3.56-4.20	3.46-3.88	50-60	7.226
3.56-4.20	3.46-3.88	60-70	2.900	3.56-4.20	3.88-4.30	10-20	2.011
3.56-4.20	3.88-4.30	20-30	3.044	3.56-4.20	3.88-4.30	30-40	0.889
3.56-4.20	3.88-4.30	40-50	0.001	3.56-4.20	3.88-4.30	50-60	1.463

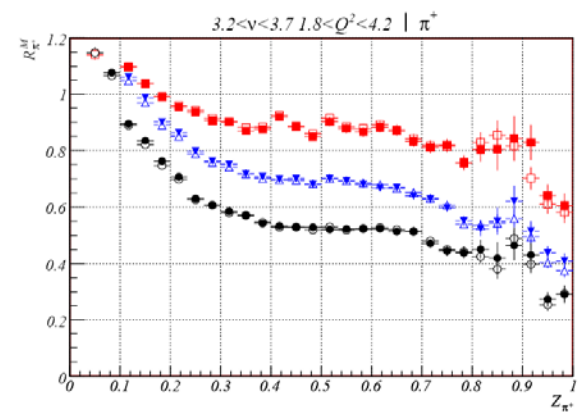
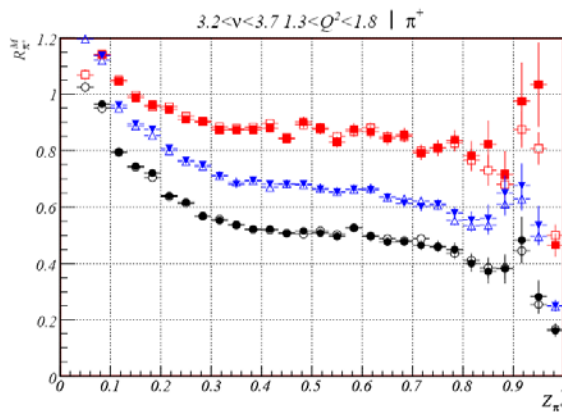
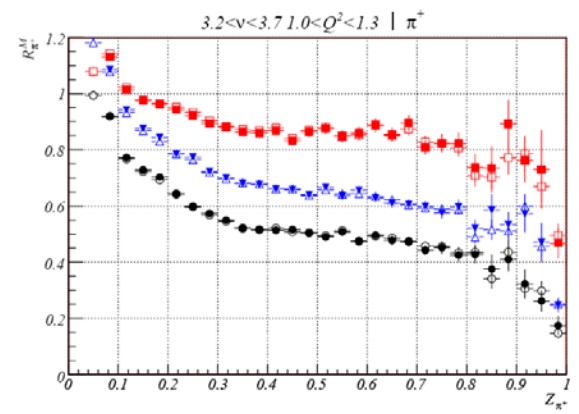
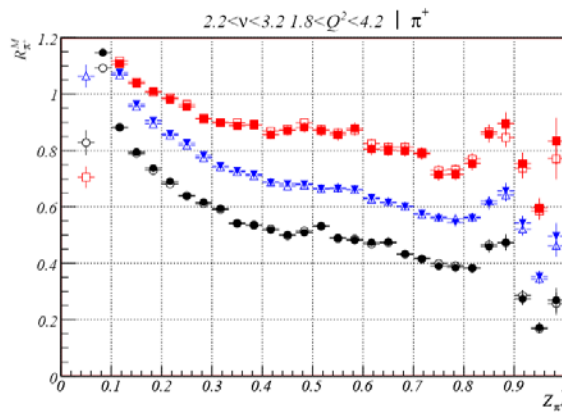
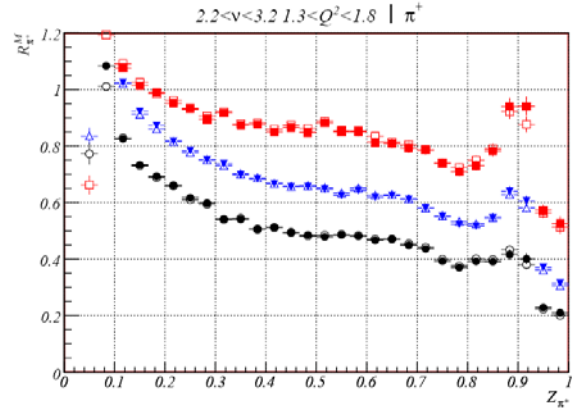
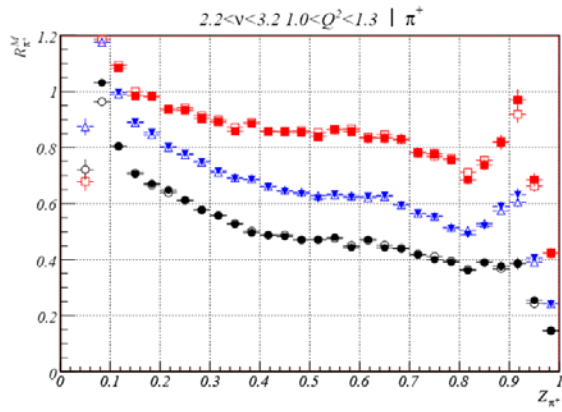
Appendix II







Appendix III



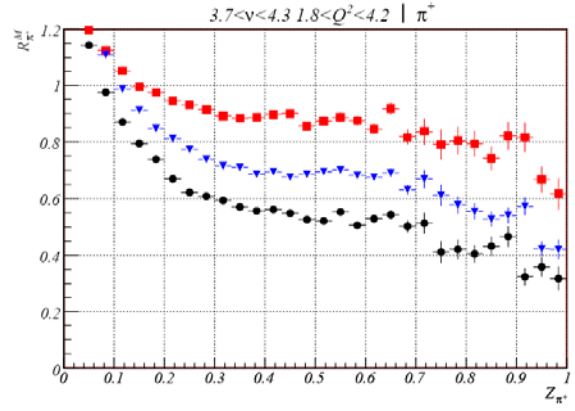
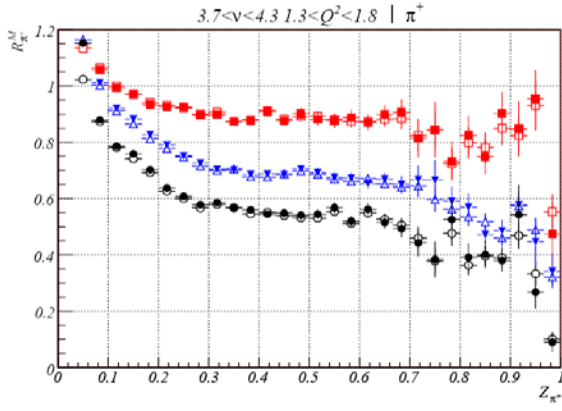


Table A2. Data points for hadronic multiplicity ratio dependence on z_{π^+} for positive pions in different (ν, Q^2) kinematical bins. In the top of each block of the table is presented the corresponding (ν, Q^2) kinematical bin with mean values of the Q^2 and ν distributions. The first column presents the bin number, the second column presents the limits of each z_{π^+} bin, and the following columns present the values of the hadronic multiplicity ratio and the corresponding statistical errors for carbon, iron and lead, respectively.

bin	z_{π^+} range	C	C error	Fe	Fe error	Pb	Pb error
2.2 < ν < 3.2 1 < Q^2 < 1.33							
2	0.033-0.067	1.454	0.0869	1.958	0.09303	1.619	0.09703
3	0.067-0.100	1.256	0.01235	1.267	0.01049	1.032	0.01033
4	0.100-0.133	1.083	0.008446	0.9977	0.006681	0.8053	0.006572
5	0.133-0.167	0.9853	0.007926	0.8919	0.006194	0.7054	0.006062
6	0.167-0.200	0.9809	0.008509	0.854	0.006393	0.6719	0.006267
7	0.200-0.233	0.9377	0.008831	0.8037	0.006542	0.6488	0.006643
8	0.233-0.267	0.9332	0.009612	0.7787	0.006957	0.6106	0.006852
9	0.267-0.300	0.9041	0.0102	0.75	0.007319	0.5763	0.007181
10	0.300-0.333	0.8916	0.01096	0.7164	0.007633	0.5579	0.007642
11	0.333-0.367	0.8578	0.01107	0.6893	0.007757	0.5258	0.007651
12	0.367-0.400	0.8854	0.01212	0.6866	0.008157	0.4955	0.007709
13	0.400-0.433	0.8578	0.0124	0.6594	0.008341	0.4882	0.008154
14	0.433-0.467	0.8547	0.01327	0.6434	0.008746	0.4824	0.008626
15	0.467-0.500	0.8535	0.01418	0.6344	0.00924	0.47	0.009071
16	0.500-0.533	0.8394	0.01487	0.6177	0.009595	0.4704	0.009725
17	0.533-0.567	0.8638	0.01629	0.6336	0.0104	0.48	0.01047
18	0.567-0.600	0.8572	0.01688	0.6226	0.01073	0.4433	0.01041
19	0.600-0.633	0.8313	0.01717	0.6254	0.01127	0.4721	0.01151
20	0.633-0.667	0.8336	0.01792	0.6288	0.01168	0.4422	0.01116
21	0.667-0.700	0.8316	0.01822	0.5942	0.01126	0.4378	0.01155
22	0.700-0.733	0.7826	0.01763	0.5658	0.01104	0.4175	0.01139
23	0.733-0.767	0.7778	0.01793	0.5531	0.01088	0.4	0.01109
24	0.767-0.800	0.7554	0.01743	0.5111	0.0102	0.3907	0.01108
25	0.800-0.833	0.6853	0.01676	0.4893	0.01032	0.3609	0.0112
26	0.833-0.867	0.7383	0.02005	0.5193	0.0121	0.3902	0.01328
27	0.867-0.900	0.8192	0.0272	0.5899	0.01698	0.3772	0.01654
28	0.900-0.933	0.9704	0.03828	0.632	0.02162	0.3861	0.02029

29	0.933-0.967	0.6858	0.02438	0.4067	0.01291	0.2547	0.0134
30	0.967-1.000	0.4211	0.01757	0.2423	0.009265	0.1457	0.009735

2.2 < V < 3.2 1.33 < Q² < 1.76

2	0.033-0.067	1.448	0.08599	1.942	0.09012	1.747	0.1008
3	0.067-0.100	1.26	0.01204	1.308	0.01041	1.084	0.01051
4	0.100-0.133	1.077	0.008303	1.025	0.006711	0.825	0.006647
5	0.133-0.167	1.014	0.008144	0.9225	0.006305	0.733	0.006278
6	0.167-0.200	0.9895	0.008525	0.8726	0.00644	0.6934	0.006444
7	0.200-0.233	0.9518	0.008888	0.817	0.00655	0.6615	0.006684
8	0.233-0.267	0.9307	0.009478	0.7841	0.006868	0.6176	0.006921
9	0.267-0.300	0.8948	0.009997	0.7513	0.007205	0.5983	0.007389
10	0.300-0.333	0.917	0.01108	0.7375	0.007671	0.5416	0.007448
11	0.333-0.367	0.8733	0.01108	0.6978	0.007646	0.5413	0.007784
12	0.367-0.400	0.8766	0.01167	0.6845	0.007904	0.5059	0.007775
13	0.400-0.433	0.8499	0.01201	0.6669	0.008227	0.5127	0.008364
14	0.433-0.467	0.8656	0.0132	0.6555	0.008732	0.4937	0.008714
15	0.467-0.500	0.8483	0.01385	0.6563	0.009306	0.4856	0.009258
16	0.500-0.533	0.8825	0.01526	0.6472	0.009751	0.4786	0.009648
17	0.533-0.567	0.8506	0.01545	0.6253	0.009919	0.486	0.01036
18	0.567-0.600	0.8506	0.01637	0.6434	0.01067	0.4809	0.01084
19	0.600-0.633	0.8134	0.01628	0.6187	0.01066	0.4666	0.01119
20	0.633-0.667	0.8093	0.0169	0.6254	0.0111	0.4713	0.0117
21	0.667-0.700	0.7934	0.01692	0.6115	0.01112	0.4491	0.01148
22	0.700-0.733	0.7857	0.01713	0.5812	0.01078	0.4358	0.0115
23	0.733-0.767	0.74	0.01622	0.5519	0.01039	0.3924	0.01076
24	0.767-0.800	0.7095	0.01608	0.5227	0.01006	0.3698	0.0106
25	0.800-0.833	0.7305	0.01747	0.5171	0.01053	0.3918	0.01171
26	0.833-0.867	0.7827	0.02114	0.5451	0.01247	0.3906	0.01334
27	0.867-0.900	0.9404	0.03124	0.6398	0.0182	0.416	0.01793
28	0.900-0.933	0.9412	0.03383	0.6054	0.01855	0.4008	0.01935
29	0.933-0.967	0.5728	0.02003	0.3708	0.01122	0.229	0.01158
30	0.967-1.000	0.5258	0.02504	0.3143	0.01335	0.2102	0.01452

2.2 < V < 3.2 1.76 < Q² < 4.2

2	0.033-0.067	1.493	0.09517	2.252	0.1107	1.809	0.1133
3	0.067-0.100	1.28	0.01493	1.35	0.01329	1.147	0.0139
4	0.100-0.133	1.107	0.011	1.075	0.009259	0.8827	0.009464
5	0.133-0.167	1.039	0.01089	0.9648	0.008749	0.7947	0.0091
6	0.167-0.200	1.01	0.01132	0.9061	0.008842	0.7375	0.009145
7	0.200-0.233	0.9818	0.01189	0.8595	0.009096	0.6911	0.009395
8	0.233-0.267	0.9548	0.01269	0.8265	0.009588	0.6376	0.009648
9	0.267-0.300	0.913	0.01336	0.7835	0.009969	0.6172	0.01037
10	0.300-0.333	0.8992	0.01417	0.7447	0.01032	0.5944	0.01084
11	0.333-0.367	0.8885	0.01447	0.7283	0.01044	0.5404	0.0104
12	0.367-0.400	0.892	0.01531	0.7161	0.01092	0.5364	0.01091
13	0.400-0.433	0.8563	0.01592	0.6868	0.01127	0.518	0.01143
14	0.433-0.467	0.871	0.01733	0.6824	0.01202	0.5008	0.01197
15	0.467-0.500	0.8821	0.01855	0.6814	0.01271	0.5087	0.01289
16	0.500-0.533	0.8703	0.01952	0.6651	0.01322	0.5316	0.01422
17	0.533-0.567	0.8558	0.0201	0.6655	0.01378	0.4901	0.01409
18	0.567-0.600	0.8783	0.02163	0.6616	0.01422	0.4821	0.0146
19	0.600-0.633	0.8047	0.02072	0.6319	0.01421	0.4743	0.01519
20	0.633-0.667	0.8014	0.02116	0.616	0.01404	0.4769	0.01573
21	0.667-0.700	0.8	0.02154	0.6014	0.01418	0.4332	0.01524
22	0.700-0.733	0.789	0.02177	0.577	0.01395	0.417	0.01479
23	0.733-0.767	0.7147	0.0201	0.5594	0.0136	0.3895	0.01421
24	0.767-0.800	0.7159	0.02082	0.5448	0.01379	0.3839	0.01458
25	0.800-0.833	0.7536	0.02381	0.5606	0.01547	0.3818	0.01611
26	0.833-0.867	0.8582	0.03128	0.6108	0.01927	0.4591	0.02174
27	0.867-0.900	0.895	0.04151	0.6578	0.02676	0.474	0.02826
28	0.900-0.933	0.7535	0.04019	0.5434	0.02546	0.2737	0.02197
29	0.933-0.967	0.5961	0.03507	0.3539	0.01882	0.1726	0.01793
30	0.967-1.000	0.8338	0.08331	0.4962	0.04558	0.2695	0.04248

3.2 < V < 3.73 1 < Q² < 1.33

2	0.033-0.067	1.389	0.02842	1.539	0.02608	1.296	0.02626
3	0.067-0.100	1.131	0.009536	1.086	0.007888	0.9193	0.007928
4	0.100-0.133	1.013	0.008512	0.9428	0.006912	0.7726	0.006818
5	0.133-0.167	0.9762	0.008998	0.8759	0.007053	0.7282	0.007087
6	0.167-0.200	0.9648	0.009901	0.8441	0.007584	0.703	0.007657
7	0.200-0.233	0.9435	0.01078	0.7855	0.007902	0.6439	0.007971
8	0.233-0.267	0.9214	0.01187	0.7736	0.008747	0.5988	0.008451
9	0.267-0.300	0.8932	0.01228	0.7229	0.008808	0.574	0.008773
10	0.300-0.333	0.8802	0.01259	0.6999	0.00895	0.5501	0.008858
11	0.333-0.367	0.8633	0.01355	0.6811	0.009524	0.5206	0.009293
12	0.367-0.400	0.86	0.01479	0.676	0.01038	0.5166	0.01007
13	0.400-0.433	0.8686	0.01632	0.6608	0.01114	0.5134	0.011
14	0.433-0.467	0.8312	0.01682	0.6583	0.01186	0.5163	0.01209
15	0.467-0.500	0.864	0.01931	0.6398	0.01258	0.5033	0.01285
16	0.500-0.533	0.876	0.02081	0.6665	0.01392	0.4898	0.01351
17	0.533-0.567	0.8482	0.02165	0.6362	0.01441	0.5077	0.01478
18	0.567-0.600	0.8595	0.02324	0.6562	0.01552	0.4757	0.01516
19	0.600-0.633	0.8873	0.02553	0.6288	0.01579	0.496	0.01684
20	0.633-0.667	0.8543	0.02561	0.6107	0.01592	0.478	0.01672
21	0.667-0.700	0.8958	0.02834	0.6062	0.01671	0.4729	0.01748
22	0.700-0.733	0.809	0.02642	0.599	0.017	0.4426	0.01714
23	0.733-0.767	0.8234	0.03144	0.5755	0.01895	0.4522	0.02116
24	0.767-0.800	0.8224	0.03937	0.5974	0.02538	0.425	0.02426
25	0.800-0.833	0.7362	0.04871	0.5204	0.02967	0.4278	0.03295
26	0.833-0.867	0.7345	0.07747	0.5853	0.05546	0.3757	0.05145
27	0.867-0.900	0.8922	0.08513	0.5334	0.04496	0.41	0.04193
28	0.900-0.933	0.7627	0.07834	0.5713	0.06433	0.3227	0.05074
29	0.933-0.967	0.7302	0.1397	0.4708	0.069	0.2622	0.03814
30	0.967-1.000	0.4678	0.05434	0.2475	0.02641	0.1745	0.03326

3.2 < V < 3.73 1.33 < Q² < 1.76

2	0.033-0.067	1.358	0.02753	1.542	0.02595	1.337	0.02745
3	0.067-0.100	1.14	0.009459	1.138	0.008197	0.9651	0.008305
4	0.100-0.133	1.045	0.008609	0.9619	0.006903	0.7964	0.00695
5	0.133-0.167	0.9884	0.008902	0.8958	0.007059	0.745	0.007164
6	0.167-0.200	0.9622	0.009544	0.8761	0.007673	0.7205	0.007719
7	0.200-0.233	0.9468	0.01047	0.8075	0.007878	0.6405	0.007802
8	0.233-0.267	0.9112	0.01129	0.7653	0.008327	0.6174	0.008482
9	0.267-0.300	0.9014	0.01206	0.7496	0.008844	0.5674	0.008552
10	0.300-0.333	0.8741	0.01215	0.7104	0.008777	0.5521	0.00872
11	0.333-0.367	0.8739	0.01333	0.6805	0.009193	0.5363	0.009367
12	0.367-0.400	0.8749	0.01452	0.6955	0.01024	0.522	0.009972
13	0.400-0.433	0.8799	0.01589	0.6822	0.01098	0.522	0.01101
14	0.433-0.467	0.8419	0.01627	0.6813	0.01178	0.5067	0.01148
15	0.467-0.500	0.9021	0.01895	0.6821	0.01267	0.5155	0.01263
16	0.500-0.533	0.8778	0.01979	0.664	0.0131	0.5081	0.01326
17	0.533-0.567	0.8309	0.02003	0.6537	0.01381	0.4957	0.0139
18	0.567-0.600	0.8758	0.02213	0.6644	0.01467	0.5268	0.01547
19	0.600-0.633	0.8668	0.02338	0.6611	0.01556	0.4957	0.01594
20	0.633-0.667	0.8435	0.024	0.6356	0.01571	0.4768	0.01624
21	0.667-0.700	0.857	0.02522	0.6139	0.0155	0.4773	0.01677
22	0.700-0.733	0.7918	0.02442	0.6012	0.01586	0.4649	0.01672
23	0.733-0.767	0.8091	0.02825	0.61	0.01845	0.4607	0.01984
24	0.767-0.800	0.8369	0.03692	0.5784	0.0227	0.4497	0.02534
25	0.800-0.833	0.7825	0.05178	0.5545	0.03052	0.4008	0.03094
26	0.833-0.867	0.8225	0.08398	0.5596	0.05064	0.3717	0.04343
27	0.867-0.900	0.716	0.08357	0.6501	0.06114	0.3803	0.05183
28	0.900-0.933	0.9765	0.1363	0.6761	0.07864	0.4832	0.08296
29	0.933-0.967	1.035	0.1496	0.5352	0.06889	0.2819	0.05889
30	0.967-1.000	0.4652	0.04079	0.2508	0.0209	0.1616	0.02244

3.2 < V < 3.73 1.76 < Q² < 4.2

2	0.033-0.067	1.47	0.0273	1.746	0.02707	1.505	0.02841
3	0.067-0.100	1.219	0.00908	1.249	0.008112	1.077	0.008524
4	0.100-0.133	1.096	0.00804	1.061	0.006851	0.8956	0.007182
5	0.133-0.167	1.038	0.008239	0.988	0.006956	0.8355	0.007343
6	0.167-0.200	0.9914	0.008602	0.9025	0.006985	0.7631	0.007467
7	0.200-0.233	0.9544	0.009117	0.8641	0.007384	0.7074	0.007715
8	0.233-0.267	0.9373	0.009927	0.798	0.00754	0.6298	0.007778
9	0.267-0.300	0.9064	0.01023	0.7632	0.007728	0.6075	0.008119
10	0.300-0.333	0.9018	0.01066	0.7515	0.007935	0.585	0.0082
11	0.333-0.367	0.8706	0.01116	0.717	0.008272	0.5694	0.008728
12	0.367-0.400	0.8765	0.01222	0.7081	0.008919	0.542	0.009157
13	0.400-0.433	0.9202	0.01377	0.699	0.009491	0.5334	0.009854
14	0.433-0.467	0.8874	0.0143	0.701	0.01024	0.5286	0.01052
15	0.467-0.500	0.8501	0.01463	0.6807	0.01054	0.5282	0.01121
16	0.500-0.533	0.9031	0.01633	0.7006	0.01141	0.5205	0.01161
17	0.533-0.567	0.8782	0.01683	0.6931	0.01205	0.5224	0.01249
18	0.567-0.600	0.8664	0.01755	0.6804	0.01232	0.522	0.01323
19	0.600-0.633	0.883	0.01894	0.6678	0.01252	0.5232	0.01394
20	0.633-0.667	0.8735	0.0196	0.6687	0.01339	0.5129	0.0144
21	0.667-0.700	0.833	0.01972	0.6397	0.0133	0.5141	0.01541
22	0.700-0.733	0.8123	0.02007	0.6276	0.0136	0.471	0.01479
23	0.733-0.767	0.8194	0.02315	0.5972	0.01484	0.4444	0.01654
24	0.767-0.800	0.7573	0.02765	0.5509	0.0183	0.4375	0.02092
25	0.800-0.833	0.8043	0.04334	0.5239	0.02603	0.4502	0.03318
26	0.833-0.867	0.805	0.07531	0.5497	0.04835	0.4191	0.0572
27	0.867-0.900	0.843	0.08065	0.6208	0.0544	0.4645	0.05361
28	0.900-0.933	0.8299	0.06253	0.5151	0.03414	0.43	0.04311
29	0.933-0.967	0.6408	0.03908	0.4374	0.02403	0.2723	0.02552
30	0.967-1.000	0.6044	0.04438	0.4088	0.02818	0.2896	0.03076

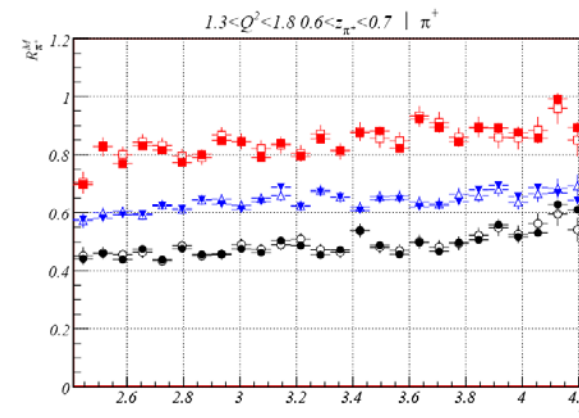
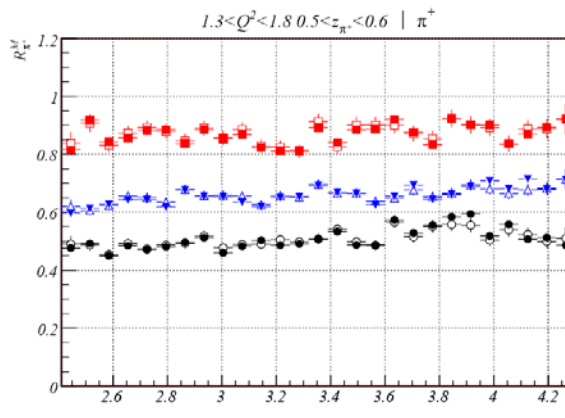
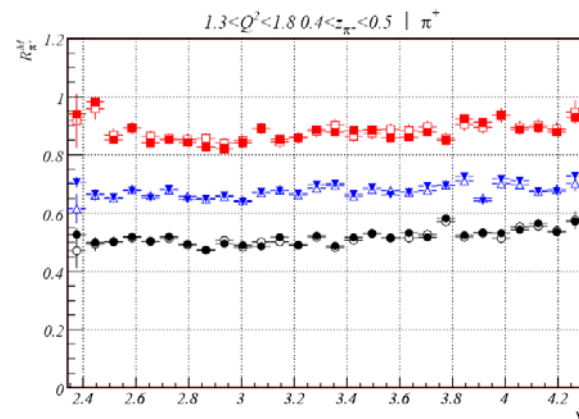
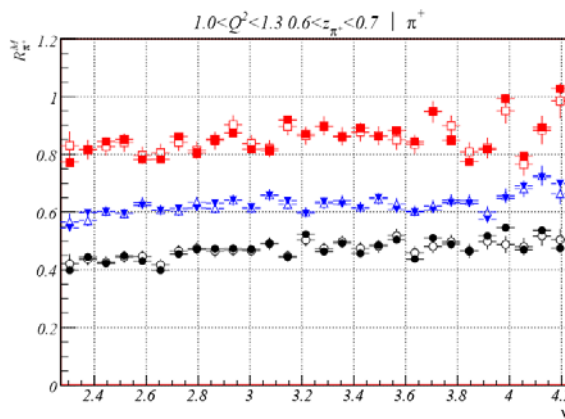
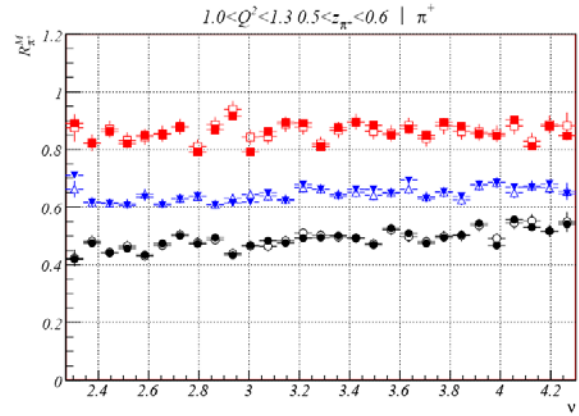
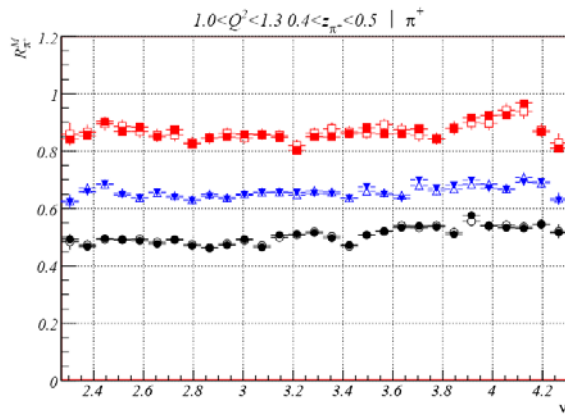
3.73 < V < 4.3 1.33 < Q² < 1.76

2	0.033-0.067	1.248	0.01549	1.318	0.01422	1.153	0.01484
3	0.067-0.100	1.057	0.007864	1.012	0.006726	0.8795	0.006935
4	0.100-0.133	0.9931	0.007911	0.9206	0.006556	0.7858	0.006728
5	0.133-0.167	0.9725	0.008706	0.8828	0.007112	0.759	0.007345
6	0.167-0.200	0.9333	0.009472	0.8268	0.007559	0.7026	0.007869
7	0.200-0.233	0.9253	0.01069	0.7908	0.008274	0.6374	0.008284
8	0.233-0.267	0.9249	0.01164	0.7516	0.008551	0.6076	0.00867
9	0.267-0.300	0.8975	0.01206	0.7267	0.008879	0.5783	0.008926
10	0.300-0.333	0.8984	0.01342	0.7045	0.009559	0.586	0.01007
11	0.333-0.367	0.8737	0.01449	0.7017	0.01054	0.5655	0.01077
12	0.367-0.400	0.8771	0.01598	0.6858	0.01127	0.5599	0.01195
13	0.400-0.433	0.9096	0.0178	0.6871	0.01225	0.5447	0.01264
14	0.433-0.467	0.8768	0.01903	0.6853	0.0134	0.5485	0.0141
15	0.467-0.500	0.9013	0.02109	0.7061	0.01481	0.5409	0.01527
16	0.500-0.533	0.8809	0.02198	0.6925	0.01572	0.5445	0.01661
17	0.533-0.567	0.8771	0.02439	0.6754	0.01649	0.5675	0.01862
18	0.567-0.600	0.8885	0.02646	0.6732	0.0181	0.5204	0.01894
19	0.600-0.633	0.8704	0.02812	0.6531	0.01883	0.5621	0.02193
20	0.633-0.667	0.8991	0.03284	0.6688	0.02188	0.5151	0.02199
21	0.667-0.700	0.9066	0.04743	0.6503	0.03024	0.4925	0.02999
22	0.700-0.733	0.8151	0.06924	0.6677	0.05012	0.4424	0.04836
23	0.733-0.767	0.8445	0.09913	0.6654	0.07129	0.3836	0.0634
24	0.767-0.800	0.7321	0.07063	0.5909	0.05193	0.5254	0.07205
25	0.800-0.833	0.8247	0.07048	0.5693	0.04799	0.3914	0.04945
26	0.833-0.867	0.748	0.06167	0.4722	0.03412	0.4016	0.04892
27	0.867-0.900	0.902	0.07653	0.4856	0.0395	0.3804	0.04049
28	0.900-0.933	0.8476	0.09847	0.5777	0.04718	0.5428	0.1066
29	0.933-0.967	0.9541	0.1037	0.4468	0.08521	0.2674	0.05825
30	0.967-1.000	0.4742	0.1117	0.3417	0.06099	0.08915	0.0333

3.73 < V < 4.3 1.76 < Q² < 4.2

2	0.033-0.067	1.323	0.01545	1.467	0.01493	1.307	0.01595
3	0.067-0.100	1.117	0.007654	1.127	0.006896	0.9889	0.007276
4	0.100-0.133	1.051	0.007687	1.005	0.006543	0.888	0.007097
5	0.133-0.167	1.001	0.00811	0.9423	0.006859	0.8283	0.007437
6	0.167-0.200	0.9765	0.008816	0.8662	0.007045	0.7551	0.007659
7	0.200-0.233	0.9473	0.009614	0.8217	0.007508	0.6791	0.007921
8	0.233-0.267	0.9299	0.01019	0.7831	0.007765	0.6334	0.008091
9	0.267-0.300	0.9122	0.01047	0.7456	0.007836	0.6187	0.008399
10	0.300-0.333	0.8823	0.01123	0.7176	0.008342	0.601	0.009086
11	0.333-0.367	0.8819	0.01237	0.7073	0.009038	0.5734	0.009646
12	0.367-0.400	0.8881	0.01365	0.6918	0.009705	0.5575	0.01035
13	0.400-0.433	0.8931	0.01497	0.7023	0.01064	0.5731	0.01159
14	0.433-0.467	0.8906	0.01604	0.6745	0.01102	0.5456	0.01195
15	0.467-0.500	0.856	0.01654	0.7009	0.01233	0.5289	0.01262
16	0.500-0.533	0.8791	0.01826	0.713	0.01332	0.5385	0.01401
17	0.533-0.567	0.8796	0.01963	0.7046	0.01418	0.5603	0.0154
18	0.567-0.600	0.8781	0.02077	0.6757	0.01454	0.5097	0.01546
19	0.600-0.633	0.8458	0.02147	0.665	0.01513	0.5277	0.01679
20	0.633-0.667	0.9183	0.02596	0.699	0.01796	0.5424	0.01967
21	0.667-0.700	0.8336	0.03123	0.6356	0.02133	0.5058	0.0241
22	0.700-0.733	0.8432	0.0544	0.6713	0.03898	0.5117	0.04265
23	0.733-0.767	0.8987	0.07582	0.638	0.04902	0.4472	0.05325
24	0.767-0.800	0.8085	0.05865	0.6422	0.04448	0.4441	0.04742
25	0.800-0.833	0.8309	0.06136	0.5599	0.03607	0.4246	0.04106
26	0.833-0.867	0.7263	0.05225	0.557	0.04018	0.4302	0.04114
27	0.867-0.900	0.8575	0.07888	0.5299	0.03933	0.4264	0.03791
28	0.900-0.933	0.8131	0.09897	0.6152	0.06554	0.3485	0.06316
29	0.933-0.967	0.5827	0.05839	0.4612	0.04542	0.353	0.05803
30	0.967-1.000	0.6145	0.08225	0.4297	0.05031	0.3408	0.07194

Appendix IV



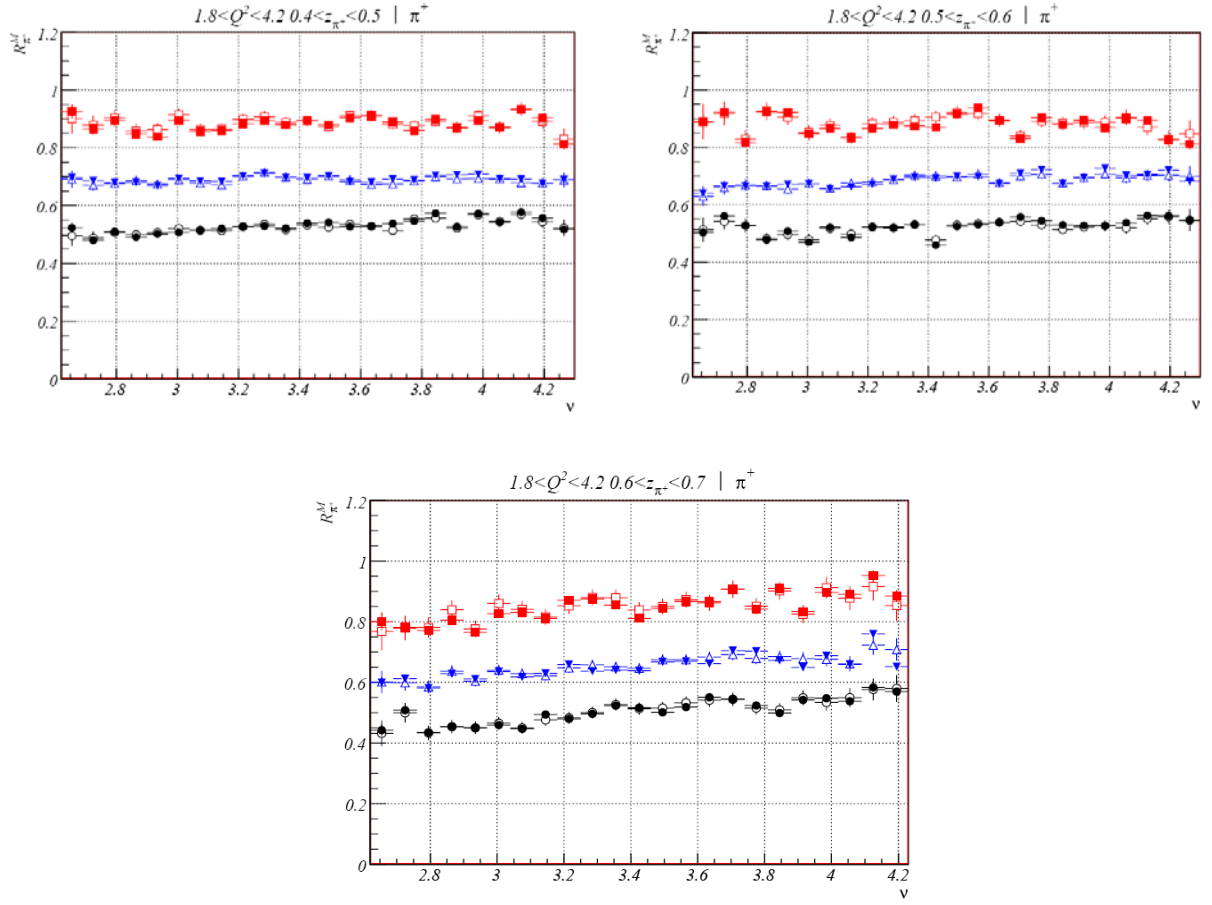


Table A3. Data for the hadronic multiplicity ratio dependence on ν for positive pions in different (Q^2, z_{π^+}) kinematical bins. In the top of each block of the table is presented the corresponding (Q^2, z_{π^+}) kinematical bin with mean values of the Q^2 and z_{π^+} distributions. The first column presents the bin number of the ν distributions, the second column presents the limits of each ν bin, and the following columns present the hadronic multiplicity ratio's values and statistical errors for carbon, iron and lead.

bin	ν range	C	C error	Fe	Fe error	Pb	Pb error
$1 < Q^2 < 1.33$ $0.4 < z_{\pi^+} < 0.5$							
1	2.20-2.27	1.15	0.01708	0.9466	0.01005	0.6906	0.01086
2	2.27-2.34	0.8415	0.007698	0.6215	0.004498	0.4925	0.005307
3	2.34-2.41	0.8541	0.006698	0.6582	0.004061	0.4669	0.004478
4	2.41-2.48	0.9033	0.007302	0.6858	0.004373	0.4954	0.004751
5	2.48-2.55	0.8691	0.007086	0.6468	0.004186	0.49	0.004785
6	2.55-2.62	0.8831	0.007263	0.6368	0.004151	0.487	0.004785
7	2.62-2.69	0.8499	0.00711	0.6568	0.004321	0.4764	0.004756
8	2.69-2.76	0.8742	0.007304	0.6384	0.004292	0.4918	0.004979
9	2.76-2.83	0.825	0.006916	0.6278	0.004213	0.4698	0.004779
10	2.83-2.90	0.8465	0.007156	0.6424	0.004334	0.4614	0.004684

11	2.90-2.97	0.8498	0.007251	0.6336	0.004343	0.4718	0.004799
12	2.97-3.04	0.8594	0.007393	0.6476	0.004535	0.4929	0.005015
13	3.04-3.11	0.8575	0.007309	0.6551	0.00455	0.4644	0.004808
14	3.11-3.18	0.8486	0.007466	0.6553	0.004677	0.508	0.005249
15	3.18-3.25	0.8039	0.007164	0.6554	0.004787	0.5114	0.00534
16	3.25-3.32	0.8508	0.007741	0.6526	0.004919	0.5144	0.005591
17	3.32-3.39	0.8493	0.007939	0.6511	0.004885	0.4964	0.005403
18	3.39-3.46	0.861	0.008038	0.6357	0.00489	0.4726	0.005369
19	3.46-3.53	0.8806	0.008372	0.6756	0.005225	0.5084	0.00579
20	3.53-3.60	0.8611	0.008283	0.6494	0.005185	0.5217	0.005967
21	3.60-3.67	0.8619	0.008491	0.6342	0.005157	0.5336	0.006135
22	3.67-3.74	0.8772	0.008801	0.6993	0.005711	0.5394	0.006342
23	3.74-3.81	0.8422	0.008743	0.67	0.005613	0.5354	0.006497
24	3.81-3.88	0.8798	0.008972	0.6801	0.005718	0.5098	0.006233
25	3.88-3.95	0.9172	0.00972	0.6983	0.006031	0.5764	0.00701
26	3.95-4.02	0.9244	0.009617	0.6699	0.005903	0.5405	0.006885
27	4.02-4.09	0.9252	0.009808	0.6667	0.005856	0.5333	0.006695
28	4.09-4.16	0.9673	0.01027	0.6908	0.006135	0.5304	0.00676
29	4.16-4.23	0.8669	0.009121	0.6925	0.006242	0.5445	0.007002
30	4.23-4.30	0.8099	0.01272	0.6278	0.008414	0.5158	0.009696

$1 < Q^2 < 1.33$ $0.5 < z_{\pi^+} < 0.6$

1	2.20-2.27	1.127	0.02006	0.3868	0.005807	0.6776	0.01275
2	2.27-2.34	0.8898	0.009711	0.7113	0.005934	0.4201	0.00573
3	2.34-2.41	0.8224	0.007862	0.6173	0.004732	0.475	0.005452
4	2.41-2.48	0.8611	0.008716	0.6125	0.004855	0.4414	0.005334
5	2.48-2.55	0.8207	0.008271	0.6062	0.004886	0.4565	0.005579
6	2.55-2.62	0.8496	0.008746	0.6349	0.005238	0.4353	0.005461
7	2.62-2.69	0.8518	0.008764	0.6075	0.005045	0.4743	0.005902
8	2.69-2.76	0.8765	0.009116	0.6284	0.005269	0.5005	0.006142
9	2.76-2.83	0.7915	0.008445	0.6382	0.00535	0.4719	0.006006
10	2.83-2.90	0.8687	0.009281	0.6088	0.005221	0.4945	0.006214
11	2.90-2.97	0.9165	0.009817	0.6141	0.005392	0.4338	0.005858
12	2.97-3.04	0.7919	0.00872	0.6186	0.005454	0.4682	0.006066
13	3.04-3.11	0.8612	0.009452	0.6488	0.005816	0.4834	0.006407
14	3.11-3.18	0.8944	0.009802	0.6225	0.00554	0.4757	0.006313
15	3.18-3.25	0.8914	0.01007	0.6782	0.006282	0.4922	0.006678
16	3.25-3.32	0.8107	0.009349	0.6623	0.006173	0.494	0.006796
17	3.32-3.39	0.8757	0.01035	0.6378	0.006161	0.5019	0.006938
18	3.39-3.46	0.8935	0.01052	0.6619	0.006379	0.4929	0.00701
19	3.46-3.53	0.8833	0.01067	0.6616	0.006451	0.4686	0.006892
20	3.53-3.60	0.8503	0.01026	0.6477	0.006418	0.5275	0.00757
21	3.60-3.67	0.8706	0.01066	0.6932	0.006983	0.5098	0.007477
22	3.67-3.74	0.8488	0.01062	0.6297	0.006498	0.4742	0.007175
23	3.74-3.81	0.894	0.01117	0.6534	0.006872	0.4938	0.007657
24	3.81-3.88	0.8797	0.01118	0.6376	0.00672	0.5038	0.007654
25	3.88-3.95	0.8529	0.01097	0.6784	0.007065	0.5445	0.008258
26	3.95-4.02	0.8477	0.01082	0.6845	0.007297	0.4676	0.007454
27	4.02-4.09	0.9028	0.01171	0.669	0.007417	0.5569	0.008604
28	4.09-4.16	0.8111	0.01056	0.6691	0.007332	0.5304	0.008386
29	4.16-4.23	0.8803	0.01164	0.6808	0.007702	0.5172	0.008296
30	4.23-4.30	0.8479	0.01664	0.6461	0.01056	0.5413	0.01218

$1 < Q^2 < 1.33$ $0.6 < z_{\pi^+} < 0.7$

1	2.20-2.27	0.8021	0.01636	0.5554	0.008319	0.5723	0.01332
2	2.27-2.34	0.773	0.009311	0.5449	0.005375	0.3985	0.006307
3	2.34-2.41	0.8151	0.0091	0.5981	0.005235	0.4446	0.006106
4	2.41-2.48	0.8442	0.009566	0.6016	0.00555	0.4227	0.006003
5	2.48-2.55	0.8513	0.009969	0.596	0.005628	0.4491	0.006368
6	2.55-2.62	0.7826	0.009253	0.6234	0.005983	0.4306	0.00633
7	2.62-2.69	0.7831	0.009775	0.606	0.005945	0.3988	0.006284
8	2.69-2.76	0.8609	0.01045	0.6135	0.006039	0.4555	0.006846
9	2.76-2.83	0.8049	0.01029	0.6142	0.006322	0.4713	0.007231

10	2.83-2.90	0.8514	0.01093	0.6311	0.006568	0.4736	0.00741
11	2.90-2.97	0.8745	0.01169	0.6424	0.006875	0.4742	0.007409
12	2.97-3.04	0.8173	0.01079	0.6173	0.006707	0.4715	0.007407
13	3.04-3.11	0.8132	0.01096	0.6578	0.007112	0.4918	0.007872
14	3.11-3.18	0.919	0.01257	0.6394	0.007064	0.4446	0.007425
15	3.18-3.25	0.8708	0.01205	0.595	0.006811	0.5235	0.008468
16	3.25-3.32	0.8969	0.01271	0.6362	0.007366	0.4638	0.008068
17	3.32-3.39	0.8603	0.01241	0.6272	0.007521	0.4918	0.008353
18	3.39-3.46	0.8912	0.01304	0.6141	0.007342	0.4574	0.008179
19	3.46-3.53	0.8617	0.01272	0.6499	0.008063	0.4856	0.008722
20	3.53-3.60	0.882	0.01329	0.6092	0.007521	0.5035	0.009124
21	3.60-3.67	0.8438	0.01333	0.6002	0.00773	0.4378	0.0083
22	3.67-3.74	0.9492	0.01481	0.6073	0.007763	0.5101	0.009556
23	3.74-3.81	0.8482	0.01296	0.6324	0.008015	0.4886	0.009237
24	3.81-3.88	0.7743	0.01217	0.6296	0.008166	0.4669	0.009374
25	3.88-3.95	0.8171	0.01305	0.5753	0.00777	0.5178	0.01008
26	3.95-4.02	0.9933	0.01597	0.6479	0.008596	0.5461	0.01054
27	4.02-4.09	0.795	0.01295	0.6904	0.009496	0.4694	0.009425
28	4.09-4.16	0.8943	0.01522	0.7207	0.01033	0.5367	0.01092
29	4.16-4.23	1.027	0.0182	0.6997	0.01076	0.4748	0.01045
30	4.23-4.30	0.8454	0.02233	0.6489	0.01336	0.6415	0.01859

$1.33 < Q^2 < 1.76$ $0.4 < z_{\pi^+} < 0.5$

3	2.34-2.41	0.9396	0.03276	0.7054	0.01857	0.5262	0.02143
4	2.41-2.48	0.9813	0.01473	0.666	0.007871	0.4992	0.008954
5	2.48-2.55	0.8508	0.01019	0.6541	0.006156	0.5013	0.006987
6	2.55-2.62	0.8913	0.009272	0.6778	0.005605	0.5195	0.006362
7	2.62-2.69	0.8405	0.008786	0.6524	0.005367	0.5031	0.006289
8	2.69-2.76	0.851	0.009004	0.682	0.00567	0.5201	0.006455
9	2.76-2.83	0.8418	0.008782	0.6468	0.005405	0.4944	0.006158
10	2.83-2.90	0.8266	0.008671	0.6497	0.005411	0.4733	0.005938
11	2.90-2.97	0.8209	0.00873	0.6612	0.005583	0.4956	0.006214
12	2.97-3.04	0.8409	0.008942	0.6389	0.005471	0.4899	0.006255
13	3.04-3.11	0.8904	0.009424	0.6726	0.005719	0.4865	0.006261
14	3.11-3.18	0.8529	0.009144	0.6782	0.005869	0.5175	0.006647
15	3.18-3.25	0.8604	0.009281	0.6676	0.00589	0.4914	0.006454
16	3.25-3.32	0.8859	0.009682	0.6972	0.006147	0.5224	0.006819
17	3.32-3.39	0.8775	0.009768	0.7011	0.006253	0.488	0.006551
18	3.39-3.46	0.8824	0.009831	0.6646	0.006059	0.5168	0.0069
19	3.46-3.53	0.8851	0.009977	0.688	0.006328	0.5309	0.007163
20	3.53-3.60	0.8575	0.009839	0.662	0.006141	0.5146	0.007049
21	3.60-3.67	0.8593	0.009806	0.6716	0.006358	0.532	0.007311
22	3.67-3.74	0.8776	0.01022	0.6933	0.006537	0.517	0.007312
23	3.74-3.81	0.8493	0.009859	0.6961	0.006633	0.5826	0.008059
24	3.81-3.88	0.9239	0.01106	0.7253	0.007085	0.5242	0.007594
25	3.88-3.95	0.9111	0.01081	0.6416	0.006448	0.5331	0.007838
26	3.95-4.02	0.9359	0.01115	0.7169	0.007215	0.5312	0.007856
27	4.02-4.09	0.886	0.01054	0.7112	0.007149	0.5425	0.007973
28	4.09-4.16	0.8927	0.01075	0.6756	0.006923	0.5653	0.008329
29	4.16-4.23	0.8781	0.01053	0.6756	0.006951	0.5348	0.007967
30	4.23-4.30	0.9278	0.0167	0.7275	0.01115	0.5712	0.01252

$1.33 < Q^2 < 1.76$ $0.5 < z_{\pi^+} < 0.6$

3	2.34-2.41	1.056	0.04159	0.7023	0.02189	0.4839	0.02327
4	2.41-2.48	0.8155	0.01496	0.5969	0.008737	0.4758	0.01048
5	2.48-2.55	0.9175	0.01296	0.6139	0.006981	0.4923	0.008364
6	2.55-2.62	0.8439	0.01073	0.6281	0.00635	0.4497	0.006976
7	2.62-2.69	0.8565	0.01091	0.643	0.006502	0.4844	0.007345
8	2.69-2.76	0.8818	0.01149	0.6432	0.006644	0.4709	0.007476
9	2.76-2.83	0.8854	0.01149	0.6191	0.006547	0.4802	0.007475
10	2.83-2.90	0.8369	0.01103	0.6765	0.007072	0.4965	0.007684
11	2.90-2.97	0.8851	0.01166	0.6557	0.006939	0.5124	0.007986
12	2.97-3.04	0.8548	0.01147	0.6543	0.007056	0.4597	0.007374

13	3.04-3.11	0.8684	0.01152	0.6345	0.006854	0.4821	0.007716
14	3.11-3.18	0.8229	0.01143	0.6203	0.006954	0.5034	0.008128
15	3.18-3.25	0.811	0.01115	0.651	0.007206	0.4862	0.008135
16	3.25-3.32	0.8135	0.01134	0.6535	0.007393	0.4906	0.008366
17	3.32-3.39	0.892	0.01242	0.6923	0.007764	0.507	0.008497
18	3.39-3.46	0.8417	0.01181	0.6679	0.007576	0.5332	0.008715
19	3.46-3.53	0.8842	0.01272	0.6651	0.007699	0.4867	0.008472
20	3.53-3.60	0.8872	0.01282	0.6257	0.007442	0.4867	0.00858
21	3.60-3.67	0.9203	0.01343	0.6555	0.007886	0.5735	0.00985
22	3.67-3.74	0.8766	0.01272	0.6932	0.00848	0.5289	0.009385
23	3.74-3.81	0.8337	0.01238	0.6453	0.008014	0.5558	0.009827
24	3.81-3.88	0.9225	0.01371	0.6619	0.008161	0.5837	0.01039
25	3.88-3.95	0.9024	0.01335	0.6889	0.00866	0.5935	0.01048
26	3.95-4.02	0.9007	0.01355	0.7084	0.008735	0.5188	0.009592
27	4.02-4.09	0.8357	0.01267	0.6809	0.008706	0.5578	0.01007
28	4.09-4.16	0.8705	0.01301	0.7156	0.009302	0.5071	0.009441
29	4.16-4.23	0.8928	0.01363	0.6792	0.008889	0.5132	0.009696
30	4.23-4.30	0.9212	0.02101	0.7125	0.01384	0.4859	0.01375

$1.33 < Q^2 < 1.76$ $0.6 < z_{\pi^+} < 0.7$

3	2.34-2.41	0.589	0.02636	0.5574	0.0188	0.4545	0.02221
4	2.41-2.48	0.6965	0.01478	0.5764	0.009393	0.4411	0.01135
5	2.48-2.55	0.8289	0.01341	0.5799	0.007418	0.4589	0.008846
6	2.55-2.62	0.7684	0.01117	0.5926	0.006813	0.4382	0.007809
7	2.62-2.69	0.8301	0.01221	0.5955	0.007041	0.4751	0.008325
8	2.69-2.76	0.8151	0.01209	0.6242	0.007388	0.4378	0.007997
9	2.76-2.83	0.7732	0.0116	0.6139	0.007382	0.4762	0.008543
10	2.83-2.90	0.8011	0.01266	0.6455	0.007934	0.4553	0.008525
11	2.90-2.97	0.8478	0.01335	0.6292	0.008017	0.4555	0.008986
12	2.97-3.04	0.8437	0.01337	0.6112	0.00791	0.4756	0.009359
13	3.04-3.11	0.7904	0.01298	0.6385	0.008464	0.4621	0.009215
14	3.11-3.18	0.8375	0.01386	0.688	0.009283	0.5037	0.01015
15	3.18-3.25	0.7937	0.01338	0.6214	0.008407	0.4868	0.009772
16	3.25-3.32	0.8541	0.01464	0.6716	0.009339	0.4538	0.009794
17	3.32-3.39	0.8152	0.01411	0.6546	0.009252	0.4723	0.01009
18	3.39-3.46	0.8743	0.01544	0.6078	0.008886	0.5386	0.011
19	3.46-3.53	0.8815	0.01578	0.6458	0.009374	0.4884	0.01068
20	3.53-3.60	0.8215	0.01478	0.6463	0.009641	0.4559	0.01049
21	3.60-3.67	0.9223	0.01677	0.6199	0.009564	0.4976	0.01121
22	3.67-3.74	0.8949	0.01642	0.6259	0.009674	0.4666	0.01075
23	3.74-3.81	0.8446	0.01543	0.6383	0.009806	0.4976	0.01138
24	3.81-3.88	0.8923	0.0164	0.679	0.01042	0.5072	0.0115
25	3.88-3.95	0.8924	0.01638	0.6938	0.01081	0.5579	0.01245
26	3.95-4.02	0.8758	0.01622	0.6559	0.01018	0.517	0.01199
27	4.02-4.09	0.8557	0.01649	0.6865	0.01126	0.5306	0.01263
28	4.09-4.16	0.9916	0.01869	0.6671	0.01106	0.6285	0.01441
29	4.16-4.23	0.8943	0.0182	0.6423	0.01124	0.6103	0.0144
30	4.23-4.30	0.8835	0.02599	0.6436	0.01627	0.5882	0.02156

$1.76 < Q^2 < 4.2$ $0.4 < z_{\pi^+} < 0.5$

6	2.55-2.62	1.279	0.1292	0.4091	0.03366	0.5312	0.05947
7	2.62-2.69	0.9251	0.02429	0.6967	0.01389	0.5235	0.01593
8	2.69-2.76	0.8659	0.01599	0.6862	0.009924	0.4798	0.0109
9	2.76-2.83	0.8942	0.01346	0.6794	0.008238	0.51	0.009436
10	2.83-2.90	0.8485	0.01174	0.6801	0.007602	0.491	0.008403
11	2.90-2.97	0.8381	0.01074	0.6692	0.006995	0.5018	0.00799
12	2.97-3.04	0.8943	0.01097	0.6934	0.006949	0.5074	0.007721
13	3.04-3.11	0.8569	0.01001	0.6845	0.006594	0.5161	0.007558
14	3.11-3.18	0.8604	0.009821	0.6834	0.006446	0.5211	0.007322
15	3.18-3.25	0.8834	0.009774	0.7021	0.00641	0.5267	0.007306
16	3.25-3.32	0.893	0.009644	0.7117	0.006382	0.5294	0.00718
17	3.32-3.39	0.8799	0.00942	0.6962	0.006268	0.522	0.007151
18	3.39-3.46	0.8931	0.009394	0.6958	0.006251	0.5395	0.007204

19	3.46-3.53	0.8797	0.009195	0.7022	0.006257	0.5416	0.007216
20	3.53-3.60	0.9032	0.009386	0.6821	0.006073	0.5271	0.007079
21	3.60-3.67	0.9094	0.009528	0.6806	0.006057	0.5294	0.007122
22	3.67-3.74	0.8889	0.009359	0.691	0.006164	0.5378	0.007226
23	3.74-3.81	0.8596	0.009071	0.6879	0.006134	0.5465	0.007306
24	3.81-3.88	0.8981	0.009331	0.7044	0.006217	0.5731	0.007391
25	3.88-3.95	0.8686	0.009056	0.7063	0.006248	0.527	0.006939
26	3.95-4.02	0.8934	0.009367	0.7084	0.006215	0.5719	0.007365
27	4.02-4.09	0.8698	0.008995	0.6913	0.006222	0.5422	0.007172
28	4.09-4.16	0.9309	0.009924	0.6905	0.006228	0.577	0.00753
29	4.16-4.23	0.9027	0.009655	0.6773	0.006195	0.5571	0.007377
30	4.23-4.30	0.8125	0.01314	0.6891	0.009436	0.5176	0.01064

1.76 < Q^2 < 4.2 0.5 < z_{π^+} < 0.6

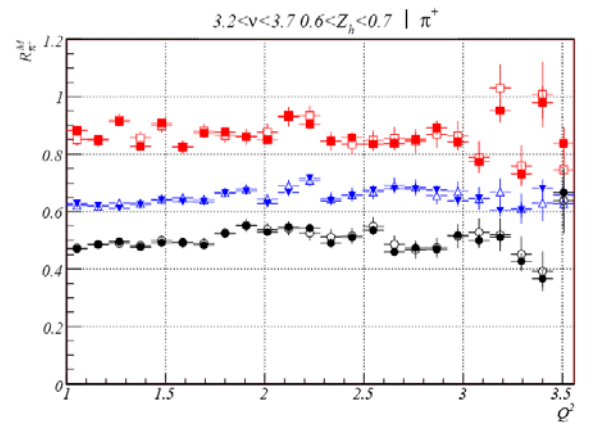
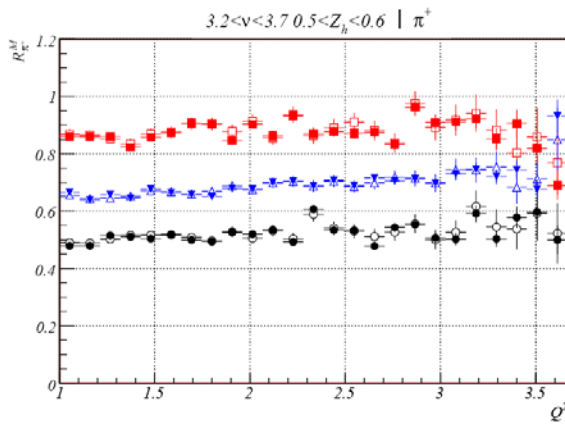
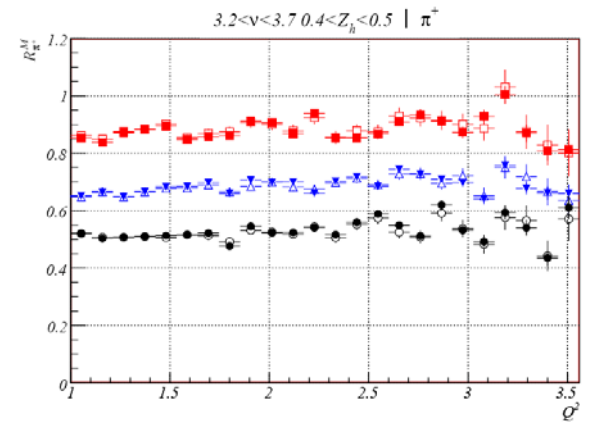
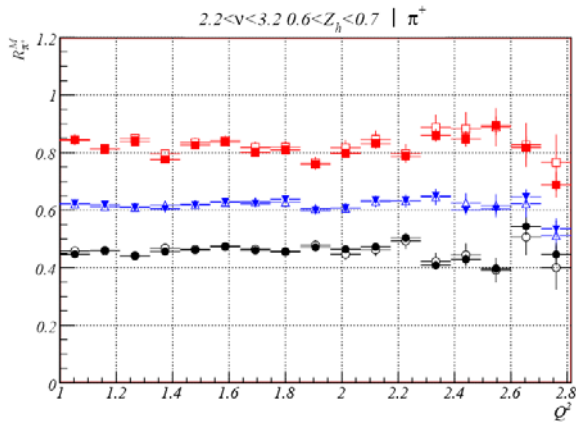
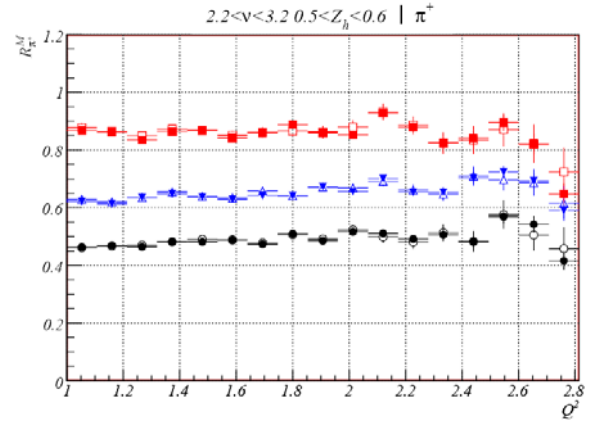
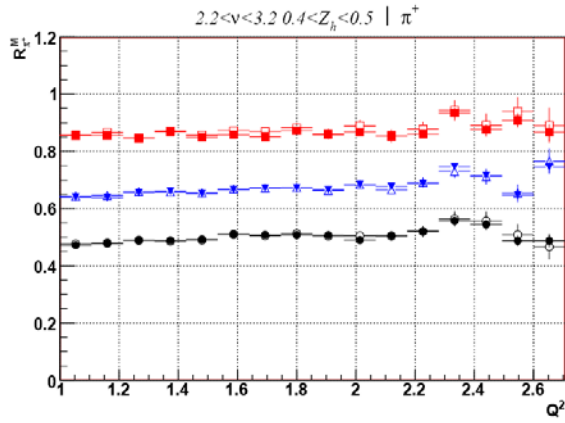
6	2.55-2.62	0.5208	0.0789	1.79	0.1474	0.5758	0.08138
7	2.62-2.69	0.8894	0.02765	0.6401	0.01555	0.5034	0.01853
8	2.69-2.76	0.9223	0.02044	0.6653	0.0115	0.5607	0.0143
9	2.76-2.83	0.8167	0.01533	0.6655	0.009998	0.5277	0.01198
10	2.83-2.90	0.9238	0.01545	0.6647	0.009167	0.4785	0.01013
11	2.90-2.97	0.9218	0.0144	0.6722	0.008519	0.5075	0.009864
12	2.97-3.04	0.8478	0.01281	0.6735	0.008374	0.4696	0.009178
13	3.04-3.11	0.8659	0.01253	0.6554	0.007812	0.5217	0.009263
14	3.11-3.18	0.8357	0.01144	0.6621	0.007623	0.4863	0.008667
15	3.18-3.25	0.8657	0.0118	0.6714	0.007693	0.5215	0.009034
16	3.25-3.32	0.8784	0.01191	0.6894	0.007727	0.5212	0.008838
17	3.32-3.39	0.8742	0.01154	0.6964	0.007779	0.5308	0.008946
18	3.39-3.46	0.8696	0.01138	0.6926	0.00774	0.4589	0.008029
19	3.46-3.53	0.9162	0.012	0.6991	0.007825	0.5243	0.008843
20	3.53-3.60	0.9368	0.01222	0.6981	0.007853	0.5308	0.008955
21	3.60-3.67	0.8928	0.01179	0.6736	0.007621	0.5384	0.009157
22	3.67-3.74	0.8314	0.01106	0.7094	0.007993	0.5573	0.009264
23	3.74-3.81	0.9035	0.01205	0.7219	0.008161	0.5451	0.009257
24	3.81-3.88	0.8788	0.01169	0.6742	0.007762	0.53	0.009135
25	3.88-3.95	0.895	0.01197	0.6946	0.008044	0.5282	0.008942
26	3.95-4.02	0.8691	0.01146	0.7266	0.008185	0.5268	0.008909
27	4.02-4.09	0.9013	0.01216	0.7017	0.008131	0.5378	0.009076
28	4.09-4.16	0.8938	0.01208	0.7049	0.008284	0.5627	0.009545
29	4.16-4.23	0.8254	0.01127	0.7201	0.008604	0.5613	0.00952
30	4.23-4.30	0.8113	0.0166	0.6828	0.01206	0.5459	0.01376

1.76 < Q^2 < 4.2 0.6 < z_{π^+} < 0.7

6	2.55-2.62	0.8123	0.1033	0.2919	0.034	0.3568	0.06247
7	2.62-2.69	0.7999	0.02919	0.5993	0.01633	0.4423	0.01918
8	2.69-2.76	0.781	0.01938	0.612	0.01202	0.5082	0.01502
9	2.76-2.83	0.7709	0.01629	0.5812	0.01008	0.4346	0.01151
10	2.83-2.90	0.8048	0.01526	0.6286	0.00973	0.4534	0.01093
11	2.90-2.97	0.7648	0.01366	0.6109	0.008978	0.45	0.01038
12	2.97-3.04	0.8262	0.01444	0.6353	0.009073	0.4592	0.01006
13	3.04-3.11	0.8309	0.01375	0.6176	0.008531	0.4469	0.009924
14	3.11-3.18	0.8106	0.01317	0.6297	0.008637	0.4939	0.01027
15	3.18-3.25	0.8703	0.01386	0.6589	0.008844	0.4796	0.009979
16	3.25-3.32	0.8749	0.01382	0.6369	0.008689	0.4962	0.01023
17	3.32-3.39	0.8548	0.01379	0.6403	0.008747	0.5232	0.01061
18	3.39-3.46	0.8111	0.01313	0.6383	0.00867	0.5162	0.01057
19	3.46-3.53	0.8439	0.01352	0.6674	0.009199	0.5012	0.01051
20	3.53-3.60	0.8664	0.01398	0.6693	0.009208	0.5183	0.01074
21	3.60-3.67	0.8663	0.01429	0.6617	0.009291	0.5508	0.01142
22	3.67-3.74	0.9071	0.01493	0.7048	0.009818	0.5451	0.01131
23	3.74-3.81	0.8416	0.01398	0.7028	0.009909	0.5236	0.01122
24	3.81-3.88	0.9099	0.01485	0.6727	0.009682	0.4989	0.01067
25	3.88-3.95	0.8332	0.01416	0.6494	0.009431	0.5419	0.01157
26	3.95-4.02	0.896	0.01507	0.6875	0.009922	0.5477	0.01165
27	4.02-4.09	0.8905	0.01521	0.6594	0.009702	0.5377	0.01178

28	4.09-4.16	0.9527	0.01657	0.7596	0.01128	0.5833	0.01251
29	4.16-4.23	0.8847	0.01531	0.6518	0.01013	0.5695	0.01297
30	4.23-4.30	0.7628	0.0196	0.4843	0.01163	0.4921	0.01715

Appendix V



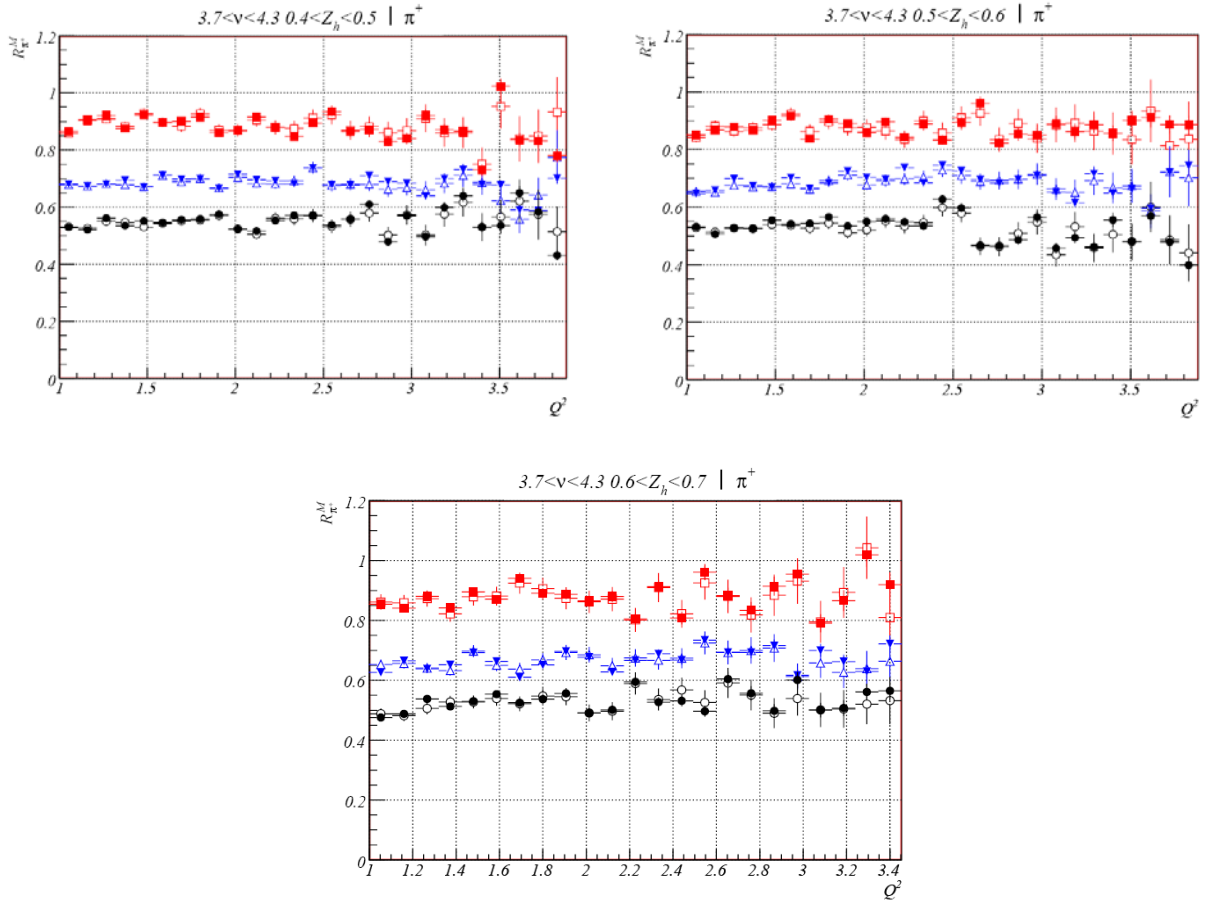


Table A4. Data points for the hadronic multiplicity ratio dependence on Q^2 for positive pions in different (ν, z_{π^+}) kinematical bins. In the top of each block of the table is shown the corresponding (ν, z_{π^+}) kinematical bin with the mean values of the ν and z_{π^+} distributions. The first column presents the bin number of the Q^2 distributions, the second column gives the limits of each Q^2 bin, and the following columns present the values and statistical errors of the hadronic multiplicity ratio for carbon, iron and, lead.

bin	Q^2 range	C	C error	Fe	Fe error	Pb	Pb error
2.2 < V < 3.2 0.4 < z_{\pi^+} < 0.5							
1	1.000-1.107	0.8567	0.003055	0.6406	0.001843	0.4721	0.002022
2	1.107-1.213	0.8561	0.003373	0.6383	0.002005	0.4783	0.002258
3	1.213-1.320	0.8463	0.003885	0.6554	0.002405	0.4897	0.002685
4	1.320-1.427	0.8686	0.004608	0.6611	0.002796	0.4889	0.003102
5	1.427-1.533	0.8495	0.005156	0.6515	0.003184	0.4923	0.003592
6	1.533-1.640	0.8579	0.006082	0.6663	0.003743	0.509	0.004273
7	1.640-1.747	0.8511	0.006901	0.6717	0.004279	0.5081	0.004838
8	1.747-1.853	0.8724	0.007875	0.673	0.004902	0.5074	0.005592
9	1.853-1.960	0.8584	0.008873	0.6656	0.005557	0.507	0.006436
10	1.960-2.067	0.8673	0.01012	0.6846	0.006452	0.49	0.007069

11	2.067-2.173	0.8541	0.01155	0.6772	0.00753	0.506	0.008534
12	2.173-2.280	0.8607	0.01348	0.6877	0.008943	0.5206	0.01026
13	2.280-2.387	0.9339	0.01791	0.7458	0.01162	0.5576	0.0129
14	2.387-2.493	0.876	0.01964	0.7153	0.01353	0.545	0.01556
15	2.493-2.600	0.9087	0.02481	0.647	0.01513	0.4878	0.01753
16	2.600-2.707	0.8668	0.03035	0.7454	0.02148	0.488	0.02232
17	2.707-2.813	0.7803	0.04035	0.8135	0.03351	0.6115	0.03838
18	2.813-2.920	0.6576	0.07193	0.5141	0.0495	0.8322	0.1116

2.2 < V < 3.2 0.5 < z_{π⁺} < 0.6

1	1.000-1.107	0.8675	0.003881	0.6214	0.002232	0.4627	0.002505
2	1.107-1.213	0.8621	0.004234	0.6132	0.002431	0.4687	0.00277
3	1.213-1.320	0.8354	0.004732	0.6347	0.002878	0.4642	0.003169
4	1.320-1.427	0.8649	0.005699	0.6476	0.003448	0.4811	0.003791
5	1.427-1.533	0.868	0.006477	0.6358	0.003829	0.4811	0.004331
6	1.533-1.640	0.8417	0.007444	0.6288	0.004422	0.4868	0.005085
7	1.640-1.747	0.8596	0.008622	0.6418	0.005088	0.4734	0.00569
8	1.747-1.853	0.8875	0.01001	0.6412	0.005835	0.509	0.006927
9	1.853-1.960	0.86	0.01091	0.6734	0.006908	0.4853	0.007602
10	1.960-2.067	0.8525	0.01209	0.6558	0.007694	0.5157	0.009212
11	2.067-2.173	0.9291	0.01522	0.7013	0.009555	0.5107	0.01067
12	2.173-2.280	0.8784	0.01642	0.6534	0.01024	0.4914	0.0119
13	2.280-2.387	0.8248	0.0188	0.6531	0.01229	0.5057	0.01494
14	2.387-2.493	0.8414	0.024	0.7027	0.01597	0.4813	0.01735
15	2.493-2.600	0.8946	0.02966	0.7242	0.01965	0.5691	0.02383
16	2.600-2.707	0.8202	0.03483	0.6934	0.02444	0.5421	0.02903
17	2.707-2.813	0.6471	0.03852	0.5907	0.02898	0.416	0.03306
18	2.813-2.920	1.145	0.1414	0.5672	0.06153	0.3925	0.07308

2.2 < V < 3.2 0.6 < z_{π⁺} < 0.7

1	1.000-1.107	0.843	0.004383	0.6236	0.002622	0.4471	0.002878
2	1.107-1.213	0.8123	0.004682	0.6185	0.002868	0.461	0.003215
3	1.213-1.320	0.8392	0.005647	0.6092	0.003294	0.4421	0.003613
4	1.320-1.427	0.7753	0.006002	0.6048	0.003766	0.4564	0.004253
5	1.427-1.533	0.8265	0.007273	0.617	0.004347	0.4612	0.004945
6	1.533-1.640	0.8376	0.008507	0.6283	0.005123	0.4748	0.005878
7	1.640-1.747	0.8016	0.009338	0.6223	0.005754	0.4601	0.006583
8	1.747-1.853	0.8096	0.0105	0.6375	0.006645	0.4573	0.007323
9	1.853-1.960	0.7583	0.01108	0.5982	0.007127	0.4708	0.008506
10	1.960-2.067	0.7984	0.01303	0.6072	0.008263	0.4642	0.009869
11	2.067-2.173	0.8311	0.0158	0.6337	0.01006	0.4727	0.01145
12	2.173-2.280	0.7871	0.01693	0.6332	0.01142	0.5038	0.01382
13	2.280-2.387	0.8595	0.02244	0.6498	0.01416	0.4087	0.01492
14	2.387-2.493	0.848	0.02728	0.6003	0.01561	0.4291	0.0186
15	2.493-2.600	0.894	0.03267	0.6038	0.01871	0.3968	0.02035
16	2.600-2.707	0.8182	0.03875	0.6451	0.02586	0.5439	0.03189
17	2.707-2.813	0.6885	0.04447	0.5346	0.03063	0.4462	0.03893
18	2.813-2.920	0.966	0.1234	0.7506	0.09203	0.7251	0.1264

3.2 < V < 3.73 0.4 < z_{π⁺} < 0.5

1	1.000-1.107	0.8529	0.004709	0.6518	0.002944	0.5213	0.003372
2	1.107-1.213	0.8383	0.005058	0.6631	0.003294	0.5031	0.003594
3	1.213-1.320	0.8715	0.005731	0.6485	0.0035	0.5086	0.004002
4	1.320-1.427	0.8841	0.006455	0.6657	0.003911	0.5108	0.004435
5	1.427-1.533	0.8951	0.007061	0.6826	0.004377	0.5133	0.004862
6	1.533-1.640	0.8484	0.007205	0.6838	0.00473	0.5168	0.005266
7	1.640-1.747	0.8578	0.007832	0.6976	0.005208	0.5225	0.005784
8	1.747-1.853	0.8613	0.008474	0.6603	0.00541	0.4763	0.005919
9	1.853-1.960	0.9125	0.009546	0.7063	0.006193	0.5453	0.007124
10	1.960-2.067	0.907	0.0102	0.6988	0.006628	0.5234	0.007423
11	2.067-2.173	0.8684	0.0108	0.6998	0.007098	0.5244	0.00817
12	2.173-2.280	0.9386	0.01229	0.6615	0.007299	0.5412	0.008869

13	2.280-2.387	0.8538	0.01183	0.7028	0.008245	0.517	0.009229
14	2.387-2.493	0.8535	0.01266	0.7181	0.009029	0.5598	0.01055
15	2.493-2.600	0.8679	0.01377	0.6841	0.009385	0.5886	0.01204
16	2.600-2.707	0.9094	0.01585	0.7445	0.01089	0.5494	0.01219
17	2.707-2.813	0.9344	0.01726	0.7281	0.01175	0.5121	0.01261
18	2.813-2.920	0.9126	0.01812	0.7099	0.012	0.6205	0.01541
19	2.920-3.027	0.8721	0.01935	0.6972	0.01331	0.5325	0.01571
20	3.027-3.133	0.9285	0.02277	0.6413	0.01439	0.4916	0.0168
21	3.133-3.240	1.004	0.0303	0.7572	0.01996	0.5938	0.02296
22	3.240-3.347	0.8694	0.03015	0.677	0.02003	0.5408	0.02592
23	3.347-3.453	0.8083	0.03502	0.6615	0.02353	0.4354	0.0256
24	3.453-3.560	0.8133	0.04224	0.6603	0.02835	0.6111	0.03974
25	3.560-3.667	1.055	0.0636	0.8594	0.04464	0.6084	0.04388
26	3.667-3.773	0.8514	0.06678	0.6508	0.04979	0.5964	0.067
27	3.773-3.880	0.9003	0.1117	0.5523	0.06772	0.2469	0.04939

3.2 < V < 3.73 0.5 < z_{π⁺} < 0.6

1	1.000-1.107	0.8606	0.005936	0.6658	0.003748	0.4789	0.003983
2	1.107-1.213	0.8603	0.006538	0.6391	0.004012	0.4793	0.004437
3	1.213-1.320	0.8619	0.007211	0.6583	0.004458	0.515	0.005085
4	1.320-1.427	0.8234	0.007556	0.6454	0.00482	0.5105	0.005556
5	1.427-1.533	0.8576	0.00854	0.6773	0.005504	0.5041	0.006061
6	1.533-1.640	0.8729	0.009407	0.665	0.005831	0.5191	0.006702
7	1.640-1.747	0.9064	0.01052	0.6582	0.006185	0.4994	0.007077
8	1.747-1.853	0.9042	0.011	0.6509	0.00673	0.4943	0.007644
9	1.853-1.960	0.8464	0.01124	0.6794	0.007551	0.5256	0.008733
10	1.960-2.067	0.9032	0.01289	0.6772	0.008192	0.5201	0.009439
11	2.067-2.173	0.8632	0.0133	0.7007	0.009109	0.5337	0.01029
12	2.173-2.280	0.9328	0.01511	0.7042	0.009624	0.493	0.01041
13	2.280-2.387	0.8702	0.01517	0.6877	0.01031	0.6069	0.01291
14	2.387-2.493	0.8779	0.01649	0.7077	0.01126	0.5334	0.0129
15	2.493-2.600	0.8716	0.01743	0.689	0.01166	0.5327	0.01388
16	2.600-2.707	0.8752	0.01888	0.7158	0.01298	0.4783	0.01353
17	2.707-2.813	0.8336	0.01902	0.7059	0.01405	0.5434	0.01641
18	2.813-2.920	0.9631	0.02262	0.7121	0.01477	0.5533	0.01739
19	2.920-3.027	0.9091	0.02538	0.6976	0.01665	0.5065	0.01875
20	3.027-3.133	0.9107	0.02876	0.7299	0.01982	0.5027	0.02157
21	3.133-3.240	0.9226	0.03354	0.7461	0.02296	0.5918	0.02829
22	3.240-3.347	0.8527	0.03598	0.7204	0.02563	0.5037	0.02846
23	3.347-3.453	0.906	0.04817	0.744	0.03206	0.5786	0.03774
24	3.453-3.560	0.8194	0.04954	0.6766	0.03259	0.5977	0.04627
25	3.560-3.667	0.6894	0.05057	0.9322	0.05596	0.4995	0.04983
26	3.667-3.773	0.9106	0.08403	0.8285	0.06662	0.2936	0.04404
27	3.773-3.880	0.6383	0.1123	1.165	0.1504	0.2332	0.06517

3.2 < V < 3.73 0.6 < z_{π⁺} < 0.7

1	1.000-1.107	0.8829	0.007556	0.6279	0.004464	0.4703	0.004855
2	1.107-1.213	0.8512	0.008047	0.6211	0.004813	0.4844	0.00552
3	1.213-1.320	0.9138	0.009391	0.6116	0.005186	0.4958	0.006071
4	1.320-1.427	0.827	0.009497	0.6239	0.005805	0.4765	0.006587
5	1.427-1.533	0.9073	0.01131	0.6404	0.006568	0.4912	0.007524
6	1.533-1.640	0.8259	0.01101	0.6345	0.00696	0.4908	0.008014
7	1.640-1.747	0.8728	0.01249	0.634	0.007587	0.4825	0.008554
8	1.747-1.853	0.8776	0.01362	0.6643	0.00853	0.5232	0.009919
9	1.853-1.960	0.8609	0.01407	0.6702	0.009222	0.5499	0.01116
10	1.960-2.067	0.8488	0.01493	0.6279	0.009423	0.5289	0.01157
11	2.067-2.173	0.9333	0.01767	0.6668	0.01076	0.547	0.01284
12	2.173-2.280	0.9046	0.01805	0.7171	0.01206	0.5422	0.0137
13	2.280-2.387	0.846	0.01794	0.6375	0.01168	0.4902	0.01406
14	2.387-2.493	0.8576	0.01962	0.6563	0.01283	0.5095	0.01505
15	2.493-2.600	0.8344	0.01998	0.6738	0.01391	0.5353	0.01686
16	2.600-2.707	0.8369	0.02185	0.679	0.01458	0.4601	0.01583
17	2.707-2.813	0.8512	0.02342	0.6778	0.01591	0.4739	0.01774

18	2.813-2.920	0.8917	0.02566	0.6745	0.0169	0.4685	0.01803
19	2.920-3.027	0.8421	0.02619	0.6372	0.01798	0.5183	0.02196
20	3.027-3.133	0.7736	0.02923	0.6455	0.0204	0.4991	0.02447
21	3.133-3.240	0.9512	0.04036	0.6035	0.02218	0.5104	0.02885
22	3.240-3.347	0.7313	0.03667	0.6063	0.02676	0.4272	0.02952
23	3.347-3.453	0.9798	0.05624	0.6797	0.03325	0.3669	0.03201
24	3.453-3.560	0.8381	0.05571	0.6581	0.04096	0.6663	0.0559
25	3.560-3.667	0.5812	0.05066	0.668	0.04913	0.4746	0.05517
26	3.667-3.773	0.913	0.0994	0.46	0.04393	0.6444	0.09118

3.73 < V < 4.3 0.4 < z_{π⁺} < 0.5

1	1.000-1.107	0.8645	0.005347	0.6812	0.003471	0.5293	0.003891
2	1.107-1.213	0.9065	0.006012	0.6744	0.003717	0.5205	0.004153
3	1.213-1.320	0.9211	0.006651	0.6812	0.004119	0.5612	0.004808
4	1.320-1.427	0.875	0.006822	0.6939	0.004491	0.5347	0.005048
5	1.427-1.533	0.9219	0.007646	0.6711	0.004706	0.5512	0.005609
6	1.533-1.640	0.8959	0.008051	0.7114	0.005394	0.5464	0.006081
7	1.640-1.747	0.9009	0.008721	0.6979	0.005676	0.5562	0.006552
8	1.747-1.853	0.9159	0.009557	0.6996	0.006163	0.5587	0.00715
9	1.853-1.960	0.8619	0.009514	0.6656	0.006303	0.5747	0.007853
10	1.960-2.067	0.8671	0.01029	0.7149	0.007219	0.522	0.007834
11	2.067-2.173	0.9159	0.01176	0.6958	0.00772	0.516	0.008518
12	2.173-2.280	0.8801	0.01229	0.6922	0.00814	0.5533	0.009519
13	2.280-2.387	0.8466	0.0127	0.6823	0.008571	0.5708	0.01066
14	2.387-2.493	0.895	0.01445	0.7364	0.0101	0.5697	0.01136
15	2.493-2.600	0.9341	0.01628	0.6788	0.01008	0.5381	0.01171
16	2.600-2.707	0.8637	0.01602	0.6777	0.01057	0.5585	0.01291
17	2.707-2.813	0.8716	0.01664	0.7101	0.01158	0.6093	0.01452
18	2.813-2.920	0.8297	0.01683	0.6901	0.01169	0.4796	0.0129
19	2.920-3.027	0.8405	0.01885	0.6841	0.01236	0.5694	0.01521
20	3.027-3.133	0.9211	0.02104	0.6395	0.0123	0.4968	0.01487
21	3.133-3.240	0.8712	0.02072	0.7001	0.0143	0.5989	0.01803
22	3.240-3.347	0.8654	0.02127	0.7306	0.01621	0.6395	0.01971
23	3.347-3.453	0.7295	0.01997	0.6797	0.01563	0.5306	0.0175
24	3.453-3.560	1.023	0.02742	0.6771	0.01667	0.5353	0.01985
25	3.560-3.667	0.8351	0.0243	0.59	0.01543	0.6495	0.02361
26	3.667-3.773	0.8325	0.02501	0.5867	0.01533	0.583	0.02425
27	3.773-3.880	0.7801	0.02259	0.701	0.01814	0.4309	0.01666
28	3.880-3.987	1.226	0.03153	0.6991	0.01529	0.8205	0.0262

3.73 < V < 4.3 0.5 < z_{π⁺} < 0.6

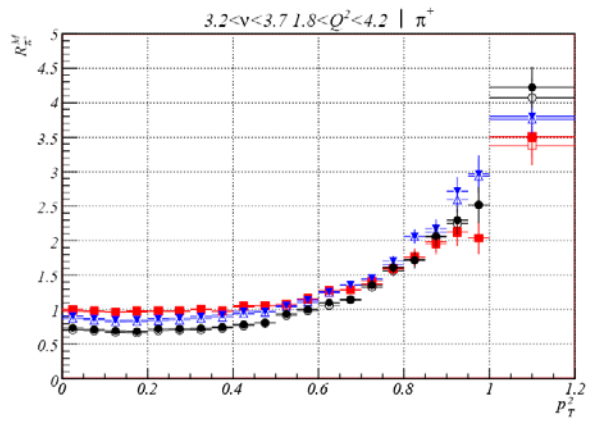
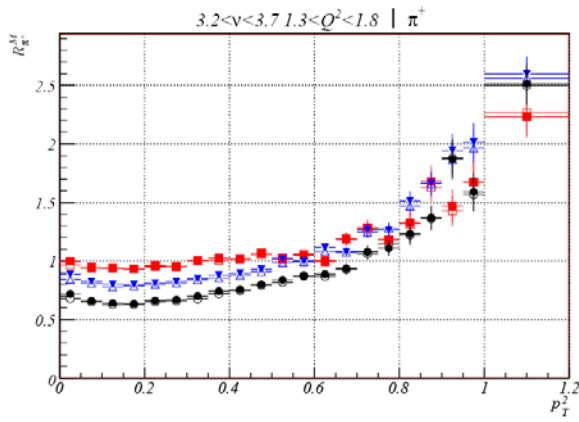
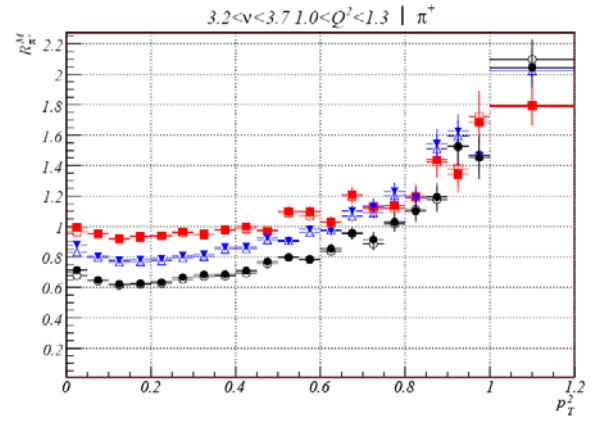
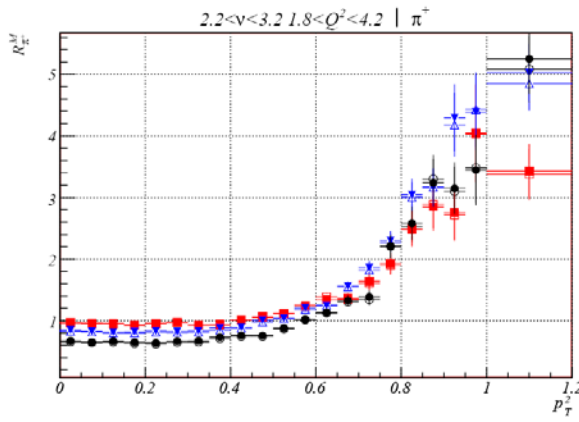
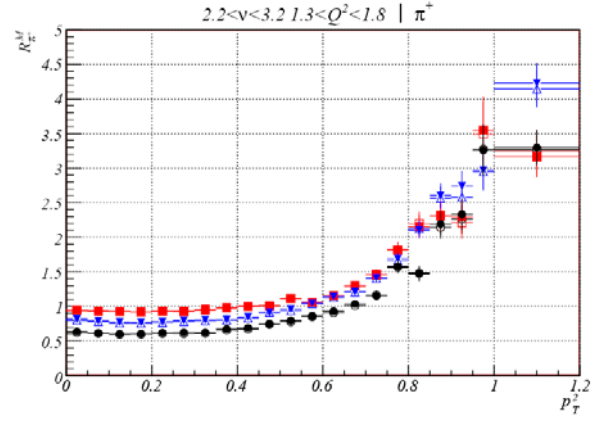
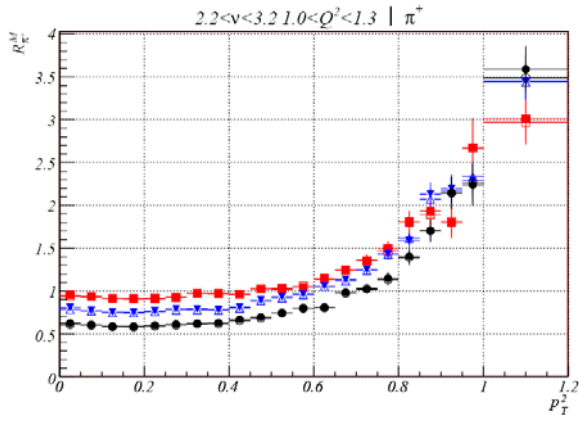
1	1.000-1.107	0.8511	0.006424	0.6473	0.004109	0.532	0.004784
2	1.107-1.213	0.8685	0.007123	0.6587	0.004485	0.5063	0.005063
3	1.213-1.320	0.8793	0.007843	0.698	0.005213	0.5274	0.005632
4	1.320-1.427	0.8665	0.008279	0.674	0.005485	0.5258	0.006103
5	1.427-1.533	0.901	0.00946	0.6686	0.005848	0.5544	0.006973
6	1.533-1.640	0.9163	0.01031	0.7022	0.006683	0.5414	0.007452
7	1.640-1.747	0.8372	0.01038	0.6649	0.006979	0.543	0.008248
8	1.747-1.853	0.9055	0.0118	0.6835	0.007742	0.5655	0.009203
9	1.853-1.960	0.8912	0.0125	0.7261	0.008777	0.5341	0.009466
10	1.960-2.067	0.8599	0.01304	0.7032	0.009097	0.5497	0.01048
11	2.067-2.173	0.8965	0.01511	0.6964	0.009915	0.5588	0.01157
12	2.173-2.280	0.8428	0.01518	0.7371	0.01123	0.5484	0.01231
13	2.280-2.387	0.8892	0.01669	0.6847	0.01126	0.5348	0.0127
14	2.387-2.493	0.8334	0.01739	0.746	0.01295	0.6273	0.01558
15	2.493-2.600	0.8942	0.02009	0.7267	0.01404	0.5972	0.01612
16	2.600-2.707	0.9608	0.02248	0.695	0.01429	0.4665	0.01502
17	2.707-2.813	0.8222	0.02045	0.6829	0.01467	0.4654	0.01586
18	2.813-2.920	0.8549	0.02248	0.6956	0.01605	0.4859	0.01732
19	2.920-3.027	0.8503	0.02388	0.7102	0.0174	0.565	0.02007
20	3.027-3.133	0.8902	0.02663	0.6522	0.01587	0.4564	0.01826
21	3.133-3.240	0.8629	0.02677	0.6154	0.01718	0.4935	0.0197
22	3.240-3.347	0.8858	0.02722	0.7169	0.02006	0.4616	0.02015

23	3.347-3.453	0.857	0.02721	0.6489	0.0195	0.5553	0.02442
24	3.453-3.560	0.9011	0.03212	0.6624	0.02006	0.4801	0.02252
25	3.560-3.667	0.9107	0.03332	0.5957	0.01923	0.5685	0.027
26	3.667-3.773	0.8867	0.03186	0.721	0.02465	0.4782	0.02347
27	3.773-3.880	0.8864	0.03046	0.7447	0.02316	0.399	0.0221
28	3.880-3.987	0.9188	0.03053	0.8617	0.02314	0.6802	0.02586
29	3.987-4.093	1.026	0.08021	1.604	0.07308	0.7723	0.05516

3.73 < V < 4.3 0.6 < z_{π⁺} < 0.7

1	1.000-1.107	0.854	0.00801	0.6267	0.004878	0.4758	0.005454
2	1.107-1.213	0.8411	0.008745	0.6652	0.005736	0.4878	0.006312
3	1.213-1.320	0.8803	0.009766	0.6381	0.006015	0.5378	0.007326
4	1.320-1.427	0.8419	0.01015	0.6521	0.006628	0.5126	0.007457
5	1.427-1.533	0.8952	0.01156	0.6926	0.007516	0.53	0.008407
6	1.533-1.640	0.8708	0.01235	0.6634	0.007875	0.5538	0.00983
7	1.640-1.747	0.941	0.01465	0.61	0.008241	0.525	0.01011
8	1.747-1.853	0.8911	0.01492	0.6517	0.00936	0.537	0.01128
9	1.853-1.960	0.8874	0.01609	0.6971	0.0107	0.5562	0.01248
10	1.960-2.067	0.8652	0.01666	0.677	0.01127	0.4905	0.01222
11	2.067-2.173	0.88	0.01829	0.6279	0.0115	0.5015	0.01362
12	2.173-2.280	0.8051	0.01832	0.6669	0.01315	0.5949	0.01691
13	2.280-2.387	0.9127	0.02229	0.6884	0.01459	0.5271	0.0165
14	2.387-2.493	0.808	0.02125	0.6675	0.01525	0.5313	0.01834
15	2.493-2.600	0.9616	0.02643	0.7343	0.0179	0.4965	0.01837
16	2.600-2.707	0.8832	0.02603	0.6937	0.01838	0.6041	0.02356
17	2.707-2.813	0.834	0.02739	0.6934	0.01969	0.5567	0.02384
18	2.813-2.920	0.9147	0.03186	0.7155	0.02057	0.4979	0.02206
19	2.920-3.027	0.9545	0.03403	0.617	0.01866	0.601	0.02664
20	3.027-3.133	0.7906	0.02985	0.7	0.02188	0.5002	0.02414
21	3.133-3.240	0.8663	0.03492	0.6627	0.02278	0.5073	0.02612
22	3.240-3.347	1.019	0.03951	0.6294	0.02239	0.5611	0.0272
23	3.347-3.453	0.9192	0.04133	0.7216	0.0276	0.5649	0.0314
24	3.453-3.560	0.7276	0.03285	0.6338	0.02315	0.672	0.03648
25	3.560-3.667	0.8182	0.0377	0.715	0.02788	0.4682	0.02919
26	3.667-3.773	0.7056	0.03149	0.6324	0.02511	0.3979	0.02565
27	3.773-3.880	0.7399	0.0359	0.6441	0.02377	0.2776	0.02166
28	3.880-3.987	0.6919	0.0253	0.6198	0.02063	0.7904	0.03302

Appendix VI



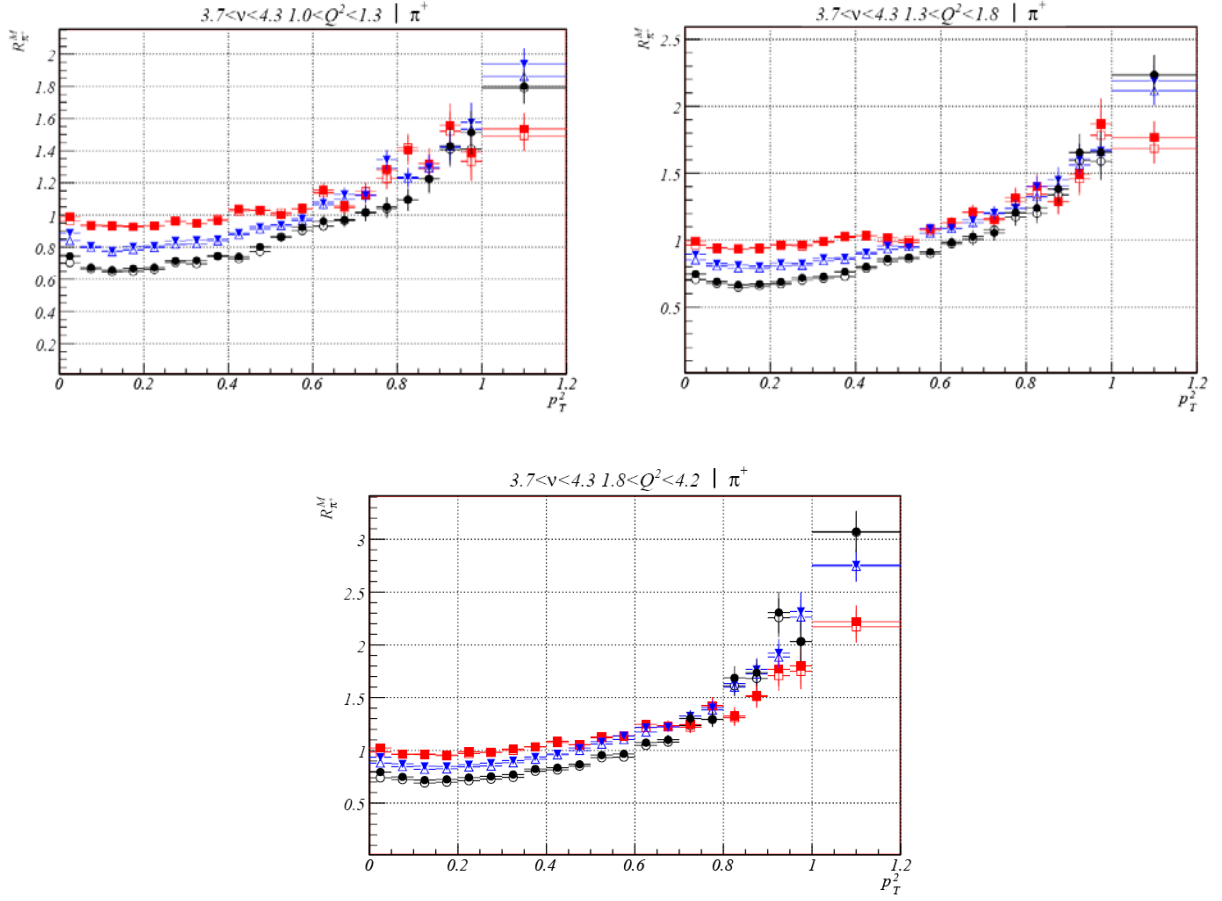


Table A5. Data for the hadronic multiplicity ratio dependence on p_T^2 for positive pions in different (Q^2, ν) kinematical bins, when $0.4 < z_{\pi^+} < 0.7$. In the top of each block of the table is shown the corresponding (Q^2, ν) kinematical bin with the mean values of the Q^2 and ν distributions. The first column presents the bin number of the p_T^2 distributions, the second column gives the limits of each p_T^2 bin, and the following columns present the values and statistical errors of the hadronic multiplicity ratio for carbon, iron and lead.

bin	p_T^2 range	C	C error	Fe	Fe error	Pb	Pb error
2.2 < ν < 3.2 1 < Q^2 < 1.33							
1	0-0.05	0.8175	0.01251	0.577	0.00771	0.4234	0.007736
2	0.05-0.1	0.7721	0.02404	0.5973	0.01729	0.3861	0.01307
3	0.1-0.15	0.8012	0.02323	0.573	0.01457	0.4195	0.01485
4	0.15-0.2	0.8419	0.01946	0.5809	0.01224	0.4266	0.01135
5	0.2-0.25	0.8269	0.01849	0.6118	0.01236	0.4551	0.01179
6	0.25-0.3	0.8178	0.01931	0.6252	0.01317	0.4679	0.01294
7	0.3-0.35	0.8699	0.02197	0.6227	0.01389	0.4666	0.01359
8	0.35-0.4	0.8592	0.02346	0.6237	0.01494	0.4598	0.01477
9	0.4-0.45	0.8494	0.02572	0.642	0.01696	0.4898	0.01705

10	0.45-0.5	0.8369	0.02829	0.6803	0.01964	0.5084	0.01949
11	0.5-0.55	0.8843	0.03348	0.6994	0.02252	0.5576	0.02383
12	0.55-0.6	0.8852	0.03827	0.7783	0.02782	0.5888	0.02799
13	0.6-0.65	1.025	0.04943	0.8508	0.03378	0.6375	0.03409
14	0.65-0.7	1.087	0.05989	0.9346	0.04188	0.7853	0.04653
15	0.7-0.75	1.257	0.08304	1.035	0.05207	0.7925	0.05362
16	0.75-0.8	1.348	0.1002	1.245	0.07254	0.9539	0.07249
17	0.8-0.85	1.631	0.1435	1.342	0.0882	1.109	0.09591
18	0.85-0.9	1.836	0.1928	1.95	0.1554	1.357	0.1313
19	0.9-0.95	1.601	0.1969	2.025	0.1837	2.01	0.2079
20	0.95-1	2.572	0.4005	2.064	0.2119	1.985	0.2641
21	1-1.2	3.025	0.3201	3.568	0.2674	3.541	0.3206
22	1.2-2	3.668	0.4941	4.839	0.4572	3.993	0.4115

2.2 < V < 3.2 1.33 < Q² < 1.76

1	0-0.05	0.825	0.01127	0.5918	0.00703	0.4394	0.007151
2	0.05-0.1	0.8079	0.01993	0.5905	0.01305	0.4298	0.01278
3	0.1-0.15	0.8451	0.02377	0.61	0.01584	0.4748	0.01674
4	0.15-0.2	0.789	0.01915	0.5769	0.01245	0.4493	0.01248
5	0.2-0.25	0.8041	0.01825	0.6196	0.01258	0.448	0.012
6	0.25-0.3	0.8179	0.02002	0.6302	0.01354	0.4566	0.01297
7	0.3-0.35	0.8162	0.02083	0.6167	0.01373	0.4678	0.01391
8	0.35-0.4	0.8327	0.02272	0.6476	0.01529	0.4879	0.01542
9	0.4-0.45	0.8333	0.02501	0.6327	0.01628	0.4977	0.01705
10	0.45-0.5	0.8684	0.02877	0.6941	0.01964	0.5374	0.02013
11	0.5-0.55	0.994	0.03684	0.749	0.02356	0.58	0.02496
12	0.55-0.6	0.9038	0.03886	0.8204	0.02897	0.6409	0.03011
13	0.6-0.65	1.006	0.04863	0.907	0.03598	0.7157	0.03816
14	0.65-0.7	1.134	0.06403	0.9645	0.04334	0.7712	0.04705
15	0.7-0.75	1.266	0.08306	1.113	0.05793	0.9642	0.0667
16	0.75-0.8	1.589	0.1221	1.37	0.08187	1.2	0.09178
17	0.8-0.85	1.753	0.1691	1.682	0.1198	1.203	0.1097
18	0.85-0.9	2.029	0.228	2.438	0.2084	1.706	0.1732
19	0.9-0.95	1.988	0.2532	2.35	0.2154	2.024	0.235
20	0.95-1	3.29	0.5227	2.681	0.3075	2.731	0.3732
21	1-1.2	3.415	0.3829	4.307	0.3483	3.13	0.2871
22	1.2-2	3.811	0.5468	4.656	0.423	4.64	0.4721

2.2 < V < 3.2 1.76 < Q² < 4.2

1	0-0.05	0.836	0.01396	0.6163	0.009146	0.4536	0.009444
2	0.05-0.1	0.8192	0.02148	0.6118	0.0143	0.4347	0.01418
3	0.1-0.15	0.7754	0.02618	0.6369	0.02063	0.4543	0.01872
4	0.15-0.2	0.8288	0.02617	0.6364	0.01798	0.4594	0.01757
5	0.2-0.25	0.8234	0.02619	0.6437	0.01921	0.4381	0.01789
6	0.25-0.3	0.8053	0.02582	0.6012	0.01737	0.484	0.01878
7	0.3-0.35	0.7884	0.02684	0.6112	0.01873	0.4679	0.01978
8	0.35-0.4	0.7906	0.02869	0.6347	0.01996	0.4977	0.02134
9	0.4-0.45	0.8851	0.03475	0.6919	0.02384	0.536	0.02488
10	0.45-0.5	0.8553	0.03797	0.7203	0.02739	0.5606	0.02891
11	0.5-0.55	0.9532	0.04767	0.7724	0.03267	0.6587	0.03771
12	0.55-0.6	1.028	0.05777	0.872	0.04179	0.6711	0.04409
13	0.6-0.65	1.069	0.07087	0.9281	0.04974	0.7153	0.05339
14	0.65-0.7	0.988	0.07649	1.079	0.06675	0.8859	0.07491
15	0.7-0.75	1.438	0.1305	1.362	0.09703	1.026	0.09928
16	0.75-0.8	1.685	0.1799	1.691	0.1424	1.755	0.1896
17	0.8-0.85	2.015	0.2678	2.369	0.2471	2.156	0.2792
18	0.85-0.9	2.275	0.36	2.878	0.353	2.425	0.3697
19	0.9-0.95	2.875	0.5829	4.173	0.6363	2.808	0.477
20	0.95-1	3.62	0.8526	4.416	0.7773	3.756	0.7952
21	1-1.2	3.503	0.5319	4.96	0.5463	4.916	0.6399
22	1.2-2	3.76	0.723	4.287	0.512	3.993	0.5567

3.2 < V < 3.73 1 < Q² < 1.33

1	0-0.05	0.8282	0.02341	0.5872	0.01455	0.442	0.01484
2	0.05-0.1	0.8191	0.01795	0.5782	0.01143	0.421	0.01092
3	0.1-0.15	0.7466	0.04317	0.6319	0.03818	0.4754	0.03433
4	0.15-0.2	0.8699	0.02687	0.6037	0.01679	0.4559	0.01613
5	0.2-0.25	0.8452	0.02402	0.5947	0.01552	0.4626	0.01522
6	0.25-0.3	0.848	0.02568	0.6378	0.0174	0.5067	0.01768
7	0.3-0.35	0.86	0.02799	0.632	0.01876	0.5132	0.0189
8	0.35-0.4	0.8597	0.02981	0.6837	0.02109	0.4967	0.01973
9	0.4-0.45	0.8533	0.03306	0.6582	0.02265	0.5016	0.02223
10	0.45-0.5	0.8818	0.03725	0.6965	0.02614	0.584	0.02798
11	0.5-0.55	0.9948	0.04735	0.6846	0.02796	0.5608	0.02975
12	0.55-0.6	0.9071	0.04763	0.7835	0.03493	0.5832	0.03418
13	0.6-0.65	0.8916	0.05028	0.699	0.03415	0.6003	0.0391
14	0.65-0.7	1.099	0.07231	0.8129	0.04421	0.646	0.04399
15	0.7-0.75	0.9969	0.07032	0.8483	0.05115	0.6493	0.05061
16	0.75-0.8	0.9086	0.07321	0.903	0.05956	0.7717	0.06464
17	0.8-0.85	1.045	0.09272	0.8825	0.0659	0.7132	0.07049
18	0.85-0.9	1.275	0.1326	1.304	0.1111	0.9193	0.09776
19	0.9-0.95	1.088	0.1266	1.323	0.1223	1.174	0.1341
20	0.95-1	1.46	0.1922	1.177	0.1222	1.022	0.1354
21	1-1.2	1.455	0.1286	1.699	0.1154	1.719	0.1412
22	1.2-2	2.484	0.2946	3.845	0.3259	3.385	0.3231

3.2 < V < 3.73 1.33 < Q² < 1.76

1	0-0.05	0.8323	0.01773	0.5958	0.0112	0.4504	0.01164
2	0.05-0.1	0.6841	0.1181	0.4445	0.1224	0.3889	0.04648
3	0.1-0.15	0.7334	0.07706	0.5882	0.05391	0.4541	0.06085
4	0.15-0.2	0.794	0.02675	0.6217	0.02099	0.468	0.01959
5	0.2-0.25	0.8553	0.0244	0.6391	0.01681	0.4924	0.01649
6	0.25-0.3	0.845	0.02482	0.6277	0.01646	0.4871	0.0167
7	0.3-0.35	0.8289	0.02598	0.6508	0.01806	0.5036	0.01832
8	0.35-0.4	0.933	0.03125	0.7098	0.02111	0.5607	0.02138
9	0.4-0.45	0.8547	0.03122	0.6689	0.02184	0.5433	0.02301
10	0.45-0.5	0.9203	0.03715	0.6643	0.02355	0.5628	0.02591
11	0.5-0.55	0.9506	0.0424	0.7483	0.02914	0.5927	0.02983
12	0.55-0.6	0.9054	0.04517	0.7459	0.03199	0.6059	0.03292
13	0.6-0.65	0.8169	0.04517	0.792	0.03757	0.615	0.03715
14	0.65-0.7	1.035	0.06606	0.7379	0.03929	0.6502	0.04471
15	0.7-0.75	1.088	0.07861	0.8885	0.05264	0.6735	0.0517
16	0.75-0.8	0.9767	0.07898	0.9372	0.06191	0.735	0.06241
17	0.8-0.85	1.153	0.1029	1.2	0.08858	0.8829	0.08638
18	0.85-0.9	1.487	0.1543	1.31	0.1106	1.02	0.1061
19	0.9-0.95	1.33	0.1631	1.472	0.1371	1.251	0.1545
20	0.95-1	1.318	0.1821	1.421	0.1532	1.089	0.1472
21	1-1.2	1.935	0.1875	2.205	0.1582	1.973	0.1713
22	1.2-2	2.212	0.2687	3.626	0.3098	2.845	0.2799

3.2 < V < 3.73 1.76 < Q² < 4.2

1	0-0.05	0.8274	0.01214	0.6263	0.008294	0.4587	0.008597
2	0.05-0.1	0.7982	0.02751	0.6024	0.01875	0.4605	0.01915
3	0.1-0.15	0.8216	0.04556	0.6353	0.03363	0.4948	0.03532
4	0.15-0.2	0.8912	0.03252	0.6558	0.02349	0.4352	0.01943
5	0.2-0.25	0.8836	0.02696	0.6413	0.01775	0.4756	0.01743
6	0.25-0.3	0.877	0.02376	0.6573	0.01651	0.4899	0.01622
7	0.3-0.35	0.8898	0.02424	0.6552	0.01652	0.5071	0.01722
8	0.35-0.4	0.8428	0.02379	0.6818	0.01776	0.5202	0.01809
9	0.4-0.45	0.8944	0.02731	0.7017	0.01941	0.5421	0.0206
10	0.45-0.5	0.8958	0.03022	0.7026	0.02092	0.5172	0.02168
11	0.5-0.55	0.9097	0.03392	0.7804	0.02545	0.6144	0.02735
12	0.55-0.6	0.9505	0.03988	0.7877	0.0291	0.6651	0.03319
13	0.6-0.65	1.03	0.0494	0.8177	0.03325	0.754	0.04127
14	0.65-0.7	1.015	0.05479	0.9826	0.04549	0.7524	0.04764
15	0.7-0.75	1.137	0.07059	0.9987	0.05198	0.9438	0.06537
16	0.75-0.8	1.396	0.102	1.148	0.0691	1.1	0.08591

17	0.8-0.85	1.402	0.1207	1.426	0.09601	1.086	0.0986
18	0.85-0.9	1.752	0.1749	1.528	0.1192	1.253	0.1305
19	0.9-0.95	1.65	0.1977	2.058	0.1907	1.585	0.186
20	0.95-1	1.753	0.2532	2.45	0.2644	2.091	0.2864
21	1-1.2	3.008	0.3043	3.227	0.2419	3.342	0.2957
22	1.2-2	3.764	0.4701	5.194	0.4555	4.684	0.4651

3.73<V <4.3 1<Q²<1.33

1	0-0.05	0.7073	0.08413	0.5544	0.0582	0.4584	0.03652
2	0.05-0.1	0.8307	0.02031	0.6113	0.01351	0.426	0.01254
3	0.1-0.15	0.9641	0.05621	0.5858	0.0327	0.4856	0.03405
4	0.15-0.2	0.8331	0.02878	0.6103	0.01953	0.4569	0.01832
5	0.2-0.25	0.881	0.02683	0.6069	0.01678	0.4734	0.01642
6	0.25-0.3	0.8587	0.02695	0.6395	0.01792	0.5202	0.01863
7	0.3-0.35	0.8383	0.02801	0.6439	0.01936	0.5214	0.02021
8	0.35-0.4	0.8433	0.03025	0.673	0.02184	0.4982	0.02076
9	0.4-0.45	0.9169	0.03718	0.7141	0.02555	0.5148	0.02394
10	0.45-0.5	0.86	0.03796	0.6934	0.02671	0.5481	0.02894
11	0.5-0.55	0.8602	0.0423	0.7229	0.03093	0.6024	0.03283
12	0.55-0.6	0.9132	0.04933	0.7433	0.03497	0.654	0.03849
13	0.6-0.65	0.9693	0.05804	0.7818	0.04047	0.6718	0.04329
14	0.65-0.7	0.9424	0.06457	0.8689	0.05068	0.6204	0.04607
15	0.7-0.75	1.003	0.07217	0.817	0.05256	0.7345	0.05858
16	0.75-0.8	1.009	0.08307	0.9705	0.06797	0.663	0.06007
17	0.8-0.85	1.279	0.1206	0.9767	0.07385	0.7794	0.07635
18	0.85-0.9	1.141	0.1168	0.9377	0.07969	0.8179	0.08991
19	0.9-0.95	1.416	0.1603	1.091	0.1008	1.002	0.1199
20	0.95-1	1.03	0.1343	1.071	0.115	0.9092	0.1229
21	1-1.2	1.321	0.1124	1.479	0.09955	1.298	0.1059
22	1.2-2	2.444	0.2589	3.103	0.2546	2.119	0.187

3.73<V <4.3 1.33<Q²<1.76

1	0-0.05	0.7999	0.04861	0.602	0.03402	0.4534	0.03208
2	0.05-0.1	0.8065	0.01963	0.6134	0.01365	0.4495	0.01333
3	0.1-0.15	0.8912	0.0673	0.6681	0.05604	0.4423	0.04699
4	0.15-0.2	0.8311	0.03123	0.6447	0.02314	0.4928	0.02255
5	0.2-0.25	0.9323	0.02907	0.6484	0.01856	0.515	0.01949
6	0.25-0.3	0.9029	0.02797	0.6626	0.01892	0.5016	0.01861
7	0.3-0.35	0.8968	0.02953	0.6486	0.01934	0.5558	0.02167
8	0.35-0.4	0.9005	0.03217	0.6773	0.02178	0.5125	0.02189
9	0.4-0.45	0.9379	0.03649	0.7136	0.0253	0.5833	0.02623
10	0.45-0.5	0.8936	0.03845	0.707	0.02715	0.637	0.03159
11	0.5-0.55	0.8617	0.04005	0.7031	0.02929	0.5949	0.03264
12	0.55-0.6	0.9538	0.04982	0.805	0.03736	0.6123	0.03674
13	0.6-0.65	0.9454	0.05565	0.7989	0.04133	0.6995	0.04515
14	0.65-0.7	0.9767	0.06393	0.8638	0.0495	0.6429	0.04821
15	0.7-0.75	0.9955	0.07099	0.821	0.05186	0.7126	0.05808
16	0.75-0.8	1.157	0.09502	0.8963	0.0631	0.8535	0.07628
17	0.8-0.85	1.08	0.1042	1.025	0.0792	0.8184	0.08464
18	0.85-0.9	0.9628	0.09965	0.9709	0.08427	0.9874	0.1075
19	0.9-0.95	1.161	0.1384	1.199	0.118	1.21	0.1455
20	0.95-1	1.615	0.2103	1.322	0.1377	1.205	0.1626
21	1-1.2	1.259	0.1091	1.587	0.1135	1.5	0.1296
22	1.2-2	2.09	0.2438	2.881	0.2378	2.319	0.2177

3.73<V <4.3 1.76<Q²<4.2

1	0-0.05	0.8517	0.02212	0.6073	0.01467	0.4648	0.01599
2	0.05-0.1	0.6175	0.2	0.6066	0.01148	0.4625	0.01191
3	0.1-0.15	0.8684	0.1003	0.6047	0.07584	0.6314	0.125
4	0.15-0.2	0.8448	0.03846	0.6396	0.02562	0.4768	0.02389
5	0.2-0.25	0.8569	0.02577	0.6588	0.01884	0.4963	0.01887
6	0.25-0.3	0.8731	0.02499	0.6614	0.01736	0.5089	0.0179
7	0.3-0.35	0.8535	0.02458	0.7021	0.01872	0.5298	0.01913

8	0.35-0.4	0.8605	0.02634	0.6893	0.01907	0.5516	0.02016
9	0.4-0.45	0.9241	0.03052	0.694	0.02083	0.5407	0.02209
10	0.45-0.5	0.8621	0.03153	0.7461	0.02414	0.6106	0.02611
11	0.5-0.55	0.9478	0.03795	0.7719	0.02747	0.5963	0.02858
12	0.55-0.6	0.9316	0.04075	0.7941	0.03127	0.5952	0.0318
13	0.6-0.65	0.9902	0.04901	0.8347	0.03607	0.6258	0.03654
14	0.65-0.7	1.023	0.05571	0.8169	0.03954	0.6772	0.04282
15	0.7-0.75	0.9768	0.061	0.913	0.04963	0.736	0.05429
16	0.75-0.8	1.077	0.07777	0.9047	0.05417	0.8133	0.06503
17	0.8-0.85	0.9911	0.08095	1.042	0.07196	0.9814	0.09016
18	0.85-0.9	1.157	0.1046	1.22	0.09536	1.073	0.105
19	0.9-0.95	1.379	0.1502	1.392	0.1237	1.623	0.1772
20	0.95-1	1.392	0.174	1.592	0.1596	1.218	0.1521
21	1-1.2	1.63	0.1379	1.971	0.1355	2.254	0.1842
22	1.2-2	3.068	0.347	4.752	0.419	3.799	0.3741